



**ISSN: 2067-3809**

**ACTA TECHNICA  
CORVINIENSIS  
- Bulletin  
of Engineering**

**Tome XI [2018]  
Fascicule 4  
[October - December]**

**Editura Politehnica  
2018**



Edited by:

UNIVERSITY POLITEHNICA TIMISOARA



with kindly supported by:

THE GENERAL ASSOCIATION OF ROMANIAN ENGINEERS (AGIR)  
– branch of HUNEDOARA



Editor / Technical preparation / Cover design:

Assoc. Prof. Eng. KISS Imre, PhD.  
UNIVERSITY POLITEHNICA TIMISOARA,  
FACULTY OF ENGINEERING HUNEDOARA

Commenced publication year:  
2008

## ASSOCIATE EDITORS and REGIONAL COLLABORATORS

### MANAGER & CHAIRMAN

**ROMANIA**  **Imre KISS**, University Politehnica TIMIȘOARA, Faculty of Engineering HUNEDOARA, Department of Engineering & Management, General Association of Romanian Engineers (AGIR) – branch HUNEDOARA

### EDITORS from:

**ROMANIA**  **Dragoș UȚU**, University Politehnica TIMIȘOARA – TIMIȘOARA  
**Vasile ALEXA**, University Politehnica TIMIȘOARA – HUNEDOARA  
**Sorin Aurel RAȚIU**, University Politehnica TIMIȘOARA – HUNEDOARA  
**Vasile George CIOATĂ**, University Politehnica TIMIȘOARA – HUNEDOARA  
**Simona DZIȚAC**, University of Oradea – ORADEA  
**Valentin VLĂDUȚ**, Institute of Research-Development for Machines & Installations – BUCUREȘTI  
**Dan Ludovic LEMLE**, University Politehnica TIMIȘOARA – HUNEDOARA  
**Emanoil LINUL**, University Politehnica TIMIȘOARA – TIMIȘOARA  
**Virgil STOICA**, University Politehnica TIMIȘOARA – TIMIȘOARA  
**Cristian POP**, University Politehnica TIMIȘOARA – TIMIȘOARA  
**Sorin Ștefan BIRIȘ**, University Politehnica BUCUREȘTI – BUCUREȘTI  
**Mihai G. MATACHE**, Institute of Research-Development for Machines & Installations – BUCUREȘTI  
**Adrian DĂNILĂ**, “Transilvania” University of BRASOV – BRASOV

### REGIONAL EDITORS from:

**SLOVAKIA**  **Juraj ŠPALEK**, University of ŽILINA – ŽILINA  
**Peter KOŠTÁL**, Slovak University of Technology in BRATISLAVA – TRNAVA  
**Otakav BOKŮVKA**, University of ŽILINA – ŽILINA  
**Tibor KRENICKÝ**, Technical University of KOŠICE – PREŠOV  
**Beata HRICOVÁ**, Technical University of KOŠICE – KOŠICE  
**Peter KRIŽAN**, Slovak University of Technology in BRATISLAVA – BRATISLAVA

**HUNGARY**  **Tamás HARTVÁNYI**, Széchenyi István University in GYŐR – GYŐR  
**Arpád FERENCZ**, Pallasz Athéné University – KECSKEMÉT  
**József SÁROSI**, University of SZEGED – SZEGED  
**Attila BARCZI**, Szent István University – GÖDÖLLŐ  
**György KOVÁCS**, University of MISKOLC – MISKOLC  
**Zsolt Csaba JOHANYÁK**, Pallasz Athéné University – KECSKEMÉT  
**Gergely DEZSÓ**, College of NYÍREGYHÁZA – NYÍREGYHÁZA  
**Krisztián LAMÁR**, Óbuda University BUDAPEST – BUDAPEST  
**Loránt KOVÁCS**, Pallasz Athéné University – KECSKEMÉT  
**Valeria NAGY**, University of SZEGED – SZEGED  
**Sándor BESZÉDES**, University of SZEGED – SZEGED

**SERBIA**  **Zoran ANIŠIĆ**, University of NOVI SAD – NOVI SAD  
**Milan RACKOV**, University of NOVI SAD – NOVI SAD  
**Igor FÜRSTNER**, SUBOTICA Tech – SUBOTICA  
**Eleonora DESNICA**, University of NOVI SAD – ZRENJANIN  
**Blaža STOJANOVIĆ**, University of KRAGUJEVAC – KRAGUJEVAC  
**Aleksander MILTENOVIC**, University of NIŠ – NIŠ  
**Milan BANIC**, University of NIŠ – NIŠ  
**Slobodan STEFANOVIĆ**, Graduate School of Applied Professional Studies – VRANJE  
**Sinisa BIKIĆ**, University of NOVI SAD – NOVI SAD  
**Masa BUKUROV**, University of NOVI SAD – NOVI SAD  
**László GOGOLÁK**, SUBOTICA Tech – SUBOTICA  
**Ana LANGOVIC MILICEVIC**, University of KRAGUJEVAC – VRNJAČKA BANJA  
**Imre NEMEDI**, SUBOTICA Tech – SUBOTICA  
**Živko PAVLOVIĆ**, University of NOVI SAD – NOVI SAD

**BULGARIA**  **Krasimir Ivanov TUJAROV**, “Angel Kanchev” University of ROUSSE – ROUSSE  
**Ognyan ALIPIEV**, “Angel Kanchev” University of ROUSSE – ROUSSE  
**Ivanka ZHELEVA**, “Angel Kanchev” University of ROUSSE – ROUSSE  
**Atanas ATANASOV**, “Angel Kanchev” University of ROUSSE – ROUSSE

 CROATIA	Gordana BARIC, University of ZAGREB – ZAGREB Goran DUKIC, University of ZAGREB – ZAGREB
 BOSNIA & HERZEGOVINA	Tihomir LATINOVIC, University in BANJA LUKA – BANJA LUKA Sabahudin JASAREVIC, University of ZENICA – ZENICA Šefket GOLETIĆ, University of ZENICA – ZENICA
 POLAND	Jarosław ZUBRZYCKI, LUBLIN University of Technology – LUBLIN Maciej BIELECKI, Technical University of LODZ – LODZ Bożena GAJDZIK, The Silesian University of Technology – KATOWICE
 TURKEY	Önder KABAŞ, Akdeniz University – KONYAAALTI/Antalya
 CHINA	Yiwen JIANG, Military Economic Academy – WUHAN
 SPAIN	César GARCÍA HERNÁNDEZ, University of ZARAGOZA – ZARAGOZA
 GREECE	Apostolos TSAGARIS, Alexander Technological Educational Institute of THESSALONIKI – THESSALONIKI Panagiotis KYRATSISS, Western Macedonia University of Applied Sciences – KOZANI

The Editor and editorial board members do not receive any remuneration. These positions are voluntary. The members of the Editorial Board may serve as scientific reviewers.

We are very pleased to inform that our journal **ACTA TECHNICA CORVINIENSIS – Bulletin of Engineering** is going to complete its ten years of publication successfully. In a very short period it has acquired global presence and scholars from all over the world have taken it with great enthusiasm. We are extremely grateful and heartily acknowledge the kind of support and encouragement from you.

**ACTA TECHNICA CORVINIENSIS – Bulletin of Engineering** seeking qualified researchers as members of the editorial team. Like our other journals, **ACTA TECHNICA CORVINIENSIS – Bulletin of Engineering** will serve as a great resource for researchers and students across the globe. We ask you to support this initiative by joining our editorial team. If you are interested in serving as a member of the editorial team, kindly send us your resume to [redactie@fih.upt.ro](mailto:redactie@fih.upt.ro).



ISSN: 2067-3809

copyright © University POLITEHNICA Timisoara,  
Faculty of Engineering Hunedoara,  
5, Revolutiei, 331128, Hunedoara, ROMANIA  
<http://acta.fih.upt.ro>

# INTERNATIONAL SCIENTIFIC COMMITTEE MEMBERS and SCIENTIFIC REVIEWERS

## MANAGER & CHAIRMAN

**ROMANIA**  **Imre KISS**, University Politehnica TIMIȘOARA, Faculty of Engineering HUNEDOARA, Department of Engineering & Management, General Association of Romanian Engineers (AGIR) – branch HUNEDOARA

## INTERNATIONAL SCIENTIFIC COMMITTEE MEMBERS & SCIENTIFIC REVIEWERS from:

**ROMANIA**  **Viorel–Aurel ȘERBAN**, University Politehnica TIMIȘOARA – TIMIȘOARA  
**Teodor HEPUȚ**, University Politehnica TIMIȘOARA – HUNEDOARA  
**Caius PĂNOIU**, University Politehnica TIMIȘOARA – HUNEDOARA  
**Mircea BEJAN**, Tehnical University of CLUJ-NAPOCA – CLUJ-NAPOCA  
**Liviu MIHON**, University Politehnica TIMIȘOARA – TIMIȘOARA  
**Ilare BORDEAȘU**, University Politehnica TIMIȘOARA – TIMIȘOARA  
**Corneliu CRĂCIUNESCU**, University Politehnica TIMIȘOARA – TIMIȘOARA  
**Liviu MARȘAVIA**, University Politehnica TIMIȘOARA – TIMIȘOARA  
**Nicolae HERIȘANU**, University Politehnica TIMIȘOARA – TIMIȘOARA  
**Dumitru TUCU**, University Politehnica TIMIȘOARA – TIMIȘOARA  
**Valer DOLGA**, University Politehnica TIMIȘOARA – TIMIȘOARA  
**Ioan VIDA-SIMITI**, Technical University of CLUJ-NAPOCA – CLUJ-NAPOCA  
**Csaba GYENGE**, Technical University of CLUJ-NAPOCA – CLUJ-NAPOCA  
**Sava IANICI**, “Eftimie Murgu” University of REȘIȚA – REȘIȚA  
**Ioan SZÁVA**, “Transilvania” University of BRASOV – BRASOV  
**Liviu NISTOR**, Technical University of CLUJ-NAPOCA – CLUJ-NAPOCA  
**Sorin VLASE**, “Transilvania” University of BRASOV – BRASOV  
**Horatiu TEODORESCU DRĂGHICESCU**, “Transilvania” University of BRASOV – BRASOV  
**Maria Luminița SCUTARU**, “Transilvania” University of BRASOV – BRASOV  
**Iulian RIPOȘAN**, University Politehnica BUCUREȘTI – BUCUREȘTI  
**Ioan DZITAC**, Agora University of ORADEA – ORADEA  
**Daniel STAN**, University Politehnica TIMIȘOARA – TIMIȘOARA  
**Adrian STUPARU**, University Politehnica TIMIȘOARA – TIMIȘOARA  
**Corina GRUESCU**, University Politehnica TIMIȘOARA – TIMIȘOARA  
**Carmen ALIC**, University Politehnica TIMIȘOARA – HUNEDOARA  
**Dan GLĂVAN**, University “Aurel Vlaicu” ARAD – ARAD

**SLOVAKIA**  **Štefan NIZNIK**, Technical University of KOŠICE – KOŠICE  
**Karol VELIŠEK**, Slovak University of Technology BRATISLAVA – TRNAVA  
**Juraj ŠPALEK**, University of ŽILINA – ŽILINA  
**Ervin LUMNITZER**, Technical University of KOŠICE – KOŠICE  
**Miroslav BADIDA**, Technical University of KOŠICE – KOŠICE  
**Milan DADO**, University of ŽILINA – ŽILINA  
**Ladislav GULAN**, Slovak University of Technology – BRATISLAVA  
**Ľubomir ŠOOŠ**, Slovak University of Technology in BRATISLAVA – BRATISLAVA  
**Miroslav VEREŠ**, Slovak University of Technology in BRATISLAVA – BRATISLAVA  
**Milan SAGA**, University of ŽILINA – ŽILINA  
**Imrich KISS**, Institute of Economic & Environmental Security – KOŠICE  
**Michal CEHLÁR**, Technical University KOSICE – KOSICE  
**Pavel NEČAS**, Armed Forces Academy of General Milan Rastislav Stefanik – LIPTOVSKÝ MIKULÁŠ  
**Vladimir MODRAK**, Technical University of KOSICE – PRESOV  
**Michal HAVRILA**, Technical University of KOSICE – PRESOV

**CROATIA**  **Drazan KOZAK**, Josip Juraj Strossmayer University of OSIJEK – SLAVONKI BROD  
**Predrag COSIC**, University of ZAGREB – ZAGREB  
**Milan KLJAJIN**, Josip Juraj Strossmayer University of OSIJEK – SLAVONKI BROD  
**Miroslav CAR**, University of ZAGREB – ZAGREB  
**Antun STOIĆ**, Josip Juraj Strossmayer University of OSIJEK – SLAVONKI BROD  
**Ivo ALFIREVIĆ**, University of ZAGREB – ZAGREB

- GREECE**  Nicolaos VAXEVANIDIS, University of THESSALY – VOLOS
- HUNGARY**   
Imre DEKÁNY, University of SZEGED – SZEGED  
Béla ILLÉS, University of MISKOLC – MISKOLC  
Imre RUDAS, Óbuda University of BUDAPEST – BUDAPEST  
Tamás KISS, University of SZEGED – SZEGED  
Cecilia HODÚR, University of SZEGED – SZEGED  
Árpád FERENCZ, Pallasz Athéné University – KECSKEMÉT  
Imre TIMÁR, University of Pannonia – VESZPRÉM  
Kristóf KOVÁCS, University of Pannonia – VESZPRÉM  
Károly JÁRMAI, University of MISKOLC – MISKOLC  
Gyula MESTER, University of SZEGED – SZEGED  
Ádám DÖBRÖCZÖNI, University of MISKOLC – MISKOLC  
György SZEIDL, University of MISKOLC – MISKOLC  
István PÁCZELT, University of Miskolc – MISKOLC – BUDAPEST  
István JÓRI, BUDAPEST University of Technology & Economics – BUDAPEST  
Miklós TISZA, University of MISKOLC – MISKOLC  
Attila BARCZI, Szent István University – GÖDÖLLŐ  
István BIRÓ, University of SZEGED – SZEGED  
Gyula VARGA, University of MISKOLC – MISKOLC  
József GÁL, University of SZEGED – SZEGED  
Ferenc FARKAS, University of SZEGED – SZEGED  
Géza HUSI, University of DEBRECEN – DEBRECEN  
Ferenc SZIGETI, College of NYÍREGYHÁZA – NYÍREGYHÁZA  
Zoltán KOVÁCS, College of NYÍREGYHÁZA – NYÍREGYHÁZA
- BULGARIA**  Kliment Blagoev HADJOV, University of Chemical Technology and Metallurgy – SOFIA  
Nikolay MIHAILOV, “Anghel Kanchev” University of ROUSSE – ROUSSE  
Krassimir GEORGIEV, Institute of Mechanics, Bulgarian Academy of Sciences – SOFIA  
Stefan STEFANOV, University of Food Technologies – PLOVDIV
- SERBIA**   
Sinisa KUZMANOVIC, University of NOVI SAD – NOVI SAD  
Zoran ANIŠIĆ, University of NOVI SAD – NOVI SAD  
Mirjana VOJINOVIĆ MILORADOV, University of NOVI SAD – NOVI SAD  
Miroslav PLANČAK, University of NOVI SAD – NOVI SAD  
Milosav GEORGIJEVIC, University of NOVI SAD – NOVI SAD  
Vojislav MILTENOVIC, University of NIŠ – NIŠ  
Aleksandar RODIĆ, “Mihajlo Pupin” Institute – BELGRADE  
Milan PAVLOVIC, University of NOVI SAD – ZRENJANIN  
Radomir SLAVKOVIĆ, University of KRAGUJEVAC, Technical Faculty – CACAK  
Zvonimir JUGOVIĆ, University of KRAGUJEVAC, Technical Faculty – CACAK  
Branimir JUGOVIĆ, Institute of Technical Science of Serbian Academy of Science & Arts – BELGRAD  
Miomir JOVANOVIĆ, University of NIŠ – NIŠ  
Vidosav MAJSTOROVIC, University of BELGRADE – BELGRAD  
Predrag DAŠIĆ, Production Engineering and Computer Science – TRSTENIK  
Lidija MANČIĆ, Institute of Technical Sciences of Serbian Academy of Sciences & Arts – BELGRAD  
Vlastimir NIKOLIĆ, University of NIŠ – NIŠ  
Nenad PAVLOVIĆ, University of NIŠ – NIŠ
- ITALY**   
Alessandro GASPARETTO, University of UDINE – UDINE  
Alessandro RUGGIERO, University of SALERNO– SALERNO  
Adolfo SENATORE, University of SALERNO– SALERNO  
Enrico LORENZINI, University of BOLOGNA – BOLOGNA
- BOSNIA & HERZEGOVINA**   
Tihomir LATINOVIC, University of BANJA LUKA – BANJA LUKA  
Safet BRDAREVIĆ, University of ZENICA – ZENICA  
Ranko ANTUNOVIC, University of EAST SARAJEVO – East SARAJEVO  
Isak KARABEGOVIĆ, University of BIHAĆ – BIHAĆ
- MACEDONIA**   
Valentina GECEVSKA, University “St. Cyril and Methodius” SKOPJE – SKOPJE  
Zoran PANDILOV, University “St. Cyril and Methodius” SKOPJE – SKOPJE  
Robert MINOVSKI, University “St. Cyril and Methodius” SKOPJE – SKOPJE
- PORTUGAL**   
João Paulo DAVIM, University of AVEIRO – AVEIRO  
Paulo BÁRTOLO, Polytechnique Institute – LEIRIA  
José MENDES MACHADO, University of MINHO – GUIMARÃES

- SLOVENIA**  
 Janez GRUM, University of LJUBLJANA – LJUBLJANA  
Štefan BOJNEC, University of Primorska – KOPER
- POLAND**  
 Leszek DOBRZANSKI, Silesian University of Technology – GLIWICE  
Stanisław LEGUTKO, Polytechnic University – POZNAN  
Andrzej WYCISLIK, Silesian University of Technology – KATOWICE  
Antoni ŚWIC, University of Technology – LUBLIN  
Marian Marek JANCZAREK, University of Technology – LUBLIN  
Michał WIECZOROWSKI, POZNAN University of Technology – POZNAN  
Jarosław ZUBRZYCKI, LUBLIN University of Technology – LUBLIN  
Aleksander SŁADKOWSKI, Silesian University of Technology – KATOWICE  
Tadeusz SAWIK, Akademia Górniczo-Hutnicza University of Science & Technology – CRACOW
- AUSTRIA**  
 Branko KATALINIC, VIENNA University of Technology – VIENNA
- FRANCE**  
 Bernard GRUZZA, Universite Blaise Pascal – CLERMONT-FERRAND  
Abdelhamid BOUCHAIR, Universite Blaise Pascal – CLERMONT-FERRAND  
Khalil EL KHAMLICHI DRISSI, Universite Blaise Pascal – CLERMONT-FERRAND  
Mohamed GUEDDA, Université de Picardie Jules Verne – AMIENS  
Ahmed RACHID, Université de Picardie Jules Verne – AMIENS  
Yves DELMAS, University of REIMS – REIMS  
Jean GRENIER GODARD, L'ecole Superieure des Technologies et des Affaires – BELFORT  
Jean-Jacques WAGNER, Universite de Franche-Comte – BELFORT
- ARGENTINA**  
 Gregorio PERICHINSKY, University of BUENOS AIRES – BUENOS AIRES  
Atilio GALLITELLI, Institute of Technology – BUENOS AIRES  
Carlos F. MOSQUERA, University of BUENOS AIRES – BUENOS AIRES  
Elizabeth Myriam JIMENEZ REY, University of BUENOS AIRES – BUENOS AIRES  
Arturo Carlos SERVETTO, University of BUENOS AIRES – BUENOS AIRES
- SPAIN**  
 Patricio FRANCO, Universidad Politecnica de CARTAGENA – CARTAGENA  
Luis Norberto LOPEZ De LACALLE, University of Basque Country – BILBAO  
Aitzol Lamikiz MENTXAKA, University of Basque Country – BILBAO  
Carolina Senabre BLANES, Universidad Miguel Hernández – ELCHE
- CUBA**  
 Norge I. COELLO MACHADO, Universidad Central "Marta Abreu" LAS VILLAS – SANTA CLARA  
José Roberto Marty DELGADO, Universidad Central "Marta Abreu" LAS VILLAS – SANTA CLARA
- INDIA**  
 Sugata SANYAL, Tata Consultancy Services – MUMBAI  
Siby ABRAHAM, University of MUMBAI – MUMBAI  
Anjan KUMAR KUNDU, University of CALCUTTA – KOLKATA
- TURKEY**  
 Ali Naci CELIK, Abant Izzet Baysal University – BOLU  
Önder KABAŞ, Akdeniz University –KONYAALTI/Antalya
- CZECH REPUBLIC**  
 Ivo SCHINDLER, Technical University of OSTRAVA – OSTRAVA  
Jan VIMMR, University of West Bohemia – PILSEN  
Vladimir ZEMAN, University of West Bohemia – PILSEN
- ISRAEL**  
 Abraham TAL, University TEL-AVIV, Space & Remote Sensing Division – TEL-AVIV  
Amnon EINAV, University TEL-AVIV, Space & Remote Sensing Division – TEL-AVIV
- LITHUANIA**  
 Egidijus ŠARAUSKIS, Aleksandras Stulginskis University – KAUNAS  
Zita KRIAUCIŪNIENĖ, Experimental Station of Aleksandras Stulginskis University – KAUNAS
- FINLAND**  
 Antti Samuli KORHONEN, University of Technology – HELSINKI  
Pentti KARJALAINEN, University of OULU – OULU
- NORWAY**  
 Trygve THOMESSEN, Norwegian University of Science and Technology – TRONDHEIM  
Gábor SZIEBIG, Narvik University College – NARVIK  
Terje Kristofer LIEN, Norwegian University of Science and Technology – TRONDHEIM  
Bjoern SOLVANG, Narvik University College – NARVIK
- UKRAINE**  
 Sergiy G. DZHURA, Donetsk National Technical University – DONETSK  
Alexander N. MIKHAILOV, DONETSK National Technical University – DONETSK  
Heorhiy SULYM, Ivan Franko National University of LVIV – LVIV  
Yevhen CHAPLYA, Ukrainian National Academy of Sciences – LVIV

**SWEEDEN** Ingvar L. SVENSSON, JÖNKÖPING University – JÖNKÖPING



**BRAZIL**



Alexandro Mendes ABRÃO, Universidade Federal de MINAS GERAIS – BELO HORIZONTE

Márcio Bacci da SILVA, Universidade Federal de UBERLÂNDIA – UBERLÂNDIA

Sergio Tonini BUTTON, Universidade Estadual de CAMPINAS – CAMPINAS

Leonardo Roberto da SILVA, Centro Federal de Educação Tecnológica – BELO HORIZONTE

Juan Campos RUBIO, Universidade Federal de MINAS GERAIS – BELO HORIZONTE

**USA**



David HUI, University of NEW ORLEANS – NEW ORLEANS

**CHINA**



Wenjing LI, Military Economic Academy – WUHAN

Zhonghou GUO, Military Economic Academy – WUHAN

The Scientific Committee members and Reviewers do not receive any remuneration. These positions are voluntary.

We are extremely grateful and heartily acknowledge the kind of support and encouragement from all contributors and all collaborators!

**ACTA TECHNICA CORVINIENSIS – Bulletin of Engineering** is dedicated to publishing material of the highest engineering interest, and to this end we have assembled a distinguished Editorial Board and Scientific Committee of academics, professors and researchers.

**ACTA TECHNICA CORVINIENSIS – Bulletin of Engineering** publishes invited review papers covering the full spectrum of engineering. The reviews, both experimental and theoretical, provide general background information as well as a critical assessment on topics in a state of flux. We are primarily interested in those contributions which bring new insights, and papers will be selected on the basis of the importance of the new knowledge they provide.

**ACTA TECHNICA CORVINIENSIS – Bulletin of Engineering** encourages the submission of comments on papers published particularly in our journal. The journal publishes articles focused on topics of current interest within the scope of the journal and coordinated by invited guest editors. Interested authors are invited to contact one of the Editors for further details.

**ACTA TECHNICA CORVINIENSIS – Bulletin of Engineering** accept for publication unpublished manuscripts on the understanding that the same manuscript is not under simultaneous consideration of other journals. Publication of a part of the data as the abstract of conference proceedings is exempted.

Manuscripts submitted (original articles, technical notes, brief communications and case studies) will be subject to peer review by the members of the Editorial Board or by qualified outside reviewers. Only papers of high scientific quality will be accepted for publication. Manuscripts are accepted for review only when they report unpublished work that is not being considered for publication elsewhere.

The evaluated paper may be recommended for:

- **ACCEPTANCE without any changes** – in that case the authors will be asked to send the paper electronically in the required .doc format according to authors' instructions;
- **ACCEPTANCE with minor changes** – if the authors follow the conditions imposed by referees the paper will be sent in the required .doc format;
- **ACCEPTANCE with major changes** – if the authors follow completely the conditions imposed by referees the paper will be sent in the required .doc format;
- **REJECTION** – in that case the reasons for rejection will be transmitted to authors along with some suggestions for future improvements (if that will be considered necessary).

The manuscript accepted for publication will be published in the next issue of **ACTA TECHNICA CORVINIENSIS – Bulletin of Engineering** after the acceptance date.

All rights are reserved by **ACTA TECHNICA CORVINIENSIS – Bulletin of Engineering**. The publication, reproduction or dissemination of the published paper is permitted only by written consent of one of the Managing Editors.

All the authors and the corresponding author in particular take the responsibility to ensure that the text of the article does not contain portions copied from any other published material which amounts to plagiarism. We also request the authors to familiarize themselves with the good publication ethics principles before finalizing their manuscripts.



ISSN: 2067-3809

copyright © University POLITEHNICA Timisoara,  
Faculty of Engineering Hunedoara,  
5, Revolutiei, 331128, Hunedoara, ROMANIA  
<http://acta.fih.upt.ro>

## TABLE of CONTENTS

1.	Dávid GÖNCZI – HUNGARY ANALYSIS OF ROTATING FUNCTIONALLY GRADED DISKS WITH ARBITRARY MATERIAL PROPERTIES	11
2.	Modestus O. OKWU, Bright EDWARD, Thaddeus C. NWAHOHA, Kingsley C. EZEKIEL – NIGERIA / UNITED KINGDOM CRACK DETECTION IN STRUCTURES USING VIBRATION MODAL PARAMETERS AND TIME DOMAIN RESPONSE	17
3.	Mihaela OSACI – ROMANIA COMPARATIVE STUDY OF SOME TERRESTRIAL ATMOSPHERE MODELS IN HYDROSTATIC BALANCE	25
4.	Dominika PALAŠČÁKOVÁ – SLOVAKIA NUMERICAL SYSTEMS IN THE LEARNING PROCESS	29
5.	Ákos CSERVENÁK – HUNGARY MOTION PLANNING FOR AUTOMATED GUIDED VEHICLE	33
6.	A.O. AKINOLA, A. OYETUNJI – NIGERIA EFFECTS OF DIFFERENT ENVIRONMENTS ON THE CORROSION PROPERTIES OF WELDED MILD STEEL PLATE	39
7.	Predrag ŽIVKOVIĆ, Mladen TOMIĆ, Dragana DIMITRIJEVIĆ JOVANOVIĆ, Dušan PETKOVIĆ, Jelena JANEVSKI, Mirko DOBRNJAC – SERBIA / BOSNIA & HERZEGOVINA WIND ENERGY IN JABLANICA-TOPLICA REGION OF SOUTH SERBIA	43
8.	Vitalii PANCHUK, Oleh ONYSKO, Iuliia MEDVID – UKRAINE TECHNOLOGY OF THE OIL AND GAS DRILL PIPE CONNECTOR MANUFACTURING WITH LOW-PERMEABILITY LEVEL OF THE DRILLING MUD IN ITS SCREW PART	47
9.	Sinisa KUZMANOVIC, Zlatko BUNDALO, Dušanka BUNDALO, Boris NEDIC – BOSNIA & HERZEGOVINA APPLICATION OF DRIVE-BY-WIRE CONCEPT AND CAN PROTOCOL IN AUTOMOBILES	55
10.	Yilmaz UYAROGLU, Selcuk EMIROGLU – TURKEY ANALYSIS AND FORMING MECHANISM OF A NEW CHAOTIC ATTRACTOR	63
11.	Pavel KOVAC, Mirfad TARIC, Dragan RODIC, Borislav SAVKOVIC, Dušan JESIC, Dušan GOLUBOVIC – SERBIA / BOSNIA & HERZEGOVINA NEURO-FUZZY SYSTEMS MODELLING OF HARD STEEL SURFACE ROUGHNESS PARAMETERS	67
12.	O.A. ADETAYO, O.A. BUCKNOR – NIGERIA COMPARATIVE STUDY ON THE EFFECT OF GRINDED RICE HUSK AND RICE HUSK ASH ON COMPRESSIVE STRENGTH OF CONCRETE	73
13.	P. Jaya PRAKASH, S. Sunil Kumar REDDY – INDIA STUDY ON DI DIESEL ENGINE SUBSTITUTED WITH GROOVED PISTON AND POWERED USING NANO ADDITIVE BIODIESEL	77
14.	B.S. LUKA, J.A. JAPHET, P.A. DAUDA – NIGERIA SINGLE LAYER DRYING CHARACTERISTICS OF HOSPITAL TOO FAR LEAVES ( <i>JATROPHA TANJORENSIS</i> ) UNDER OPEN SUN AND IN SOLAR DRYER	83
15.	Iliia ZUMBILEV, Angel ZUMBILEV – BULGARIA STUDYING THE POSSIBILITY THE ACOUSTIC EMISSION TO BE APPLIED IN THE PROCESSES OF MATERIALS DESTRUCTION	89

16.	S.E. UWADIAE, O.E. IHAZA – NIGERIA OPTIMIZATION OF PROCESS PARAMETERS IN TREATMENT OF BREWERY EFFLUENT	95
17.	Irena Barbara JAŁMUŻNA, Jan KROLIKOWSKI, Justyna SAŁATA – POLAND METHODOLOGY OF RAPID VERIFICATION OF WORK STANDARDS	101
18.	Mihai–Paul TODOR, Ciprian BULEI, Imre KISS – ROMANIA AN OVERVIEW ON KEY TRENDS IN COMPOSITE MATERIALS CONTINUOUS INNOVATION AND IMPROVEMENTS WITH FOCUS ON COMPOSITES BASED ON CELLULOSE FIBERS	107
19.	Ishaque KHAN, Lalsingh KHALSA, Vinod VARGHESE – INDIA UNSTEADY-STATE HEAT CONDUCTION PROBLEM ON A THICK CIRCULAR PLATE AND ITS ASSOCIATED THERMAL STRESSES	113
20.	M.A. BODUDE, R.N. NNAJI, L.O. OSOBA – NIGERIA COMPARATIVE STUDIES ON THE HIGH TEMPERATURE OXIDATION BEHAVIOUR OF HAYNES 282 AND INCONEL 718 NICKEL–BASED SUPERALLOYS	119
21.	Sorina Gabriela ȘERBAN – ROMANIA REINTRODUCTION OF IRON–CONTAINING WASTE AND STEEL ALLOYING ELEMENTS INTO THE ECONOMIC CIRCUIT	127
22.	Samir REMLI, Aissa BENSELHOUB, Issam ROUAIGUIA – ALGERIA / UKRAINE EXPERIMENTATION OF A BLASTING THEORY FOR THE DIGGING OF AN UNDERGROUND HORIZONTAL EXCAVATION FROM BOUKHADRA IRON MINE (EASTERN ALGERIA)	133
23.	S.I. ADEDOKUN, M.A. ANIFOWOSE, S.O. ODEYEMI – NIGERIA ASSESSMENT OF STEEL SLAG AS REPLACEMENT FOR COARSE AGGREGATE IN CONCRETE: A REVIEW	139
24.	Ciprian BULEI, Mihai–Paul TODOR, Imre KISS – ROMANIA RESEARCHES ON IDENTIFYING SOLUTIONS, DESIGNING AND IMPLEMENTING INNOVATIVE TECHNOLOGIES FOR RECYCLING AND REUSE OF NON–FERROUS METAL BASED RAW MATERIALS	147
25.	Y.L. SHUAIB-BABATA, Y.O. BUSARI, R.A. YAHYA, J. M. ABDUL – NIGERIA CORROSION INHIBITION OF AISI 1007 STEEL IN HYDROCHLORIC ACID USING <i>CUCUMIS SATIVUS</i> (CUCUMBER) EXTRACTS AS GREEN INHIBITOR	153
***	MANUSCRIPT PREPARATION – GENERAL GUIDELINES	163

The ACTA TECHNICA CORVINIENSIS – Bulletin of Engineering, Tome XI [2018], Fascicule 4 [October – December] include original papers submitted to the Editorial Board, directly by authors or by the regional collaborators of the Journal. Also, the ACTA TECHNICA CORVINIENSIS – Bulletin of Engineering, Tome XI [2018], Fascicule 4 [October – December], includes scientific papers presented in the sections of the following scientific events:

— The INTERNATIONAL CONFERENCE ON APPLIED SCIENCES – ICAS 2018, organized by UNIVERSITY POLITEHNICA TIMISOARA, Faculty of Engineering Hunedoara (ROMANIA) and UNIVERSITY OF BANJA LUKA, Faculty of Mechanical Engineering (BOSNIA & HERZEGOVINA), in cooperation with the Academy of Romanian Scientists, Academy of Sciences Republic of Srpska, Academy of Technical Sciences of Romania – Timisoara Branch and General Association of Romanian Engineers – Hunedoara Branch, in Banja Luka, BOSNIA & HERZEGOVINA, 9–11 May 2018. The current identification numbers of the papers are the #7–11, according to the present contents list.

— The 9<sup>th</sup> INTERNATIONAL CONFERENCE “MANAGEMENT OF TECHNOLOGY – STEP TO SUSTAINABLE PRODUCTION” – MOTSP 2017, organized by Faculty of Mechanical Engineering and Naval Architecture of the University of Zagreb (CROATIA) and University North, Varaždin (CROATIA), in Dubrovnik, CROATIA, 5–7 April 2017. The current identification number of the selected paper is the # 17, according to the present contents list.



ISSN: 2067-3809

copyright © University POLITEHNICA Timisoara,  
Faculty of Engineering Hunedoara,  
5, Revolutiei, 331128, Hunedoara, ROMANIA  
<http://acta.fih.upt.ro>

# ANALYSIS OF ROTATING FUNCTIONALLY GRADED DISKS WITH ARBITRARY MATERIAL PROPERTIES

<sup>1</sup>University of Miskolc, Institute of Applied Mechanics, Miskolc, HUNGARY

**Abstract:** This paper deals with the steady-state thermoelastic problem of functionally graded rotating disks and rings with arbitrary thickness profile and material distribution within the structural component. The material properties are arbitrary functions of the radial coordinate and the temperature field. The thin disk is subjected to axisymmetric mechanical and thermal loads. The linear thermoelastic problem is solved by multilayered approach in two steps, in which the solution of the thermal part of the problem and the solution of the pure mechanical problem with constant pressure and body forces are presented. The superposition of these solutions is used to solve the original problem. The temperature field is determined by the solution of the heat conduction problem using finite difference method. The results are compared to finite element simulations.

**Keywords:** FGM, thermoelastic, arbitrary properties, temperature dependency

## INTRODUCTION

As technology progresses at an ever increasing rate, the need for advanced materials becomes a priority in the engineering of more complex systems. This need can be seen in many fields in which engineers are exploring the applications of these new materials, such as composites or functionally graded materials. Functionally Graded Materials (FGMs) are advanced material in which the composition and structure gradually change resulting in a corresponding change in the properties of the material. In functionally graded materials the sharp interfaces between the constituent materials –which are present in composites- are eliminated. Although one of most advanced manufacturing method of FGMs known as solid freeform (SFF) method, where the components is built layer by layer. To produce bulk functionally graded components –such as disks or rings with special profile- the laser based SFF methods are utilized generally, such as 3D printing, laser cladding based method (Fig. 1), selective laser sintering and selective laser melting. SFF involves five basic steps, which are the generation of CAD data from CAD software, conversion of the CAD data to Standard Triangulation Language (STL) file, slicing the geometry (STL) into two dimensional cross section profiles, creating the component layer by layer, and the finishing operation –due to poor surface quality.

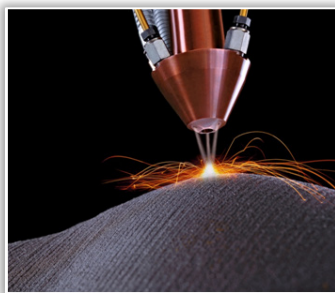


Figure 1. Additive manufacturing of FGM components  
[www.amcor-project.eu, (2018)]

Some textbooks such as Timoshenko and Goodier [1], Barber [2], Solecki and Conant [3], Baroumi and Ragab [4], Hetnarski and Eslami [5], Noda et. al [6] gave detailed analysis for the thermal stress problem for isotropic elastic disks with axisymmetric temperature field. Furthermore these books and papers [1-6] neglect the convective heat exchange on the lower and upper plane surfaces of the disks. Numerous papers, such as [7-11], present thermomechanical problems of functionally graded disks but the material parameters are special functions of the radial coordinate.

In a papers by Pen, X. and Li, X. [12] the thermoelastic problem of isotropic functionally graded disk with arbitrary radial non-homogeneity was considered. The numerical solution of the steady-state thermoelastic problem was reduced to a solution of a Fredholm integral equation.

Zamani N. and Rahimi [13] investigated thermal and mechanical stresses under plane stress and generalized plane strain assumptions. Concerning the stress analysis of cylindrical and spherical structural elements, Tutuncu and Temel [14] presented a novel approach to the stress analysis of pressurized FGM disks, cylindrical bodies and spheres. In these axisymmetric problems the displacements and stresses of functionally graded hollow cylinders, disks and spheres subjected to constant internal pressure were calculated using plane elasticity theory and complementary functions method.

A paper by Gönczi and Ecsedi [15] tackled the thermoelastic problems of radially graded thin disks with constant thickness and arbitrary material properties, although the body forces coming from the rotation and the temperature dependency were neglected. Multilayered approach is an effective way to approximate complex problems and solve them faster and more easily. Papers [16-18] deals with the problem of heterogeneous curved structural components, and demonstrate the efficiency and versatility of multilayered structures. Paper [19] dealt with the problem of multilayered

spherical pressure vessels using the superposition of the solutions of the problem with the thermal and with the mechanical boundary conditions.

This paper tackles the steady-state problem of rotating radially graded thin disks and rings mounted on a cylindrical body, and subjected to combined axisymmetric temperature field and constant pressure. All of the material parameters are arbitrary functions of the radial coordinate  $r$  and temperature (such as  $E=E(r, T(r))$ ), while the thickness of the disk is arbitrary function of radial coordinate. The sketch of the thermoelastic problem of a functionally graded rotating disk is displayed in Figure 2. The inner radius of the disk is denoted by  $a$ , the outer radius is  $b$  and the thickness is denoted by  $w(r)$ . Figure 2 shows the boundary conditions and the loading. For this problem a cylindrical coordinate system  $(r\phi z)$  will be used. There are thermal boundary conditions of the third-kind prescribed on the inner and outer cylindrical surfaces, furthermore there are no internal heat sources.  $\gamma_a$  and  $\gamma_b$  denote the heat transfer coefficients on the boundary surfaces ( $r=a$  and  $r=b$ , respectively).  $T_{ea}$  and  $T_{eb}$  are the environment temperatures at the inner and outer cylindrical surfaces, respectively. If  $\gamma \rightarrow \infty$ , then we have thermal boundary conditions of the first-kind on these surfaces.

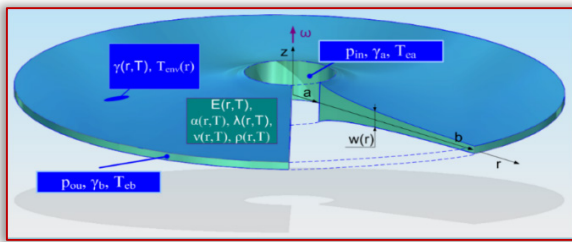


Figure 2. The disk with the loading and thermal boundary conditions

On the other two boundary surfaces the environmental temperatures are arbitrary functions of the radial coordinate. Let's assume that the heat transfer coefficient  $\gamma = \gamma(r, T(r))$  is coordinate and temperature-dependent. The angular velocity  $\omega$  is constant,  $p_{in}$  is the constant pressure exerted on the inner boundary surface, while  $p_{ou}$  is the constant outer pressure. The problem of the previously presented functionally graded disk will be solved based on the equations of the steady-state heat conduction, the field equations of the thermoelasticity and an approximate multilayered model will be used.

### CALCULATION OF THE TEMPERATURE FIELD

The approximate model can be seen in Fig. 3. The number of layers is denoted by  $n$ , the layers have constant thicknesses where  $w_i > 0$ , furthermore the material properties are discretized too. It is assumed, that the layers are perfectly bonded. Let the index  $i$  denote the quantities of the  $i$ -th layer. At first let's discretize the geometry of the disk and the thermal boundary conditions.

$$\begin{aligned} R_{mi} &= \frac{R_i + R_{i+1}}{2}, \lambda_i(T) = \lambda(r=R_{mi}, T), \\ \gamma_i &= \gamma(r=R_{mi}, T), w_i = w(r=R_{mi}), \\ t_{env,i} &= T_{env}(r=R_{mi}), i=1, \dots, n, \end{aligned} \quad (1)$$

where  $\lambda$  denotes the thermal conductivity,  $t$  denotes the specific values of the temperature function at certain radial coordinate values.

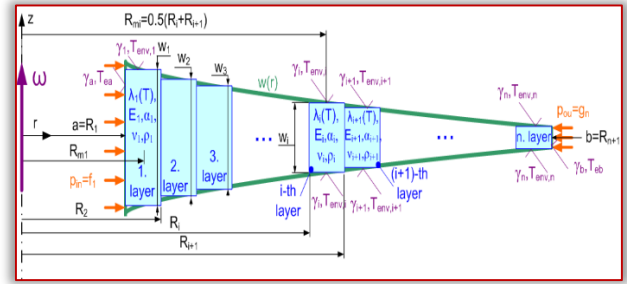


Figure 3. The approximate model of the functionally graded disk For this case the nonlinear differential equation for the temperature field of the  $i$ -th layer  $(T_i(r))$  has the following form [20]:

$$\frac{1}{r} \frac{d}{dr} \left( r \lambda_i \frac{dT_i}{dr} \right) - \frac{2\gamma_i}{w_i} (T_i - t_{env,i}) = 0. \quad (2)$$

Finding the closed form analytical solution for differential Eq. (2) is very hard, therefore a numerical method will be utilized to solve it. The points of the temperature field will be calculated with finite difference method. The nonlinear system of equations (with  $m$  points in each layer, the number of layers is  $n$ ) for the whole model can be expressed as:

$$\begin{aligned} 0 &= \frac{\lambda_i(T=t_{k+(i-1)m})}{a+(i-1)d_m + k\Delta r} \frac{t_{k+(i-1)m} - t_{k+(i-1)m-1}}{\Delta r} + \\ &+ \frac{t_{k+(i-1)m} - t_{k+(i-1)m-1}}{\Delta r} \frac{d\lambda_i(T=t_{k+(i-1)m})}{dr} + \\ &+ \frac{t_{k+(i-1)m+1} - 2t_{k+(i-1)m} + t_{k+(i-1)m-1}}{\Delta r^2} \lambda_i(T=t_{k+(i-1)m}) - \\ &- \frac{2\gamma_i(T=t_{k+(i-1)m})}{w_i} (t_{k+(i-1)m} - t_{env,i}), \end{aligned} \quad (3)$$

$$\begin{aligned} \text{where } d_m &= \frac{b-a}{n}, \Delta r = \frac{b-a}{nm}, \\ i &= 1, \dots, n, \text{ while } k = 1, \dots, m-1. \end{aligned}$$

In many cases the effective material properties can be expressed as a nonlinear functions of the temperature [21]:

$$M_p(T) = P_0(P_{-1}t^{-1} + 1 + P_1t + P_2t^2 + P_3t^3). \quad (4)$$

In Eq. (4)  $M_p(T)$  denotes the function of the considered effective material property,  $P_0, P_{-1}, P_1, P_2$  and  $P_3$  are material dependent coefficients of absolute temperature  $t$  in [K]. Using these results we can present functions for the temperature- and position-dependent functionally graded material parameters [21]:

$$M_p(r, T) = [M_p_1(T) - M_p_2(T)] [G(r)]^m + M_p_2(T) \quad (5)$$

$$\text{e.g. for disks or spheres: } G(r) = \frac{r-a}{b-a},$$

furthermore, indices 1 and 2 denote the constituent materials – in many cases metal and ceramic components. If the thermal conductivity has the form of Eqs. (4,5) then we write for the previous system of nonlinear Eqs. (3):

$$\lambda_i (T=t_{k+(i-1)m}) = K_{0,i} + K_{-1,i} t_{k+(i-1)m}^{-1} + K_{1,i} t_{k+(i-1)m} + K_{2,i} t_{k+(i-1)m}^2 + K_{3,i} t_{k+(i-1)m}^3, \quad (6)$$

$$\frac{d\lambda_i (T=t_{k+(i-1)m})}{dr} = (-K_{-1,i} t_{k+(i-1)m}^{-2} + 2K_{2,i} t_{k+(i-1)m} + K_{1,i} + 3K_{3,i} t_{k+(i-1)m}^2) \frac{t_{k+(i-1)m} - t_{k+(i-1)m-1}}{\Delta r}, \quad (7)$$

where

$$K_{-1,i} = (P_1^1 \lambda_0^1 - P_1^2 \lambda_0^2) \times G(r=R_{mi}) + P_1^2 \lambda_0^2, \quad (8)$$

$$K_{0,i} = (\lambda_0^1 - \lambda_0^2) \times G(r=R_{mi}) + \lambda_0^2,$$

$$K_{1,i} = (P_1^1 \lambda_0^1 - P_1^2 \lambda_0^2) \times G(r=R_{mi}) + P_1^2 \lambda_0^2,$$

$$K_{2,i} = (P_2^1 \lambda_0^1 - P_2^2 \lambda_0^2) \times G(r=R_{mi}) + P_2^2 \lambda_0^2,$$

$$K_{3,i} = (P_3^1 \lambda_0^1 - P_3^2 \lambda_0^2) \times G(r=R_{mi}) + P_3^2 \lambda_0^2,$$

where  $\lambda_0^j$  ( $j=1,2$ : number of the constituent material) are material constants. We assume that the surface temperatures of the adjacent layers are equal and the radial heatflow  $q$  is constant.

$$-w_i \lambda_i (T=t_{(i-1)m}) \frac{t_{(i-1)m+1} - t_{(i-1)m}}{\Delta r} = -w_{i-1} \lambda_{i-1} (T=t_{(i-1)m}) \frac{t_{(i-1)m} - t_{(i-1)m-1}}{\Delta r}, \quad (9)$$

$$= -w_{i-1} \lambda_{i-1} (T=t_{(i-1)m}) \frac{t_{(i-1)m} - t_{(i-1)m-1}}{\Delta r}, \quad i=2, \dots, n.$$

From the third-kind thermal boundary conditions it follows that

$$\frac{t_2 - t_1}{\Delta r} - (t_1 - t_{env,a}) w_1 (T=t_1) = 0, \quad (10)$$

$$\frac{t_{nm} - t_{nm-1}}{\Delta r} + (t_{nm} - t_{env,b}) w_n (T=t_{nm}) = 0.$$

The points of the temperature field can be calculated from the nonlinear system of equations (3), (9) and (10). Then a polynomial curve can be fitted to these calculated values (via least squares method), for power-law distributions and for smaller power index values ( $m < 7$ ) we can use

$$T_{appr} = J_6 r^6 + J_5 r^5 + J_4 r^4 + J_3 r^3 + J_2 r^2 + J_1 r + J_0 + J_{-1} r^{-1} + J_{-2} r^{-2} + J_{-3} r^{-3}. \quad (11)$$

### THE SOLUTION OF THE THERMOELASTIC PROBLEM

In our case the time dependency of the problem is neglected, and the thermoelastic problem is uncoupled which means that previously determined temperature field is an input function for the field equations of the boundary value problem of linear elasticity and  $Mp_f(r, T(r)) \rightarrow Mp_f(r)$ . The thermoelastic problem will be divided into two parts, then the principle of superposition will be used to solve it.

Using the approximate temperature field, the material parameters for each layer can be discretized as

$$E_i = E(r=R_{mi}, T=t_{mi}), \quad (12)$$

$$v_i = v(r=R_{mi}, T=t_{mi}),$$

$$\alpha_i = \alpha(r=R_{mi}, T=t_{mi}),$$

$$\rho_i = \rho(r=R_{mi}, T=t_{mi}),$$

$$i=1, \dots, n,$$

where  $E$  is the modulus of elasticity,  $v$  is Poisson's ratio,  $\alpha$  is the coefficient of linear thermal expansion and  $\rho$  denotes the density of the material. At first we consider the case when the  $i$ -th layer is under thermal loading and has a steady-state temperature field, furthermore the boundary surfaces of the layers are assumed to be traction free. The  $u_i^T(r)$  thermal radial displacement function and the  $\sigma_{rr,i}^T(r)$ ,  $\sigma_{\varphi\varphi,i}^T(r)$  thermal stresses can be determined as [22]:

$$u_i^T(r) = \frac{1+v_i}{r} \alpha_i \int_{R_i}^r r T_i(r) dr + \frac{(1+v_i)R_i^2 + (1-v_i)r^2}{r(R_{i+1}^2 - R_i^2)} \alpha_i \int_{R_i}^{R_{i+1}} r T_i(r) dr, \quad (13)$$

$$\sigma_{rr,i}^T(r) = \frac{\alpha_i E_i}{R_{i+1}^2 - R_i^2} \left( 1 - \frac{R_i^2}{r^2} \right) \int_{R_i}^{R_{i+1}} r T_i(r) dr - \frac{\alpha_i E_i}{r^2} \int_{R_i}^r r T_i(r) dr, \quad (14)$$

$$\sigma_{\varphi\varphi,i}^T(r) = E_i \alpha_i \left[ \frac{1}{r^2} \int_{R_i}^r r T_i(r) dr - T_i(r) + \frac{1}{R_{i+1}^2 - R_i^2} \left( \frac{R_i^2}{r^2} + 1 \right) \int_{R_i}^{R_{i+1}} r T_i(r) dr \right], \quad i=1, \dots, n. \quad (15)$$

The sketch of a layer is illustrated in Fig. 4.

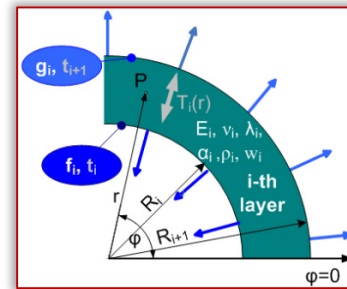


Figure 4. The sketch of a quarter of the  $i$ -th layer. We will assume that there are constant mechanical loading  $f_i = \sigma_{rr,i}^M(R_i)$  and  $g_i = \sigma_{rr,i}^M(R_{i+1})$  on the inner and outer cylindrical boundary surfaces of the  $i$ -th layer. The differential equation of the radial displacement field can be derived from the basic equation of linear elasticity for the plane stress state of thin disks (equilibrium equation, kinematic equations and stress-strain relations):

$$\frac{d\sigma_{rr}}{dr} + \frac{\sigma_{rr} - \sigma_{\varphi\varphi}}{r} + \omega^2 pr = 0, \quad (16)$$

$$\varepsilon_{rr} = \frac{du}{dr}, \quad \varepsilon_{\varphi\varphi} = \frac{u}{r}, \quad (17)$$

$$\sigma_{rr} = \frac{E}{1-\nu^2} [\varepsilon_{rr} + \nu \varepsilon_{\varphi\varphi} - \alpha(1+\nu)T],$$

$$\sigma_{\varphi\varphi} = \frac{E}{1-\nu^2} [\nu \varepsilon_{rr} + \varepsilon_{\varphi\varphi} - \alpha(1+\nu)T].$$

$$\frac{d^2 u_i^M(r)}{dr^2} + \frac{du_i^M(r)}{dr} \frac{1}{r} - \frac{u_i^M(r)}{r^2} + K_i r = 0, \quad (18)$$

$$K_i = \frac{(1-\nu_i^2) \rho_i \omega^2}{E_i}.$$

After solving Eq. (18) we get the following expressions for the displacement field and the normal stresses:

$$u_i^M(r) = C_i r + \frac{B_i}{r} - \frac{K_i}{8} r^3, \quad (19)$$

$$\sigma_{rr,i}^M(r) = \frac{E_i C_i}{1-\nu_i} - \frac{E_i B_i}{1+\nu_i} \frac{1}{r^2} - A_i r^2, \quad (20)$$

$$A_i = \frac{E_i (3+\nu_i) K_i}{8(1-\nu_i^2)},$$

$$\sigma_{\varphi\varphi,i}^M(r) = \sigma_{\varphi\varphi,i}^M(r) = \frac{E_i C_i}{1-\nu_i} + \frac{E_i B_i}{1+\nu_i} \frac{1}{r^2} - A_i r^2, \quad (21)$$

$i=1, \dots, n.$

Using the equations of the boundary conditions, the unknown parameters  $B_i$  and  $C_i$  can be determined:

$$B_i = \frac{(1+\nu_i) R_{i+1}^2 R_i^2 (A_i (R_i^2 - R_{i+1}^2) + f_i - g_i)}{E_i (R_i^2 - R_{i+1}^2)}, \quad (22)$$

$$C_i = \frac{(1-\nu_i) (A_i (R_i^4 - R_{i+1}^4) + R_{i+1}^2 g_i - R_i^2 f_i)}{E_i (R_i^2 - R_{i+1}^2)}. \quad (23)$$

The superposition principle is utilized for this problem, because both the previously used field equations and the boundary conditions are linear. This means that we can add the stresses and displacements caused by the mechanical loading (8-13) to the thermal stresses and displacements (13-15) in order to solve this problem. For the computation of the combined loads the following equations are used:

$$u_i(r) = u_i^T(r) + u_i^M(r), \quad (24)$$

$$\sigma_{rr,i}(r) = \sigma_{rr,i}^T(r) + \sigma_{rr,i}^M(r), \quad (25)$$

$$\sigma_{\varphi\varphi,i}(r) = \sigma_{\varphi\varphi,i}^T(r) + \sigma_{\varphi\varphi,i}^M(r), \quad i=1, \dots, n. \quad (26)$$

The unknown parameters  $f_i$  ( $i=2 \dots n$ ) and  $g_i$  ( $i=1 \dots n-1$ ) in the equations (19-23) can be calculated from the following system of equations

$$u_i(R_{i+1}) = u_{i+1}(R_{i+1}), \quad i=1, \dots, n-1, \quad (27)$$

which ensure the continuity of the radial displacement field furthermore  $f_1$  and  $g_n$  are given.

$$\sigma_{rr,1}(R_1) = f_1 = -p_{in}, \quad (28)$$

$$\sigma_{rr,n}(R_{n+1}) = g_n = -p_{ou}.$$

The system of equations (27) has the following form with  $2(n-1)$  equations:

$$\begin{aligned} & u_{i+1}^T(R_{i+1}) - u_i^T(R_{i+1}) = \\ & \left[ \frac{(1-\nu_i)(A_i(R_{i+1}^4 - R_i^4) + R_{i+1}^2 g_i - R_i^2 f_i)}{E_i(R_i^2 - R_{i+1}^2)} R_{i+1} + \right. \\ & \left. + \frac{(1+\nu_i) R_{i+1}^2 R_i^2 (A_i(R_i^2 - R_{i+1}^2) + f_i - g_i)}{E_i(R_i^2 - R_{i+1}^2) R_{i+1}} - \frac{K_i}{8} R_{i+1}^3 \right] - \\ & \left[ \frac{(1-\nu_{i+1})(A_{i+1}(R_{i+1}^4 - R_{i+2}^4) + R_{i+2}^2 g_{i+1} - R_{i+1}^2 f_{i+1})}{E_{i+1}(R_{i+1}^2 - R_{i+2}^2)} R_{i+1} + \right. \\ & \left. + \frac{(1+\nu_{i+1}) R_{i+1}^2 R_{i+2}^2 (A_{i+1}(R_{i+1}^2 - R_{i+2}^2) + f_{i+1} - g_{i+1})}{E_{i+1}(R_{i+1}^2 - R_{i+2}^2) R_{i+1}} - \frac{K_{i+1}}{8} R_{i+1}^3 \right], \quad g_i = \frac{w_{i+1}}{w_i} f_{i+1}. \end{aligned} \quad (29)$$

Using the previously determined parameters  $f_i$ ,  $g_i$  and equations (24-26) the radial displacements and the normal stresses of the multilayered body can be calculated. Due to

the multilayered model the curve of the tangential normal stress function may contain significant steps, but in certain cases there are certain point where the stress values have good accuracy. For example the middle points of the layers of a disk with constant thickness ( $w=\text{const.}$ ) have the least errors, thus fitting an approximate curve is recommended.

## NUMERICAL EXAMPLES

In this section a numerical example is presented for rotating radially graded disks with a prescribed  $w(r)$  thickness and temperature-dependent material properties. The results of the presented methods are compared to results obtained by finite element simulation in Abaqus. The following numerical data will be used for the computations:

$$a=0.1\text{m}, b=0.3\text{m}, w=0.0115-0.025r \text{ [m]},$$

$$T_{env}(r)=398(r-0.09)^{0.01} a^{-0.01} - t_{ref} \text{ [K], [K]},$$

$$T_{in}=100\text{K}, T_{ou}=400\text{K}, t_{ref}=273\text{K}, m=3 \text{ and for } \lambda$$

$$\text{and } \gamma: m_1=2.3, p_{in}=60\text{MPa}, p_{ou}=0\text{MPa}, \omega=400 \text{ rad/s.}$$

Table 1 contains the material properties of the constituent materials based on Eqs. (4) and (5). Figure 5 shows that the temperature field of thin disks depends only on the radial coordinate by these symmetric boundary conditions.

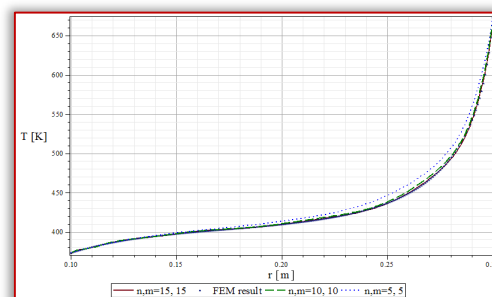
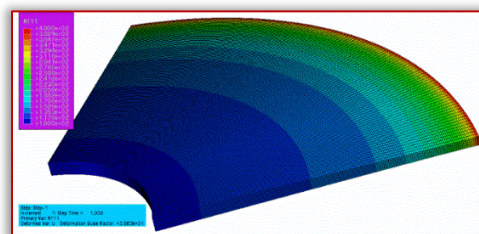


Figure 5. The finite element model with the absolute temperature field and the graphs

Table 1. Material properties of the FGM

Material Property (MPa)	Material (1)			
	$P_{m0}$	$P_{m1}(10^{-3})$	$P_{m2}(10^{-7})$	$P_{m3}(10^{-10})$
$\lambda(\text{W/mK})$	15.39	-2.364	20.92	-7.223
$\gamma(\text{W/m}^2\text{K})$	10	0	0	0
$\rho(\text{kg/m}^3)$	7200	0.3079	-6.53	0
$\alpha(1/\text{K})$	$12.33 \cdot 10^{-6}$	0.8086	0	0
$E(\text{Pa})$	$2.01 \cdot 10^{11}$	0.3079	-6.53	0
$\nu(-)$	0.326	-0.1	0.38	0
(MPa)	Material (2)			
	$P_{c0}$	$P_{c1}(10^{-3})$	$P_{c2}(10^{-7})$	$P_{c3}(10^{-11})$
$\lambda(\text{W/mK})$	1.7	-0.1276	0.06648	-1
$\gamma(\text{W/m}^2\text{K})$	2	0	0	0
$\rho(\text{kg/m}^3)$	$10^4$	-0.307	2.16	-8.946
$\alpha(1/\text{K})$	$3.87 \cdot 10^{-6}$	0.909	0	0
$E(\text{Pa})$	$3.484 \cdot 10^{11}$	-0.31	2.16	-8.94
$\nu(-)$	0.24	0	0	0

The results of the displacements and normal stresses are in good agreement as it can be seen in Figs. 6-8. The approximation of the normal stresses can improve the accuracy of the multilayered method. For the finite element calculations Abaqus CAE FE software was used. The two dimensional axisymmetric model can be seen in Fig. 6, the method of modelling is similar to the one presented in paper [23].

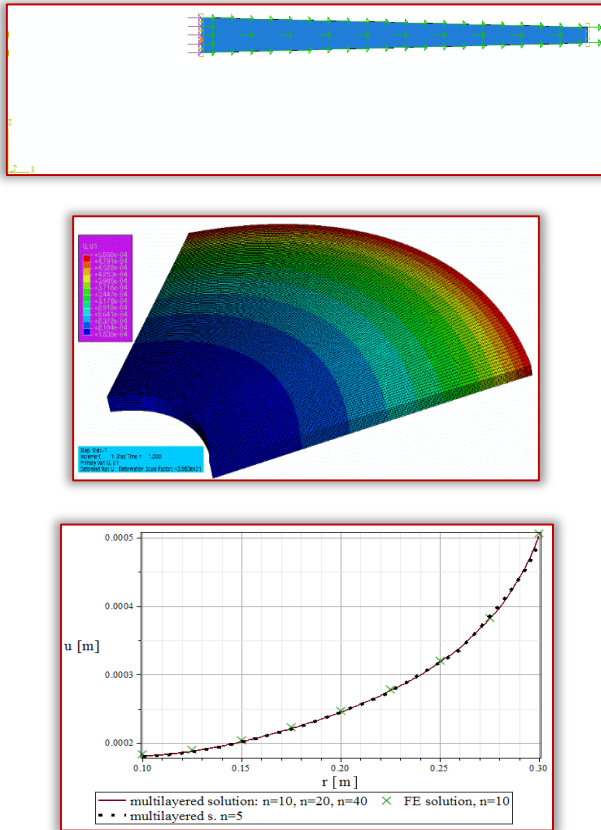


Figure 6. The finite element model of the disk with the radial displacement and the graphs of the different solutions

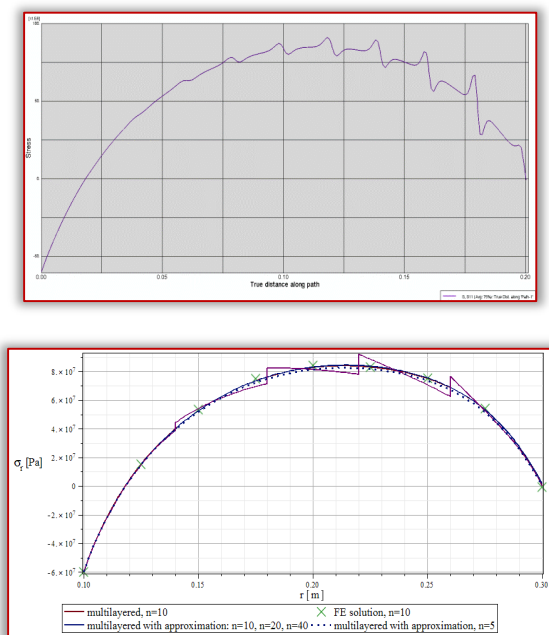


Figure 7. The radial normal stresses within the radially graded disk

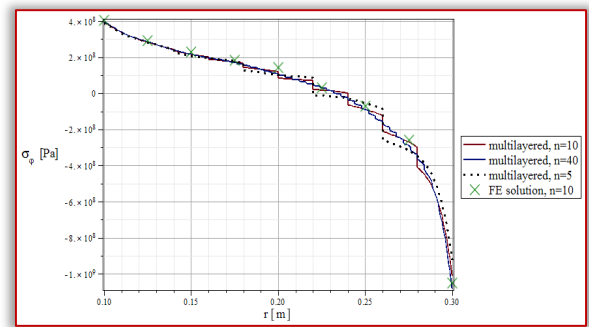
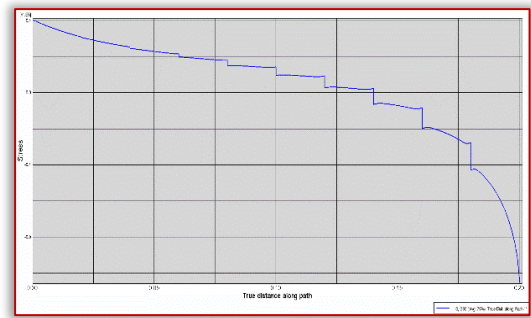


Figure 8. The graphs of the tangential normal stresses. For disks with complicated thickness function, we can use different point –where the relative errors are small- to fit approximate curves to them. For example in this numerical problem, the average values of the tangential stresses at the boundary surfaces of the layers have decent accuracy.

**CONCLUSIONS**

A steady-state thermoelastic problem of radially graded thin disks subjected to combined mechanical and thermal loads was solved based on a multilayered approach and the principle of superposition. The thickness of the disk was an arbitrary function of the radial coordinate, while the material properties were arbitrary functions of the radial coordinate and the temperature field. The temperature field was calculated using the method of finite differences, and was only the function of the radial coordinate.

The results were compared to finite element calculations and they were in good agreement. One of the advantages of the method presented in this paper -over FEM- is the speed of the calculation for the elasticity problem and the accuracy of the method can be improved with properly chosen approximate function. Furthermore finite element software are expensive, out of reach for small- and medium-sized companies which makes other numerical solutions more desirable.

**References**

- [1] Timoshenko S., Goodier I. N.: Theory of Elasticity, McGraw-Hill, New York, 1951.
- [2] Barber I. N.: Intermediate Mechanics of Materials, 2nd edition, Springer, New York, 2011.
- [3] Solecki R., Conant R, I.: Advanced Mechanics of Materials, Oxford University Press, Oxford, 2003.
- [4] Ragab A. R., Bayoumi S. E.: Engineering Solid Mechanics (Fundamentals and Applications), CRC Press, London, 1999.
- [5] Hetnarski, R. B., Eslami, M. R.: Thermal Stresses – Advanced Theory and Applications, Springer, New York, 2010.

- [6] Noda N., Hetnarski R. B. and Tanigawa Y.: Thermal Stresses. Lastran Corporation, Rochester, New York, 2000.
- [7] Loghman A., Ghorbanpour A. A., Shajari R. A., Amir s.: Time-dependent thermoelastic creep analysis of rotating disk made of Al-SiC composite. *Archive of Applied Mechanics*, Springer, 81 (12), 1853-1864, 2011.
- [8] Afsar A. M., Go J.: Finite element analysis of thermoelastic field in a rotating FGM circular disk. *Applied Mathematical Modelling*, Elsevier, 34(11), 3309-3320, 2010.
- [9] Hassani A., Hojjati M. H., Mahdavi E., Alashti R. A., Farrahi G.: Thermo-mechanical analysis of rotating disks with non-uniform thickness and material properties. *International Journal of Pressure Vessels and Piping*, Elsevier, 98., 95-101, 2012.
- [10] Dhamirchelli M., Azadi M.: Temperature and thickness effects on thermal and mechanical stresses of rotating FG-disks. *Journal of Mechanical Science and Technology*, Springer, pp. 11-23., 2011.
- [11] Vivio F., Vullo V., Cifani P.: Theoretical stress analysis of rotating hyperbolic disk without singularities subjected to thermal load. *Journal of Thermal Stresses*. 37, 117–136., 2014.
- [12] Pen X., Li X.: Thermoelastic analysis of functionally graded annulus with arbitrary gradient, *Applied Mathematics and Mechanics* (English Edition), 1211-1220, 2009.
- [13] Zamani N. M., Rahimi G.H.: Deformations and stresses in rotating FGM pressurized thick hollow cylinder under thermal load. *Sci. Res. Essay*, 4(3), 131–140, 2009.
- [14] Tutuncu N., Temel B.: A novel approach to stress analysis of pressurized FGM cylinders, disks and spheres. *Compos. Struct.*, 91, 385–390, 2009.
- [15] Gönczi D., Ecsedi I.: Thermoelastic analysis of functionally graded hollow circular disk. *Achieve of Mechanical Engineering*, Vol 62. (1), 5-18, 2015.
- [16] Kiss L.P., Szeidl Gy.: Vibrations of pinned-fixed heterogeneous circular beams pre-loaded by a vertical force at the crown point, *Journal of Sound and Vibration*, Vol 393.C, 92-113, 2017.
- [17] Kiss L.P., Szeidl Gy.: In-plane stability of fixed-fixed heterogeneous curved beams under a concentrated radial load at the crown point, *Technische Mechanik*, Vol 35 (1), 31-48, 2015.
- [18] Lengyel Á., Ecsedi I.: Analysis of bimetallic beam with weak shear connection. *Acta Technica Corviniensis – Bulletin of Engineering*, Vol 9. (3), 85-90, 2016.
- [19] Gönczi D.: The determination of displacement field and normal stresses in multilayered spherical bodies. XXVIII. MicroCAD International Scientific Conference, Miskolci Egyetem (ME), Paper D35, 2014.
- [20] Carslaw H. S., Jaeger I. C.: *Conduction of Heat in solids*, Clarendon Press, Oxford, 1959.
- [21] Shen H-S. *Functionally Graded Materials: Nonlinear Analysis of Plates and Shells*. CRC Press, London, 2009.
- [22] Boley B. A., Weiner J. H.: *Theory of Thermal Stresses*, John Wiley & Sons Inc., New York, 1960.
- [23] Gönczi D., Ecsedi I.: Finite element modelling of functionally graded spherical pressure vessels. *Annals of Faculty of Engineering Hunedoara- International Journal of Engineering*, Vol 12. (2), 179-184, 2014.



ISSN: 2067-3809

copyright © University POLITEHNICA Timisoara,  
Faculty of Engineering Hunedoara,  
5, Revolutiei, 331128, Hunedoara, ROMANIA  
<http://acta.fih.upt.ro>

<sup>1</sup>Modestus O. OKWU, <sup>1</sup>Bright EDWARD, <sup>2</sup>Thaddeus C. NWAHOHA, <sup>3</sup>Kingsley C. EZEKIEL

## CRACK DETECTION IN STRUCTURES USING VIBRATION MODAL PARAMETERS AND TIME DOMAIN RESPONSE

<sup>1</sup>Mechanical Engineering Department, Federal University of Petroleum Resources Effurun, Warri, Delta State, NIGERIA

<sup>2</sup>Marine Engineering Department, Federal University of Petroleum Resources Effurun, Warri, Delta State, NIGERIA

<sup>3</sup>Department of Maintenance Engineering and Asset Management, School of Mechanical, Aerospace and Civil Engineering, Manchester, UNITED KINGDOM

**Abstract:** Detection of cracks in engineering materials, structures and machines at the early stage is an important issue of concern in the field of engineering. Cracks often occur first on the surface of concrete structures under load and provide an indication for further degradation. Fatigue can have significant influence on crack. It is therefore imperative to detect crack at the early stage to avoid catastrophic effects. For this reason, a number of methods have been developed by researchers to meet this objective. In this paper, a simple cantilever beam was considered to detect the presence of crack from measured vibration data. A beam with crack at different locations and another beam without crack were considered for the experiments. At different crack locations, natural frequencies, mode shapes and acceleration responses were determined. It was found that natural frequencies and mode shapes gave no significant presence of crack but time domain acceleration response method was able to detect the presence of crack.

**Keywords:** Modal parameters; natural frequencies; mode space; time domain; acceleration response; crack detection

### INTRODUCTION

The ability to monitor the health of structures and detect damages at the earliest stage is of great importance to industries for variety of reasons. For this reason, various crack detection techniques have been proposed by researchers [1,2]. Research is also ongoing in the area of damage detection. Significant efforts have been made by scientists and researchers in the last few years to develop non-destructive techniques (NDT) that can reliably detect faults, diagnose the type of faults, localize the fault, determine its severity and predict the remaining life of structures. Literatures show that vibration based technique is one of the methods that is widely used for damage recognition in a beam like dynamic structure.

In order to detect a crack, the whole component requires scanning which becomes uneconomical for long beams and pipelines which are widely used in bridges, power plants, railway etc. This makes the process tedious, time consuming and costly [3]. Traditional localized NDT methods for crack detection in machine and structural components pose some drawbacks. It is paramount that the location of the damage is identified and the exact area of the structural component being scrutinized is easily accessible [4]. However, global vibration based damage detection methods provide an accurate, timely, non-destructive and inexpensive means of locating or detecting cracks [5,6]. According to [7], about 80% of failures of rotating machinery lead to significant changes in vibration. By examining these changes, fault detection can be determined from the vibration data [8]. The change in vibration parameters e.g. reduction in the natural frequency, mode shapes, stiffness and increase in damping therefore

becomes a major source of information available from the machinery for fault detection and diagnosis [2,3]. [8] posited that crack or damages in structures especially overloaded zones is potential due to operation of members of engineering structures under loading conditions. Therefore, for assessment of structural integrity, performance and safety, it is suitable to monitor changes in response parameters of structures.

Cracks regarded as physical discontinuity in the geometry of structures changes the dynamic behavior of a component [6,9]. They may be as a result of fatigue, mechanical defects, environmental effects or faults from manufacturing process; cracks however could be on the surface or inside the material [10,11]. The presence of cracks and its location can be characterized by change in its vibration parameters. It is therefore the purpose of this paper to present a parametric study aimed at investigating the suggested methods for crack detection.

### CRACK DETECTION METHODS

As reviewed from literature, the presence of crack changes the vibration parameters of dynamic systems. [6] classified them as modal and structural parameters. According to them, the modal parameters include: mode shapes, modal frequencies and modal damping values. On the other hand, the structural parameters include: mass and damping matrices, stiffness or flexibility. According to [12], structural parameters pose some limitations, which include low sensitivity to initial tiny damage in structure, measurement of parameters are expensive and time consuming. While the modal parameters is based on online measurement, detection of small damages may be possible, measures

vibration response at few locations in the structure, done without affecting production in industrial settings and interference from other structures are minimal. Using vibration response to determine damages in structures proofs to be efficient as seen from the extensive review by [13], where time-domain approach was used.

In this work, the crack modelling suggested by [14] have been used. The model is the Euler-Bernoulli beam element for the Finite Element (FE) modelling with some modification in local flexibility within the cracked region. This method is simpler and deals with the crack location and depth directly. FE model of a cantilever beam was carried out and the natural frequencies and mode shapes were calculated for both healthy and faulty states of the beam. The changes in modal parameter were analysed and used for the estimation of the presence and location of crack; to show the applicability and efficiency of the vibration modal parameters for crack detection. All simulations were done using MATLAB.

### — Changes in Natural Frequencies

[2] conducted a deep search considering multiple crack discovery method in moving parts of structures and beams. This was achieved by constant monitoring of natural frequency to predict the depth and crack location of the existing structure. According to [9], the natural frequency of a system changes noticeably due to the presence of crack, and these significant changes is subject to the location and size of cracks. They further scrutinized that when crack locations are constant i.e. at specific crack location, the natural frequencies of a cracked or fractured beam are inversely proportional to the depth of the crack. It was further observed that the variation in frequencies is not only a function of crack depth, and crack location, but also a change in the mode number. Similar results were also reported by [15].

[8] reported that during crack location in systems and structures, natural frequencies are comparatively easier and far more accurate to measure than other modal parameters. It is reported in literature that most researchers used this method since the reduction in natural frequencies can be detected easily [16]. Hence, this method will be used to validate the applicability and effectiveness of crack detection.

### — Changes in Mode Shapes

[8] demonstrated the use of mode shape to identify damages in structure. They reported that the mode shape of a structure is a function of the physical properties of that structure in a given system. Also, the variations in the physical properties of a structure as a result of fault will affect or cause a drastic change in the mode shape of that structure. [17], used the variations in alternation of mode shape as an investigative constraint to identify the presence of damage in a structure (using a steel plate model). Though the mode shapes of a structure are sensitive to small damages than the natural frequencies; one notable drawback in adopting the mode shape based method is that accuracy in measurement is critically subject to the distribution and volume of available sensors [3]. Hence, a comparison between the mode shapes

of healthy and faulty state of the structure is examined to validate the use of this technique for crack detection.

### — Time Domain Responses

[13] established and formulated a time domain function for effective prediction of cracks and damages in structures and beams using compiled dataset from the linear beam-oscillator dynamic interaction. The proficiencies of this established invention was extended to include the likelihood of the cracked and damaged beam structure undergoing nonlinear vibration. Hence, the time domain acceleration responses would be used to estimate the presence of crack for the healthy and cracked beam.

### RESULTS AND DISCUSSION

Euler Bernoulli Beam element is used for constructing the finite element model of the cantilever beam. The beam was divided into 12 elements and each element has two degree of freedom, one rotational and one translation. Hence, the total degree of freedom (DOF) is 26. Figure 1 shows the cantilever and Table 1 gives its properties. The details of the finite element (FE) modeling, response computation and crack breathing simulation can be found in [1].

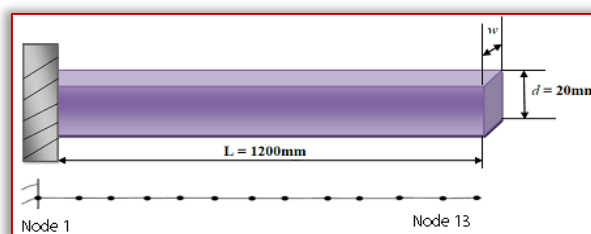


Figure 1. FE Modelling and dynamic behaviour of cantilever beam  
Table 1: Properties of the cantilever beam

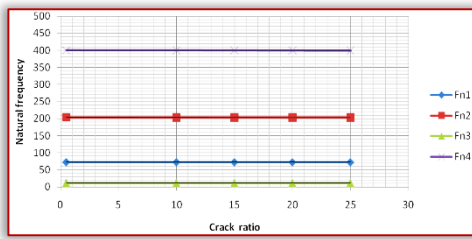
Boundary condition	Cantilever
Young Modules, E	210e09 N/m <sup>2</sup>
Mass Density	7800 kg/m <sup>3</sup>
Beam length, L	1200 mm
Beam width, w	20 mm
Beam depth, d	20 mm

The different crack location  $x_c$  where measurements were taken varied from 0.05 to 0.65mm in steps of 0.20mm with the crack ratio,  $(C_r = d_c / d)$ , which varies from 0 to 0.25 in steps of 0.5.

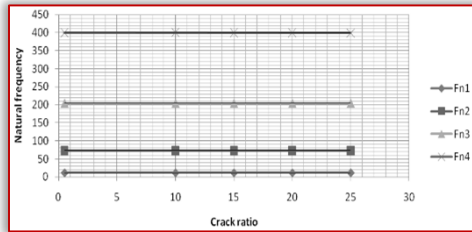
### — Natural Frequency

The natural frequencies for the different crack locations and sizes calculated are presented in Table 2 and represented graphically in Figures 2.

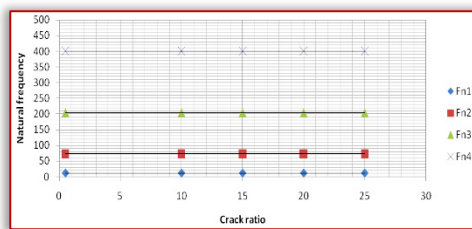
From Table 2 and Figure 2, it was observed that the changes in natural frequencies from the healthy state of the beam to the damaged state at the different crack location is very small and do not provide enough information to aid crack detection. They do not indicate the change in the natural frequencies clearly, hence for clear observation, these natural frequencies were re-arranged as given in Tables 3-6 for all cases for Mode 1 to Mode 4 respectively and also represented in the 3D plot as shown in Figures 3-6. In the 3D plot, x-axis, y-axis and z-axis represents the crack location, crack ratio and modes respectively.



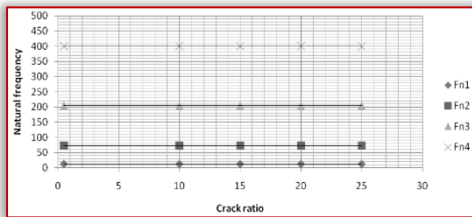
(a)



(b)



(c)



(d)

Figure 2. Natural frequencies vs crack ratio for the 4 different crack locations: a)  $x_c = 50\text{mm}$ ; b)  $x_c = 250\text{mm}$ ; c)  $x_c = 450\text{mm}$ ; d)  $x_c = 650\text{mm}$   
Table 2: Changes in Natural Frequency at Different Crack Locations

Cases	Crack Location	Crack ratio (Cr)%	Natural frequency fn1 (Hz)	Natural frequency fn2 (Hz)	Natural frequency fn3 (Hz)	Natural frequency fn4 (Hz)
1	50	0	11.637	72.925	204.21	400.28
2	50	5	11.633	72.908	204.17	400.24
3	50	10	11.623	72.862	204.08	400.12
4	50	15	11.606	72.789	203.94	399.93
5	50	20	11.585	72.694	203.75	399.96
6	50	25	11.559	72.579	203.53	399.41
7	250	0	11.637	72.925	204.21	400.28
8	250	5	11.634	72.908	204.19	400.23
9	250	10	11.629	72.862	204.16	400.08
10	250	15	11.619	72.789	204.10	399.84
11	250	20	11.607	72.694	204.02	399.54
12	250	25	11.592	72.579	204.02	399.17
13	450	0	11.637	72.925	204.21	400.28
14	450	5	11.636	72.918	204.19	400.28
15	450	10	11.633	72.897	204.12	400.27
16	450	15	11.628	72.865	203.03	400.25
17	450	20	11.622	72.822	203.90	400.24
18	450	25	11.615	72.771	203.75	400.22
19	650	0	11.637	72.925	204.21	400.28
20	650	5	11.636	72.912	204.20	400.23
21	650	10	11.635	72.874	204.19	400.08
22	650	15	11.634	72.816	204.17	399.84
23	650	20	11.632	72.739	204.15	399.54
24	650	25	11.629	72.646	204.11	399.17

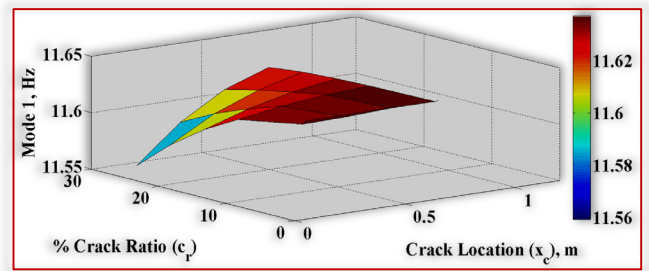


Figure 3. Variation of the first natural frequency with crack location and size

From Figure 3, it was observed that the highest frequency is the frequency of the beam at the healthy state whereas the lowest natural frequency occurs at the point when the crack is located at 50mm of the beam length with a crack ratio of 20%. The difference between the two natural frequencies is:  $11.635 - 11.606 = 0.031$  Hz.

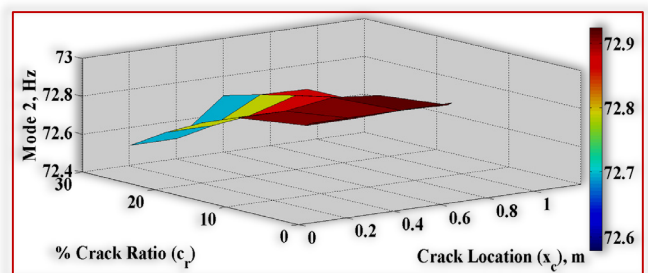


Figure 4. Variation of the second natural frequency with crack location and size

From Figure 4, it is observed that the highest frequency is the frequency of the beam at healthy state, whereas, the lowest natural frequency occurs at the point when the crack is located at 50mm of the beam length with a crack ratio is 25%. The difference between the two natural frequencies is:  $72.925 - 72.579 = 0.346$  Hz.

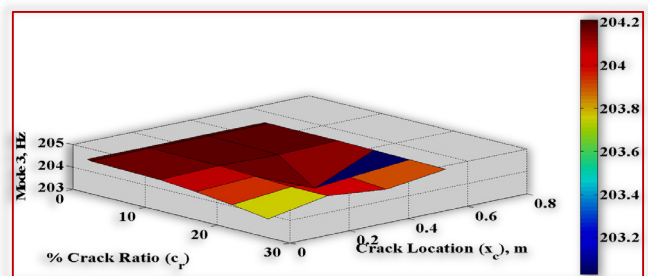


Figure 5. Variation of the third natural frequency with crack location and size

The highest frequency is the frequency of the beam at healthy state, whereas, the lowest natural frequency occurs at the point when the crack located at 450 mm of the beam length with a crack ratio is 15%. The difference between the two natural frequencies is:  $204.21 - 203.03 = 1.18$  Hz.

From Figure 6, it is observed that the highest frequency is the frequency of the beam at healthy state, whereas, the lowest natural frequency occurs at the point when the crack location is  $x_c = 250$  mm and 650 mm and crack ratio is 25%. The difference between the two natural frequencies is:  $73.00 - 71.89 = 1.11$  Hz.

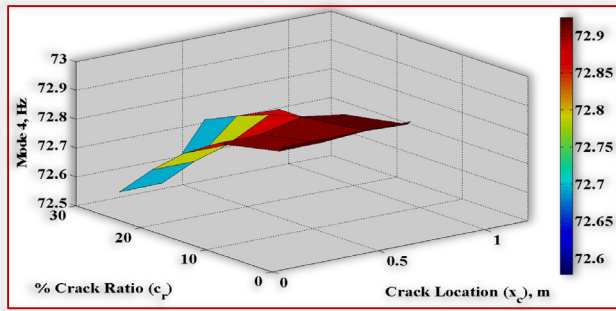


Figure 6. Variation of the fourth natural frequency with crack location and size

From the analysis of the natural frequencies, it was gathered that the changes in natural frequencies is very small ( $< 2\text{Hz}$ ) and it is only noticeable at the fixed end of the beam. Hence, crack detection by changes in natural frequencies is not possible due to the insignificant changes in natural frequencies.

Table 3: The First Natural Frequency

Crack location, $x_c$	50mm	250mm	450mm	650mm
Natural Freq. Hz	$fn_1$	$fn_1$	$fn_1$	$fn_1$
Crack ratio				
0	11.637	11.637	11.637	11.637
0.5	11.633	11.634	11.636	11.636
10	11.623	11.629	11.633	11.635
15	11.606	11.619	11.628	11.634
20	11.585	11.607	11.622	11.632
25	11.559	11.592	11.615	11.629

Table 4: Second Natural Frequency

Crack location, $x_c$	50mm	250mm	450mm	650mm
Natural Freq Hz	$fn_2$	$fn_2$	$fn_2$	$fn_2$
Crack ratio				
0	72.925	72.925	72.925	72.925
0.5	72.908	72.908	72.918	72.912
10	72.862	72.862	72.897	72.874
15	72.789	72.789	72.865	72.816
20	72.694	72.694	72.822	72.739
25	72.579	72.579	72.771	72.646

Table 5: Third Natural Frequency

Crack location, $x_c$	50mm	250mm	450mm	650mm
Natural Freq Hz	$fn_3$	$fn_3$	$fn_3$	$fn_3$
Crack ratio				
0	204.21	204.21	204.21	204.21
0.5	204.17	204.19	204.19	204.20
10	204.08	204.16	204.12	204.19
15	203.94	204.10	203.03	204.17
20	203.75	204.02	203.90	204.15
25	203.53	204.02	203.75	204.11

Table 6: Fourth Natural Frequency

Crack location, $x_c$	50mm	250mm	450mm	650mm
Natural Freq Hz	$fn_4$	$fn_4$	$fn_4$	$fn_4$
Crack ratio				
0	400.28	400.28	400.28	400.28
0.5	400.24	400.23	400.28	400.23
10	400.12	400.08	400.27	400.08
15	399.93	399.84	400.25	399.84
20	399.96	399.54	400.24	399.54
25	399.41	399.17	400.22	399.17

### MODE SHAPES

Few typical mode shapes are shown in Figures 7-9 for 3 different cases: Case 1, 8, and 15.

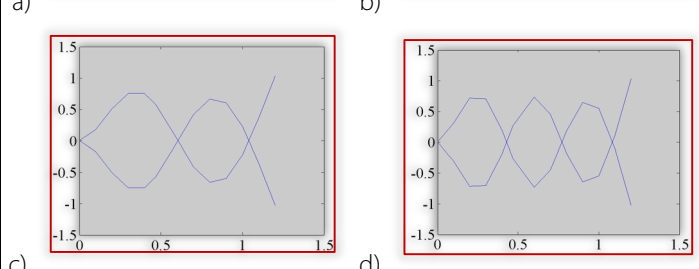
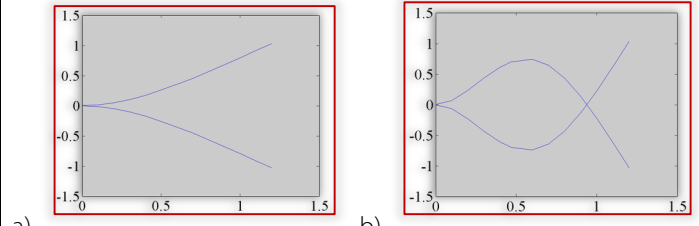


Figure 7. Mode shape for Case 1 (Healthy): (a) Mode shape 1; (b) Mode shape 2; (c) Mode shape 3; (d) Mode Shape 4

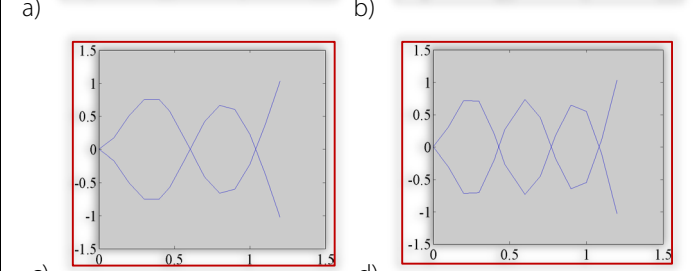
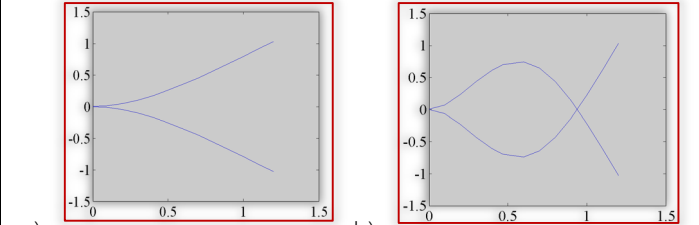


Figure 8. Mode shape for Case 8 ( $x_c = 250\text{mm}$ ,  $c_r = 5\%$ ): (a) Mode shape 1; (b) Mode shape 2; (c) Mode shape 3; (d) Mode Shape 4

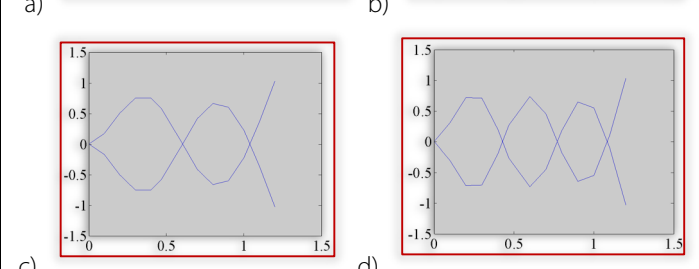
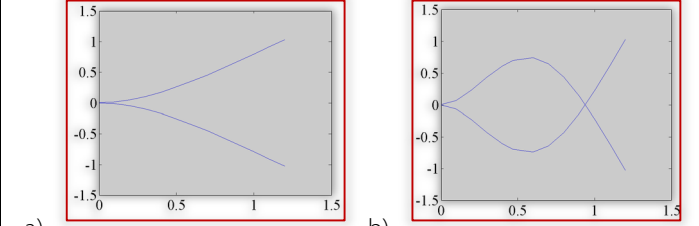


Figure 9. Mode shape for crack case 15 ( $x_c = 450\text{mm}$ ,  $c_r = 10\%$ ): (a) Mode shape 1; (b) Mode shape 2; (c) Mode shape 3; (d) Mode Shape 4

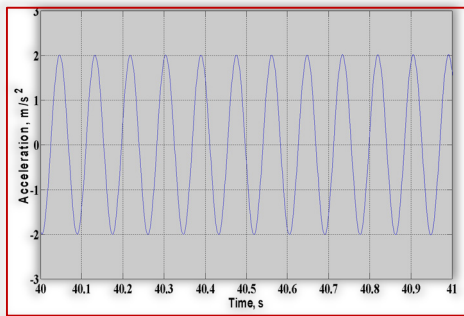
### ACCELERATION RESPONSE

The changes in the natural frequencies and mode shapes were insignificant which makes detection of crack location and size difficult using this method. Hence, there was need

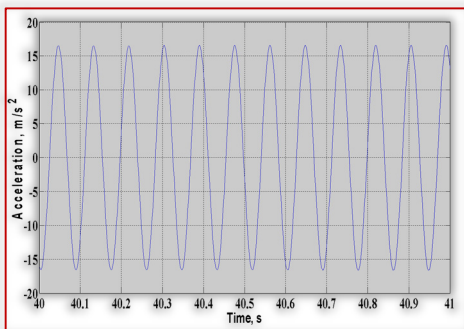
to explore other methods of crack detection. The simulation is carried out for both the healthy state (Case 1) and for crack in different locations (Case 8, 15 and 22) as presented in Table 7, for which comparisons between the healthy and faulty states were made from Figures 10-13.

Table 7: The four cases used for further analysis

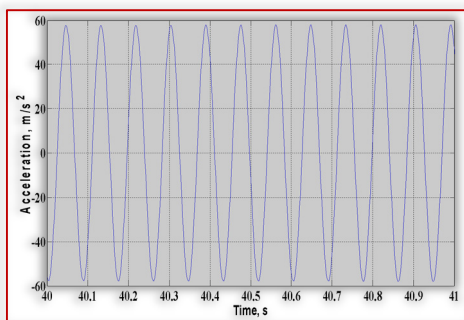
Case	Crack location ( $x_c$ )mm	Crack ratio ( $C_r$ ) %
1	50	0
8	250	5
15	450	10
22	650	15



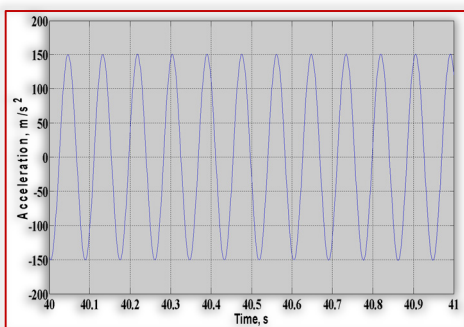
(a)



(b)



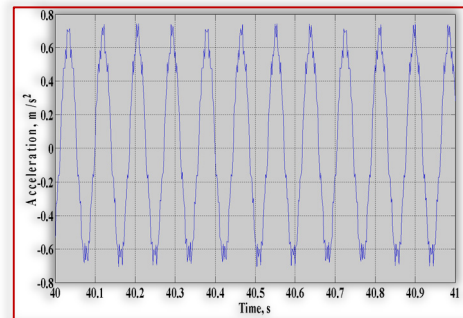
(c)



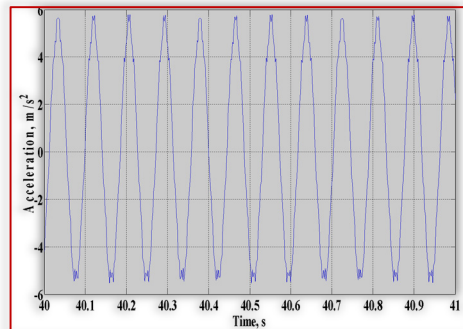
(d)

Figure 10. Acceleration Responses at different node for Case 1 (Healthy case): (a) Node 2; (b) Node 4; (c) Node 7; (d) Node 12

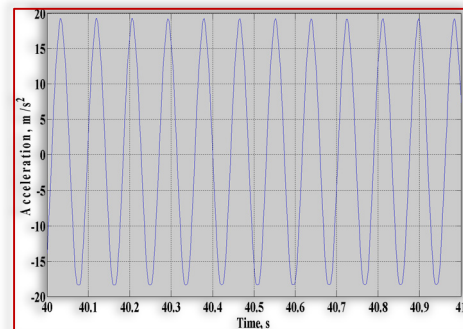
Since excitation is at first natural frequency, the time domain response shows an increase in acceleration across the beam towards its free end and there is no distortion in the wave form.



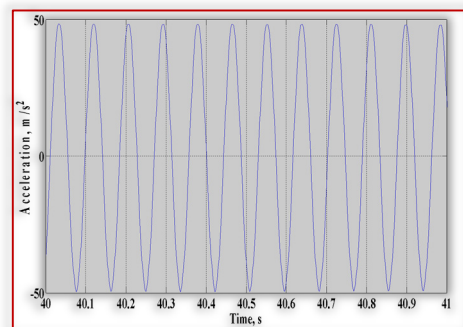
(a)



(b)



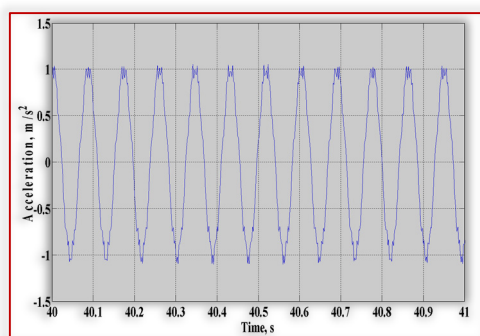
(c)



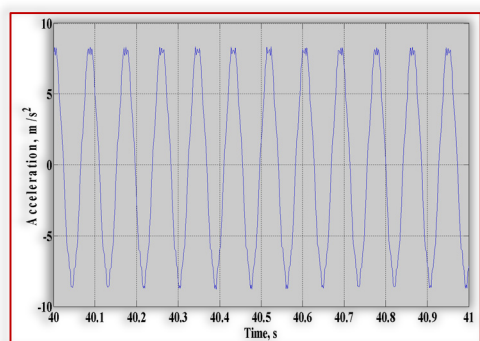
(d)

Figure 11. Acceleration Responses at different node for Case 8 ( $x_c = 250$ ,  $C_r = 5\%$ ): (a) Node 2; (b) Node 4; (c) Node 7; (d) Node 12

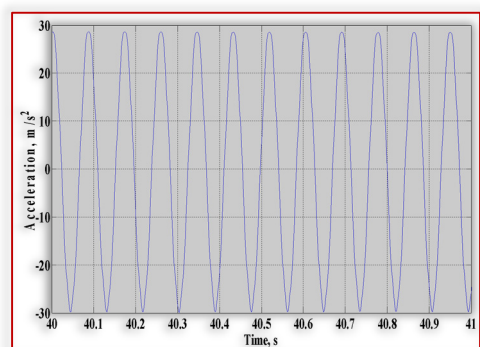
A decrease in amplitude of acceleration along the beam is observed and a change in wave form for node 2 and 4 but not towards the free end (nodes 7 and 12).



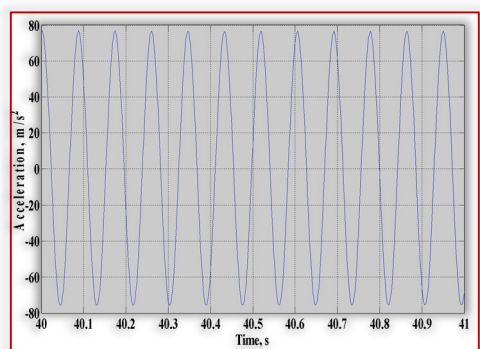
(a)



(b)



(c)

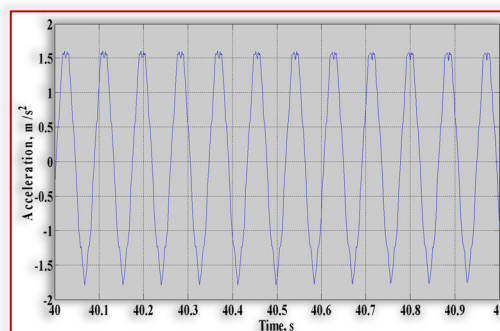


(d)

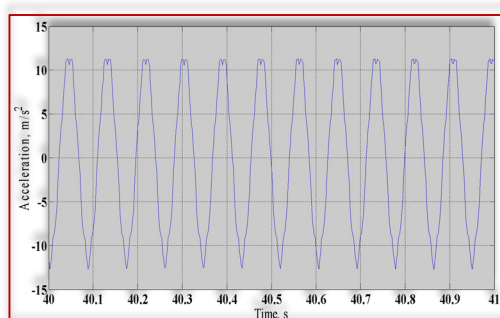
Figure 12. Acceleration Responses at different node for Case 15 ( $x_c = 450$ ,  $c_r = 10\%$ ): (a) Node 2; (b) Node 4; (c) Node 7; (d) Node 12. There (Figure 12) is a change in wave form for nodes 2 and 4 when compared with that of the healthy state but no visible change in wave form for nodes 7 and 12.

In the healthy state of the cantilever beam, the acceleration response was a pure sine wave as expected and since the excitation is at first natural frequency, the amplitude of the acceleration responses increasing from the fixed end to free end of the cantilever beam. Also, for the crack condition, amplitude pattern is the same; however, it seems to be less

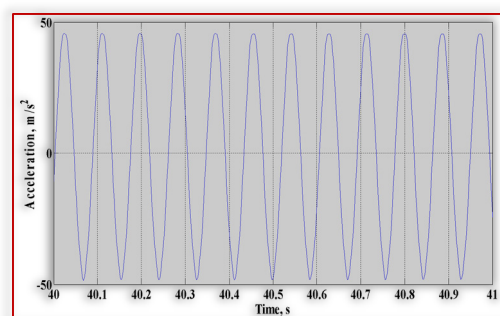
than that of the healthy state which is due to the presence of crack. The same changes were confirmed in the experiment carried out by [18]. Hence this method is capable of estimating the presence of cracks.



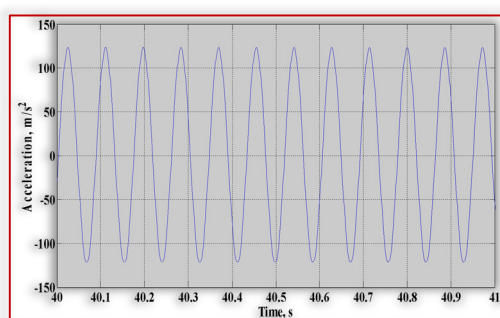
(a)



(b)



(c)



(d)

Figure 13. Acceleration Responses at different nodes for Case 22 ( $x_c = 650$ ,  $c_r = 15\%$ ): (a) Node 2; (b) Node 4; (c) Node 7; (d) Node 12.

## CONCLUSION

Using the natural frequencies, mode shapes and time domain acceleration responses, it was observed that the changes in natural frequencies from the healthy state of the beam to the damaged state at the different crack location were very small and do not provide enough information to aid crack detection. Representing the changes in 3D plot, changes in natural frequencies were very small and it was only noticeable

at the fixed end of the beam. The mode shapes gave no significant change between the healthy and crack states of the beam. The presence of crack was detected without difficulty using the time domain acceleration changes as significant changes were noticed.

#### References

- [1] Ezekiel K.C., Okwu M.O., Fadeyi J. (2013). Detection of crack location and size in structures using higher harmonics of excited frequency. *Research Journal of Engineering and Applied Sciences*, Volume. 2(5) 392-396.
- [2] Baviskar P.R. and Vinod B. Tungikar. (2013). Multiple Cracks Assessment using Natural Frequency Measurement and Prediction of Cracks Properties by Artificial Neural Network. *International Journal of Advanced Science and Technology*, Vol. 54.
- [3] Deokar A. V. and Wakchaure V. D. (2011). Experimental Investigation of Crack Detection in Cantilever Beam Using Natural Frequency as Basic Criterion. *International Conference on Current Trends in Technology*. Institute of Technology, Nirma University, Ahmedabad. 382-481.
- [4] Yadav S., Roy S.C., J. N. Mahto and R. S. Prasad. (2014) Experimental Investigation of Crack in Brass Cantilever Beam Using Natural Frequency as Basic Criteria. *International Journal of Scientific and Engineering Research*. 5 (4) 447 - 455.
- [5] Özer H., Mustafa A. Ornek (2012). A Comparative Analysis of the Beam Length Effect on Free Vibration of Cracked Beams. Paper Ref: 3758. 15<sup>th</sup> International Conference on Experimental Mechanics. Faculty of Engineering, University of Porto.
- [6] Allurkar B. S. and Shruddha S. Patil (2016). Investigation and Review on Crack Detection in Stepped Cantilever Beam. *International Journal of Research in Advent Technology*. 4 (4)185 – 193.
- [7] Ravi K. Prakash Babu, B Raghu Kumar and K Mallikarjuna Rao (2015). Vibration Analysis of Low Pressure Steam Turbine Blades with Crack. *Canadian Journal of Basic and Applied Sciences*, CJBAS. 3(1) 8 – 28.
- [8] Gade G.G., Amol S. Awari and Sachin S. Kanawade (2016). To Study Effect of Crack on Natural Frequency by using FEA. *International Advanced Research Journal in Science, Engineering and Technology*. 2<sup>nd</sup> International Conference on Advances in Advances in Mechanical Engineering (ICAME). 3 (1) 2393 – 8021.
- [9] Sathe R. and Pathak A. (2016). A Review on Vibration Analysis and Effect of Impact Loading on Cracked Beam. *International Journal of Modern Trends in Engineering and Research*. 2349 – 9745.
- [10] Parhi D. R., Manoj Kumar Muni and Chinmaya Sahu (2012). Diagnosis of Cracks in Structures Using FEA Analysis. *International Science Press: India (IJAAIES)*. 4(1) 27- 42.
- [11] Fegade P.V., Mahajan J.A. and Bhode G.P. (2014). Study on Vibration Analysis of an Uncrack and Cracked Cantilever Beam. *International Journal of Emerging Technologies in Computational and Applied Sciences*. 340 – 343.
- [12] Yan Y.J, Cheng L., Wu Z.Y, Yam L.H. (2007). Development in vibration-based structural damage detection technique. *Mechanical Systems and Signal Processing* 5(21) 2198–2211.
- [13] Majumder, L., Manohar, C.S., (2003). A time-domain approach for damage detection in beam structures using vibration data with a moving oscillator as an excitation source. *Journal of Sound and Vibration* 268 (4), 699–716.
- [14] Sinha J.K, Friswell M.I, Edwards S. (2001). Simplified Models For the Location of Cracks in Beam Structures Using Measured Vibration Data. *Journal of sound and vibration* 251(1) 13-38.
- [15] Garud M.A. and V. G. Bhamre (2015). A Review Paper on Structural Damage Identification of Cantilever Beam by Using Vubration Technique, Finite Element Analysis and Artificial Neural Network. *International Journal of Research Granthaalayah*. Vol. 3.
- [16] Yamuna P. and Sambasivarao K (2014). Vibration Analysis of Beam with Varying Crack Location. *International Journal of Engineering Research and General Science*. 2(6)1008 – 1018.
- [17] Kim J.T, Ryu Y.S, Cho H.M, Stubbs N. (2003), Damage identification in beam-type structures: frequency-based method vs. mode-shape based method. *Engineering Structures* 25 (1) 57–67.
- [18] Saavedra P.N, Cuitino L.A. (2001). Crack detection and vibration behavior of beam. *Computer and Structures* 79(9) 1451-1459.



ISSN: 2067-3809

copyright © University POLITEHNICA Timisoara,  
Faculty of Engineering Hunedoara,  
5, Revolutiei, 331128, Hunedoara, ROMANIA  
<http://acta.fih.upt.ro>

# Fascicule 4

## [October - December]

t o m e

# XI

[2018]

**ACTA**Technica**CORVINIENSIS**  
BULLETIN OF ENGINEERING



**ISSN: 2067-3809**

copyright © University POLITEHNICA Timisoara,  
Faculty of Engineering Hunedoara,  
5, Revolutiei, 331128, Hunedoara, ROMANIA  
<http://acta.fih.upt.ro>

# COMPARATIVE STUDY OF SOME TERRESTRIAL ATMOSPHERE MODELS IN HYDROSTATIC BALANCE

<sup>1</sup>University Politehnica Timisoara, Faculty of Engineering Hunedoara, Hunedoara, ROMANIA

**Abstract:** The atmospheric pressure strongly influences the air pollution by triggering the convective and advective movements in which the masses of air are entrained. A high pressure favours a stable weather, the appearance of mist and thermal inversion in the cold season, or the occurrence of high temperatures in summertime. In these situations, the concentrations of pollutants increase significantly. When the atmospheric pressure is low, there are atmospheric precipitations that lead to the purification of atmosphere. According to the measured data on the vertical distribution of pressure and temperature, the hydrostatic approximation can well assess the real state of the atmosphere with quasi-static movements of the air masses. This paper presents a graphical user interface (GUI) programmed in Matlab providing support for a comparative study of the atmosphere models in hydrostatic balance. The application has equally a didactical and scientific importance.

**Keywords:** terrestrial atmosphere models, hydrostatic approximation, GUI application, Matlab

## INTRODUCTION

The atmosphere is the gaseous shell of the Earth made up of 78.08% nitrogen, 20.94% oxygen, 0.93% argon and 0.03% carbon dioxide, the remaining few hundredths consisting of methane, ozone, water vapours, some nitrogen and sulphur compounds, as well as rare gases, i.e. hydrogen, neon, helium and krypton [1], [2]. In the study of atmosphere and the fluid mechanics, some fundamental physical variables are generally important, such as: pressure, density, temperature, speed, as well as the deterministic-statistical relationships established between them, based on the substantiating of appropriate mathematical models [3]. The atmospheric air is generally treated on a macroscopic scale in the hypothesis of continuum, and on microscopic scale as an ideal gas, according to the kinetic-molecular theory.

Under 100 km, the atmospheric composition is relatively constant (20% molecular oxygen and 80% molecular hydrogen), so that the mean molecular weight is constant. The atmosphere region is referred to as homogeneous. Over 100 km, the atmospheric components are changed and the atmosphere region is referred to as heterogeneous.

The vertical structure of the atmosphere was established in relation to the variation of the air temperature with the altitude and the chemical composition of the air, being divided into certain regions, called "layers": the troposphere, the stratosphere, the mesosphere, the thermosphere and the exosphere [1].

The hydrostatic approximation is fully justified for a resting atmosphere. The experimental data on the vertical distribution of pressure and temperature show that the hydrostatic approximation represents a very good assessment for the real state of the atmosphere [3].

The most used models of terrestrial atmosphere in hydrostatic balance, along with the Matlab GUI application

which provides support for the comparative study of the models, are presented below.

## TERRESTRIAL ATMOSPHERE MODELS IN HYDROSTATIC BALANCE

The terrestrial atmosphere models in hydrostatic balance consider the atmospheric air to be an ideal gas, and are based on the hydrostatic approximation [1], [2], [3] according to which the elementary variation of pressure is expressed in the form:

$$dp = -\rho g dz \quad (1)$$

where  $\rho$  is the air density,  $g$  is the gravitational acceleration, and  $dz$  is the elementary variation of the altitude. For a greater accuracy, the geopotential gravitational acceleration was taken into consideration in the relationship (1):

$$g(z) = g_0 \cdot \frac{R_p^2}{(R_p + z)^2} \quad (2)$$

with  $g_0 = 9.8 \text{ m/s}^2$ ,  $z = \text{altitude}$  and  $R_p = 6369 \text{ km}$  (radius of the Earth, considered spherical, at the sea level) – Figure 1.

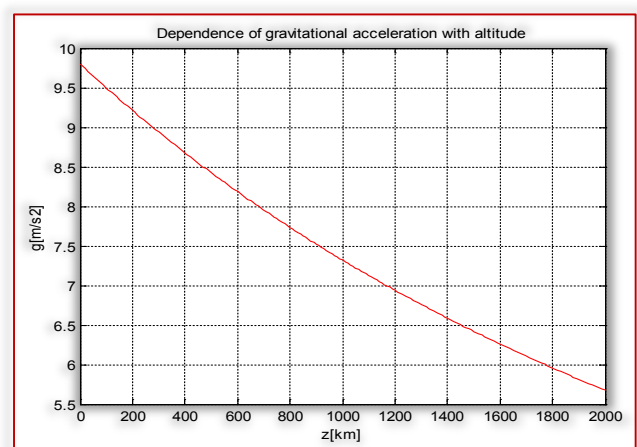


Figure 1. Dependence on altitude of the gravity acceleration

Figure 1 shows that, up to 100 km, the variation of gravitational acceleration with altitude is insignificant. The models of terrestrial atmosphere in hydrostatic balance are presented below.

**a. The model of isothermal atmosphere**

For the atmospheric air considered an ideal gas, the density is expressed using the thermal state equation and, after replacement in the expression of hydrostatic approximation, it results:

$$\frac{dp}{p} = -\frac{\mu_a}{RT} g dz \quad (3)$$

where  $\mu_a$  is the molar mass of air,  $R$  is the universal constant of ideal gas, and  $T$  is the absolute temperature of the air.

In the case of an isothermal atmosphere model, the temperature was considered constant, independent of the altitude. By integrating the differential equation (3) under these conditions, we find the law of temperature dependence of altitude for an isothermal atmosphere:

$$p = p_0 e^{-\frac{\mu_a g}{RT} z} \quad (4)$$

where  $p_0$  is the atmospheric pressure for  $z = 0$ .

As the temperature of terrestrial atmosphere varies with the height, the isothermal atmosphere model can only be used within limited height intervals.

**b. The model of homogeneous atmosphere**

For this model, the atmospheric density remains constant,  $\rho_0$ . By integrating the relationship (1), we obtain a linear relationship of the atmospheric pressure with altitude:

$$p = p_0 - \rho_0 g z \quad (5)$$

i.e. the pressure decreases linearly with increasing altitude.

**c. The model of polytropic atmosphere**

In this model, it is considered that the temperature decreases linearly with the altitude, based on the following relationship:

$$T = T_0 - \gamma_a z \quad (6)$$

where  $\gamma_a$  is the vertical gradient of temperature:

$$\gamma_a = -\frac{dT}{dz} \quad (7)$$

By introducing the relationship (6) into (3) and integrating, it results:

$$p(z) = p_0 \left( \frac{T_0 - \gamma_a z}{T_0} \right)^{\frac{\mu_a g}{R \gamma_a}} \quad (8)$$

**d. The international standard atmosphere model (ISA atmosphere)**

The ISA atmosphere is a standardised mathematical model applied to the variation of atmospheric parameters (pressure, temperature, density, etc.) with the altitude [1]-[3].

Within the model, the ISA atmosphere is divided into layers – where the temperature varies linearly, as in the polytropic atmosphere model – table 1.

Table 1. Characteristics of atmospheric layers in the international standard atmosphere model

Layer name in ISA	Geopotential altitude at base h (in km)	Geometric altitude at base z (in km)	Temperature gradient $\alpha$ (in °C/km)	Temperature at the base of the layer T (in °C)	Pressure at the base of the layer p (in Pa)
Troposphere	0.0	0.0	6.5	+15.0	101325
Tropopause	11.000	11.019	0.0	-56.5	22632
Stratosphere	20.000	20.063	-1.0	-56.5	5474.9
Stratosphere	32.000	32.162	-2.8	-44.5	868.02
Stratopause	47.000	47.350	0.0	-2.5	110.91
Mesosphere	51.000	51.413	2.8	-2.5	66.939
Mesosphere	71.000	71.802	2.0	-58.5	3.9564
Mesopause	84.852	86.000	-	-86.2	0.3734

**PRESENTATION OF THE COMPUTER APPLICATION ENTITLED “GRAPHICAL USER INTERFACE” (GUI), USED FOR THE STUDY OF TERRESTRIAL ATMOSPHERE MODELS IN HYDROSTATIC BALANCE**

Nowadays, the increase of didactic performance is achieved by skilfully combining the traditional teaching techniques with the modern ones of multimedia type. In this regard, it is of particular importance to make and use multimedia applications for various subjects taught at courses [4] - [9].

The application for the comparative study of the terrestrial atmosphere models in hydrostatic balance is programmed in Matlab [6], [10], [11], using the GUIDE utility (Figure 2).

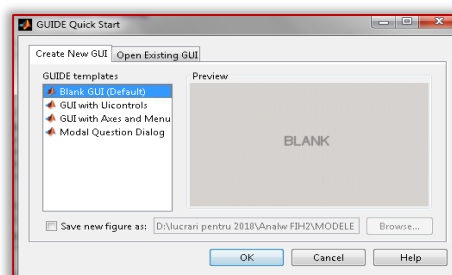


Figure 2. Running the Matlab GUIDE utility

The GUIDE utility is used to make, one by one, the application programming interfaces. For each interface, the GUIDE utility generates a graphic file “name.fig” (Figure 3) and a script with the same name “name.m” (Figure 4). The functions of the GUI elements on the interface are programmed in the Matlab script.

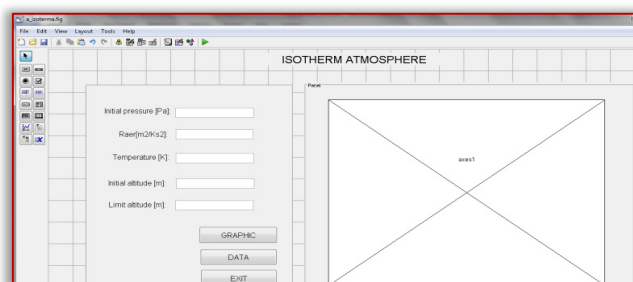


Figure 3. Graphic file of a GUI interface

```

169 =
170 =
171 =
172 =
173 =
174 =
175 =
176 =
177 =
178 =
179 =
180 =
181 =
182 =
183 =
184 =
185 =
186 =
187 =
188 =
189 =
190 =
191 =
192 =
193 =
    
```

Figure 4. Matlab script afferent to a GUI interface  
The file which starts the application is "start.m". For running the application, the file name is entered into the Matlab Command Window (Figure 5).

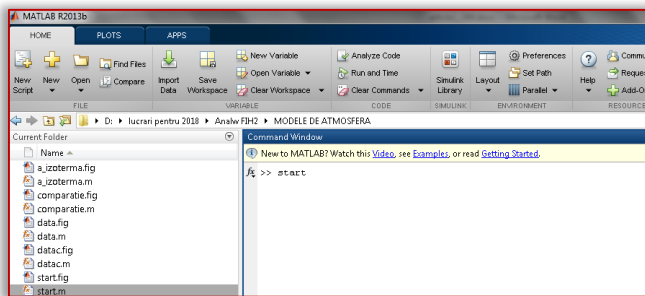


Figure 5. Running the application  
From the main interface shown in Figure 6, we can reach the interfaces of the four terrestrial atmosphere models in hydrostatic balance and the interface for comparative analysis.

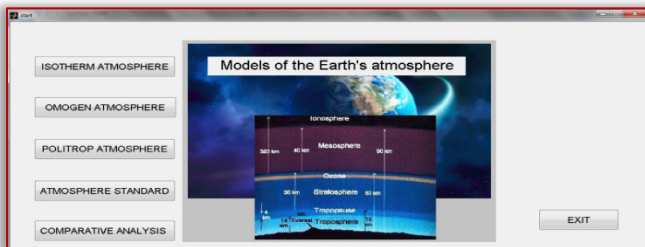


Figure 6. Main interface of the application  
The interface of a model (figure 7) contains input fields for entering the calculation parameters, and two buttons. One is for the graphic representation of the atmospheric pressure versus altitude, and one for the numerical values of interest.

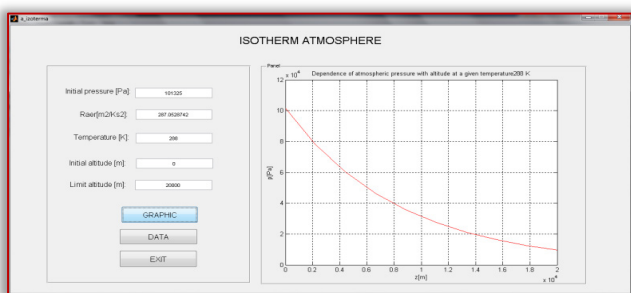


Figure 7. The interface for a terrestrial atmosphere model in hydrostatic balance

The data interface (numerical values of interest) afferent to an atmosphere model (Figure 8) presents a table with values representing the dependence of atmospheric pressure of altitude, as well as the possibility of performing a specific pressure calculation for a given altitude.

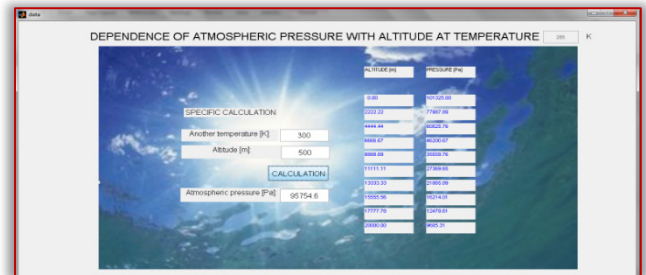


Figure 8. Data interface for a terrestrial atmosphere model in hydrostatic balance

The figures 9 and 10 show the interfaces used for the comparative analysis of the various types of terrestrial atmosphere in hydrostatic balance.

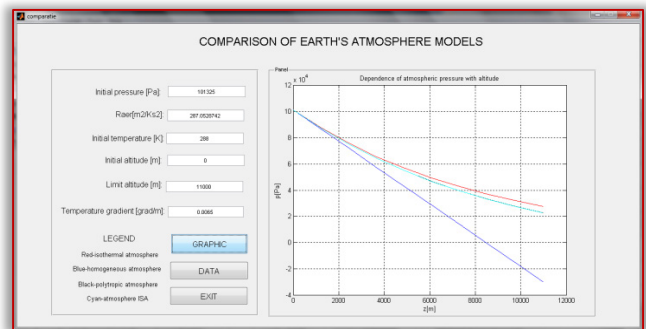


Figure 9. The interface showing the comparative study of the terrestrial atmosphere models in hydrostatic balance

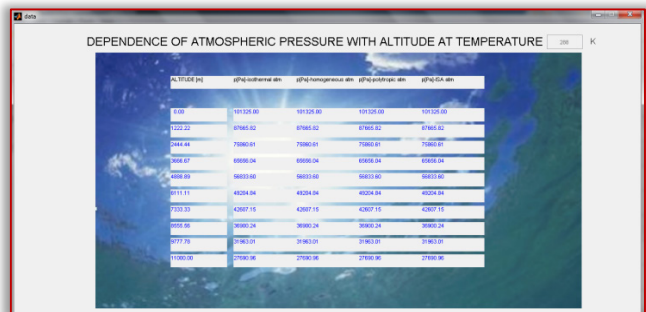


Figure 10. Numerical value interface for the comparative study of terrestrial atmosphere models in hydrostatic balance

### CONCLUSIONS

The paper presents an application with graphical interface programmed in Matlab for comparative study of terrestrial atmosphere models in hydrostatic balance. The application enables the generation of graphs and numerical values to illustrate the dependence of the atmospheric pressure on altitude for the four models of terrestrial atmosphere in hydrostatic balance.

The Figures 9 and 10 present a comparative image of the four models for troposphere. It is found that the homogeneous atmosphere model can be used for troposphere, with indulgence at low altitudes up to 8,000 m. It is also noted that

for troposphere, the isothermal atmosphere model and the polytropic atmosphere model provide very little differing data. For troposphere, the polytropic atmosphere model coincides with the international standard atmosphere model (ISA atmosphere).

The application can be successfully used as a teaching material for the course of Atmospheric Physics and for generating values for more complex scientific analyses. The programming modality enables the application to be completed with other computational and analytical facilities useful for didactic purposes and scientific research.

#### References

- [1] Stih, C., (2009), Fizica mediului și climatologie [Environmental Physics and Climatology], Publisher: Bibliotheca, Târgoviște.
- [2] Caunei Florescu, G., (2013), Elemente de fizică atmosferică [Elements of atmospheric physics], Publisher: Coresi, Bucharest.
- [3] Drăghici, I., (1988), Dinamica atmosferei [Dynamics of atmosphere], Publisher: Tehnică Bucharest.
- [4] Cunțan, C.D., Baci, I., Osaci, M., (2015), Studies on the Necessity to Integrate the FPGA (Field Programmable Gate Array) Circuits in the Digital Electronics Lab Didactic Activity, International Journal of Modern Education and Computer Science, 7(6).
- [5] Kong, Y., Xie, I., (2010), Professional Courses for Computer Engineering Education, I.J. Modern Education and Computer Science, 1.
- [6] Osaci, M., (2012), Matlab in Educational Activities on Physics, Acta Technica Corviniensis-Bulletin of Engineering, 5(4).
- [7] Osaci, M., Berdie, A.D., Lup A.E., (2012), Educational soft presenting particularities through special functions of ABAP List Viewer in Web Dynpro technology, Procedia - Social and Behavioural Sciences, 46.
- [8] Osaci, M., Pănoiu, M., Pănoiu, C., Muscalagiu, I., (2012), Matlab Graphical User Interface for Study through Modelling and Simulation of the Waiting Systems without Priorities, Advances in Applied Information Science.
- [9] Pănoiu, M., Muscalagiu, I., Osaci M., Iordan A., (2005), Multimedia Educational Software for Binary Tree and their Application Present, Annals of the Faculty of Engineering Hunedoara, 3(3).
- [10] Ghinea, M., Firețeanu, V., (1997), Matlab, calcul numeric, grafică, aplicații [Matlab, numerical calculation, graphics, applications], Publisher: Teora.
- [11] Osaci, M., (2007), Matlab pentru prelucrarea datelor în laboratorul de fizică [Matlab for data processing in physics laboratory], Publisher: Cermi, Iași.



ISSN: 2067-3809

copyright © University POLITEHNICA Timisoara,  
Faculty of Engineering Hunedoara,  
5, Revolutiei, 331128, Hunedoara, ROMANIA  
<http://acta.fih.upt.ro>

# NUMERICAL SYSTEMS IN THE LEARNING PROCESS

<sup>1</sup>Technical University of Kosice, Faculty of Mechanical Engineering, Department of Production Technology, SLOVAKIA

**Abstract:** Linking industrial networks to corporate networks enables companies to test new applications and services and access to information anywhere, anytime. Equally, the increasing use of the Internet provides access to critical real-time and is a competitive advantage. Improvements in industrial networks include the ability to transmit and industrial serial protocol over Ethernet in a wireless environment. Joining different networks (enterprise networks and network management and data collection), avoiding collisions, high transfer efficiency and the ability to add new devices to the network without interrupting the flow of traffic – these are all benefits of the new practice. Industrial fieldbuses different types of transfer's data at lower levels of process control and production. Their use shall be replaced by "classic" – analogue process variables, whereby there is a significant reduction in wiring. However, the actual limit the scope of wiring is not the main benefit of these communication systems. It lies mainly in manageability and diagnostic devices connected to the bus through which the device can be parameterized and continuously evaluate their condition.

**Keywords:** fieldbus, Publisher/ subscriber, Master/slave

## INTRODUCTION

Industrial fieldbuses in Anglo-Saxon literature refers to as "Fieldbus". They are used for the lower end of the automated production system. These are levels of equipment and parts. Industrial fieldbuses were originally developed to replace the current loop digital interface for the transmission of information between intelligent field devices and equipment's and senior management level. Transferring those short blocks of data at the level of sensors, actuators and controllers.

Systems with industrial communication bus have the following characteristics:

- Flexibility and modularity – a system with industrial communication bus is easily extensible than a centralized system.
  - » Configurability – communication network enables parameter setting and configuration of field devices, which simplifies system installation and commissioning. Configurable via the communication network is a prerequisite for the use of intelligent field devices.
  - » Maintainability – use of industrial communication bus allows monitoring devices and equipment, introduction of firmware.
- Distribution – communication network is a prerequisite for the implementation of distributed systems. Data processing may not be executed in the central controller, but may be performed in the field devices.

## PROPERTIES OF FIELDBUS AND INDUSTRIAL FIELDBUSES IN THE REFERENCE MODEL ISO / OSI

Properties fieldbus can be summarized as follows:

- A high volume of short data blocks:

- » the baud rate is compared with a global network cabling (up to 12 Mbit / s, in systems with industrial Ethernet up to 100 Mbit / s), but quite a large range of distances (tens of meters to several kilometers),
- » time synchronization of the devices connected to the communication bus (at microsecond),
- » simple installation carried out by trained personnel,
- » high integrity (high degree of treatment failure to receive data).

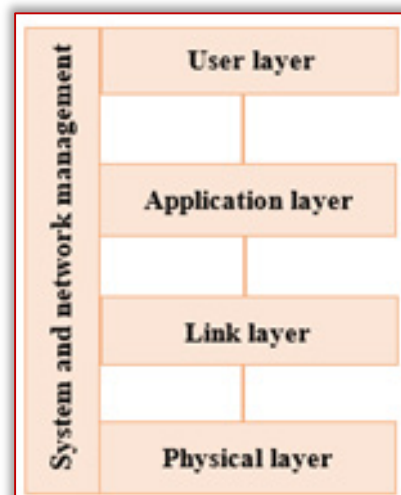


Figure 1. Layer model of industrial communication bus showing the position of the layers in the OSI layered model (application layer is not part of the OSI model)

For the operation of industrial communication buses are not required (and desired) all layers of the OSI model. Use the following layers of the OSI model:

- The physical layer implements transmit each bit-level signals. On the physical level, each communication bus defined by the physical characteristics of the

communication circuit type of transmission medium (media), voltage levels, size of load currents, bit rate, topology, features sets fieldbus (receiving optical signals), the maximum number of connectable devices (nodes) and below.

- Link layer implements communication between devices, among which signal lines (transmission lines). Controls access to the transmission medium.
- The application layer provides translation requirements of the application layer to the link layer. It provides access to a set of communication services supporting the operation of distributed systems. Implements transfer values and administration. It may be implemented commands to work with the device (device parameterization, diagnosis, etc.).
- The user layer is defined by the structure of the data collection and management functions device connected to the fieldbus. It may be defined function blocks device description of the devices in the formal language and means of communication with different types of devices (eg. Sensors, actuators, etc.). It allows interoperability of equipment.
- System and network management provides a method for configuring bus and recovery from failures. Monitors and manages the activities of the various parts of the bus.

#### METHODS OF DATA TRANSFER

##### — Master/slave

Master device (eg. PLC) sends a request for data transmission slave (eg. Sensor, actuator). Addressing (tbc) slave then responds to the request. Examples transfer methods master/slave:

- » acyclic data transmission on PROFIBUS DP in the transfer of configuration data from the PLC to the frequency converter,
- » cyclic read data from the encoder to the control PLC and then sending output demand (value of frequency) to frequency converter.

##### — Client/server

The buses, which are not clearly defined master and slave (ie. Foundation Fieldbus), this method of transmission is called "client / server". Device acting in the capacity of a client asks for data transfer and device server responds.

The possible use of the method of client / server:

- acyclic data transmission between the device (device on the bus – server) and operator workstation (client) – transmission configuration data, monitoring and visualization.

##### — Publisher/ subscriber

A device that performs the function of "publisher" sends the value to be able to take several devices simultaneously and to act in the capacity of "subscribers".

The advantage is that the transferred value is transmitted to multiple devices simultaneously.

This data transfer method is used in the Fieldbus Foundation in feedback management (closed-loop control).

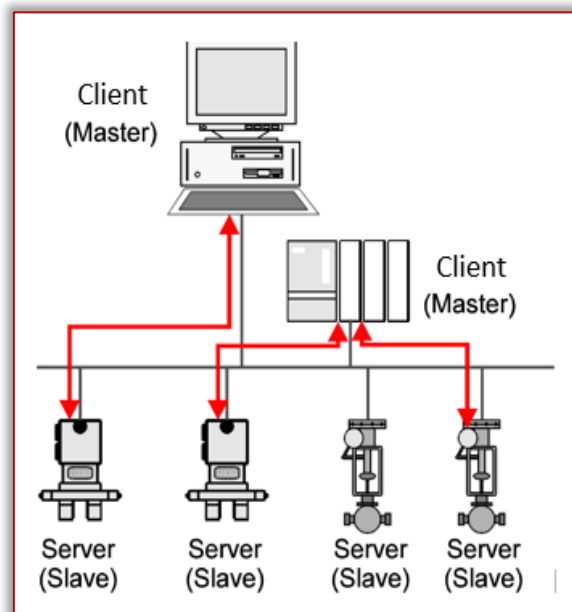


Figure 2. Data transmission on a "client / server" („master/slave“)

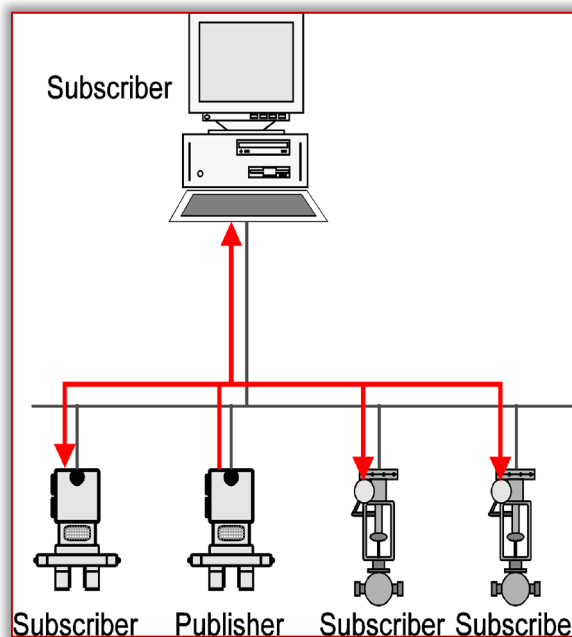


Figure 3. Data transmission method „publisher/subscriber“

Publisher remembers devices that act as recipients of his messages (subscriber): When a device wants to receive these messages, the device sends a request to the publisher to be included in the list of beneficiaries. Message transmission using group addressing.

If the data is transmitted between devices directly, without having to transfer via the master device, such transfer shall be marked „peer-to-peer“. Possible methods of use publisher / subscriber: cyclic transmission of process variable from sensor.

— **Transmission of data without request (source/sink)**

A device that performs the function of "source" device transmits a "sink", without requiring the device management "sink". Data transmission is carried out a cyclically, for example, when an alarm. Application: Alarm transmission and fault data from devices on the operator panel, the appearance of faults.

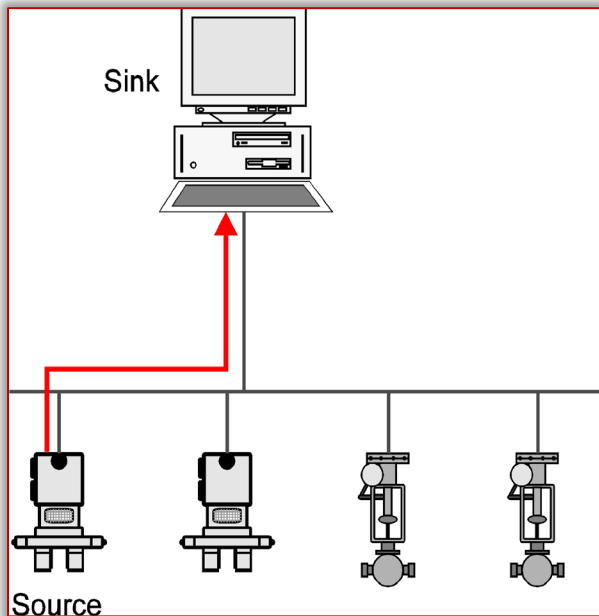


Figure 4. Transmission of data without request

**SYSTEMS OF NUMERICAL CONTROL**

Numerical control systems can be divided into two basic groups:

- » NC
- » CNC

Computer-controlled systems (CNC), for their benefits fully enforced and NC systems are both technically and morally obsolete and are used only to run out of their life.

— **NC control systems**

- » the system's memory is loaded only one sentence, which is carried out,
- » following sentence is loading new,
- » when you load a new sentence, the current contents of memory lubricates,
- » information is entered as a program on punched tape or manually from the keyboard,
- » program on punched tape is read again and again in the manufacture of other pieces,
- » the execution of the next piece to be tape rewinds to the beginning,
- » any modification program is possible only by adjusting punched tapes,
- » the program cannot use parameters and user subroutines program cannot branch out.

— **CNC control systems**

The system loads the entire program into memory from either disk or other media for storing information, or through LAN network, either wired or dateless.

In contrast to the NC of the interpolator it is not hardware but software issue.

The generation of the track can be used direct mathematical description of the shape of the track. It is thus possible to generate parabolas and higher order curve (spline) control systems with high computing power and carry out circular interpolation in space, but practically you do with linear and circular interpolation.

For the processing of technological information with the CNC system uses a programmable logic controller (PLC – Programmable Logic Controller).



Figure 5. Control systems CNC

The CNC systems are possible:

- easy edit program,
- branch program,
- use parameters,
- using subprograms,
- the graphical simulation of machining,
- use diagnostic programs,
- to compensate for system accuracy and machine parts.

**CONCLUSION**

Industrial fieldbuses different types of transfer's data at lower levels of process control and production. Their use shall be replaced by "classic" – analogue process variables, whereby there is a significant reduction in wiring.

However, the actual limit the scope of wiring is not the main benefit of these communication systems. It lies mainly in manageability and diagnostic devices connected to the bus through which the device can be parameterized and continuously evaluate their condition.

So in addition to the process variable to / from the device transmitted and other variables.

**Acknowledgement**

The work was supported by Ministry of Education of the Slovak Republic KEGA 039 TUKE-4/2016: The creating of virtual laboratories based on web technologies to support the educational process in the field of Manufacturing Technology.

## References

- [1] Berge, J.: Fieldbuses for Process Control. ISA. 2002. ISBN 1–55617–760–7.
- [2] Felser, M.: The Fieldbus Standards: History and Structures. Technology
- [3] Leadership Day 2002, In: Microswiss Network, HTA Luzern, Švajčiarsko.  
[http://www.sjf.tuke.sk/vitralab/files/vystupy/prirucka\\_sk\\_final.pdf](http://www.sjf.tuke.sk/vitralab/files/vystupy/prirucka_sk_final.pdf)
- [4] [http://www.spslevice.sk/ucebnice/SOC/SOC%20-%20PRI/95-Princip\\_cislicoveho\\_riadenia.htm](http://www.spslevice.sk/ucebnice/SOC/SOC%20-%20PRI/95-Princip_cislicoveho_riadenia.htm)
- [5] <http://www.lpsmachine.sk/frezovanie.html>



ISSN: 2067–3809

copyright © University POLITEHNICA Timisoara,  
Faculty of Engineering Hunedoara,  
5, Revolutiei, 331128, Hunedoara, ROMANIA  
<http://acta.fih.upt.ro>

# MOTION PLANNING FOR AUTOMATED GUIDED VEHICLE

<sup>1</sup>Robert Bosch Department of Mechatronics, University of Miskolc, 3515 Miskolc, HUNGARY

**Abstract:** This paper deals with further development of an AGV (Automated Guided Vehicle) and its motion planning. The AGV can be found at the Logistic Institute at University of Miskolc. It was developed for a High-Tech Laboratory in 2011 by Gamma Digital Ltd. The system can perform delivering, picking and placing of materials. The AGV has a differential-drive with two caster wheels. A Mitsubishi 6-DoF industrial robot is mounted on it. A Wago PLC (Programmable Logic Controller) and a Linux-based PC handle the inputs and outputs. The PLC controls the lamps, switches and buttons. For safety reasons two SICK short range laser detectors were mounted on the front and rear side of the AGV. The navigation is performed by a SICK laser positioning sensor. The servomotors are controlled by Dugong servo drives, the signals for these drives are controlled by the PC. With the help of the PC both of the controllers are programmed to handle the navigation system and the safety sensors.

**Keywords:** mechatronics, mobile robot, Automated Guided Vehicle (AGV), navigation, motion planning

## INTRODUCTION

Nowadays the number of automated industrial devices exponentially raises. These devices can increase the productivity, decrease the costs and human fault [1]. However, the automation of human controlled devices is not simple. The research and education of such problems inevitable are important. The vehicle engineering education has been started last year at University of Miskolc. The preparation of lecture notes is in progress. This paper is a contribution to this task.

The Automated Guided Vehicles (AGVs) have been used usually in logistics systems, e.g. in supply chain [2], since 1950s years [3]. Automating of these vehicles is a complex task, because several problems should be handled: sensing of the environment, movements of the vehicle, safety functions, and communications inside and outside of the vehicle.

An autonomous carrier vehicle can be regarded as mobile robot or AGV [4]. An AGV can be used for a lot of application, e.g. as service robot [15]. The AGVs can operate using the outside infrastructure, e.g. optical or magnetic paths, laser scanner, inductive sensing [5]–[7]. The technologies of guidance are written in [8], i.e., the navigation can use physical or virtual path. The mobile robots have to use only on-board devices, therefore other sensors e.g. visual camera [9]–[10] are needed to navigate.

This paper deals with motion planning of an AGV. This AGV can be found at laboratory of Logistic Institute at University Miskolc [11]–[12], which is a pathless carrier [3],[13]. The investigated system in this paper navigates with onboard laser scanner, similarly to [7].

Special mirrors, which can reflect the laser beam in same direction, were placed at the edges of laboratory. The safety sensors may operate with laser method, but it can be replaced by camera [9].

The PLC, PC, wireless router, main drives, safety sensors and navigation devices are connected in a network, such as it was published in [14]. A 6 DoF industrial robot, such as in [16], was mounted on AGV, which can pick and place different workpieces. The drives of the examined AGV are differential-drive, but it can have four wheel steering [17].

The motion along a straight line can be easily performed, but the vehicle often has to move along arch, when cornering or overtaking are taking place. However, the motion along arch may have more critical situation.

The solution of differential equation system is carried out by Runge-Kutta numerical method written in Scilab software system. The program can compute vehicle X, Y position, absolute yaw angle, yaw rate and the track of wheels and vehicle's center of gravity in time.

Examples of different maneuverings, including cornering, motion along arch, and straight motion between two given points in different cases will be shown in Section 2–4. These examples are very useful in engineering education. Finally, the last section summarizes the results.

## THE MOTION OF AGV: CORNERING, WHEELS NO CONSIDERED

An AGV is shown in Figure 1, where the notations are given as follow:

- $v_{\text{left}}$  or  $v_L$ : velocity of left wheel,
- $v_{\text{right}}$  or  $v_R$ : velocity of right wheel,
- $v$ : velocity of vehicle's center,
- $\varphi$ : angle of AGV
- $\omega$ : angular velocity of AGV
- $r = 70\text{mm}$ : radius of the wheel
- $b = 250\text{mm}$ : distance between wheel and vehicle's AGV

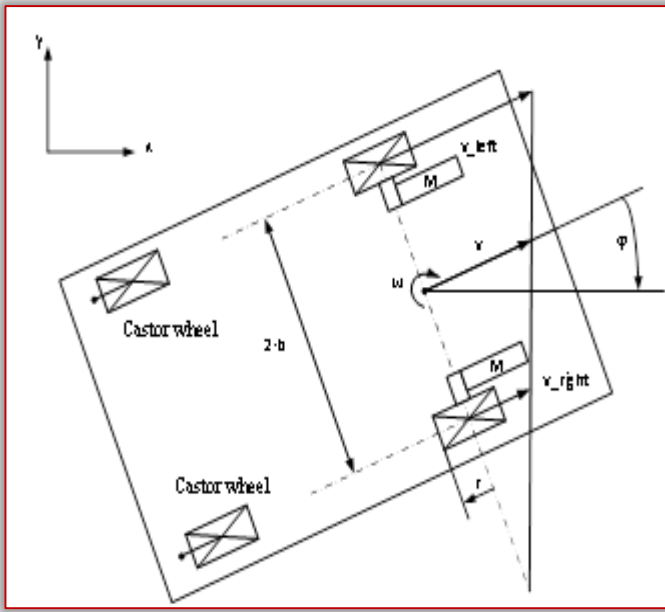


Figure 1. Kinematic model of the AGV

A differential equation system should be written for the motion. The state vector is necessary for the differential equation system as follows:

$$\underline{\mathbf{x}} = \begin{bmatrix} \mathbf{x}_1 \\ \mathbf{x}_2 \\ \mathbf{x}_3 \\ \mathbf{x}_4 \\ \mathbf{x}_5 \end{bmatrix} = \begin{bmatrix} \mathbf{x} \\ \mathbf{y} \\ \varphi \\ \mathbf{v} \\ \omega \end{bmatrix} \quad (1)$$

where  $\mathbf{x}$  and  $\mathbf{y}$  are the position of AGV in absolute coordinate system.

The derivate of the state vector gives the differential equation system:

$$\dot{\underline{\mathbf{x}}} = \begin{bmatrix} \dot{\mathbf{x}} \\ \dot{\mathbf{y}} \\ \dot{\varphi} \\ \dot{\mathbf{v}} \\ \dot{\omega} \end{bmatrix} = \begin{bmatrix} (\mathbf{v} + \mathbf{r} \cdot \omega) \cdot \cos\varphi \\ (\mathbf{v} + \mathbf{r} \cdot \omega) \cdot -\sin\varphi \\ \omega \\ \mathbf{a} \\ \varepsilon \end{bmatrix} \quad (2)$$

where the  $\mathbf{a}$  is the acceleration of the vehicle's center and  $\varepsilon$  is the angular acceleration. Here only the center of AGV is considered.

All the parameters are zero by initial time. The illustration of motion is shown on Figure 2.

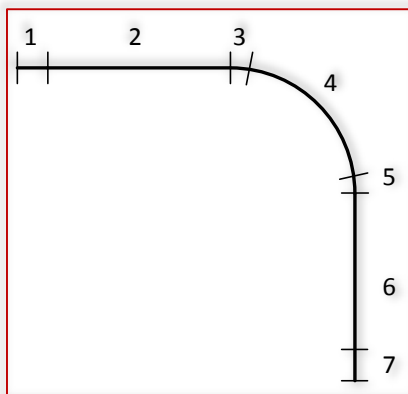


Figure 2. Illustration of path of the AGV during cornering

The acceleration and angular acceleration are changing during the motion as follows:

- Acceleration in straight line,  $\mathbf{a} = 300 \frac{\text{mm}}{\text{s}^2}$ ,  $\mathbf{v}_2 = 150 \frac{\text{mm}}{\text{s}}$ , time can be calculated  $\mathbf{t}_{1-2} = \frac{\mathbf{v}_2 - \mathbf{v}_1}{\mathbf{a}} = 0.5 \text{ s}$
- Straight line motion without acceleration,  $\mathbf{t}_{2-3} = 2 \text{ s}$
- Arch deceleration,  $\mathbf{a} = -300 \frac{\text{mm}}{\text{s}^2}$ , the rotation acceleration can be calculate  $\varepsilon = \frac{\mathbf{a}_0}{\mathbf{b}} = 1.2 \frac{\text{rad}}{\text{s}^2}$ ,  $\mathbf{v}_4 = \frac{150 + 75 \text{ mm}}{2} = 112.5 \frac{\text{mm}}{\text{s}}$ , the time can be calculate  $\mathbf{t}_{3-4} = \frac{\mathbf{v}_4 - \mathbf{v}_3}{\mathbf{a}} = 0.125 \text{ s}$
- Arch motion without acceleration,  $\omega = \frac{\mathbf{v}_4}{3\mathbf{b}} = 0.5 \frac{\text{rad}}{\text{s}}$ , time can be calculated by angle and angular velocity:  $\mathbf{t}_{4-5} = \frac{\varphi_{4-5}}{\omega} = 10.347 \text{ s}$ , where  $\varphi_{4-5} = 1.5502$
- Arch acceleration,  $\mathbf{a} = 300 \frac{\text{mm}}{\text{s}^2}$   $\varepsilon = \frac{\mathbf{a}_0}{\mathbf{b}} = 1.2 \frac{\text{rad}}{\text{s}^2}$ ,  $\mathbf{v}_6 = 150 \frac{\text{mm}}{\text{s}}$ ,  $\mathbf{t}_{5-6} = \frac{\mathbf{v}_6 - \mathbf{v}_5}{\mathbf{a}} = 0.125 \text{ s}$
- Straight line motion without acceleration,  $\mathbf{t}_{6-7} = 2 \text{ s}$
- Deceleration in straight line,  $\mathbf{a} = -300 \frac{\text{mm}}{\text{s}^2}$ ,  $\mathbf{v}_8 = 0 \frac{\text{mm}}{\text{s}}$ ,  $\mathbf{t}_{7-8} = \frac{\mathbf{v}_8 - \mathbf{v}_7}{\mathbf{a}} = 0.5 \text{ s}$

The summarized motion time is:  $\mathbf{t}_{1-8} = \sum_{i=1}^8 \mathbf{t}_i = 15.597\text{s}$

The differential equation system was solved in Scilab software system with Runge–Kutta method. The results of this cornering, i.e., X position, Y position, angle, angular velocity, and velocity of AGV during cornering are shown from Figure 3 to Figure 7, respectively.

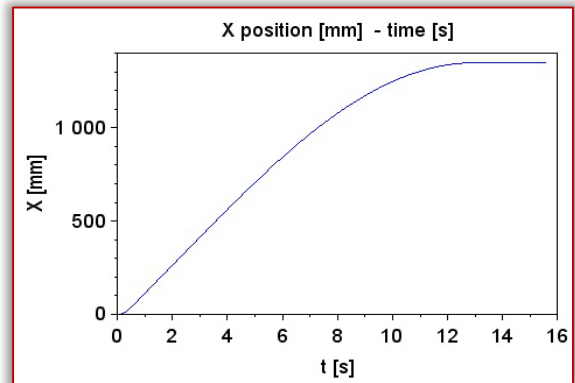


Figure 3. X position of the AGV during cornering

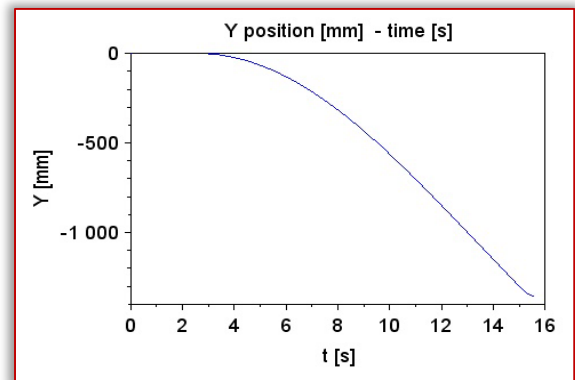


Figure 4. Y position of the AGV during cornering

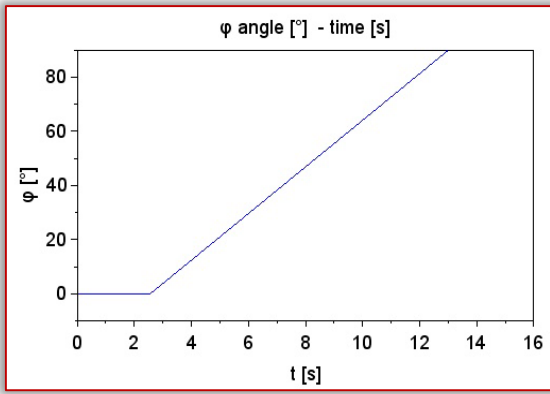


Figure 5. Angle of the AGV during cornering

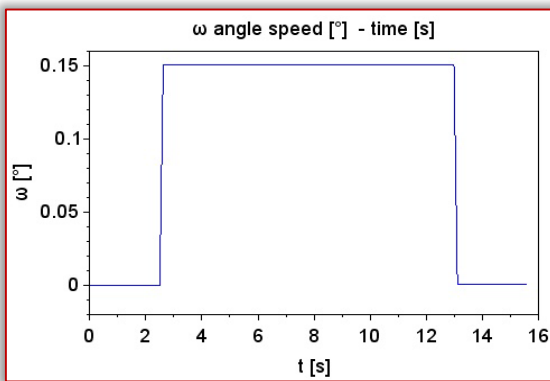


Figure 6. Angular velocity of the AGV during cornering

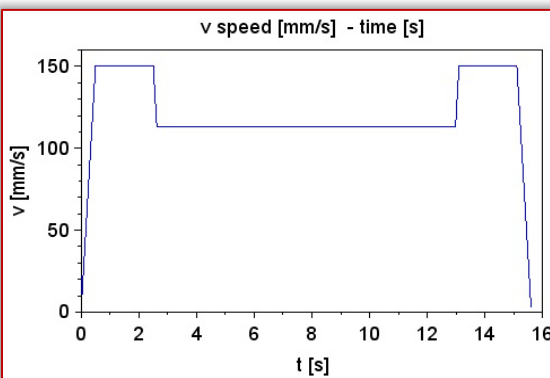


Figure 7. Velocity of the AGV during cornering

The path of the vehicle can be seen on Figure 8. The value of final X and Y position are same in absolute values.

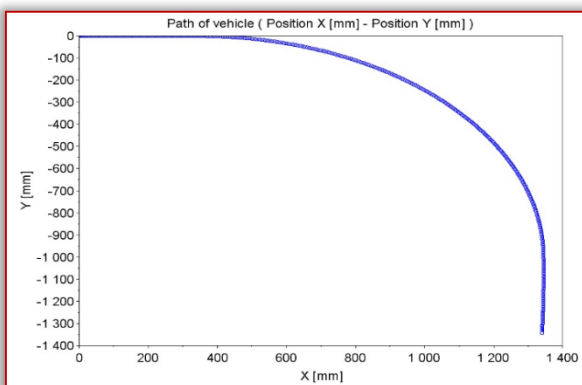


Figure 8. Path of the AGV during cornering

### THE MOTION OF AGV: ARCH LINE, WHEELS CONSIDERED

The wheels are considered in this section. A differential equation system should be changed considering of the wheels. The state vector changes as follows:

$$\underline{x} = [x_R, y_R, x_L, y_L, x, y, v_R, v_L, v, \varphi, \omega]^T \quad (3)$$

The derivate of the state vector gives the differential equation system of motion:

$$\dot{\underline{x}} = \begin{bmatrix} \dot{x}_R \\ \dot{y}_R \\ \dot{x}_L \\ \dot{y}_L \\ \dot{x} \\ \dot{y} \\ \dot{v}_R \\ \dot{v}_L \\ \dot{v} \\ \dot{\varphi} \\ \dot{\omega} \end{bmatrix} = \begin{bmatrix} v_R \cdot \cos\varphi \\ v_R \cdot \sin\varphi \\ v_L \cdot \cos\varphi \\ v_L \cdot \sin\varphi \\ \frac{v_R+v_L}{2} \cdot \cos\varphi \\ \frac{v_R+v_L}{2} \cdot \sin\varphi \\ a_R \\ a_L \\ a \\ \frac{v_R-v_L}{2 \cdot r} \\ \frac{a_R-a_L}{2 \cdot r} \end{bmatrix} \quad (4)$$

where  $a_L$  and  $a_R$  are the tangential acceleration of left and right wheels, respectively.

All the parameters are zero by initial time, except  $y_R = -150\text{mm}$ ,  $y_L = +150\text{mm}$ . The illustration of motion is shown on Figure 9.

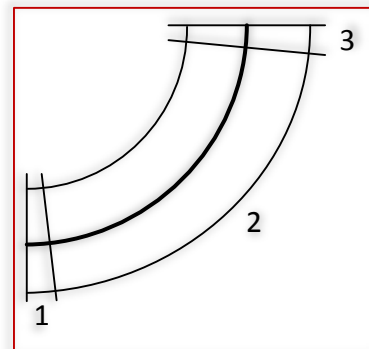


Figure 9. Illustration of path of the AGV during arch motion

The acceleration and angular acceleration are changing during the motion as follows:

- Arch acceleration,  $a_R = 300 \frac{\text{mm}}{\text{s}^2}$ ,  $a_L = 150 \frac{\text{mm}}{\text{s}^2}$ ,  $v_2 = \frac{150+75 \text{ mm}}{s} = 112.5 \frac{\text{m}}{\text{s}}$ , the time can be calculate  $t_{1-2} = \frac{v_2-v_1}{a} = 0.5 \text{ s}$ , where the  $a$  is the average acceleration of wheels
- Arch motion without acceleration,  $\omega = \frac{v_4}{3b} = 0.5 \frac{\text{rad}}{\text{s}}$ ;  $t_{2-3} = 2 \text{ s}$
- Arch deceleration,  $a_R = -300 \frac{\text{mm}}{\text{s}^2}$ ,  $a_L = -150 \frac{\text{mm}}{\text{s}^2}$ , the time can be calculate  $t_{3-4} = \frac{v_4-v_3}{a} = 0.5 \text{ s}$

The summarized motion time is:  $t_{1-4} = \sum_{i=1}^4 t_i = 3 \text{ s}$

The results of this arch motion, i.e., X position, Y position, angle, angular velocity, and velocity of AGV during cornering are shown from Figure 10 to Figure 14, respectively.

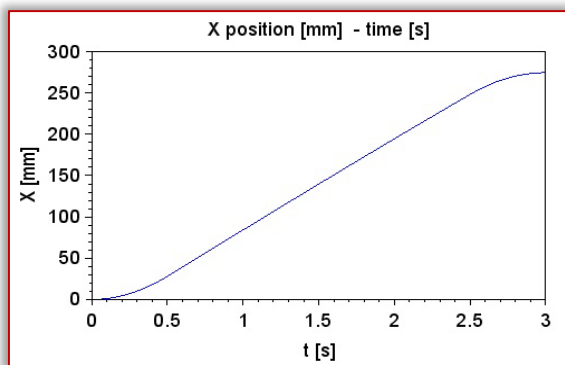


Figure 10. X position of the AGV during arch motion

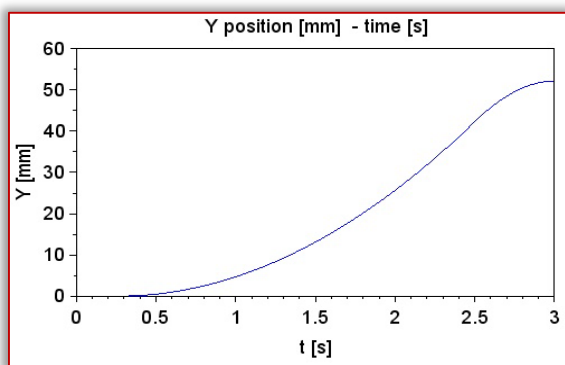


Figure 11. Y position of the AGV during arch motion

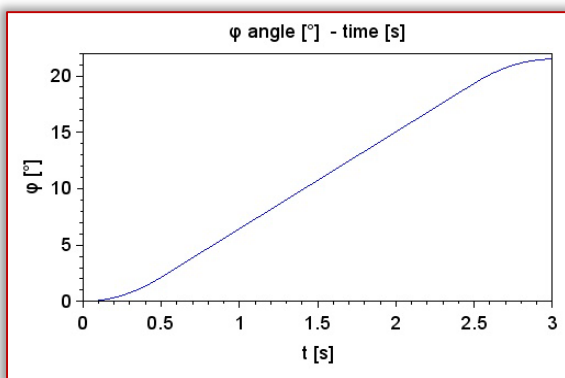


Figure 12. Angle of the AGV during arch motion

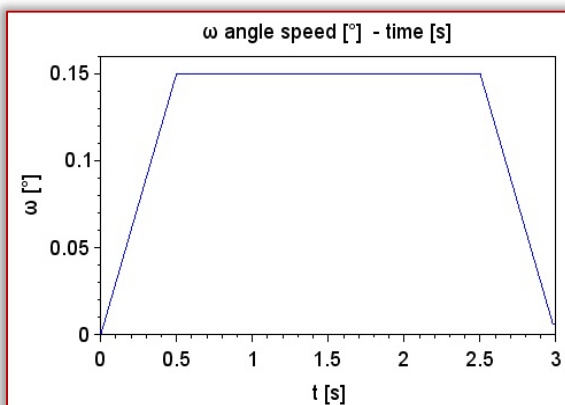


Figure 13. Angular velocity of the AGV during arch motion

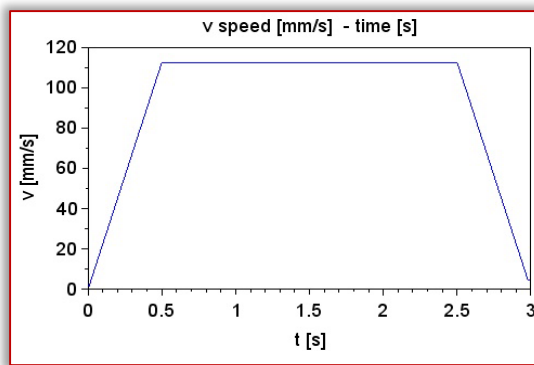


Figure 14. Velocity of the AGV during arch motion

The path of the vehicle can be seen on Figure 15. Alternatively the acceleration or deceleration of the left wheel can be zero ( $\mathbf{a}_L = \mathbf{0} \frac{\text{mm}}{\text{s}^2}$ ), only the right wheel accelerates or decelerates ( $\mathbf{a}_R = \pm 300 \frac{\text{mm}}{\text{s}^2}$ ). The velocity of left wheel is zero during motion ( $\mathbf{v}_L = \mathbf{0} \frac{\text{mm}}{\text{s}}$ ). The path of the vehicle with this small changing can be seen on Figure 16.

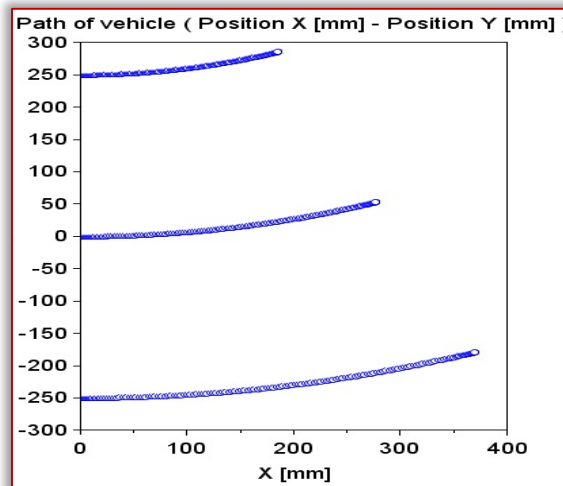


Figure 15. Path of the wheels and AGV during arch motion

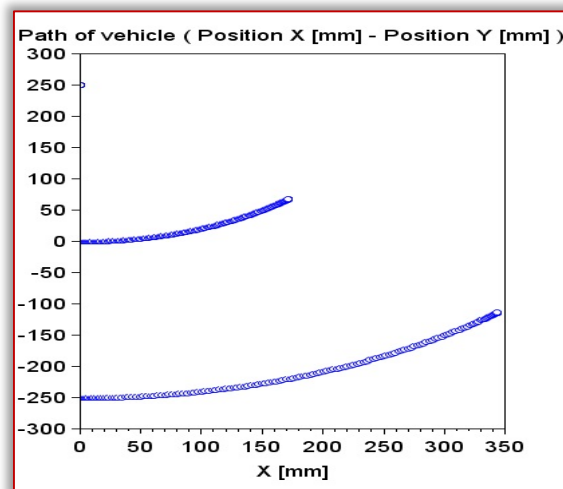


Figure 16. Path of the wheels and AGV during arch motion (only right wheel moves)

### THE MOTION OF AGV: STRAIGHT LINE, BETWEEN TWO POINTS, WHEELS CONSIDERED

The wheels are also considered and the differential equation system is same as in Section 3. In the previous section the X and Y positions are calculated from the given time values. However for the motion planning the time values should be generated automatically from X and Y positions. For this calculating a new calculating method should be performed. In this section the goal is a straight line motion from  $\mathbf{x} = 0\text{mm}$  to exactly  $\mathbf{x} = 1000\text{mm}$  position. All the parameters are zero by initial time, except  $\mathbf{y}_R = -150\text{mm}$ ,  $\mathbf{y}_L = +150\text{mm}$ . The illustration of motion is shown on Figure 17.

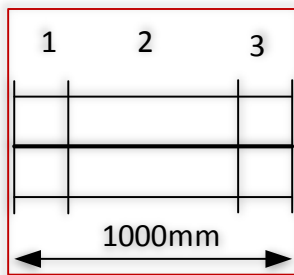


Figure 17. Illustration of path of the AGV during arch motion  
The acceleration is changing during the motion as follows:

- Acceleration,  $\mathbf{a}_R = 300 \frac{\text{mm}}{\text{s}^2}$ ,  $\mathbf{a}_L = 300 \frac{\text{mm}}{\text{s}^2}$ ,  $\mathbf{v}_2 = 150 \frac{\text{mm}}{\text{s}}$ , the X position can be calculated  $\mathbf{X}_{1-2} = \mathbf{a} \cdot \frac{\mathbf{t}_{1-2}^2}{2} = 37.5\text{mm}$ , where  $\mathbf{t}_{1-2} = 0.5\text{s}$
- Straight line motion without acceleration, the X position can be calculated using the data of further step:  $\mathbf{X}_{2-3} = 1000\text{mm} - \mathbf{X}_{3-4} - \mathbf{X}_{1-2} = 925\text{mm}$ , the time:  $\mathbf{t}_{2-3} = \frac{\mathbf{X}_{2-3}}{\mathbf{v}_2} = \frac{925\text{mm}}{150 \frac{\text{mm}}{\text{s}}} = 6.1667\text{s}$
- Deceleration,  $\mathbf{a}_R = -300 \frac{\text{mm}}{\text{s}^2}$ ,  $\mathbf{a}_L = -300 \frac{\text{mm}}{\text{s}^2}$ ,  $\mathbf{v}_2 = 0 \frac{\text{mm}}{\text{s}}$ , the X position can be calculated  $\mathbf{X}_{3-4} = \mathbf{v}_2 \cdot \mathbf{t}_{3-4} - \mathbf{a} \cdot \frac{\mathbf{t}_{3-4}^2}{2} = 37.5\text{mm}$ , where  $\mathbf{t}_{3-4} = 0.5\text{s}$

The summarized motion time is:  $\mathbf{t}_{1-4} = \sum_{i=1}^4 \mathbf{t}_i = 7.167\text{s}$   
The results of this straight line motion, i.e., angular velocity, and velocity of AGV during cornering are shown from Figure 18 to Figure 19, respectively.

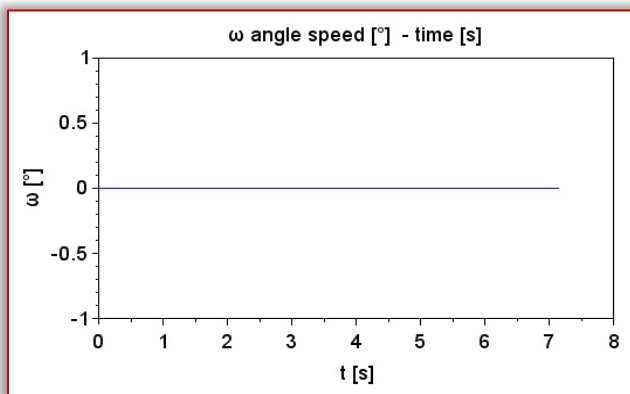


Figure 18. Angular velocity of the AGV during motion between two points

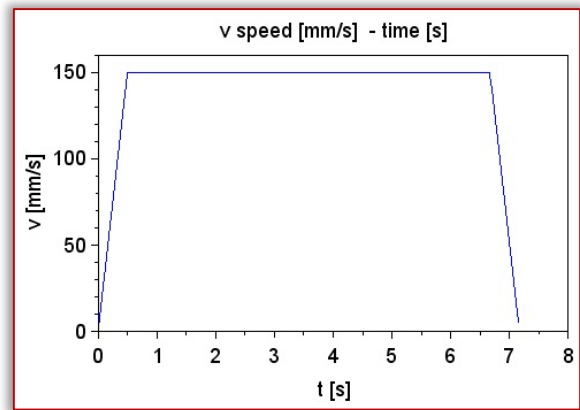


Figure 19. Velocity of the AGV during motion between two points

The path of the vehicle can be seen on Figure 20.

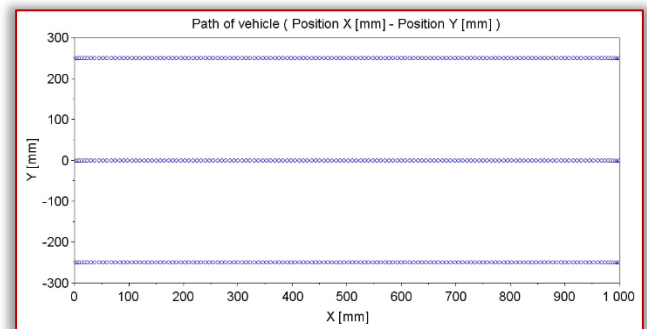


Figure 20. Path of the AGV during motion between two points

### CONCLUSIONS

A motion of AGV has been investigated in this paper. The vehicle can be controlled by prescribing the acceleration and the angular acceleration. The solution of the model provides the vehicle X and Y position, the vehicle angle, the vehicle angular velocity, the vehicle velocity and the path. Three maneuvering problems have been examined. In the first one a cornering was shown. In the second problem the wheels were considered, and the vehicle performed arch motion. In the last section a straight line motion was carried out between two points. In later stability of the maneuver will be experienced.

### Acknowledgement

„Supported BY the ÚNKP–17–3 New National Excellence Program of the Ministry of Human Capacities”

### References

- [1] GUBÁN, M., KOVÁCS, GY.: Industry 4.0 conception; Acta Technica Corviniensis – Bulletin of Engineering, 10:(1) pp. 111–114. (2017)
- [2] VARGA, Z., KOVÁCS, GY.: New supply chain concepts, flexibility as a key parameter of agile supply chains. Acta Technologia – International Scientific Journal about Technologies, Volume: 2 Issue: 4 Pages: 1–5 ISSN 2453–675X (2016).
- [3] MÜLLER, T.: Automated Guided Vehicles, IFS (Publications) Ltd, UK, Springer–Verlag, Berlin, Heidelberg, New York, ISBN 3–540–12629–5 (1983).

- [4] EDWARDS, M.: The Difference between AGVs and Mobile Robots, Cross Company (2016), <https://www.crossco.com/blog/difference-between-agvs-and-mobile-robots>, last accessed 2018/04/25.
- [5] PETRIU, E.M., BASRAN, J.S., GROEN, F.C.A.: Automated guided vehicle position recovery, IEEE Transactions on Instrumentation and Measurement 39(1), 254–258 (1990).
- [6] PETRIU, E.M.: Automated guided vehicle with absolute encoded guide–path, IEEE Transactions on Robotics and Automation 7(4), 562 – 565 (1991).
- [7] COX, I.J.: Blanche—an experiment in guidance and navigation of an autonomous robot vehicle, IEEE Transactions on Robotics and Automation 7(2), 193–204 (1991).
- [8] VALE, A., Ventura, R., Lopes, P., Ribeiro, I.: Assessment of navigation technologies for automated guided vehicle in nuclear fusion facilities, Robotics and Autonomous Systems (2017).
- [9] FRANCIS, S. L. X., ANAVATTI, S. G., GARRATT, M., SHIM, H.: A ToF–camera as a 3D Vision Sensor for Autonomous Mobile Robotics, International Journal of Advanced Robotic Systems (2015).
- [10] KELLY, A., NAGY, B., STAGER, D., UNNIKISHNAN, R.: An Infrastructure–Free Automated Guided Vehicle Based on Computer Vision, IEEE Robotics & Automation Magazine (2007).
- [11] GAMMA DIGITAL KFT.: Vezető nélküli targonca (Driverless Carrier), Budapest (original in Hungarian) (2011).
- [12] PAPP, Á., SZILASSY, L., SÁROSI, J.: Navigation of differential drive mobile robot on predefined, software designed path, Recent Innovations in Mechatronics (RIIM), Debrecen (2016).
- [13] HAMMOND, G.: AGVs at work, Automated Guided Vehicle Systems, IFS (Publications) Ltd, UK, Springer–Verlag, Berlin, Heidelberg, New York, Tokyo, ISBN 3–540–16677–7 (1986).
- [14] BAČÍK, J., ĎUROVSKÝ, F., BIROŠ, M., KYSLAN, K., PERDUKOVÁ, D., SANJEEVIKUMAR, P.: Pathfinder – Development of Automated Guided Vehicle for Hospital Logistics, IEEE Access (2017).
- [15] KARABEGOVIĆ, I.: The role of industrial and service robots in the 4<sup>th</sup> industrial revolution – “Industry 4.0”, Acta Technica Corviniensis – Bulletin of Engineering, 11:(2), pp. 11–16. (2018)
- [16] TIRIAN G. U.: Robotic arm for automated colored object sorting, Acta Technica Corviniensis – Bulletin of Engineering, 10:(4), pp. 147–150. (2017)
- [17] LAJQI N., LAJQI S.: Modeling and simulation of the terrain vehicle with four wheel steering, Acta Technica Corviniensis – Bulletin of Engineering, 10:(4), pp. 17–24. (2017)



ISSN: 2067–3809

copyright © University POLITEHNICA Timisoara,  
Faculty of Engineering Hunedoara,  
5, Revolutiei, 331128, Hunedoara, ROMANIA  
<http://acta.fih.upt.ro>

# EFFECTS OF DIFFERENT ENVIRONMENTS ON THE CORROSION PROPERTIES OF WELDED MILD STEEL PLATE

<sup>1</sup>Department of Mechanical Engineering, The Federal University of Technology, Akure, NIGERIA

<sup>2</sup>Department of Metallurgical and Materials Engineering, The Federal University of Technology, Akure, NIGERIA

**Abstract:** The study on the effects of different environment on the corrosion properties of welded mild steel was evaluated using the weight loss analysis method. Chemical analysis was done on the mild steel plate using ARX spectrometer. Three sets of samples were used; two samples were not subjected to any corrosive environment. Two other samples were immersed in 0.3 M NaCl and the last two samples were immersed in water. Results showed that the un-welded samples exhibited greater loss in weight compared to the welded samples; the rates of corrosion of welded samples were observed to be lower in comparison with their un-welded counterparts in their corresponding corrosive environment, and the maximum values of corrosion rates of the samples were obtained for un-welded steel sample immersed in 0.3 M NaCl (1.924344 mg/mm<sup>2</sup>/yr.); welded steel sample immersed in 0.3 M NaCl (0.509108 mg/mm<sup>2</sup>/yr.); un-welded steel sample immersed in water (0.001821018 mg/mm<sup>2</sup>/yr.); and welded steel sample immersed in water (0.000780731 mg/mm<sup>2</sup>/yr.).

**Keywords:** environments, corrosion, weight loss, welded and un-welded samples

## INTRODUCTION

Mild steel is a type of steel alloy that contains a low amount of carbon as a major constituent. Its carbon content falls within the range 0.10 – 0.25% of low carbon steel. Mild steel is the most common form of steel and it is the major material used in construction industry due to its low cost. Mild steel have good strength, hard and can be bent, worked or can be welded into an endless variety of shapes for from vehicles to building materials. Its unique properties such as low cost, high strength, hardness and easy availability, made it to have wide range of applications in many areas such as vehicle parts, truck bed floors, automobile doors, domestic appliances, nut bolt, chains, hinges, knives, armour, pipes, magnets and military equipment (Kumar and Yadav, 2013; Talabi, *et al.*, 2014).

The interaction of these materials with their immediate environment results in the deterioration of the mechanical properties (such as hardness, toughness, ductility and strength) and physical properties of the materials. In metals, there is actual material loss either by dissolution or by the formation of non-metallic scale or film (Callister, 2007). This material loss is as a result of corrosion. Corrosion can therefore be regarded as the gradual degradation, destruction or deterioration of a material, usually metals, by chemical reaction with its environment. This is done as a result of the electrochemical oxidation of metals in reaction with an oxidant such as oxygen. A common example of electrochemical corrosion is rusting, which is the formation of iron oxides. This type of oxides typically provides oxide(s) or salt(s) of the original metal. All environments are practically corrosive to some degree. Some examples are air and moisture; fresh, distilled, salt, and other gases such as chlorine and ammonia (Fontana, 2007).

Corrosion is a multifaceted phenomenon that adversely affects and deteriorates metals through oxidation. Corrosion degrades the useful properties of materials and structures

including strength, appearance, and permeability to liquid and gases. Katundi *et al.*, (2012) characterized the corrosion resistance in the steel sheets (Hot dip galvanizing of steel sheets) used in automotive industry. They carried out simulated corrosion tests, wet/humidity test and hot dust/dry cycle talk test in laboratory conditions. They tested dynamic behaviour of the corroded specimens dynamically to simulate under the crash test conditions. They exposed the samples to changing climatic conditions in terms of humidity. It was also observed that pitting corrosion damage and crack initiation sites were developed and propagated.

This research focuses on the evaluation of the effects of different environments on the corrosion properties of welded mild steel plate for automobile body service application using the weight loss analysis method.

## MATERIALS AND METHOD

### — Materials and Equipment

The materials used for the experiment include: low carbon steel alloy of known chemical composition, emery paper of the following grades (60, 120, 180, 220, 320, 400, 600, 800, 1200 grits), tong, plastic containers, diamond paste, and zinc rod. The chemicals used for the experiment are sodium chloride (NaCl) and distilled water.

The following equipment were used for the research: universal polishing machine; metallurgical microscope; mass spectrophotometric analyzer; universal hardness tester; cutting machine; grinding machine; digital multi-meter; pH meter; welding machine (electric-arc and oxy-acetylene); calibrated cylinder; digital vernier caliper and digital weighing balance.

### — Methods

#### » Sample Preparation

The mild steel plate was sectioned into six samples each of equal sizes (20 mm length by 20 mm thickness). The first three samples were un-welded while the remaining three samples were further sectioned into two each and welded (using

electric-arc welding). The six samples were then separated in pairs (each pair containing a welded sample and an un-welded sample) resulting into three pairs. The three pairs are  $M_1$  and  $M_2$  as un-corroded samples,  $S_1$  and  $S_2$  as samples immersed in the chloride environment and lastly  $W_1$  and  $W_2$  as samples immersed in water. Samples  $M_1$  and  $M_2$  were purposely set aside just to examine the pre-corrosion microstructure of the steel sample. The sample description is presented in Table 1.

Table 1: Sample Description

Sample	Description
$M_1$	Control sample for pre-corrosion microstructural analysis for un-welded samples
$M_2$	Control sample for pre-corrosion microstructural analysis for welded samples
$S_1$	Un-welded steel sample immersed in 0.3 M NaCl
$S_2$	Welded steel sample immersed in 0.3 M NaCl
$W_1$	Un-welded steel sample immersed in water
$W_2$	Welded steel sample immersed in water

» **Chemical Analysis:**

The chemical analysis was done on the mild steel plate using ARX spectrometer (Oyetunji, *et al.* 2013). Corrosion rate determination was done by weight loss method. In order to effectively calculate the corrosion rate of the samples, the initial weights of the samples were taken using the digital weighing balance. Two samples ( $M_1$  and  $M_2$ ) were not subjected to any corrosive environment for proper comparison. Two other samples ( $S_1$  and  $S_2$ ) were immersed in 0.3 M NaCl and the last two samples ( $W_1$  and  $W_2$ ) were immersed in sea water. The corrosion exercise lasted for 61 days and weighed at intervals of 4 days for the samples immersed in the chloride environment and samples immersed in sea water. The corrosion exercise was undertaken at room temperature, and the weight loss of each sample was obtained by calculating the difference between the initial weight and the obtained weight at each interval. The corrosion rate of each sample is then calculated using equation 1 in accordance to (Fontana, 2007; Seifedine, 2008) and the results are presented in graphic form and depicted as Figures 1–4.

$$\text{Corrosion Rate; } R = \frac{KW}{\rho AT} \quad (1)$$

where:  $K$ , a constant,  $W$ , the weight loss of the metal in gram,  $T$ , time of exposure (hours),  $A$ , the surface area of the metal exposed ( $\text{cm}^2$ ),  $P$ , the density of the metal ( $\text{kg}/\text{m}^3$ ).

**RESULTS AND DISCUSSION**

**a. The chemical analysis result**

The result of the chemical analysis of the as-received mild steel plate is as presented in Table 2.

$$\begin{aligned} \text{Percentage of alloying elements} = \\ \text{Mn } 0.82 + \text{Cr } 0.080 + \text{Ni } 0.102 + \text{Nb } 0.0054 + \text{W } 0.0001 \\ + \text{Ti } 0.0003 + \text{V } 0.0016 = 1.0094 \% \end{aligned}$$

From the above calculation, it can be deduced that the steel pipe is a plain carbon steel and definitely not an alloy steel because the percentage sum of all alloying elements is less than 2%. This implies that there is no inherent element to prevent or reduce the corrosion rate of the steel. The carbon

content falls within the range 0.1 – 0.25%, therefore the steel is a low carbon steel (Degarmo, *et al.*, 2003).

Table 2: Elemental Composition (wt%) of the As-received Mild Steel Plate

Elemental composition	Weight percent (wt%)
C	0.133
Si	0.307
Mn	0.820
P	0.0061
S	0.0081
Cr	0.080
Ni	0.102
Mo	0.038
Al	0.0036
Cu	0.178
Co	0.0085
Ti	0.0003
Nb	0.0054
V	0.0016
W	<0.0001
Pb	<0.0001
B	0.0007
Sn	0.0063
Zn	0.0042
As	0.0005
Bi	0.0010
Ca	0.0010
Ce	0.0023
Zr	0.0006
La	<0.0001
Fe	98.300

**b. Effects of distilled water and chloride environment on the cumulative weight loss of low carbon steel samples**

Samples  $S_1$  and  $S_2$  were immersed in a chloride environment and Figure 1 show the cumulative weight loss of both samples. Generally, cumulative weight losses of these two samples were said to increase with increasing exposure time. Sample  $S_1$ , being an un-welded sample, has a higher cumulative weight loss as the exposure time increases. This means that the weight lost by sample  $S_2$  over the specified number of days were much lesser than the weight lost by sample  $S_1$ . It can be inferred from the graph that the welded sample ( $S_2$ ) exhibits a better resistance to weight loss compared to un-welded sample ( $S_1$ ), because the graph shows that the rate at which sample  $S_2$  loses weight is not as high as the weight loss rate of sample  $S_1$ , (Chinwko, *et al.*, 2014).

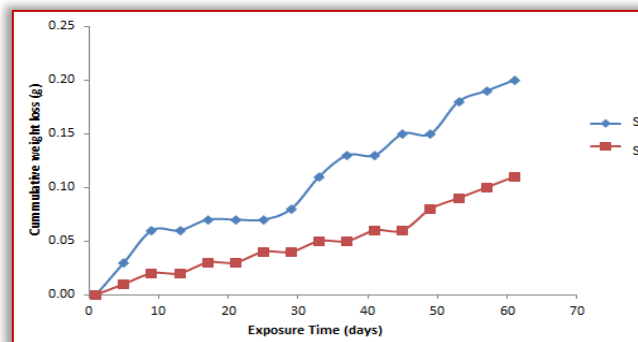


Figure 1: Variation of cumulative weight loss with exposure time of samples immersed in 0.3 M NaCl

As shown in Figure 2, the cumulative weight loss of samples  $W_1$  and  $W_2$  with reference to the exposure time was analyzed with the two samples immersed in sea water. The cumulative weight losses of these two samples increased with increasing exposure time. Figure 2 shows that sample  $W_2$  (welded) did not lose much weight as sample  $W_1$  (un-welded). This implies that the overall cumulative weight loss of sample  $W_1$  is lower than that of sample  $W_2$  which is an indication that the un-welded sample shows a better resistance to the loss of weight when immersed in water. The reason for this can be traced to the action and effect of welding on the steel sample, which had positively, affected the microstructural arrangement of the atoms (Oladele, *et al.*, 2014).

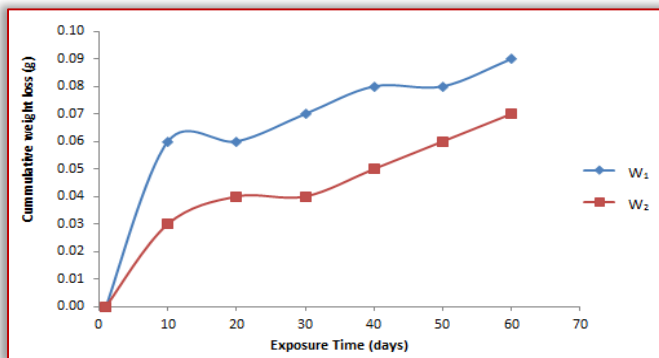


Figure 2: Variation of cumulative weight loss with exposure time of samples immersed in distilled water

Figure 3 shows the comparison among the cumulative weight loss of all samples with distinctive difference between the cumulative weight loss of samples immersed in the chloride environment and samples immersed in distilled water, including welded and un-welded samples. Generally, the welded samples ( $S_2$  and  $W_2$ ) lost lesser weight compared to their un-welded counterparts ( $S_1$  and  $W_1$ ). However, samples  $S_1$  and  $S_2$  which were immersed in the chloride environment lost much weight compared to samples  $W_1$  and  $W_2$  which were immersed in water. This is due to the fact that the chloride environment is aggressive and more corrosive than the natural water environment. The corrosive nature of the chloride was majorly due to the actions of the chloride ions on the steel sample, but the available oxygen in the water formed a corrosion cell until passive films were formed, and the rate almost became constant (Chinwko, *et al.*, 2014).

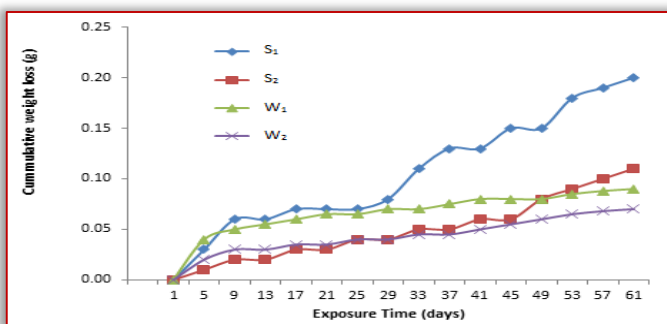


Figure 3: Variation of cumulative weight loss of all samples with the exposure time in days

### c. Effects of chloride environment on corrosion rate of low carbon steel plate samples

Figure 4 shows the relationship between the corrosion rates of the samples immersed in chloride environment. It can be seen from the figure that both samples  $S_1$  and  $S_2$  exhibited a higher corrosion rate within the first 10 days compared to the remaining days. This is usually expected holding to the fact that the chloride environment, in which the samples were subjected, tends to decrease in potency over time. However, the corrosion rate of sample  $S_1$  was far higher than that of sample  $S_2$  because the weldment of sample  $S_2$  undoubtedly acted against the corrosion reaction of the sample compared to the other sample  $S_1$  which had no weldment. In addition, sample  $S_2$  was observed to exhibit a more uniform corrosion than sample  $S_1$  with increase in exposure time.

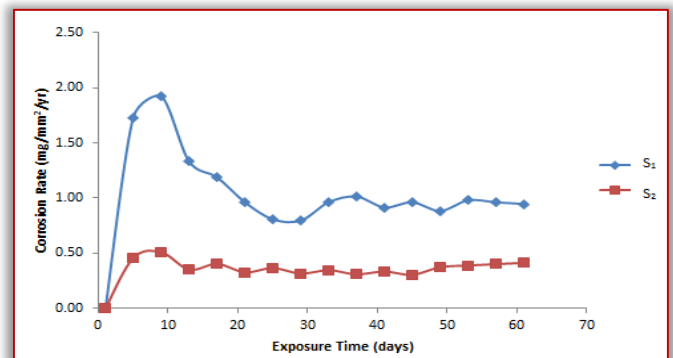


Figure 4: Variation of corrosion rate of samples  $S_1$  and  $S_2$  with the Exposure Time in Days.

The rate of corrosion of samples  $W_1$  and  $W_2$  in water can be seen on Figure 5. Sample  $W_1$  (un-welded) exhibited a very low resistance to corrosion when compared to its counterpart (sample  $W_2$  – welded). This is an indication of the fact that the welded sample exhibited a better corrosion resistance as a function of the action of the weldment with particular to the effect of the welding electrode. Although both samples shows a slightly noticeable uniform corrosion, however, their corrosion rate was very minimal and did not exceed 0.0018 mg/mm<sup>2</sup>/yr. which implies that their rates of corrosion were within the passive extreme. To this end, the mechanical properties of the steels sample will only be slightly affected.

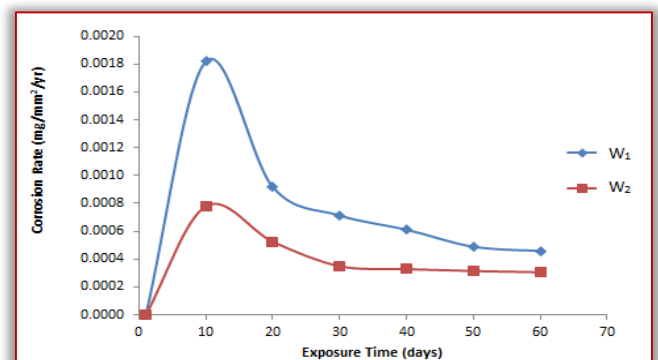


Figure 5: Variation of Corrosion Rate of Samples  $W_1$  and  $W_2$  with the Exposure Time in Days.

The corrosion rates of all samples were calculated and Figure 6 was plotted. Figure 6 therefore explains the corrosion

relationship of all the samples immersed in different corrosive environments. Generally, the corrosion rates of the samples ( $S_1$  and  $S_2$ ) immersed in the chloride environment were distinctively higher than those ( $W_1$  and  $W_2$ ) immersed in water. This was mainly due to the actions of chloride ion on steel samples, which is more corrosive than water. These chloride ions react with the  $Fe^{2+}$  in the steel sample and hence, form passive corrosive films on the steel samples and these makes the corrosion of mild steel faster in the chloride environment than in water. Moreover, the welded samples were observed to possess a lower corrosion rate when directly compared with their un-welded counterpart immersed in the same corrosive environment (Seidu and Kutelu, 2013).

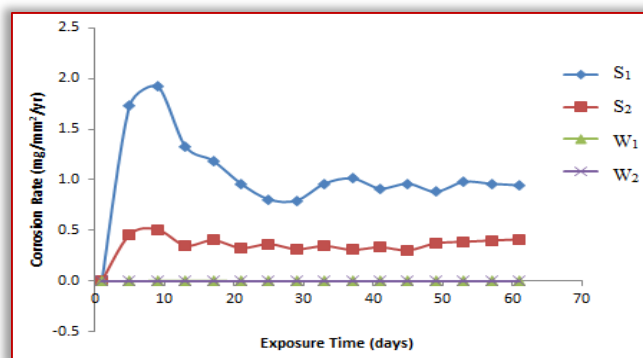


Figure 6: Variation of Corrosion Rate of all Samples with the Exposure Time in Days

## CONCLUSIONS

The effects of different environments on the corrosion properties of welded and un-welded mild steel were investigated, and the following conclusions were drawn:

- The un-welded samples exhibited greater loss in weight compared to the welded samples. This is due to the fact that the weldment of the welded samples reduced the rate of weight loss in the steel samples.
- The rates of corrosion of welded samples were observed to be lower in comparison with their un-welded counterparts in their corresponding corrosive environment.
- The maximum values of corrosion rates of the samples are  $S_1$  (1.924344 mg/mm<sup>2</sup>/yr.),  $S_2$  (0.509108 mg/mm<sup>2</sup>/yr.),  $W_1$  (0.001821018 mg/mm<sup>2</sup>/yr.),  $W_2$  (0.000780731 mg/mm<sup>2</sup>/yr.). This implies that samples ( $S_1$  and  $S_2$ ) immersed in the chloride environment exhibited the higher corrosion rate than samples ( $W_1$  and  $W_2$ ) immersed in distilled water. The factor responsible for this can be traced to the actions of chloride ions which tends to form passive films on the on the steel samples ( $S_1$  and  $S_2$ ) unlike the other samples ( $W_1$  and  $W_2$ ) that corrode uniformly under the influence of water.
- The corrosion behaviour of all the steel samples were within the passive region even-though there was a noticeable discrepancy between the corrosion behavior of samples immersed in the chloride environment and the distilled water environment. This implies that because all

the values of corrosion rate fell within 0.00030583 mg/mm<sup>2</sup>/yr. to 1.924344 mg/mm<sup>2</sup>/yr. (i.e. they did not exceed 5 mg/mm<sup>2</sup>/yr. because active corrosion is known to be within the range of 10 mg/mm<sup>2</sup>/yr. – 200 mg/mm<sup>2</sup>/yr. or greater), the overall corrosion behaviour of the steel samples in the given corrosive environment can be regarded as being *Passive*.

## References

- [1] Callister, W. D. Jr. (2007). Materials Science and Engineering: An Introduction, John Wiley and Sons, Inc., New York, 349 – 351.
- [2] Chinwko, E. C., Odio, B. O., Chukwunke, J. L. and Sinebe, J. E. (2014): Investigation of the Effect of Corrosion on Mild Steel in Five Different Environments. International Journal of Scientific and Technological Research, 3, 7, 306 – 310.
- [3] DeGarmo, E. P., Black, J. T., and Kohser, R. A. (2003), Materials and Processes in Manufacturing (9th ed.), John Wiley and Sons, Inc., New York.
- [4] Fontana, M. G. (2007): Corrosion Engineering, Tata McGraw-Hill Publishing Company Limited, New Delhi, 14.
- [5] Katundi, D., Tosun-Bayraktar, A., Bayraktar, E., and Toueix, E. (2012). Corrosion behaviour of the welded steel sheets used in automotive industry. Journal Of Achievements In Materials And Manufacturing Engineering, 2012, 38(2), 146–153.
- [6] Kumar, H. and Yadav, K. (2013): Corrosion Characteristics of Mild Steel Under Different Atmospheric Conditions by Vapour Phase Corrosion Inhibitors. American Journal of Materials Science and Engineering, 2013, 1, 3, 34–39, Science & Education Publishing DOI:10.12691/ajmse-1-3-1.
- [7] Oladele, I. O., Daramola, O. O. and Oyetunji, A. (2014): Appropriate Technological Procedures for Fusion Welding of Low Alloy Carbon Steel. Journal of Engineering and Engineering Technology, 8, 1, 49 – 53.
- [8] Oyetunji, A., Kutelu, B. J., and Akinola, A. O. (2013). Effects of Welding Speeds and Power Inputs on the Hardness Property of Type 304L Austenitic Stainless Steel Heat Affected Zone (HAZ). Journal of Metallurgical Engineering (ME), Volume 2, Issues 4. October 2013. www.me-journal, 124 – 129.
- [9] Seidu, S. O. and Kutelu, B. J. (2013): Effect of Heat Treatments on Corrosion of Welded Low-Carbon Steel in Acid and Salt Environments. Journal of Minerals & Materials Characterization and Engineering, 1, 95 – 100.
- [10] Seifedine, K. (2008): Corrosion Analysis of Stainless Steel. European Journal of Scientific Research, 22, 4, 508 – 516.
- [11] Talabi, S. I., Owolabi, O. B., Adebisi, J. A., and Yahaya, T. (2014). Effect of Welding Variables on Mechanical Properties of Low Carbon Steel Welded Joint. Advances in Production Engineering & Management ISSN 1854-6250, 9, 4, 2014, 181–186 <http://dx.doi.org/10.14743/apem>.



ISSN: 2067-3809

copyright © University POLITEHNICA Timisoara,  
Faculty of Engineering Hunedoara,  
5, Revolutiei, 331128, Hunedoara, ROMANIA  
<http://acta.fih.upt.ro>

<sup>1</sup>Predrag ŽIVKOVIĆ, <sup>2</sup>Mladen TOMIĆ, <sup>3</sup>Dragana DIMITRIJEVIĆ JOVANOVIĆ,  
<sup>1</sup>Dušan PETKOVIĆ, <sup>1</sup>Jelena JANEVSKI, <sup>4</sup>Mirko DOBRNJAC

## WIND ENERGY IN JABLANICA-TOPLICA REGION OF SOUTH SERBIA

<sup>1</sup>University of Niš, Faculty of Mechanical Engineering, Niš, SERBIA

<sup>2</sup>University of Novi Sad, Faculty of Technical Sciences, Novi Sad, SERBIA

<sup>3</sup>University of Belgrade, Institute of Nuclear Sciences Vinca, Belgrade, SERBIA

<sup>4</sup>University of Banjaluka, Faculty of Mechanical Engineering, Banja Luka, BOSNIA & HERZEGOVINA

**Abstract:** Obtaining of all acceptable locations is one of the main tasks for siting of wind turbines. Very thorough analyses are needed in order to ensure the finalization of the project. However, economic factors are usually very limiting. One of the possibilities to increase the efficiency of the wind farm is to reduce the transport losses, as well as the initial investment, by using produced energy as close to the production site as possible. This paper focuses on the possibilities of the Radan Mountain wind potentials usage in the nearby city of Leskovac, located between the Jablanica and Toplica regions of the Southern Serbia. The estimations were obtained using the WAsP simulation software. The results are compared by means of the quality and quantity of the wind data and capacity factor. Finally, the economic analysis of the acceptability of the installing of wind turbines was done. This paper is concerned by the National Program of Energy Efficiency, project number: TR33036, funded by the Government of Republic of Serbia.

**Keywords:** wind turbines, wind potentials, Radan Mountain, Southern Serbia, WAsP simulation software

### INTRODUCTION

Energy, especially electrical, is of vital importance in the world today. Many assessments of the fuel resources, mostly fossil, clearly marks the fact that such resources, especially for oil, are close to the end. The need for energy constantly rises, so introduction of new resources is inevitable. All these facts points to the necessity of transition to the sustainable development, especially to the usage of renewable energy sources. Wind energy clearly takes its place, considering its large potentials, purity and availability. The present constrains are mostly of financial nature. The most important task is the siting of wind turbines (obtaining the best possible locations for installing of the turbines, considering the possibility for energy production and minimization of losses). For that purpose, the wind atlas method is developed, which became easy for use with the fast development of computers. Position of wind turbine is in strong correlation with energy production. According to the previous research [1,2,3], linear models can not estimate correctly the wind energy potentials in the terrain where the ruggedness index (index that represents the terrain slope value) exceeds 0.3. In such a case, using full CFD models, followed by experimental validation is necessary. Even if all of the above mentioned is satisfied, there is possibility that the wind warm is not going to have the predicted outpun during the project lifetime, which is 25-30 years, which is about the same as the climatic periode, which lasts for 32 years.

### MATHEMATICAL MODEL

CFD models are more precise, but they need much more computational time. Considering the need to obtain the results as soon as possible, the best micro model was extracted from the larger macro model using the fast linear software [4]. Then the best wind turbine locations were obtained by using CFD software [5]. In this paper combination of a linear and full nonlinear model is used.

### — LINEAR MODEL

Linear model is expressed by the subsequent set of equations.

≡ Continuity equation

$$\frac{\partial}{\partial x_i}(\rho U_i) = 0 \quad (1)$$

≡ Logarithmic vertical wind profile

$$U_z = \frac{U_*}{\kappa} \left( \ln \frac{z}{z_0} - \psi \right) \quad (2)$$

≡ Weibull distribution equations

$$f(U) = \frac{k}{A} \left( \frac{U}{A} \right)^{k-1} \exp \left[ - \left( \frac{U}{A} \right)^k \right] \quad (3)$$

$$F(U) = \exp \left[ - \left( \frac{U}{A} \right)^k \right] \quad (4)$$

### — NONLINEAR MODEL

Nonlinear model solves the full set of governing equations of steady fluid flow.

≡ Continuity equation

$$\frac{\partial}{\partial x_i}(\rho U_i) = 0 \quad (5)$$

≡ Momentum equations

$$U_j \frac{\partial U_i}{\partial x_j} - \frac{\partial}{\partial x_j} \nu_{eff} \left( \frac{\partial U_i}{\partial x_j} + \frac{\partial U_j}{\partial x_i} \right) = - \frac{1}{\rho} \frac{\partial P}{\partial x_i} \quad (6)$$

≡ Turbulence model equations

$$U_j \frac{\partial k}{\partial x_j} - \frac{\partial}{\partial x_j} \left[ \left( \nu + \frac{\nu_T}{\sigma_k} \right) \frac{\partial k}{\partial x_j} \right] = P_k - \varepsilon \quad (7)$$

$$U_j \frac{\partial \varepsilon}{\partial x_j} - \frac{\partial}{\partial x_j} \left[ \left( \nu + \frac{\nu_T}{\sigma_\varepsilon} \right) \frac{\partial \varepsilon}{\partial x_j} \right] = \frac{\varepsilon}{k} (C_{\varepsilon 1} P_k - C_{\varepsilon 2} \varepsilon) \quad (8)$$

where:

$$P_k = v_T \left( \frac{\partial U_i}{\partial x_j} + \frac{\partial U_j}{\partial x_i} \right) \frac{\partial U_i}{\partial x_j} \quad (9)$$

$$v_{eff} = v + v_T \quad (10)$$

$$v_T = C_\mu k^2 / \varepsilon \quad (11)$$

The modified set of model coefficients are:  $C_\mu = 0.0324$ ,  $C_{\varepsilon 1} = 1.44$ ,  $C_{\varepsilon 2} = 1.92$ ,  $\sigma_k = 1.0$ ,  $\sigma_\varepsilon = 1.85$

The set of the nonlinear partial differential equations is solved by the WindSim [5] software package.

### COMBINED METHODOLOGY

CFD models are more precise, but they need much more computational time. Considering the need to obtain the results as soon as possible, the best micro model was extracted from the larger macro model.

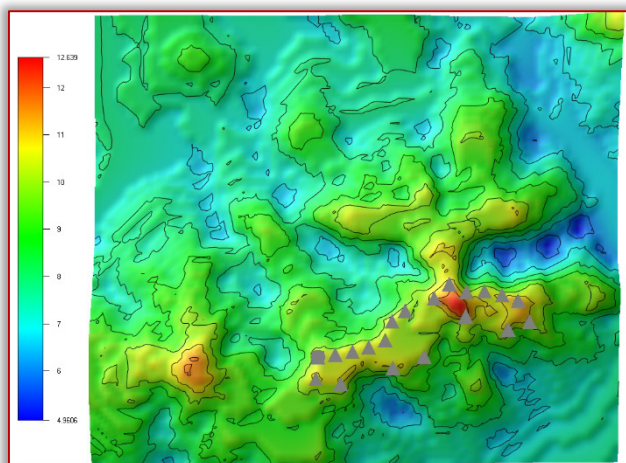
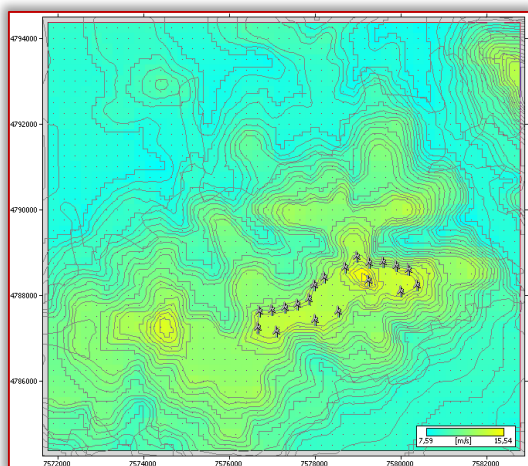


Figure 1. Mean wind speed fields obtained by simulations in WAsP (left) and WindSim (right)

The differences in wind energy estimations while using these different approaches are considerable. Many investigations were done on this subject, dealing with different aspects of the software operation.

Test model of Seličevica mountain [3] was chosen by its adequate orography, as can be seen in Figure 1. It was shown that the WAsP predictions are about 30% larger than WindSim [5] ones (estimated wind speed is in range 7.75-15.54m/s for WAsP, and 4.96-12.64m/s for WindSim), due to

neglecting of the second-order terms in the momentum equation, i.e. (6).

For obtaining of the results the nesting technique is used. Simulations were done for the Enercon E82 wind turbine. It is very appropriate to use WAsP as the initial software on mezzo level estimations, and WindSim for more precise micro level estimations, as the computational time for WAsP is about 20 times less than for WindSim.

In the previous papers [6,7,8] results obtained by numerical simulation on over a dozen micro locations are presented. The considered locations mainly covers the mountainous regions of Southern and Eastern Serbia.

### RADAN MOUNTAIN WIND POTENTIALS

This paper considers the wind potentials of the Toplica – Jablanica regions, bounded by the river Toplica valey from the north, river Jablanica valey from the south, river South Morava valey from the east and the slopes of the Kopaonik mountain from the west. This region area is about 6000 km<sup>2</sup>. Characteristical of this region are all types of land by elevation – flatlands, hills and low mountain areas.

Highest ground is on the Radan mountain, with area of some 466 km<sup>2</sup>, highest peak being Šopot with 1409 m asl. The insolation is also very pronounced from the south and east, towards Pusta Reka valey, so the oak forests can be found even at 900 m asl. Predominant wind direstion is north-northwest all year round, which is to be expected, as it is the Morava river valey direction. Nevertheless, the wind speed is moderate, as the moderate slopes of the Radan mountain does not give high speed-up effects, although there is no high vegetation at the summit.

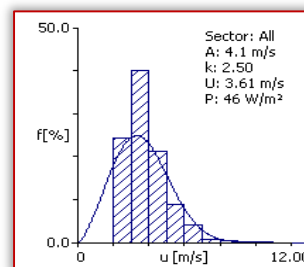
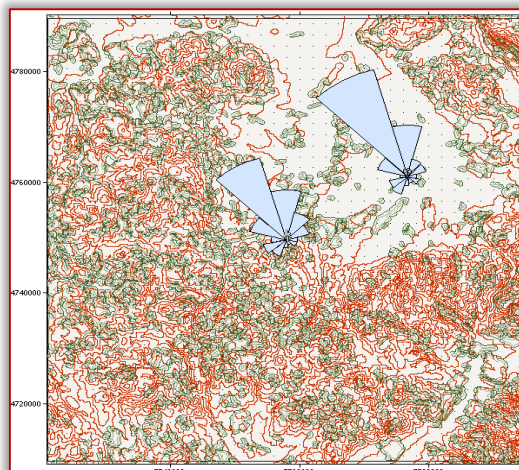


Figure 2. Macro model with wind roses (left) and Weibull distribution (right)

Chosen wind turbine type is Enercon E-48, with unit power of 800kW. Considered micro model was chosen by former simulation on the bigger model, from which, using the nesting technique, micro model for Radan wind farm is obtained.

For the turbine siting the method of wake loss minimization and maximal annual energy production was used. Also, the recommendations about distance between wind turbines for the siting were as follows: in the wind direction minimally 7D (D – rotor diameter) and in the normal direction 4D.

After the simulation were done and the fields of annual energy production (AEP) and the ruggedness index (RIX) for the macro model, and the mean wind speed, power density and AEP fields with turbine disposition for the micro model are presented on the following figures.

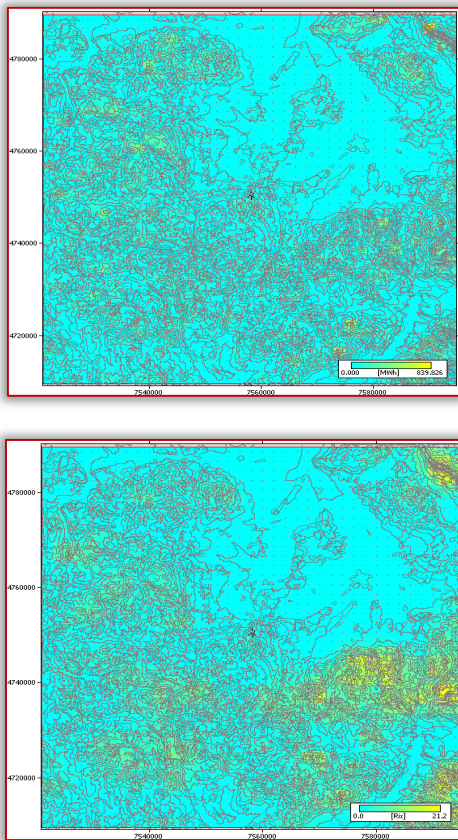


Figure 3. AEP field (left) and RIX field (right) for the macro model  
On the basis of the data obtained by simulation, and the known turbine power, the capacity factor  $C_p$  can be calculated for the considered wind farm. The capacity factor is the ratio of the eral power output of a wind farm to its nominal output (if working on the full potential) for a period of time, for the case considered, annually. This can be presented in the form:

$$C_p = \frac{AEP \cdot 0,1178}{8760 \cdot P_t \cdot 1,3} \quad (12)$$

where are:  $P_t$  installed power of the farm with 15 wind turbines Enercon E-48, 0.1178 is the percentage of accepted data (all the other can be considered as calm, i.e. <2m/s) and factor 1.3 is as the WasP software overprediction.

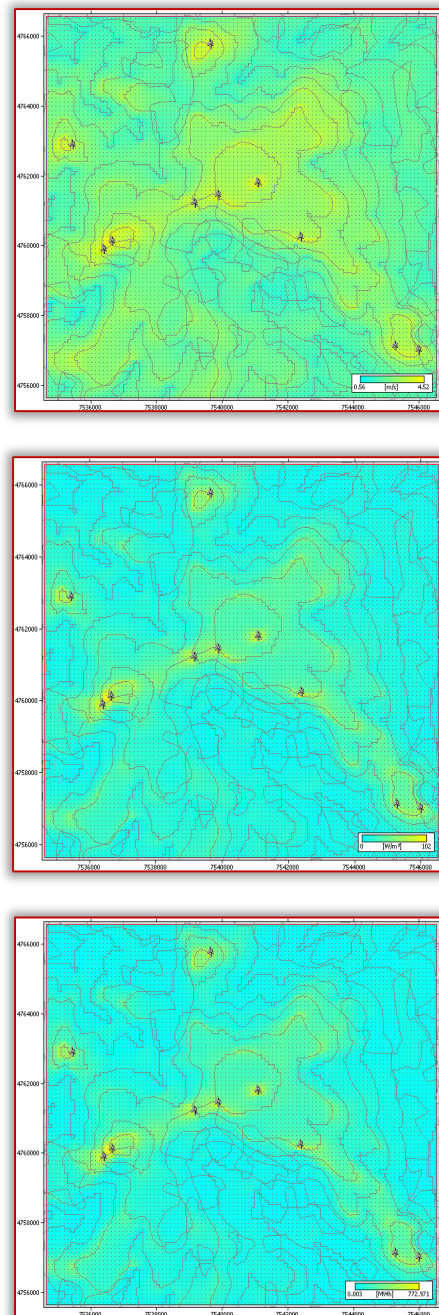


Figure 4. Mean wind speed (left), power density (middle) and AEP fields (right) for the micro model

Stable wind data were obtained from the main meteorological station Leskovac. As the turbine acceptable wind speed is in the range of 2-25m/s, only 11.78% of the wind data are in the acceptable range. Considering this, as well as the overestimation by the used software, the capacity factor (ratio between possible AEP and max AEP) is calculated to be  $C_p=0.13$ . It is considered that the economically acceptable locations are with  $C_p=0.25$  or larger:

Table 1. Predicted values for the 10 turbine wind farm Radan

Parameter	Total	Average	Minimum	Maximum
Nett AEP [MWh]	6485.46	648.54	543.833	838.266
Gross AEP [MWh]	6497.65	649.76	544.543	842.152
Wake loss [%]	0.19	-	-	-

## TECHNO-ECONOMICAL ANALYSIS

Economical analysis is one of the most important parts of every project. Renewable energy, including wind energy, is not an exception. Having in mind the current prices of wind turbines, state of the global and local financial markets, and the fact that the local infrastructure is not very developed, preliminary financial analysis was done. The initial assumptions are: the farm will operate for 25 years; initial investment is 8 million EUR; subventions will be 10%; annual discount rate will be 10%; annual inflation will be 7%; increase of the electricity price will be 5% per annum. Expected electricity price is 0.104EUR. The estimated financial indicators are shown in the following table.

Table 2. Financial indicators for the 10 turbine wind farm Radan

Rate of income (year 01)	ROI	1.70	[%]
Simple payback time	SPB	13.21	[year]
Net present value	NPV	10.743	[M EUR]
Internal rentability rate	IRR	70.93	[%]
Dynamic payback time	DPB	2.30	[year]
Benefit/cost ratio	B/C	29.57	[-]
Lifelong cost savings	LCS	1.184	[M EUR/ year]

Using above mentioned financial indicators, it was calculated that annual income of the wind farm Radan could be about 0.65 million EUR. It shows that the project payback time is about 13 years, which is not economically acceptable at this moment. There is hope that with the trend of the reducing of initial investments, considering the vicinity of the important local centres of industry and commerce such as Niš and Leskovac and the accessibility of the location, one day such project could be finalized.

In order to improve the predictions in the presented research, validation of the data should be done by on-site measurements [9,10,11]. As the potentials are well below the acceptable margin of potentials ( $C_p \sim 13\%$  of the lower limit of 25%), there is possibility for combining the system with solar or other types of RES [12,13], in order to increase the efficiency. Some new approaches to the problem of the wind farm production estimations can also be implemented [14].

## CONCLUSIONS

Wind energy is one of the fastest growing renewable energy resources. Most of the EU members are using it widely. Yet, the available usable locations are not limitless. This gives opportunity to the less developed countries to use the available funds, in the scope of 20% of energy in Europe to be produced by renewable sources.

The estimated wind potentials are relatively low, with capacity factor being about half of the minimal (13 of 25%). Simply analyzed, this project is not profitable. From the other hand, there is hope of decreasing the initial investments, which would increase the profitability. There is also the easy accessibility of the location, as well as the vicinity of important local centers of Niš and Leskovac, which are always in need of more energy.

## Acknowledgment

This paper is part of the broader research over several projects with the Government of the Republic of Serbia, and is further proof of the applicability of the proposed methodology.

## Note

This paper is based on the paper presented at INTERNATIONAL CONFERENCE ON APPLIED SCIENCES – ICAS 2018, organized by UNIVERSITY POLITEHNICA TIMISOARA, Faculty of Engineering Hunedoara (ROMANIA) and UNIVERSITY OF BANJA LUKA, Faculty of Mechanical Engineering (BOSNIA & HERZEGOVINA), in cooperation with the Academy of Romanian Scientists, Academy of Sciences Republic of Srpska, Academy of Technical Sciences of Romania – Timisoara Branch and General Association of Romanian Engineers – Hunedoara Branch, in Banja Luka, BOSNIA & HERZEGOVINA, 9 – 11 May 2018.

## References

- [1] Schaffner B., Wind Modeling in Mountains: Intercomparison and Validation of Models, study for METEOTEST, Bern, Switzerland and VECTOR AS, Tonsberg, Norway
- [2] Stevanović, Ž., 2008 Numerički aspekti turbulentnog prenošenja impulsa i toplote, Univerzitet u Nišu, Mašinski fakultet, Niš
- [3] Živković P. 2006 Wind energy estimations in terrain with complex orography - comparative methodology analysis, Master thesis, Faculty of Mechanical engineering, Niš
- [4] WASP (Wind Atlas Analysis and Application Program), Wind Energy Department at Risø National Laboratory, Denmark
- [5] WindSim - Delft University, Denmark, available as module of PHOENICS software package
- [6] Schneider, D. R. et al. 2007 Mapping the potential for decentralized energy generation based on RES in Western Balkans, Thermal Science, Vol. 11, Issue 3, pp 7-26
- [7] Živković P., Ilić G., Stevanović Ž. June 24-27 2008 Wind Power Assessment in Complex Terrains of Serbia, Proceedings, 21st International Conference on Efficiency, Cost, Optimization, Simulation and Environmental Impact of Energy Systems, Cracow-Gliwice, Poland, pp 1141-1148
- [8] Živković, P. et al. May 29-30, 2015 Possibilities of wind energy usage in the ski center Kopaonik, Proceedings, The 12th Conference DEMI 2015, Banjaluka, Bosnia and Herzegovina, pp. 373-378
- [9] Stevanović, Ž. M., Mirkov, N. S., Stevanović, Ž. Ž., Stojanović, A. D. 2010 Validation of atmospheric boundary layer turbulence model by on-site measurements, Thermal Science, Vol. 14, Issue 1, pp 199-207
- [10] Pezo, M. L., Bakić, V. V., Marković, Z. J. 2016 Structural analysis of guyed mast exposed to wind action, Thermal Science, Vol. 20, Issue Suppl. 5, pp S1473-S1483
- [11] Bakić, V. V., Živković, G. S., Pezo, M. L. 2011 Numerical simulation of the air flow around the arrays of solar collectors, Thermal Science, Vol. 15, Issue 2, pp 457-465
- [12] Bakić, V. V. et al. 2012 Technical analysis of photovoltaic/wind systems with hydrogen storage, Thermal Science, Vol. 16, Issue 3, pp 865-875
- [13] Bakić V. V., Živković, G. S., Pezo, M. L. 2016 Techno-economic analysis of stand-alone photovoltaic/wind/battery/hydrogen systems for very small-scale applications, Thermal Science, Vol. 20, Issue Suppl. 1, pp S261-S273
- [14] Živković, P. M. et al. 2012 Hybrid soft computing control strategies for improving the energy capture of a wind farm, Thermal Science, Vol. 16, Issue Suppl. 2, pp S483-S491.

copyright © University POLITEHNICA Timisoara,  
Faculty of Engineering Hunedoara,  
5, Revolutiei, 331128, Hunedoara, ROMANIA  
<http://acta.fih.upt.ro>

<sup>1</sup>Vitalii PANCHUK, <sup>2</sup>Oleh ONYSKO, <sup>3</sup>Iuliia MEDVID

# TECHNOLOGY OF THE OIL AND GAS DRILL PIPE CONNECTOR MANUFACTURING WITH LOW-PERMEABILITY LEVEL OF THE DRILLING MUD IN ITS SCREW PART

<sup>1-3</sup>Ivano–Frankivsk National Technical University of Oil and Gas, Department of Computerized Machine–Building Production, Ivano–Frankivsk, UKRAINE

**Abstract:** Impermeability of the drill pipe connector is one of the most important indicators of its quality. It is provided by the interference fit of the box and nipple joint. This leads to the deformation of the contact surface of the nipple–box coupling and next gradual loss of its tightness. The authors offer to provide connection tightness increase due to the reducing of the initial height of the gaps between the thread ridge and groove and to increase the strength and hardness tool–joint material. From the technological point of view, it requires a significant increase of the thread tool life by means of using of the back rake angle in its nose from  $-3^\circ$  to  $-5^\circ$ . The article shows the results of algorithmic calculations which prove that this will cause the deviation from the specified profile at the maximum of  $0.15^\circ$ , which is only 22% of the tolerance limit. These studies prove the technological possibility of a significant reducing of this gap without significant correction of the profile of the cutting part of the turning threading–tool.

**Keywords:** drill pipe connector, drilling mud, tool life, connection tightness

## RELEVANCE OF THE PROBLEM

In oil and gas extraction, drilling of the well is one of the most consumable parts of it. Drill string are mainly consist of the drill pipes and bottom (Figure 1). The drill pipes, as well as the bottom elements (BHA), connect between themselves with the help of the connectors, called as tool joints.

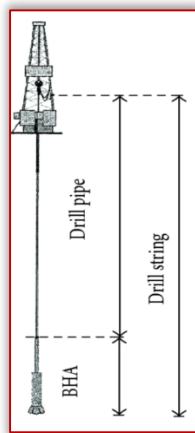


Figure 1. Drill string in general

The drill string tool–joints are located on both sides of each drill pipe (Figure 2) and of each heavy weight drill pipe and contain an female conical thread – a box and an male one – a pin (Figure 3).

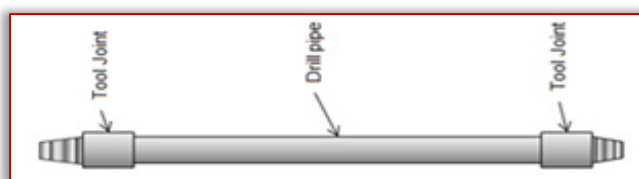


Figure 2. Drill pipe in general

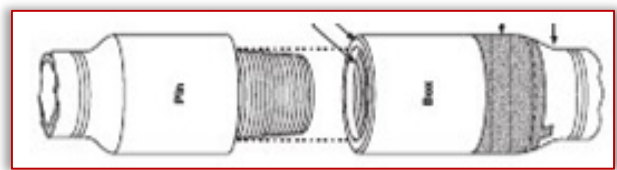


Figure 3. Pin and box before screwing

Therefore, the reliability of the entire drill string depends on reliability and quality of drill string tool–joints certainly. As is known, the tool joint is intended for quick screw–down or screw–up of the elements of the drill string and the transfer between them of hydraulic energy and torque. The mud solution fluid in the well is a hydraulic environment. The losses of the drilling fluid, which accompany the drilling process, arise from the non–densities in the drill pipe tool joints and are the result of both their operational changes and, in our opinion, the result of technological imperfections in the tapered thread manufacturing related to the non–accurate cutting edge profile of the threading tools and their un perfect geometric parameters. The authors believe that the technology of manufacturing pin and boxes (Figure 3) can be revised with minimal changes in the working part of the tool, and as a result, with a significant decrease of the drilling mud moving in the threading part of the drill string tool joint.

## EXISTING TECHNOLOGY OF THE TOOL–JOINT TAPERED THREAD MANUFACTURING

Manufacturers for the machining of the tool joint tapered thread apply turning technology (Figure 4) [1]. The cutting part of the turning tool according to [1,2] is always only one–variant in relation to the back rake angle, that is, it only has a zero value. In Figure 5 the face of the tool cutting part

coincides with the axial plane of the workpiece, which actually indicates the zero value of the back rake angle on its nose.

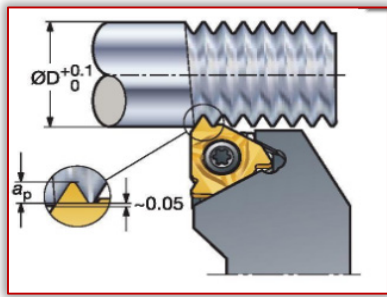


Figure 4. Scheme of the threading turning machining by the full profile tool

The tangential deviation of the cutter nose relative to the workpiece axis is  $\pm 0.1$  mm (see Figure 5).

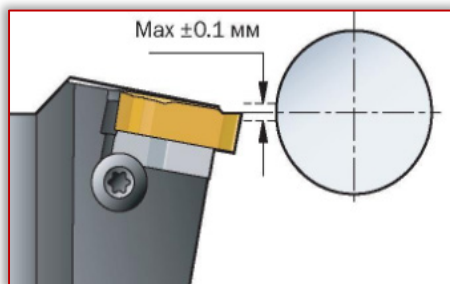


Figure 5. Scheme of the threading machining by the turning tool which face coincides with the axial plane of the workpiece. The flank clearance angle is selected at the expense of the anvil and it is equal to the helix angle of the inclination of the screw (see Figure 6).

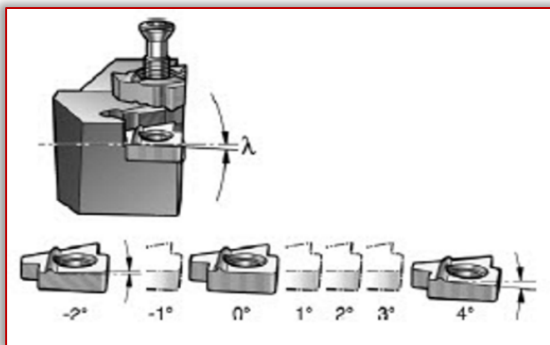


Figure 6. Scheme of the application of the anvil to create the flank clearance angle of inclination

The leading tool manufacturers do not apply the differentiation of the inserts by their profile, despite the application of the different anvil size to create a flank clearance angle.

#### THE APPLICATION OF ALGORITHMIC CALCULATION

The application of algorithmic calculation of the profile angle at the tapered thread was made by using the turning tool with an adjusted profile of the cutting edge which has non-zero values of geometric parameters.

The work [3] presents the results of the development of an application program, which, by algorithm [4] calculates the value of the half-profile angle of the turning tool cutting

edge, which provides the drilling pipe tapered thread profile of the needed accuracy. In this application, the back rake angle and the flank clearance angle are variables. The deviation of the installation of the nose of the cutter over the axis of the work piece also is the variable in the program. The article does not speak about the results of the use of tool with the unmodified profile angle of their cutting edge and at non-zero values of the back rake angle and the flank clearance angle and therefore there is no analysis of the accuracy of the implementation of that type of the instruments.

#### THE EXISTENCE OF THE GAP IN THE DRILL STRING TAPERED THREAD BETWEEN A BOX AND A NIPPLE

The gap is shown in Figure 7. It is denoted by the number 3 and occurs in a screwed form between the thread surfaces of the box 1 and the pin 2. If the end face of the 4 box and the end face of the 5 nipple are nontightly adjacent to each other, then the specified coupling connection will skip the drilling solution from the inside of the drill string into the outside of the tube space, that is, into the drilled well.

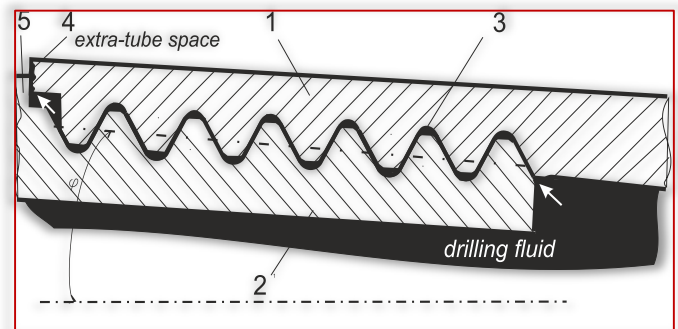


Figure 7. Existence of the technological gap between the nipple and the box in the drill string connection

Figure 8 shows the tool joint tapered thread profile according to the standard [5]. The half-angle of the section profile is  $30^\circ$ . The tolerance limits to the specified size is  $\pm 40'$ . Table 1 shows the parameters of the tapered thread for its most commonly used form 4.

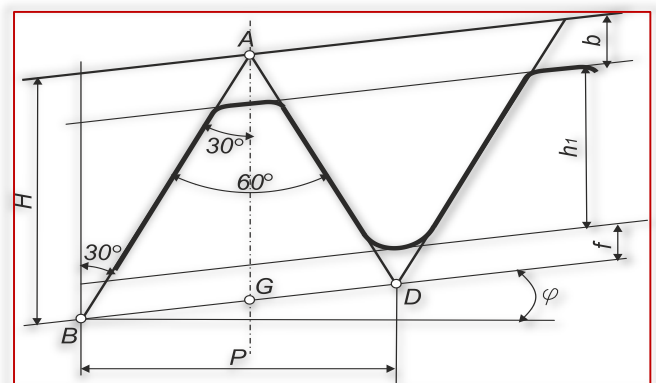


Figure 8. Scheme of the tool joint tapered thread profile according to API 7 and [5]

The tool joint tapered thread is performed so that the length of its side AB is always greater than – the AD side. Points A and G are used to identify the axis dividing a profile angle of  $60^\circ$  half in Figure 8.

Table 1. Parameters of the tool joint tapered thread according to [5] for form IV

Name of parameter	Value
Pitch	6,35 mm
Thread Height H	5,487 mm
$h_1$ work height	3,095 mm
$\varphi$ taper angle	4°45'48"
Crest truncation, $b^*$	1,427 mm
root truncation, $f$	0,965 mm
Thread height truncated $h^*$	2,633 mm
Crest flat width $a$	1,651 mm
Root flat corner radius $r$	0,965 mm

Figure 9 illustrates the gap. On the left side the dimensions are indicated, and on the right corner for clarity the gap is painted in black. The radius of rounding  $r$  is actually intended for the design of the tool, and is not a mandatory dimension of the thread root. According to Figure 8 and Table 1, the height of the gap  $h_1 - h$  is for Form IV – 0.462 mm.

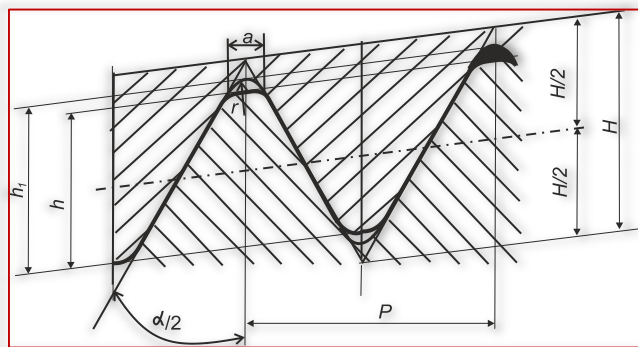


Figure 9. Illustration of the technological gap of the drill string tapered thread

### TECHNOLOGICAL NECESSITY OF THE GAP EXISTENCE IN THE THREAD SECTION OF THE DRILL STRING CONNECTION

The value of  $h_1$  as an optional element does not affect the screw quality and the strength of the thread connection, but its reducing leads to a decrease in the height of the gap. At the same time, it is known that in the existing turning machining of the thread, the cutter (Figure 4) is used in many passes, for example, in a radial cutting (Figure 10) [1,2] to reach the full depth  $a_p$  (see Figure 4). In this case, the cutting edge of the tool, which forms the thread root is worn mostly but the wear of that part of the cutting edge forming the crest is almost zero. This is obvious, since the thread crest is formed only during one or two the last passes by cutter. Thus, the existence of a gap with the value of  $h_1 - h$  is grounded only by the manufacturing technology of the thread, since the value of  $h_1$  during the machining by cutter from pass to pass and from the product to the next product decreases and even theoretically  $h_1$  can reach the value of  $h$ . As a result, the value of  $h_1 - h$  will be zero and further decrease will result in the inability to screw the tool joint due to the interference of the body of the box in the body of the pin. That is why it is necessary to consider this gap is technological, since it enables to use tool capable to cut during a certain period of its operation. This time in the machining process is called as tool life.

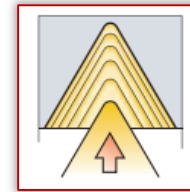


Figure 10. Scheme of multi-pass turning machining of the thread with radial cutting

**HYDRAULIC LOSSES IN THE DRILL STRING CONNECTIONS**  
Hydraulic losses that occur during the operation are described in [6]. Figures 11, 12 show graphs of the functional dependence of energy expenditure (J) on pressure (MPa) that develops in a drill string when the drilling mud is poured through it.

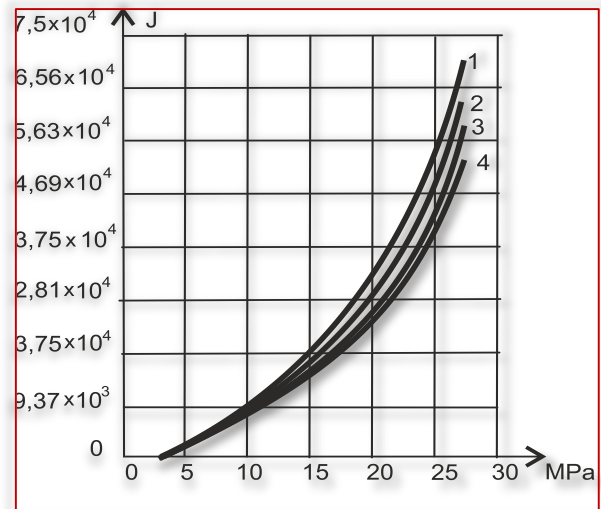


Figure 11. Dependence of losses of hydraulic energy in a connection with a diameter of 101.6 mm, depending on the pressure of the drill pump at different values of the wear of the tapered thread cut NC 46: 1.  $\Delta h = 0.1$  mm, 2.  $\Delta h = 0.075$  mm, 3  $\Delta h = 0.05$  mm, 4.  $\Delta h = 0.01$  mm

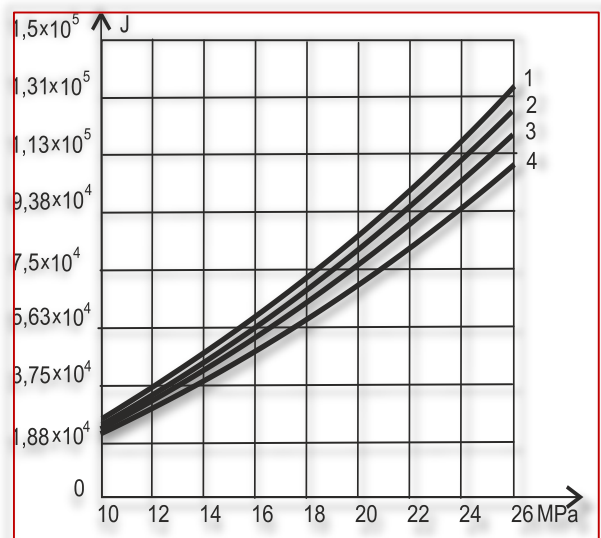


Figure 12. Dependence of losses of hydraulic energy in a connection with a diameter of 127 mm, depending on the pressure of the drill pump at different values of the wear of the tapered thread cut NC 50: 1.  $\Delta h = 0.1$  mm, 2.  $\Delta h = 0.075$  mm, 3  $\Delta h = 0.05$  mm, 4.  $\Delta h = 0.01$  mm

The rate of the energy losses as seen from the graphs increases with an increase in thread wear  $\Delta h$ . Since according to [7] the thread groove during the operation almost is not worn out, that is, the value of the height of the profile  $h_1$  remains almost unchanged, but the mainly thread ridge and its flanks are worn that is, the value of thread height truncated  $h$  decreases. This decrease is actually the value  $\Delta h$  in Figures 11, 12.

The works [8,9] represent the virtual exploration of the drill solution motion through the screw channels formed by the gap between the pin and the box of the drill string. tool joint. The authors [9] argue that with decreasing the width of the channel from the standard value  $a = 1.651$  mm (see Table 1) to  $a = 1$  mm, which corresponds to the decrease of the gap height in up about 0.3 mm, that is, from 0.46 mm to 0,15 mm, the speed of the washing fluid motion can be reduced by 20–30 times. Such a very significant decline in the opinion of the authors [9] should significantly reduce the hydraulic losses and abrasive wearing of the thread surface.

#### THE CHARACTER OF THE CHANGE OF PROFILE OF THE TOOL JOINT TAPERED THREAD DUE TO ITS WEAR DURING OPERATION

According to [7], the drill string tool joint thread root is subjected to the smallest wear in the process of operation is subjected and the crest and flanks of this thread are worn out quite intensively. Figure 13 depicts a scheme of the tapered thread according to standard [5] and additionally dotted cyan line describes the thread profile worn out during operation.

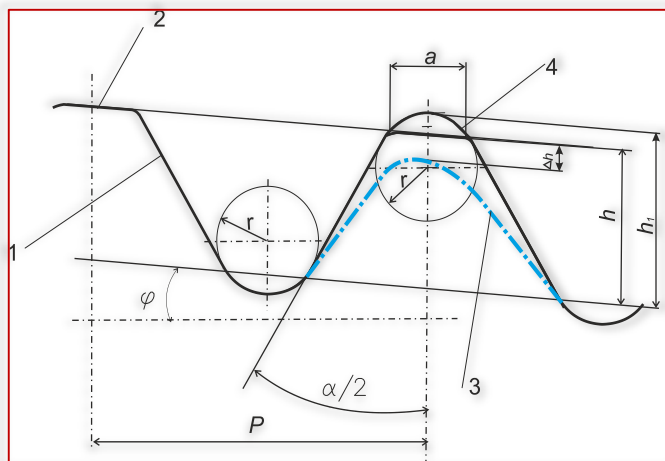


Figure 13. A diagram shows the nature of the drill pipe tapered thread wear. The numbers are indicated by: 1 – the largest flank according to the standard [5], 2 – crest, 3 –profile worn after the operation, 4 – the root

The value of  $\Delta h$ , as shown in Figure 13, indicates the value of the profile wearout of  $h$  (as in Figures 11, 12).

There is unequal thread profile wear on the different ridges. Figure 14 illustrates the fact that ridges that are closer to the pin and box face ends are worn out bigger. In fact, they are thread ridges and grooves that correspond to their largest diameters. From the graph in Figure 14, we see that for the box, the highest degree of wear out corresponds to the turn number 1, and for the pin — number 15.

Thus, the problem of the tapered thread manufacture for the drill string is the presence of the gaps between a pin and a box to ensure the necessary technological tool life which in turn leads to significant costs of hydraulic energy and the of the abrasive wearout increment of the thread during operation.

The purpose of the paper is to develop technological aspects that will ensure the manufacture of drill string tool joint with the low level of the washing fluid permeability through their threading part.

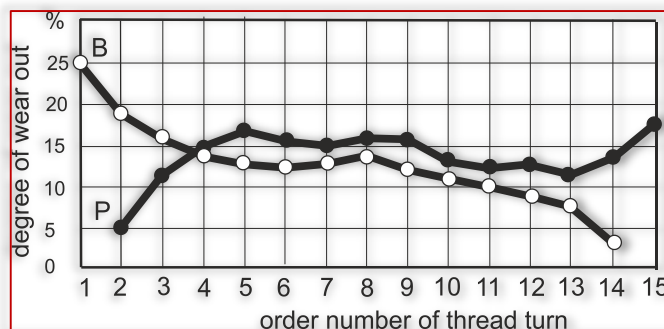


Figure 14. Degree of the wear out % of the every thread ridges on the pin P and on the box B of the tool joint NC46 after testing on the drilling stand by the use of the multy times screwing operation

#### STATEMENT OF THE PROBLEM

The task is to develop a technology to manufacture of drill string tapered thread with a reduced initial gap between groove and ridge of the box and pin, the lower intensity of wearout of the ridge and flanks by applying heat treating to increase its strength and hardness in providing the required tool life of the threading turning cutter by applying a nonzero value of its back rake angle and an optimal selection of the flank clearance angle.

#### REDUCING THE INITIAL VALUE OF TECHNOLOGICAL GAP

To reduce the initial value of the height of the gap, which is determined by the  $(h_1 - h)$  formula previously adopted, it is more expedient to increase the value of  $h$  rather than reduce the value of  $h_1$ . This is due to the fact that the thread root is formed by that part of the cutting edge threading tool, which wears out the most intensively, therefore it is inappropriate to reduce it. But it is quite reasonable to increase the value of  $h$ . That is, it is worth making this increase on the appropriate section of the cutting edge of the tool.



Figure 15. Photo of the cutting edge of the carbide insert of the cutter for drill string tapered thread machining for the form IV (executed at 20-fold increase)

Figure 15 shows a twenty-fold increase in the photo of the cutting edge tool for turning the tapered thread for drill string tool joint according to the form IV. Figure 16 according to the photo from Figure 15 shows a diagram illustrating the initial reducing of the gap  $h_1 - h$  by replacing value  $h$  with the value  $h^* > h$ . This can be done by correction of the shape of the cutting edge (red curve). In this case you can get a gap eg 0.3 mm less than the custom value.

Recommendations of standard [5] indicate that it is supposed not to increase the value of  $h$ , but only to reduce to 0.18 mm for  $h / 2$  size, but this tolerance limit is optional and serves in our opinion as the guarantee of required tool life.

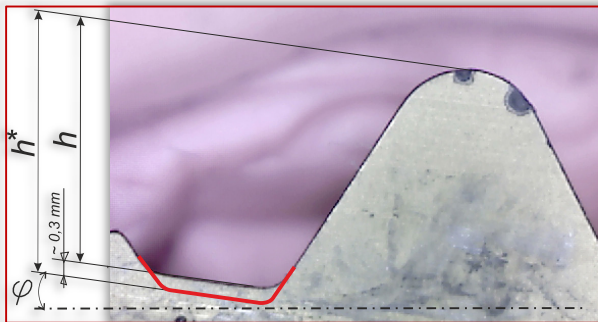


Figure 16. The same photo as in Figure 15 but it is only with the modified section of the cutting edge, which forms the crest of the tapered thread

Figure 17 illustrates the scheme for obtaining a reduced technological gap  $h_1 - h^*$ , which can be executed using a tool with modified cutting edge, as shown in Figure 16.

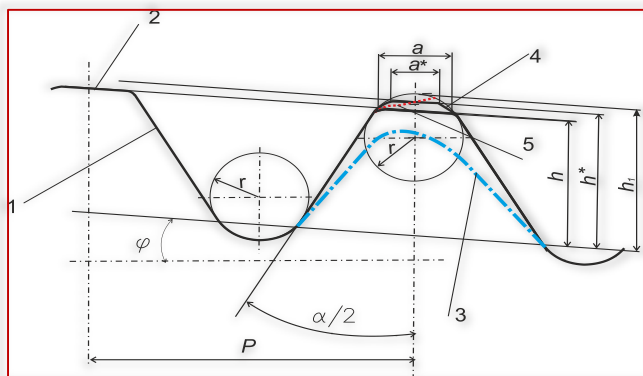


Figure 17. A diagram illustrating the reducing of the initial gap and increasing the theoretical limit of wear out by increasing the value of  $h$  to  $h^*$ . The digits are indicated by: 1 – the flank of the profile according to the standard, 2 – the crest according to the standard, 3 – the profile of the thread after prolonged operation, 4 – the crest, which is executed by the corrected cutting edge, 5 – cutting edge of the cutter after prolonged operation

The red dotted line in Figure 17 indicates the most characteristic worn out cutting edge of the tool at the time of the completion of its technological tool life  $T$ . It is obvious that the value of  $h^*$  cannot be provided with such shape of the cutting edge, since it has gone beyond the boundary of a figure placed between the dimensions  $h_1$  and  $h^*$ . In this case, it is necessary to ensure the technological tool life by adjusting its geometric parameters: in the first place of back rake angle, as well as the flank clearance angle.

## ENSURING THE TECHNOLOGICAL REQUIRED TOOL LIFE OF THE CUTTER

Modern manufacturers of the threading turning tools offer cutters only with a zero value of the back rake because otherwise it is necessary to apply a rather complicated algorithm for calculating the cutting edge profile and thus increasing the number of the cutting inserts types. In this article, unlike [3], we offer the use of a carbide insert of a standard profile, but by changing the configuration of the substrate envilby using a non-zero back rake angle in the nose (see figure 18). So the face plane A-A thus passes at an angle  $\gamma$  to the axis of the workpiece, but does not pass through the axis as in the standard cutter, which is shown in figure 5.

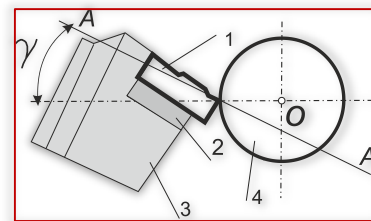


Figure 18. Scheme of installation of the cutting insert, so that a negative value of the back rake angle  $\gamma$  in its nose is ensured. The digits are indicated by: 1 – standard carbide insert, 2 – modified anvil, which implements the corresponding back rake angle, 3 – cutter, 4 – body of the workpiece

## REDUCING THREAD WEAR OUT DUE TO INCREASING STRENGTH AND HARDNESS OF THE BODY

A significant part of the steel grades for the drill string connectors manufacturing according to the strength characteristics can be classified into group of the difficult to machine materials.

The brand of 40NiCrMo4KD — chromium-nickel-molybdenum steel, belongs to the group of high-quality steels, which is used for the manufacture of tool joint of drill string specified for complicated conditions of operation. Its mechanical characteristics are given in table 2.

Table 2. Mechanical characteristics of steel at different modes of heat treatment.

Tempering °C	Yield strength $\sigma_{0,2}$ MPa	Ultimate strength $\sigma_B$ MPa	Hardness HRCa
200	1600	1750	53
300	1470	1600	49
400	1240	1370	44
500	1080	1170	38
600	860	960	28

According to [10], when the tempering of such steel is 600 for its successful cutting the back rake angle in the nose of cutter should be  $0^\circ$ . If the ultimate tensile strength exceeds 1170 MPa (release of tempering is  $500^\circ\text{C}$ ) then the back rake angle in the cutter nose for the carbide insert should be  $-5^\circ$ . According to [11], when ultimate tensile strength is 1500 – 1600 MPa (if tempering is  $300^\circ\text{C}$ ), the back rake angle for the carbide insert should be from  $-3^\circ$  to  $-5^\circ$ . Its depth of hardenability is over 15 mm. That is, the specific mechanical

characteristics will relate to the whole body of the tool joint and the thread in particular.

With such mechanical characteristics it is possible to predict:

- decrease in the intensity of abrasive abrasion of the thread surface under the influence of a drill mud flow;
- increase of the tightness of the face ends connection of the pin and the box due to the decrease in the value of plastic deformation under the influence of the Interference fit.

### ENSURING OF THE MANUFACTURING PRECISION OF THE THREAD PROFILE ANGLE

Table 3 summarizes the use results of the application for automated calculation of the size of the tapered thread half-profile angle made by cutter with the back rake angle at their nose equal from  $-3^\circ$  to  $-5^\circ$ .

Table 3. Values of the deviation of the half profile angle of the tapered thread made by a cutter with a carbide insert of the usual profile with the application of the back rake angle of  $-3^\circ$  and  $-5^\circ$

Tool joint standard size	Value of the half thread profile angle made by usual cutting edge of the turning tool, °				Fraction of half thread profile angle tolerance limit $\pm 40'$ , %	
	back rake equal $-3^\circ$		back rake equal $-5^\circ$		back rake equal $-3^\circ$	back rake equal $-5^\circ$
	AD	AB	AD	AB	equal $-3^\circ$	equal $-5^\circ$
1	2	3	4	5	6	7
NC 23	30,03	29,89	30,14	29,90	-16,4	20,9
2 3/8 Reg	30,03	29,89	30,13	29,91	-16,4	19,4
NC 26	30,03	29,91	30,13	29,92	-13,4	19,4
2 7/8 Reg	30,03	29,91	30,13	29,93	-13,4	19,4
NC 31	30,03	29,93	30,125	29,96	-10,4	18,6
3 1/2 Reg	30,03	29,93	30,12	29,96	-10,4	17,9
NC 35	30,03	29,94	30,12	29,97	-8,9	17,9
3 1/2 FN	30,025	29,94	30,11	29,98	-8,9	16,4
NC 38	30,03	29,95	30,12	29,98	-7,4	17,9
NC 40	30,03	29,95	30,12	29,98	-7,4	17,9
4 1/2 Reg	30,02	29,95	30,10	29,99	-7,4	14,9
NC 44	30,03	29,96	30,11°	29,99	-5,9	16,4
4 1/2 FH	30,02	29,96	30,10	29,99	-5,9	14,9
NC 46	30,03	29,96	30,11	29,99	-5,9	16,4
NC 50	30,03	29,97	30,105°	30,01	$\pm 4,5$	15,7
5 1/2 Reg	30,05	29,96	30,10	29,99	7,4	14,9
5 1/2 FH	30,02	29,98	30,10	30,02	$\pm 2,9$	14,9
NC 56	30,05	29,96	30,13	29,99	7,4	19,4
6 5/8 Reg	30,03	29,98	30,105	30,02	4,5	15,7
NC 61	30,05	29,97	30,13	30,00	7,4	19,4
6 5/8 FH	30,03	29,99	30,105	30,03	4,5	15,7
7 5/8 Reg	30,01	29,98	30,09	30,02	-2,9	13,4
NC 70	30,01	29,98	30,09	30,02	-2,9	13,4
8 5/8 Reg	30,00	29,98	30,08	30,03	2,9	11,9
NC 77	30,01	29,99	30,08	30,03	1,5	11,9

Column 1 lists drill string tool joints of all sizes in accordance to API 7 and [5]. Columns 2 and 3 shows data on the magnitudes of half profile angles obtained with a cutter with a standard cutting edge, but the underlay anvil provides the

value of the back rake  $c$  angle at the its nose of  $-3^\circ$ . Column 2 is filled in with data about the half profile angle at the side AD, and column 3 – at the side AB.

Columns 4 and 5 shows data on the magnitudes of half profile angles obtained with a cutter with a standard cutting edge, but the underlay anvil provides the value of the back rake  $c$  angle at the its nose of  $-5^\circ$ . Column 4 is filled in with data about the half profile angle at the side AD, and column 5 – at the side AB. Columns 6, 7 indicate the percentage of the part of the tolerance limit of the half thread profile angle of which is  $\pm 40'$ . This fraction is calculated from the greater deviation from each pair and taking into account the sign.

These tables indicate that the fraction of the half-profile angle tolerance limit does not exceed 21% when the value of the back rake angle is  $-5^\circ$  and 16.5% when the back rake angle value is  $-3^\circ$ .

The flank clearance angle in these calculations is assumed to be equal to the helix angle of inclination in the smallest diameter of the tapered thread. Proceeding from this, the most theoretically possible its values are accepted in calculations shown in table 3. However, since it is generally acceptable for the manufacturer to product a limited number of standard sizes of the anvil (see Figure 6), then the algorithmic calculation [4] should be used to obtain the most optimal values of the flank clearance angle – that is, to pick up the anvil with the nearest integer angle of inclination.

### ACCURACY OF THE MANUFACTURING OF THE MOST LOADED TAPERED THREAD RIDGES PROFILE OF THE DRILL STRING TOOL JOINT

Figure 14 proves that the greatest wear out is on the turn of the thread, which are located on larger conical diameter. This appoint a priority task to ensure the highest accuracy of the profile of the specified turns.

Accordingly, the algorithm proposed in [4] should be used to establish deviations from the half-profile angle nominal, provided that the flank clearance angle is equal to the helix angle of inclination of the tapered thread in its largest diameter. In calculations are that tool joints: of the smallest size – NC 23, one of the avengers – 4 1/2 Reg and of the largest size NC 77. To the input parameters of the algorithm, the tangential displacement of the nose of the cutter  $\pm 0,1$  mm is added, (as it is illustrated in Figure 5).

These tables show the tendency to decrease the fraction from the tolerance limit of  $\pm 40'$  from the nominal half-profile angle equal  $30^\circ$  when the tool joint size changes from the smallest to the largest. The largest fraction is 22%, the smallest 1.5%, taking into account the accuracy of the installation of the nose of the tool, the displacement of which is  $\pm 0,1$  mm. The indicated fractions demonstrate the probable feasibility to use the cutters with such parameters for their practice in the manufacture of tapered thread with a low level of permeability of the drilling solution in it.

Table 4. Accuracy of thread profile execution on the largest diameter of tapered thread NC 23, 4 1/2 Reg, NC 77.

Parameters	NC 23	4 1/2 Reg	NC 77
1	2	3	4
Calculated helix angle of inclination on the largest diameter	1,8°	0,715°	0,579
Nearest standard angle of the anvil	2°	1°	1°
Back rake angle on the cutter nose equal -3°			
Flank AB			
Value of the half profile angle when the tangential displacement is +0.1 mm	29,92°	29,96°	29,99°
Value of the half profile angle when the tangential displacement is - 0.1 mm	29,93°	29,97°	29,99°
Maximum deviation °	0,08	0,04	0,01
fraction of the tolerance limit ±40' of the half profile angle, %	12	6	1,5
Flank AD			
Value of the half profile angle when the tangential displacement is +0.1 mm	30,03°	30,01°	30,04°
Value of the half profile angle when the tangential displacement is - 0.1 mm	30,04°	30,02°	30,05°
Maximum deviation °	0,04	0,02	0,05
fraction of the tolerance limit ±40' of the half profile angle, %	6	3	7,5
Back rake angle on the cutter nose equal -5°			
Flank AB			
1	2	3	4
Value of the half profile angle when the tangential displacement is +0.1 mm	29,93°	30,00°	30,03°
Value of the half profile angle when the tangential displacement is - 0.1 mm	29,94°	30,01°	30,04°
Maximum deviation °	0,07°	0,01°	0,04°
fraction of the tolerance limit ±40' of the half profile angle, %	10	1,5	6
Flank AD			
Value of the half profile angle when the tangential displacement is +0.1 mm	30,13°	30,09°	30,07°
Value of the half profile angle when the tangential displacement is - 0.1 mm	30,15°	30,10°	30,08°
Maximum deviation °	0,15	0,10	0,08
fraction of the tolerance limit ±40' of the half	22	15	12

## CONCLUSIONS

As a result of the performed theoretical studies, the following technological measures that provide the reducing of the washing drilling fluid permeability through the threading section of the drill pipe tool joint and the increase of the threading-tool machining process efficiency are determined:

- Increase of hardness and strength of the drill string tool joint thread as the result of the treatment of the steel up to the ultimate tensile strength of 1500–1600 MPa and up to the hardness of 49 HRCa (Rockwell scale) in order to reduce the plastically deformation value in the interference fit of the box and nipple joint and increasing of the abrasion resistant during the drill fluid movement in the gap between the thread ridge and groove.
- Application of the thread-turning tools with a back rake angle  $\gamma$  in its nose from 3° to 5° that is necessary for its tool life increasing when it is difficult to machine work piece made of chrome-nickel-molybdenum tempered steel. In this case, the accuracy of the thread profile does not exceed 22% of the tolerance limit.
- Application of the thread-turning tool with the modernized cutting insert for reducing the height of the initial technological gap down to 0.3 mm.
- The using of the special designed anvil to ensure the optimal flank clearance angle for the most accurate execution of the profile of the tool joint tapered thread grooves which are exposed to the greatest wear in the process of drill string operation.

## Note

This paper is based on the paper presented at INTERNATIONAL CONFERENCE ON APPLIED SCIENCES – ICAS 2018, organized by UNIVERSITY POLITEHNICA TIMISOARA, Faculty of Engineering Hunedoara (ROMANIA) and UNIVERSITY OF BANJA LUKA, Faculty of Mechanical Engineering (BOSNIA & HERZEGOVINA), in cooperation with the Academy of Romanian Scientists, Academy of Sciences Republic of Srpska, Academy of Technical Sciences of Romania – Timisoara Branch and General Association of Romanian Engineers – Hunedoara Branch, in Banja Luka, BOSNIA & HERZEGOVINA, 9 – 11 May 2018.

## References

- [1] Ultra-rigid thread turning for all types of threads – internal and external. Sandvik Coromant. Site. [www.sandvik.coromant.com/en-gb/products/corothread\\_266/Pages/default.aspx](http://www.sandvik.coromant.com/en-gb/products/corothread_266/Pages/default.aspx). 2012 – Title from the screen
- [2] Thread\_turning/thread\_turning\_brochure\_english.pdf.[Electronic resource]://www.secotools.com/CorpWeb/Products/Turning/.-Last access: 2017. – Title from the screen
- [3] Onysko O. R. Pro funktsionalnu zalezhnist velychyny polovynnoho kuta profilu zamkovo narizi vid velychyn perednoho kuta, kuta nakhyly ta polovynnoho kuta profilu rizalnoi kromky riztsia. [Tekst] / O. R. Onysko, // Visnyk natsionalnoho universytetu « Lvivska politekhnikha ». Optyimizatsiia vyrobnychkyh protsesiv i tekhnichniy kontrol u mashynobuduvanni ta pryladobuduvanni. –2017.– №867.– S. 19–28.
- [4] Onysko O.R. Alhorytm rozrakhunku funktsionalnoi zalezhnosti formy bichnykh profiliv hvyntovoi narizi zamkovo konichnoi dlia elementiv burylnykh kolon vid heometrychnykh parametriv riztsia. [Tekst] / O. R. Onysko// Naukovii visnyk.— 2017.—1(42).—S. 77 –81.
- [5] HOST 28487–90. Mezhhosudarstvennyi standart. Rezbha konycheskaia zamkovaia dlia elementov burylnykh kolonn.

- Profyl. Razмеры. Dopusky (s Yzmeneniyem N 1 [Tekst]. Utverzhden y vnesen v deistviye postanovlenyem Hosudarstvennogo komyteta SSSR po standartam ot 05.06.80 № 2578. M.: «Standartynform», 2010. — 75 s.
- [6] Chudyk I.I. Do vtrat hidravlichnoi enerhii pid chas promyvannia sverdlovyny. Rozvidka ta rozrobka naftovykh i hazovykh rodovyshch. – 2009.– №2(31).– S34–42.
- [7] Semyn V.Y. Sovremennyye metody proektirovaniya rezbovyh soedinenyj trub neftegazovogo sortamenta dlya stroytelstva skvazhyn [Tekst]: dys. ... dokt. texn. nauk : 25.00.15, 05.02.13 / Semyn Vladimir Yvanovich – Moskva, 2005. – 344 s. – Byblyogr.: s.232–344.
- [8] Liubomyr Borushchak. Research of the impermeability of the tool-joint tapered thread size 2 7/8 reg/ Liubomyr Borushchak, Oleh Onysko, Vitalii Panchuk //Monografia “Problemy eksploatacji i zarządzenia w górnictwie” rząd Górnictwo–Kraków 2017 p.65–72.
- [9] Liubomyr Borushchak. Influence of the technological gap value of the tool-joint tapered thread on the drilling mud flow rate in its screw coupling/ Lubomyr Borushchak, Stepan Borushchak , Oleh Onysko //Ukrainian Jornal of Mechanical Engineering and Materials Sciance.–2017.– Volume 3.–№2.P. 24–31.
- [10] Fomin E. V. Povyshenye stojkosti i tochnosti rezbovyh rezcov na osnove modelirovaniya processa rezbonarezaniya [Tekst]: dys. ... kand. texn. nauk : 05.03.01 : Fomyn Evgenyj Vladymyrovych – M., 2007. – 206 s. – Byblyogr.: s. 194–202.
- [11] Ya. L. Gurevych Rezhymy rezaniya trudnoobrabatyvaemyx materialov: Spravochnyk/Ya. L. Gurevy`ch, M. V. Goroxov, V. Y. Zaxarov y dr. 2–e y`zd., pererab. y dop.—M.: Mashynostroeniye, 1986, 240 s, l.



ISSN: 2067–3809

copyright © University POLITEHNICA Timisoara,  
Faculty of Engineering Hunedoara,  
5, Revolutiei, 331128, Hunedoara, ROMANIA  
<http://acta.fih.upt.ro>

<sup>1</sup>Sinisa KUZMANOVIC, <sup>2</sup>Zlatko BUNDALO, <sup>3</sup>Dužanka BUNDALO, <sup>4</sup>Boris NEDIC

# APPLICATION OF DRIVE-BY-WIRE CONCEPT AND CAN PROTOCOL IN AUTOMOBILES

<sup>1</sup> M:tel a.d., Kneza Lazara 4, 74000 Doboj, BOSNIA & HERZEGOVINA

<sup>2</sup> University of Banja Luka, Faculty of Electrical Engineering, Patre 5, 78000 Banja Luka, BOSNIA & HERZEGOVINA

<sup>3</sup> University of Banja Luka, Faculty of Philosophy, Petra Bojovica 1A, 78000 Banja Luka, BOSNIA & HERZEGOVINA

<sup>4</sup> EIB Internationale a.d., Skendera Kulenovica 14, 78000 Banja Luka, BOSNIA & HERZEGOVINA

**Abstract:** Possibilities and ways of application of drive-by-wire concept and CAN protocol in automobiles are considered, described and proposed in the paper. Modern automobile is a system with many embedded microcontroller systems that perform and control needed operations in the automobile. For communication between that microcontroller systems it is used CAN protocol. Also, drive-by-wire concept for steering and speed control of automobile is very easy, promising and constantly developing. Basic characteristics and advantages of using drive-by-wire concept and CAN protocol in automobile are described first. Then, the way of developing and practical implementation of one drive-by-wire system in automobile using CAN protocol and microcontrollers is described. For the implementation were used two microcontroller controlled CAN nodes based on microcontroller development boards. One CAN node performs steering and speed control functions and generates appropriate control data. The data are transferred by CAN protocol to the second CAN node. The second CAN node receives and processes the data and performs functions for control of automobile speed and movement direction. Hardware and software implementations of the solution are described in more details.

**Keywords:** drive-by-wire concept, CAN protocol, microcontroller systems

## INTRODUCTION

Since the first modern automobile was built and the automobile production industry became one of the most profitable branches of industry, the automobile did not basically change much. Due to the constant demands for environment protection, there were developed electric and hybrid automobiles. The biggest changes in automobiles are result of rapid development and use of electronics. Microcontrollers are used for the control of many systems in automobiles. It was achieved a good combination of electronic and computer technologies that are applied together in many automobile subsystems. There is large amount of complex electronic devices, over 70 electronic control units (ECUs), several hundred sensors, etc. that are incorporated into the modern automobile. During driving automobile, electronic systems in vehicle continuously monitor more than a hundred different parameters from sensors and adequately control the automobile [1-3]. Every few milliseconds are read data from numerous sensors distributed in the vehicle and then are controlled certain elements of automobile. The function of electronic elements is to increase the overall performance of the vehicle. Electronic components in automobile are interconnected electronic subsystems, with their own central processor unit, working and permanent memory, exchanging data using communication protocols specially developed for automobiles. Modern automobile is a system with many networked embedded microcontroller systems that monitor, perform and control needed operations in the automobile [1-3]. The most significant improvements that are such achieved

are: increasing driving safety, reducing fuel consumption, reducing environmental pollution, increasing comfort, improving diagnostic functions [1-3].

For communication between microcontroller based systems in automobile it is used CAN (Control Area Network) protocol [1-4]. The CAN is the most widely used network and protocol in vehicles. The CAN using a twisted pair of copper wires became an ISO standard and is standard in Europe for data transmission in automotive applications, due to its low cost, robustness, and bounded communication delays [1-4].

Drive-by-wire concept for steering and speed control of automobile is very efficient and easy for use and constantly developing [1-6]. That concept integrates and implements the function of steering the direction of movement of car and function of control of speed of movement of car using electronic elements controlled by using simple stick (so called joystick) instead of using classic steering wheel.

Possibilities of application of drive-by-wire concept in automobiles, using CAN protocol, are considered, proposed and described in the paper. Basic characteristics and advantages of using drive-by-wire concept and CAN protocol in automobile are described. The way of developing and practical implementation of one drive-by-wire system in automobile using CAN protocol and microcontrollers are described. For the implementation were used two microcontroller CAN nodes based on microcontroller development boards. One CAN node performs steering and speed control functions using joystick and generates appropriate control data that are transferred by CAN protocol to the second CAN node. The second CAN node receives and

processes the data and performs needed functions for control of automobile speed and movement direction. The proposed and implemented solution is mainly intended for electric automobiles. It can be used also for the classical automobiles. The solution also shows the possibility to use standard microcontrollers and standard open source microcontroller based platforms for the implementation of such systems.

#### DRIVE-BY-WIRE CONCEPT

The drive-by-wire concept in automobiles is similar and it was created on the basis of the so-called fly-by-wire system used in aviation and avionics systems [1-6]. It is a system that replaces the classical manual mechanical steering wheel and movement control system of automobile with an electronic interface and enables electronic control of vehicle movement. The movements of the vehicle steering mechanism are converted into electric signal transmitted through the wire to the vehicle control elements. Microcontrollers for control of the movement of vehicles, based on such obtained information, determine how to control and run actuators in all vehicle control parts. In practice there are existed and used such two systems and two terms, steer-by-wire and drive-by-wire, that are often separated. But, that systems are mainly integrated into one system known under the common name drive-by-wire (or X-by-wire) [1-6]. That way of the integrated approach was also used in the solution designed, implemented and described in this paper.

Drive-by-wire (or X-by-wire) is term used when mechanical and/or hydraulic systems in vehicle are replaced by electronic ones. Used electronic systems are with intelligent microcontroller devices, networks, microcontrollers supporting software components that implement filtering, control, diagnosis and other needed functions. Drive-by-wire technology replaces traditional mechanical and hydraulic actuators and intermediate components with electronic and electric components that are interconnected only by wires, used as informational and power lines.

Drive-by-wire technologies enhance comfort, enhance control and improve vehicle performances, since they introduce completely electronic control of actuators. The main purpose of drive-by-wire systems is to assist the driver in different situations in a more flexible way. Purpose is also to decrease production and maintenance cost for vehicle braking and steering systems. Vehicles equipped with drive-by-wire system have kept traditional mechanical technologies as a backup in case the electronic ones fail. Completely drive-by-wire system has to have at least the same level of safety as traditional mechanical systems, using redundancy, replication, functional determinism and fault tolerance concepts [1-6].

The control system of automobile is a set of elements that allows the driver to determine the path and the speed of vehicle movement [1-3]. That system provides precise control of the direction of movement of the vehicle front wheels and

the speed of rotation of the vehicle driving wheels. It also reduces the amount of driver efforts needed to direct the front wheels and to change the speed of the driving wheels rotation.

The control is performed very easily using appropriate stick (so called joystick). By moving the joystick to the left or to the right changes the direction of movement of the vehicle. By moving the joystick forward or backward changes the speed of the vehicle movement. The joystick controls two potentiometers by what are changed the voltages that are applied to the control system. The values of those voltages define the speed of change of the direction and speed of the vehicle. Moving the stick to the left from the initial position causes the movement of the vehicle to the left side. Moving the stick to the right from the initial position causes the movement of the vehicle to the right side.

Also, moving the stick forward from the initial position causes increase of the speed of the vehicle movement. Moving the stick backwards from the initial position causes reduction of the speed of the vehicles movement. That principle is also used in the practical solution designed, implemented and described in this paper.

Influence of interferences is one of problems in drive-by-wire systems. Therefore, it was developed drive-by-wire technology that is resistant to the occurrence of malfunctions [1-6]. Thus, drive-by-wire systems of high integrity are implemented in a very economical way, achieving required levels of security, reliability and availability. It is used multiple redundancy in design of secure drive-by-wire systems. Thus, it is achieved full control of the driver over the vehicle in case of partial malfunction of the system.

#### CAN protocol

The CAN communication protocol is used for connection and communication of microcontroller systems in automobiles [1-4]. It was designed by company Bosch for communication between ECUs in vehicles and for decreasing length and number of dedicated wires for interconnection. In modern automobiles CAN is mainly used as network for real-time control in power train and chassis domains. It is also used as network for the electronics in the body domain of vehicle.

Before application of the CAN protocol electronic components in automobiles were interconnected directly using wires. This type of interconnection is complicated and complexity of the network increases with the increase of number of components. Such networks also significantly reduce reliability in communication between components and reliability of vehicle itself. Also, the way of wiring of automobile has effect on vehicle weight and on occupation of vehicle space.

Figure 1 shows the CAN bus and way of connection of electronic components (CAN nodes) to the CAN bus [1-4].

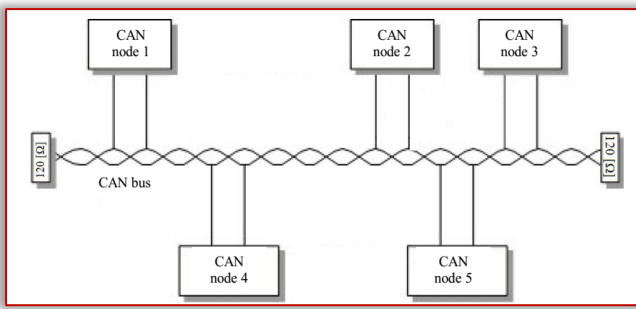


Figure 1. Connection of electronic components to CAN bus

The CAN bus has two wires called CAN\_H and CAN\_L that are terminated using 120 ohm resistors. This pair of wires is twisted what reduces electromagnetic interference. The CAN is serial communication protocol accepted by the Society of Automotive Engineers (SAE). It is called Automotive Serial Controller Area Network and was first developed for the automotive industry, for connecting electronic systems in cars. The CAN protocol was later applied in many areas, primarily in industrial plants, airline industry and medicine. CAN bus is primarily used in embedded systems and it is network established between microcontrollers. The CAN bus is two-wire network system suitable for fast applications that use short messages.

The CAN bus connects all the CAN nodes. Figure 2 shows a typical structure of the CAN node [1-4].

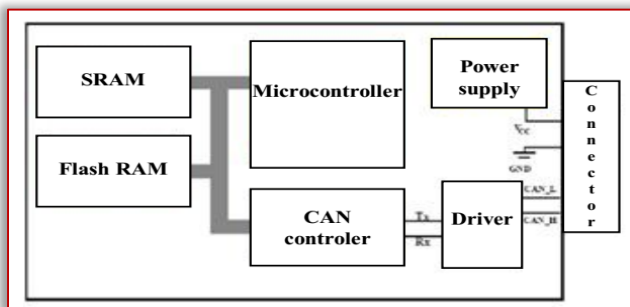


Figure 2. Structure of CAN node

The CAN node uses microcontroller that performs needed digital data processing. The shown CAN node (Figure 2) is implemented using specialized CAN controller realizing the connection of the node to the network and exchange of information with microcontroller. This type of CAN controller is so called stand-alone controller.

The CAN protocol provides communication speeds up to 1 Mbit/s, enabling real-time control and real-time applications. Transmission speed and distance between CAN nodes are inversely proportional, as is shown in Table 1 [1-4].

Table 1. Transmission speed and length of CAN bus

Transmission speed	Length of CAN bus
1 Mbit/s	25 m
800 kbit/s	50 m
500 kbit/s	100 m
250 kbit/s	250 m
125 kbit/s	500 m
50 kbit/s	1000 m
20 kbit/s	2500 m
10 kbit/s	5000 m

The CAN bus is widely used in power train communication of automobile, in the chassis domain (where is used high-speed HS-CAN at 500 kbit/s) and in the body domain (where is used low-speed LS-CAN at 125 kbit/s) [1-4].

Data is sent and received in the CAN system using message frames. The CAN is based on principle that every node in the system receives data message from the bus. Hardware within each CAN node performs local filtering that allows only certain nodes to respond to the received message. The CAN system uses four types of messages:

- Data Frame,
- Remote Frame,
- Error Frame,
- Overload Frame.

The CAN system uses data frame to transmit data over network. The data frame consists of identification and different control information. It can contain maximum of eight bytes of data. CAN system uses two types of data frames, the basic frame and the extended frame. When CAN system was developed for large systems with dense traffic of messages, the basic frame format was insufficient. The number of messages created by the transmitter was greater than the number of possible ID codes that CAN system could assign to them to ensure that each message is unique. By adding and using larger 29-bit ID field, the CAN system can create about 512 million different messages and priorities. Figure 3. shows the basic format of the data frame [1-4].

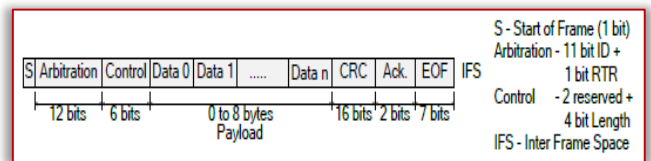


Figure 3. Basic format of CAN data frame

The data frame consists of the following sections [1-4]:

- Start of Frame - Single dominant bit (logical 0), which marks the start of Data Frame or Remote Frame. Node can only start transmission when it detects that the bus is idle. It is required that all nodes synchronise to the leading edge of the Start of Frame bit.
- Arbitration field - 11-bit node Identifier (which also defines its priority) and remote transmission request (RTR) bit (dominant for Data Frame and recessive for Remote Frame).
- Control field - 4-bit Data Length and 2 reserved bits.
- Data field - Up to 8 bytes of information (including the option for zero byte data).
- CRC field - 15-bit cyclic redundancy check (CRC) code followed by single recessive bit as the CRC delimiter.
- Acknowledgement field - 1-bit Ack slot followed by a 1-bit Ack delimiter. Any node that validates the transmitted data will override the recessive bit sent in the Ack Slot by the transmitter to indicate that the frame has been transmitted correctly. However, since CAN is a broadcast

network, the node which acknowledges the receipt of data may not be the intended recipient.

- End-of-Frame field (EOF) - Sequence of seven recessive bits followed by inter-frame space.

The CAN specification also defines special frame formats like the Error Frame and Overload Frame.

The extended format of the data frame is almost identical to the basic format of the data frame. The only difference between these two formats is in the bit of extension of identifier and the size and arrangement of the arbitration field. Both of these formats can coexist in the same CAN system. The basic format of the frame has always priority in relation to the extended format of the frame.

The CAN system is very effective in detection of errors. Each frame is simultaneously accepted or rejected by each node in the network. If the node detects an error, it transmits field of error to each node in the network and destroys the transferred frame [1-4].

The CAN protocol uses the following methods to detect errors:

- Check of bits,
- Check of frame,
- Cyclic redundancy check (CRC),
- Acknowledgement check,
- Check of filling rules.

The main risk in any system with serial bus is that one faulty node can turn off the entire network. To deal with this, CAN protocol is designed to automatically detect faulty nodes and disconnect them from the network. CAN uses two error counters for each node, one for errors in transmission and the other for errors in reception. When error in sending or receiving occurs, the corresponding counter is increased for an appropriate value. That value depends on the error type and which node has caused the error. For each successful sending or receiving, the corresponding counter is decreased for one. Typically, if the node recognizes that it is the source of the error then the counter increments by nine for the received errors and for eight for the transmitted errors. Otherwise, each node counter is increased by one. Based on these counters, each node can be in one of three states [1-4]:

- Active Error,
- Passive Error,
- Bus Off.

The remainder of the network will continue to operate and if the node is set to bus off state. Sometimes errors occur due to external factors, for example, if the network is exposed to occasional electromagnetic interference. The CAN system is therefore designed that counters of errors in nodes can be decreased if data frames are successfully received and sent.

#### IMPLEMENTATION OF DRIVE-BY-WIRE CONCEPT IN AUTOMOBILE USING CAN protocol

One practical proposal, design and implementation of a simplified drive-by-wire system in automobile using CAN

protocol is described here. Two microcontroller based CAN nodes were used and implemented. One CAD node reads the information about changes of the voltage at the A/D converter input, generated by the potentiometers of the joystick. This information is sent via the CAN bus to the second CAN node. The second CAN node processes and sends this information to the elements for control of direction and to the elements for control of speed of the car movement. This information is also displayed on the LCD display in the second CAN node. As the hardware basis for the design and implementation, the standard development boards Easy8051A (marked as Board 2) and Easy8051B (marked as Board 1) were used [7, 8]. The programs for both CAN nodes were also practically designed and implemented. Figure 4 shows simplified hardware block scheme of the implemented drive-by-wire system.

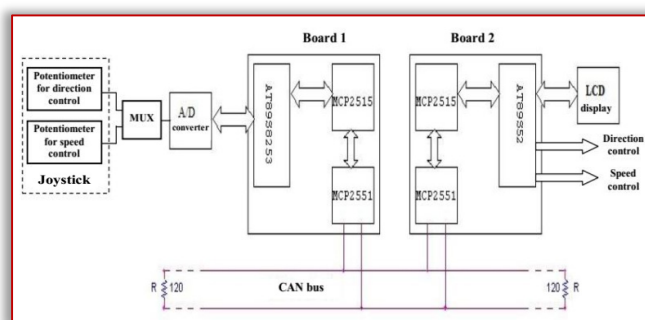


Figure 4. Simplified block scheme of implemented drive-by-wire system

The development environment model used to connect and accomplish the functionality of all the necessary components of the system is Easy8051 [7, 8]. The Easy8051 contains the following components:

- Power supply (8 V to 16 V AC/DC),
- ON/OFF switch,
- USB connector,
- USB 2.0 programmer,
- Socket for placing an 8051 microcontroller,
- Connectors of input/output ports of the microcontroller,
- Selection of pull-up/pull-down resistors,
- Keys for the input of the microcontroller input pins,
- Selection of the logical level that is applied on the keys,
- Reset button for microcontroller,
- LED for displaying the logic level on the pins,
- Using the first four switches of the SW2 group, the LEDs on the ports P0, P1, P2, P3 and P4 are connected or disconnected to the MCU, and the remaining four switches select the digits on the 7-segment display,
- Connector for alphanumeric LCD display,
- Adjustment of the contrast of the alphanumeric LCD display,
- Connector of graphic 128x64 LCD display,
- Adjustment of the contrast of the graphic 128x64 LCD display,
- Temperature sensor DS1820,

- Connector for RS-232 communication,
- Clock signal generator,
- 7-segment display,
- Switch group SW1 enables MOSI, MISO and SCK pin for SPI communication. It also enables A/D and D/A converter, RX/TX line for RS-232 communication and LCD/GLCD backlighting,
- 12-bit A/D converter,
- 12-bit D/A converter,
- Source of referent voltage of 4.096V.

The development environment is powered by a USB port. The program is downloaded via a USB programmer, and USB cable is used for connection to the personal computer. In order to load the program it is necessary to have the appropriate software installed on the computer (8051Flash Programmer and necessary drivers). Switches are used for establishing or terminating contacts with peripheral units. The switches on the Easy8051B board (Board 1 in Figure 4) in the SW1 group are set to enable the use of A/D converter and to enable SPI communication. On the Easy8051A board (Board 2 in Figure 4) switches from group SW1 are set so that SPI communication is enabled. Also, on the Easy8051B board using the J10 jumper was selected that the reference voltage has value of  $V_{cc}=5V$ , and using the J9 jumpers, was select the CH0 output.

The communication between the Easy8051B board (Board 1), with the AT89S8253 microcontroller, and the Easy8051A board (Board 2), with the AT89S52 microcontroller, is performed using the CANSPI module [8]. On the Easy8051A board the frequency of the oscillator is 12MHz, and CANSPI module with a frequency of 16MHz is installed on it [9]. On the Easy8051B board the frequency of the oscillator is 24MHz, and a CANSPI module with a frequency of 8MHz is installed on it.

The voltage changes on the joystick potentiometers, caused by movement of the joystick, are read at the output CH0 of the A/D converter and transmitted via the CAN bus from the Easy8051B board (Board 1) to the Easy8051A board (Board 2). In the Board 2 the read values are sent to the elements for control of direction and to the elements for control of speed of vehicle movement and are displayed on the LCD display. It causes change in the direction and in the speed of the vehicle movement.

In the implementation it was used the MCP2515 stand-alone CAN controller with SPI Interface [10]. It is able to receive and send messages created in both standards, messages created in the basic and extended data frame and remote frame. The MCP2515 has two masks and six filters that are used to filter out undesirable messages and thus reduces the load of the microcontroller. The MCP2515 is connected to a microcontroller via an industry standard called Serial Peripheral Interface (SPI). The MCP2515 is a stand-alone CAN controller developed to simplify access of the applications to the CAN bus. This CAN module manages all functions of receiving and transmitting messages to and from the CAN

bus. The message is transmitted when it is first entered in the buffer and the control register. The transmission is initiated using a control register bit by the SPI interface or by enabling transmission pins. States and errors can be checked by reading the appropriate registers. All messages detected on the CAN bus are checked for the presence of errors and then are compared with user-defined filters to see if they need to be moved to one of the two receiving buffers. Writing and reading of all registers is achieved by using standard SPI read and write commands.

The implementation also uses the MCP2551 high-speed CAN transceiver device that operates as an interface between the CAN protocol controller and the physical CAN bus [11]. It provides differential transmission and reception for CAN controller. It operates at speeds up to 1Mb/s. Typically each node in the CAN system must have a device to convert a digital signal created in the CAN controller into a signal suitable for transmission via the CAN bus (differential output). It also provides a buffer between the CAN controller and the voltage interference that can be created on the CAN bus from an external source.

In the development of this system it was used the software tool called mikroC PRO for 8051 [12]. Programming was performed in programming language C, after which the compiler translates the program into a hexadecimal code that was used for programming the microcontroller. To write the program into the microcontroller it was used 8051Flash Programmer software [11]. Using the mikroC PRO for the 8051 compiler and the 8051Flash Programmer software, two programs were developed and implemented, one for the AT89S52 microcontroller (Board 2) and the other for the AT89S8253 microcontroller (Board 1).

The algorithm and flow chart of the program for the Board 1 (the Easy8051B board) is shown in Figure 5.

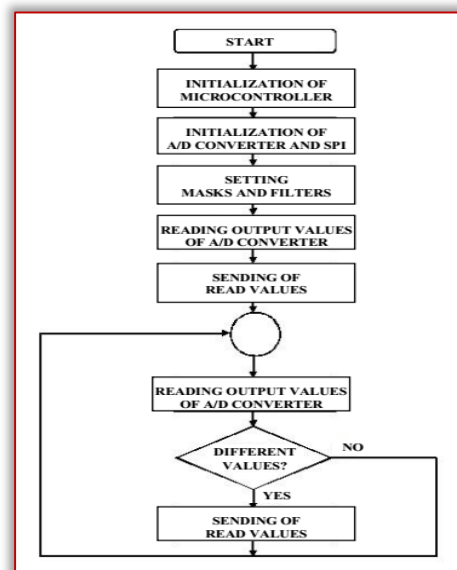


Figure 5. Flowchart of program for Board 1

As an illustration, the part of developed and implemented program for the Board 1 (the Easy8051B board) is shown in Figure 6.

```

/*
Board 1 Easy8051B
MCU: AT89S8253
Oscillator: 24.00 MHz
CANSPI module 8.00 MHz
*/

// Definition of pins of SPI and ADC
sbit MCP2515_CS at P1_0_bit;
sbit SoftSpi_Rst at P1_2_bit;
sbit SoftSpi_SDI at P1_6_bit;
sbit SoftSpi_SDO at P1_5_bit;
sbit SoftSpi_CLK at P1_7_bit;
sbit ADC_CS at P3_5_bit; // ADC - pin CS
// End of pins definition

const long ID_1st=12, ID_2nd = 13;
char RxTx_Data[8];
char value1;
char value2;
char kanal;

// Initialization of ADC and SPI
void Init() {
Soft_SPI_Init();
SPI1_Init();
MCP2515_CS=1;// deselecting of MCP2515, CS=1
ADC_CS = 1;// deselecting of ADC, CS=1
}
// End of initialization
.

```

Figure 6. Part of program for Board 1

The algorithm and flow chart of the program for the Board 2 (the Easy8051A board) is shown in Figure 7.

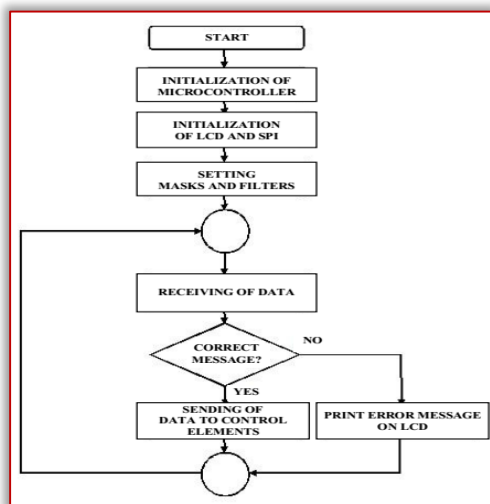


Figure 7. Flowchart of program for Board 2

The part of developed and implemented program for the Board 2 (the Easy8051A board) is shown in Figure 8.

```

/*
Board 2 Easy8051A
MCU: AT89S52
Oscillator: 12.00 MHz
CANSPI module 16 MHz
*/

// Definition of pins of LCD and SPI
sbit LCD_RS at P0_2_bit;
sbit LCD_EN at P0_3_bit;
sbit LCD_D4 at P0_4_bit;
sbit LCD_D5 at P0_5_bit;
sbit LCD_D6 at P0_6_bit;
sbit LCD_D7 at P0_7_bit;
sbit MCP2515_CS at P1_0_bit;
sbit SoftSpi_Rst at P1_2_bit;
sbit SoftSpi_SDI at P1_6_bit;
sbit SoftSpi_SDO at P1_5_bit;
sbit SoftSpi_CLK at P1_7_bit;
// End of pins definition

char RxTx_Data[8];
char ID_1st=12;
char ID_2nd = 13;
unsigned int i;
char Rx_ID;
char RX;
unsigned int rezultata;

// Initialization of LCD and SPI
void Init()
{
LCD_Init();
LCD_Cmd(LCD_CLEAR);
LCD_Cmd(LCD_CURSOR_OFF);
Soft_SPI_Init();
MCP2515_CS=1;// deselecting of MCP2515, CS=1
}
// End of initialization
.

```

Figure 8. Part of program for Board 2

In the development and implementation of the realized drive-by-wire system there were performed many tests of system operations. Figure 9 shows the voltage value that was read from the A/D converter and that was sent from the first CAN node (Board 1), received on the second control CAN node (Board 2) and displayed on the LCD display during testing of system operation.



Figure 9. Voltage value read from A/D converter and displayed on LCD display

If the data information was not transferred via the CAN bus or if the data loss occurs, on the LCD display will be shown information ERROR!. It is shown in Figure 10. From the error state, the system exits when the data information is transferred correctly.



Figure 10. Information on LED display that transmission error occurred

## CONCLUSIONS

Development and progress in the automotive industry is continual. The number of used embedded electronic components and digital microcomputers is constantly increasing, and new ways of networking are developed. This all increases the performance and safety of the automobile. An increasing number of existing automobile systems have been improved by the introduction of microprocessor control, and new systems are appearing that provide new possibilities. Without application of microcontrollers in cars it would not be possible to achieve all the requirements for performances and safety of the car. Also, it would not be possible to achieve of increasing and of more strict requirements for reducing environment pollution.

There are many possibilities and systems in the automobile where are used microcontrollers and CAN bus. Microcontrollers are used for monitoring and controlling of many systems in automobiles. Modern automobiles have many interconnected microcontroller systems that monitor, perform and control all needed operations. For networking and communication of microcontroller systems in automobile it is mostly used CAN protocol and CAN bus. The CAN bus uses twisted pair of copper wires and has very important advantages: low complexity, low cost, robustness and bounded communication delays. The CAN protocol has made a revolution in the automotive industry, enabling the increasing application of electronic systems in cars. Also, the price-quality ratio of the CAN is very good, what is very important factor for its massive usage.

Drive-by-wire control of movement direction and movement speed in automobiles is very easy and simple for use, and very efficient and inexpensive in implementation. That concept replaces mechanical and/or hydraulic systems in vehicle by

electronic microcontroller based ones. The drive-by-wire system enables that the driving of the automobile be much easier and decreases production and maintenance cost for the vehicle.

The proposed and described practical solution shows basic good characteristics of the CAN system, such as simple and secure data transfer and simple realization of the bus. Messages are constantly filtered and checked for errors, so the number of wrongly transferred messages is reduced to a minimum. It is also shown the system reaction on the occurrence of an error caused by break of the bus connection or by disabling the transmission or reception of messages. In such a situation, the CAN system immediately notices the error and sends information to the central controlling system or to the user that a transmission error occurred and that appropriate corrective measures should be taken to correct error.

Practically developed, implemented and described drive-by-wire solution uses standard microcontrollers and CAN bus. The solution is simple and inexpensive. It shows all advantages and benefits of application and implementation of drive-by-wire concept, microcontrollers and CAN protocol in automobiles. All this was tested and verified through the practical realization of this simple drive-by-wire system.

The proposed and implemented system is mainly intended for control of electric automobiles. It can be also used for control of the classical vehicles. The implemented drive-by-wire solution also shows the possibilities and advantages of using inexpensive standard microcontrollers and standard open source microcontroller based platforms for the implementation of such systems for automobiles.

#### Note

This paper is based on the paper presented at INTERNATIONAL CONFERENCE ON APPLIED SCIENCES – ICAS 2018, organized by UNIVERSITY POLITEHNICA TIMISOARA, Faculty of Engineering Hunedoara (ROMANIA) and UNIVERSITY OF BANJA LUKA, Faculty of Mechanical Engineering (BOSNIA & HERZEGOVINA), in cooperation with the Academy of Romanian Scientists, Academy of Sciences Republic of Srpska, Academy of Technical Sciences of Romania – Timisoara Branch and General Association of Romanian Engineers – Hunedoara Branch, in Banja Luka, BOSNIA & HERZEGOVINA, 9 – 11 May 2018.

#### References

- [1] Denton T 2012 Automobile electrical and electronic systems, Routledge, Taylor and Francis Group
- [2] Navet N and Simonot-Lion F 2009 Automotive Embedded Systems Handbook, CRC Press, Taylor and Francis Group
- [3] Shanker S 2016 Enhancing Automotive Embedded Systems with FPGAs, Nanyang Technological University, Singapore, Doctoral Thesis
- [4] Di Natale M, Zeng H, Giusto P and Ghosal A 2012 Understanding and using the Controller Area Network communication protocol, Springer
- [5] Bergmiller P 2015 Towards Functional Safety in Drive-by-Wire Vehicles, Springer
- [6] Yih P Steer-By-Wire: Implications for vehicle handling and safety, [http://www-cdr.stanford.edu/dynamic/bywire/defense\\_v5.pdf](http://www-cdr.stanford.edu/dynamic/bywire/defense_v5.pdf)

- [7] Easy8051A Users manual, MikroElektronika, <http://www.mikroe.com/>
- [8] Easy8051B Users manual, MikroElektronika, <http://www.mikroe.com/>
- [9] CANSPI Users manual, MikroElektronika, <http://www.mikroe.com/>
- [10] MCP2515 Stand-Alone CAN Controller With SPI™ Interface, Microchip
- [11] MCP2551 High-Speed CAN Transceiver, Microchip
- [12] mikroC for 8051 User manual, MikroElektronika, <http://www.mikroe.com/>



ISSN: 2067-3809

copyright © University POLITEHNICA Timisoara,  
Faculty of Engineering Hunedoara,  
5, Revolutiei, 331128, Hunedoara, ROMANIA  
<http://acta.fih.upt.ro>

# Fascicule 4

## [October - December]

t o m e

# [2018] XI

**ACTA**Technica**CORVINIENSIS**  
BULLETIN OF ENGINEERING



**ISSN: 2067-3809**

copyright © University POLITEHNICA Timisoara,  
Faculty of Engineering Hunedoara,  
5, Revolutiei, 331128, Hunedoara, ROMANIA  
<http://acta.fih.upt.ro>

# ANALYSIS AND FORMING MECHANISM OF A NEW CHAOTIC ATTRACTOR

<sup>1,2</sup>Sakarya University, Electrical and Electronics Engineering Department, Sakarya, TURKEY

**Abstract:** In this study, a new chaotic attractor is analyzed which is found by adding a quadratic nonlinearity to another chaotic attractor. First of all, time series analysis is performed for the new chaotic system. One of the methods to calculate the amount of chaos in a system is Lyapunov exponent which measure the exponential divergence of initially close state-space trajectories. Then, the conclusions are strengthened with analysis of the Lyapunov exponent and bifurcation diagram. Lastly, the forming mechanism of the new chaotic attractor is given with different values of a posted constant variable. In this study, the newfound chaotic attractor is investigated. Time series analysis, bifurcation diagram, and largest Lyapunov exponent decomposition of this new attractor are given for one of the constant parameters of it. This study has further given forming mechanism analysis of the attractor and sought the forming mechanism of it by explaining dynamical behaviors under varying values of a newly added constant parameter. Consequently, an exhaustive understanding is revealed for a new chaotic attractor through different ways.

**Keywords:** chaotic attractor, time series analysis, Lyapunov exponent, bifurcation diagram, forming mechanism

## INTRODUCTION

There are characteristic features of chaotic systems which meet the basic requirements of cryptology, such as randomness, ergodicity, and sensitive dependence to control [1-3]. By taking advantages of these features, Çavuşoğlu et al. developed an encryption algorithm that uses chaos based S-BOX for secures and speed image encryption. Random number generator is designed with chaotic approach for this algorithm [2]. Eq. (1) shows the chaotic system used in encryption algorithm [2].

$$\dot{x} = cy - x - bz \tag{1}$$

$$\dot{y} = axz - xy - bx$$

$$\dot{z} = dxy + b$$

The value of system parameters and the values of initial conditions are given  $a = 1, b = 1, c = 2, d = -3$  and  $x_0 = 1, y_0 = -1, z_0 = 0.01$  respectively.

Eq. (2) shows the new chaotic system produced from the chaotic system is shown on Eq. (1) by adding a product of two parameters ( $zx$ ) to the equation  $\dot{z}$ . Furthermore, the constant parameter 'a' can be omitted because of its value is 1 and there is no effect on the system. Then, the new chaotic attractor is shown below:

$$\dot{x} = cy - x - bz \tag{2}$$

$$\dot{y} = xz - xy - bx$$

$$\dot{z} = dxy + b + zx$$

Also, the value of new system parameters and the values of initial conditions are given  $c = 2, b = 0.3, d = -3$  and  $x_0 = 0.06, y_0 = 0.12, z_0 = 0.5$  respectively.

The Matlab Simulink model of the new chaotic system is given in Figure 1. Also, chaotic time series and phase portrait of the new chaotic system model system obtained by ode solver in Matlab are shown in Figure 2.

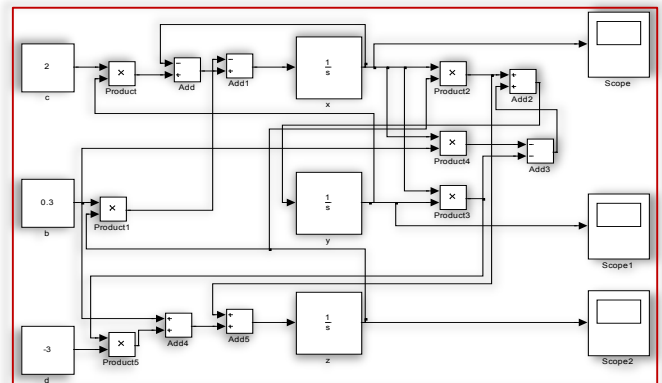
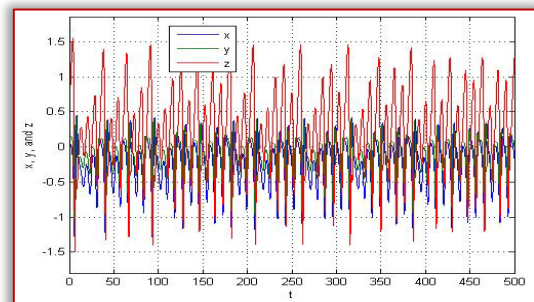
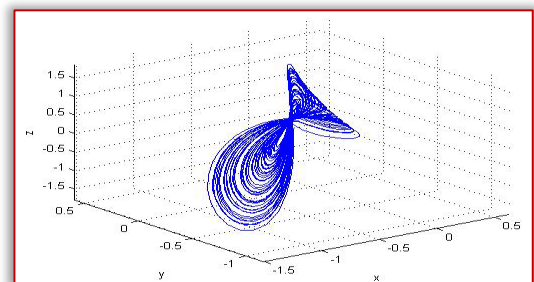


Figure 1. The Matlab-Simulink model of the system



(a)

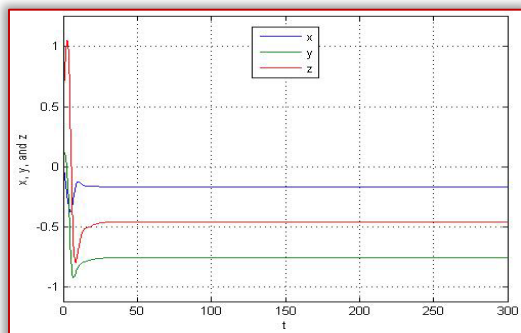


(b)

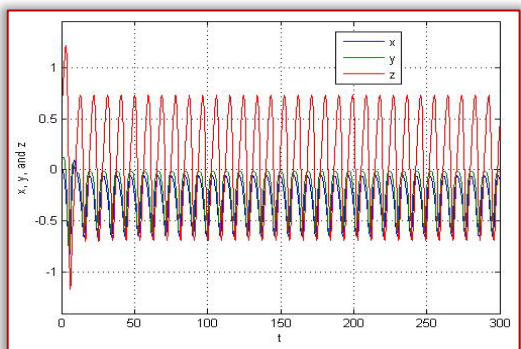
Figure 2. (a) Time series diagram and (b) phase portrait of the chaotic system

### TIME SERIES ANALYSIS OF NEW CHAOTIC SYSTEM

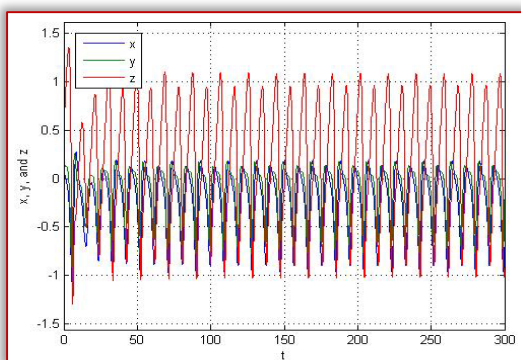
Time series is a common type of plot used for showing the long-term behavior of ordinary differential equations of the form  $x_{n+1}=f(x_n)$ ,  $n=0,1,\dots$ . This type of plot arises from a representation of the variable  $x_n$  as a function of  $n$ . The horizontal axis represents number of iteration ( $n$ ) and the vertical axis represents the variables ( $x_n$ ) [4-7].



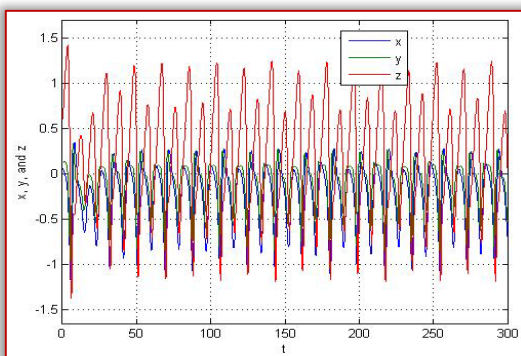
(a)



(b)



(c)



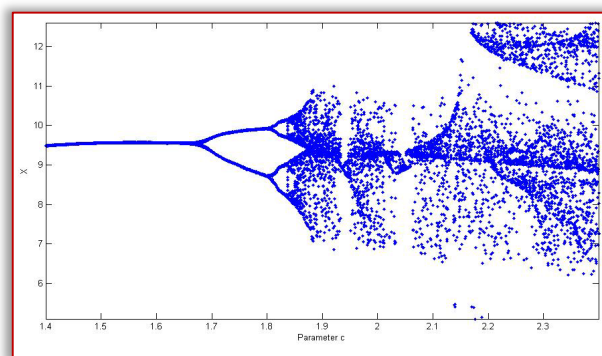
(d)

Figure 3. Time series diagram for parameter (a)  $c=0.4$ , (b)  $c=1.3$ , (c)  $c=1.7$ , and (d)  $c=1.84$

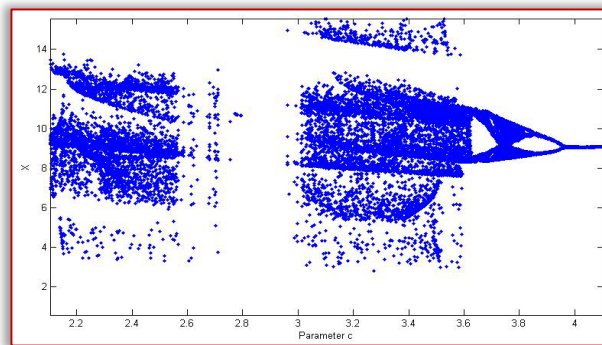
Figures 3 shows the time series plot of the attractor with respect to the changes of parameter 'c'. 300 iterations used for time parameter in these implementations and figures show the change of x, y, and z values in time. For the value of "c=0.4" system shows linear behavior and points flow to a fixed point. By increasing the value of 'c' step by step, system starts to behave chaotically. At value 1.3 the system is showing period two behavior, whereas period four behavior for c is equal to 1.7. At the Figure 3(d), the value of parameter c becomes equal to 1.84 approximately. After this value, the system is not periodic anymore and goes into chaos.

### BIFURCATION DIAGRAM ANALYSIS OF NEW CHAOTIC SYSTEM

Bifurcation diagram is used to show visited or asymptotically approached values of a system as a function of a bifurcation parameter in the system [8-11]. Generally, the sequent dots represent stable values and unstable values are omitted. The bifurcation parameter is shown on the horizontal axis and the expected result of the system for that value is shown on vertical axis.



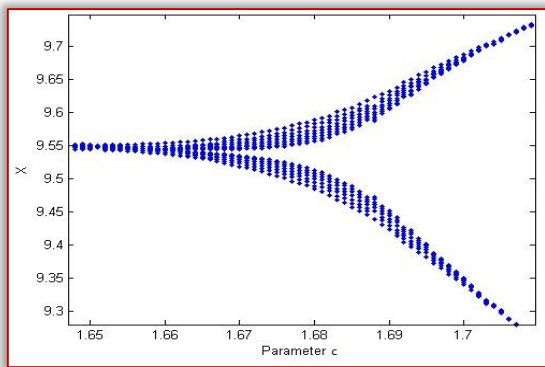
(a)



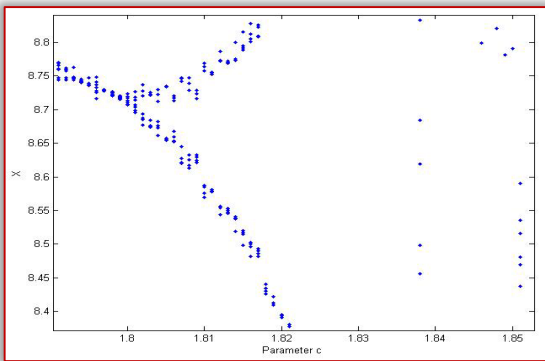
(b)

Figure 4. Bifurcation diagram of the attractor for parameter (a)  $1.4 < c < 2.4$ , (b)  $2.1 < c < 4.1$ .

Figure 4 shows the bifurcation diagram of the attractor for varying values of parameter c between 1.4 and 4.1. As shown at the previous part with time series, system puts on period two behavior for 'c' values after 1.67. Then, it shows period four behavior until reaches to a value between 1.83 and 1.84. After all, the attractor enter the chaos. However, after reaching chaos the system may have some tunnels of unstable points again and again. These tunnels are named as windows of order. At the Figure 4(b), between 2.8 and 3 approximately, there occur a window of order and it can be seen again for the next values.



(a)



(b)

Figure 5. Bifurcation diagram of the attractor for parameter (a)  $1.64 < c < 1.71$ , (b)  $1.79 < c < 1.86$ .

### LARGEST LYAPUNOV EXPONENT ANALYSIS OF NEW CHAOTIC SYSTEM

One of the methods to calculate the amount of chaos in a system is Lyapunov exponent which measure the exponential divergence of initially close state-space trajectories [12]. Diagram of largest Lyapunov exponent clues in chaotic behavior of a system. Figure 6 shows the largest Lyapunov exponent diagram of the system under the 100 initial iterations and 50000 iterations of parameter c between the values 0 and 5. E&F Chaos Program is used for this estimation [13]. Firstly, model of the system is built for the tool. Then, the parameter is chosen, minimum/maximum values of that parameter is given, and iteration numbers are selected by using “Largest Lyapunov Exponent” feature under the plot tab.

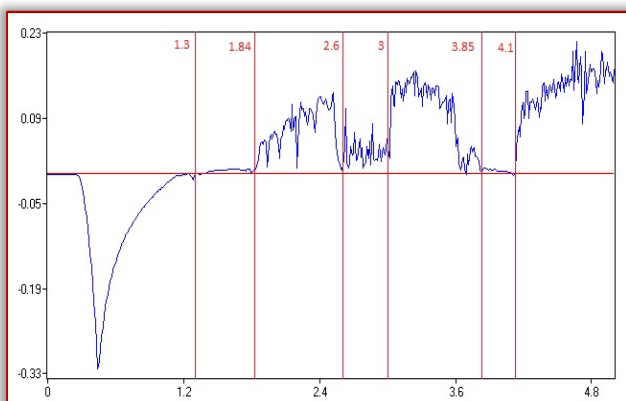


Figure 6. Largest Lyapunov exponent of new chaotic system - value of c is approximately 1.3, 1.84, 2.6, 3, 3.85 and 4.1 on the red lines

When largest Lyapunov exponent graph goes into the positive area, the system starts to behave as chaotic. As mentioned at the previous part by bifurcation diagrams, the attractor behaves chaotic when the parameter c reaches approximately a value of 1.84. Therefore, largest Lyapunov exponent of the attractor is expected to go into positive values at those values shown on the Figure 6. At the first marked line, which is 1.3, the system does not go into chaos yet but possesses a periodic behavior. This results in almost linear behavior near to the zero values of largest Lyapunov exponent. However, the attractor enters chaos after the value 1.84 which is marked by the second line. Furthermore, the system is not always in chaos as mentioned at the previous parts. As seen in the bifurcation diagram on Figure 4(b), the system is in a window of order for the values between 2.8 and 3, in addition, it is also not in chaotic form for the values close to 4. As a result of that, the largest Lyapunov exponent goes down to zero or near somewhere to zero for these values as shown on the Figure 6 between 2.6 - 3 and 3.85 - 4.1 lines. Consequently, a solid relationship is seen between bifurcation diagram and largest Lyapunov exponent of the system.

### FORMING MECHANISM OF NEW CHAOTIC SYSTEM

A controlled system of the new chaotic attractor is described with a newly added constant parameter ‘u’ in order to reveal the form mechanism of that attractor.

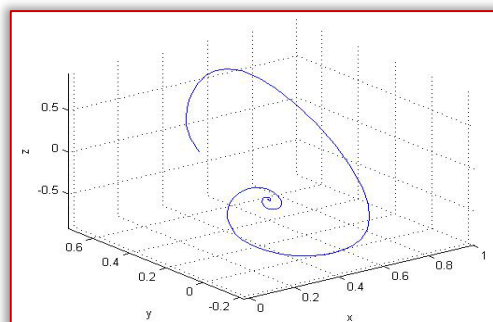
$$\begin{aligned} \dot{x}' &= cy - x - bz \\ \dot{y}' &= xz - xy - bx + u \\ \dot{z}' &= dx + b + xz \end{aligned} \quad (3)$$

Dynamical behavior of the controlled attractor (3) is studied to perform the forming mechanism. The system may show some different behaviors with varying values of parameter ‘u’ which is considered as the “controller” of the system [14].

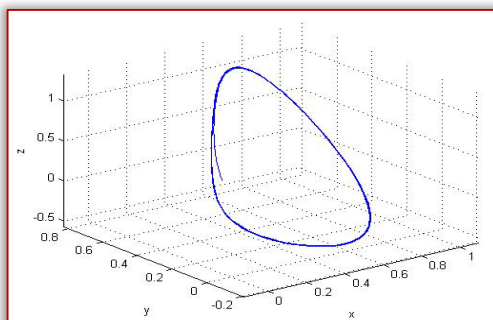
Table 1 shows that the system converges to a point when the value of parameter u is large enough. By decreasing gradually, there occur limit cycle, period-doubling, and period-four behaviors. Then, the attractor becomes a complete attractor between very small values around zero. Furthermore, the system diverges from a point when the value of parameter u is small enough [14].

Table 1. Parameter range of dynamical behaviors of the controlled system 3

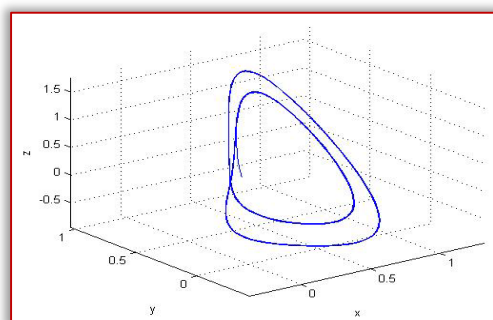
Parameter u	System behavior
For $u \geq 0.13$ and $-0.0194 > u \geq -8.9$	the system converges to a point (see Figure 7(a))
For $0.13 > u \geq 0.103$ and $-8.9 > u \geq -9.3$	the system has a limit cycle (see Figure 7(b))
For $0.103 > u \geq 0.0975$	there are period-doubling behavior (see Figure 7(c))
For $0.0975 > u \geq 0.0959$	there are period-four behavior (see Figure 7(d))
For $0.0959 > u \geq -0.0194$	the system has a complete attractor. (see Figure 2)
For $-9.3 > u$	the system diverges from a point (see Figure 7(e))



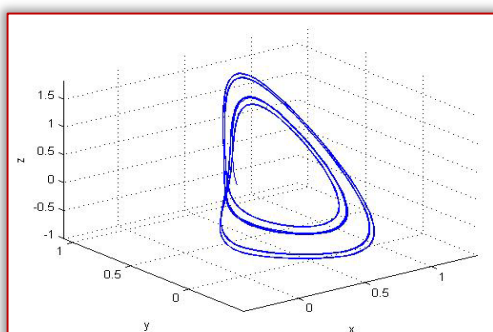
(a)



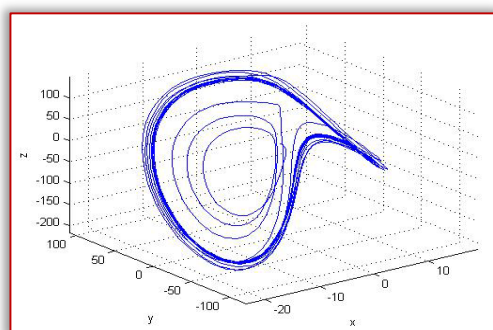
(b)



(c)



(d)



(e)

Figure 7. Phase portrait of the attractor for (a)  $u=0.3$ , (b)  $u=0.118$ , (c)  $u=0.099$ , (d)  $u=0.097$ , (e)  $u=-200$

## CONCLUSIONS

Firstly, a new chaotic attractor is found by changing an already existing one. In this study, this newfound chaotic attractor is investigated. Time series analysis, bifurcation diagram, and largest Lyapunov exponent decomposition of this new attractor are given for one of the constant parameters of it. This study has further given forming mechanism analysis of the attractor and sought the forming mechanism of it by explaining dynamical behaviors under varying values of a newly added constant parameter. Consequently, an exhaustive understanding is revealed for a new chaotic attractor through different ways.

**Note:** This paper is based on the paper presented at INTERNATIONAL CONFERENCE ON APPLIED SCIENCES – ICAS 2018, organized by UNIVERSITY POLITEHNICA TIMISOARA, Faculty of Engineering Hunedoara (ROMANIA) and UNIVERSITY OF BANJA LUKA, Faculty of Mechanical Engineering (BOSNIA & HERZEGOVINA), in cooperation with the Academy of Romanian Scientists, Academy of Sciences Republic of Srpska, Academy of Technical Sciences of Romania – Timisoara Branch and General Association of Romanian Engineers – Hunedoara Branch, in Banja Luka, BOSNIA & HERZEGOVINA, 9 – 11 May 2018.

## References

- [1] Lorenz, E 1963 Deterministic non-periodic flows, *J. Atmos.Sci.*, 20(1) 130–141.
- [2] Çavuşoğlu Ü, Kaçar S, Pehlivan I, Zengin A 2017 Secure image encryption algorithm design using a novel chaos based S-Box. *Chaos, Solitons & Fractals*, 95, 92-101.
- [3] C.X. Liu, et al. 2004 A new chaotic attractor, *Chaos, Solitons & Fractals* 22(5) 1031–1038.
- [4] Sarmah H. K, Saha, R. U. M. A, Dutta, N. I. L. I. M. A. 2018 Bifurcation and Lyapunov Exponent of a chaotic Cubic Map. *Communications in Nonlinear Science and Numerical Simulation* 57 352-358
- [5] Ikeguchi T, Iokibe T, Aihara K 2000 Chaos and Time Series Analysis. In: Liu ZQ., Miyamoto S. (eds) *Soft Computing and Human-Centered Machines. Computer Science Workbench*. Springer, Tokyo.
- [6] Sprott, J.C. 2003 *Chaos and Time-Series Analysis*, Oxford University Press.
- [7] P.R.L. Alves, L.G.S. Duarte, L.A.C.P. da Mota 2017 A new characterization of chaos from a time series *Chaos,Solitons&Fractals*,104 323-326
- [8] YuanDong Ji, Li Lai, SuChuan Zhong, Lu Zhang 2018 Bifurcation and chaos of a new discrete fractional-order logistic map *Communications in Nonlinear Science and Numerical Simulation* 57 352-358
- [9] Jihua Yang, Liqin Zhao 2015 Bifurcation analysis and chaos control of the modified Chua's circuit system *Chaos,Solitons&Fractals* 77 332-339
- [10] Le Xiong, Sen Zhang, Yicheng Zeng, Boquan Liu 2018 Dynamics of A New Composite Four - scroll Chaotic System, *Chinese Journal of Physics*
- [11] P. Gholamin, A.H. Refahi Sheikhani 2017 A new three-dimensional chaotic system: Dynamical properties and simulation *Chinese Journal of Physics* 55(4) 1300-1309
- [12] Rosenstein, M. T., Collins, J. J., & De Luca, C. J. 1993. A practical method for calculating largest Lyapunov exponents from small data sets. *Physica D: Nonlinear Phenomena*, 65(1-2), 117-134.
- [13] Diks, C., Hommes, C., Panchenko, V., & Van Der Weide, R. 2008 E&F Chaos: a user friendly software package for nonlinear economic dynamics. *Computational Economics*, 32(1), 221-244.
- [14] Lü, J., Chen, G., & Zhang, S. 2002. The compound structure of a new chaotic attractor. *Chaos, Solitons & Fractals*, 14(5), 669-672.

<sup>1</sup>Pavel KOVAC, <sup>2</sup>Mirfad TARIC, <sup>1</sup>Dragan RODIC, <sup>1</sup>Borislav SAVKOVIC,  
<sup>2</sup>Dušan JESIC, <sup>3</sup>Dušan GOLUBOVIC

## NEURO-FUZZY SYSTEMS MODELLING OF HARD STEEL SURFACE ROUGHNESS PARAMETERS

<sup>1</sup>University of Novi Sad, Faculty of Technical Sciences, Novi Sad, SERBIA

<sup>2</sup>International Technology Management Academy, Novi Sad, SERBIA

<sup>3</sup>University of East Sarajevo, Faculty of Mechanical Engineering, Lukavica, East Sarajevo, BOSNIA & HERZEGOVINA

**Abstract:** The objective of this study is to examine the influence of machining parameters on surface finish during turning of hard steel. A new approach in modelling surface roughness which uses design of experiments is described in this paper. Used were as well adaptive-neuro-fuzzy-inference system (ANFIS) model. The values of surface roughness predicted by different models were then compared. The results showed that the proposed systems can significantly increase the accuracy of the product profile when compared to the conventional approaches. The results indicate that the design of experiments with central composition plan modelling technique and ANFIS can be effectively used for the prediction of the surface roughness for hard steel.

**Keywords:** turning, hard steel, ANFIS modeling, surface roughness

### INTRODUCTION

Increasingly, research in manufacturing processes and systems is evaluating processes to improve their efficiency, productivity and quality. The quality of finished products is defined by how closely the finished product adheres to certain specifications, including dimensions and surface quality. Surface quality is defined and identified by the combination of surface finish, surface texture, and surface roughness. Surface roughness ( $R_a$ ,  $R_{max}$ ) is the commonest index for determining surface quality [1, 2].

Manufacturing processes do not allow achieving the theoretical surface roughness due to defects appearing on machined surfaces and mainly generated by deficiencies and imbalances in the process. Due to these aspects, measuring procedures are necessary; as it permits one to establish the real state of surfaces to manufacture parts with higher accuracy. To know the surface quality, it is necessary to employ theoretical models making it feasible to do predictions in function of response parameters [3, 4, 5].

A lot of analytically methods were also developed and used for predicting surface roughness. An empirical model for prediction of surface roughness in finish turning [6]. Nonlinear regression analysis, with logarithmic data transformation is applied in developing the empirical model. Metal cutting experiments and statistical tests demonstrate that the model developed in this research produces smaller errors and has a satisfactory result. The mathematical models for modeling and analyzing the vibration and surface roughness in the precision turning with a diamond cutting tool [7].

Recently, some initial investigations in applying the basic artificial intelligence approach to model of machining processes, have appeared in the literature, concludes that the modeling of surface quality in machining processes has mainly used Artificial Neural Networks and fuzzy set theory [8,

9]. Average mean roughness,  $R_a$  using neural network (NN) was predicted in [10]. Surface roughness and surface finish have been considered in [12, 13, 14]. Research of the influence of machining parameters combination to obtain a good surface finish in turning and to predict the surface roughness values using fuzzy modeling is presented in [15]. Also, may notice that the neural network used in the study, where the enabling resolution of the problem that is difficult to define and mathematically model. This can be seen in the work where the neural network was based on the face milling machining processes, where is aimed to produce the relationship of cutting force versus instantaneous angle  $\phi$  [16]. Use of coolants and lubricants in hard machining were presented in [17].

In this study, cutting speed, feed and depth of cut as machining conditions were selected. An adaptive neuro fuzzy inference system (ANFIS) were developed for modeling these cutting parameters.

### EXPERIMENTAL PROCEDURE AND MATERIAL

Terms of the experimental study:

- » The experimental machine tool was a universal lathe – Prvomajska DK480, Figure 1.



Figure 1. Turning machine

» Tool: For the study was used interchangeable plates of hard metal CNMA 120404 ABC 25/F producer ATRON from Germany. Used was insert holder for external processing PCLNR 25 25 M16.

The markings of the cutting tips according to DIN 4983 more closely define the geometry, as follows: the shape of the plate  $C \rightarrow$  rhomb; the rake angle  $N \rightarrow = 0^\circ$ ,  $C \rightarrow = 7$ ; tolerance class M; Type of tile  $\rightarrow$  with opening A, W and G; length of cutting blade  $\rightarrow$  12.7 mm (12); cutting edge thickness  $\rightarrow$  4.76 mm (04); radius of tool tip  $\rightarrow$  0.4 mm (04). All tiles have a rake angle ( $\gamma = -6^\circ$ ).

The processing regime included the following elements:

- cutting speed  $v$ , (m /min),
- feed  $f$ , (mm /rev),
- cutting depth,  $a$  (mm).

Variation of the experiment input factor (cutting regime) was performed in 5 levels of values. The mean value between the two adjacent levels was the geometric mean of these values. Selected levels of factors are shown in Table 1.

Table 1. Experimental input factor levels

Factor Levels		Cutting speed $v$ (m/min)	Cutting speed $v$ (m/s)	Feed $f$ (mm/rev)	Dept of cut $a$ (mm)
Highest	+1.41	1.143	0.285	0.286	0.593
High	+1	1.143	0.285	0.067	0.796
Middle	0	4.571	0.033	1.667	0.197
Small	-1	0.286	0.593	0.067	0.796
Smallest	-1.41	1.143	0.285	0.077	0.782

Before the experimental performance, preparation of the workpiece was carried out. The workpiece is thermally treated steel Č3840 (90MnCrV8) whose working hardness was 55 HRC, circular cross-section  $\varnothing 34$  mm and length 500 mm. To make it easier to perform, and for more credible measurement results, the workpiece tends to the chuck head at one end, and relies on the other end to the spike. It is necessary to remove a certain layer of material in order to avoid throwing-ovality and the results were more reliable. The length of the workpiece bar of 500 mm, it was divided into 24 fields with a length of 10 mm on which the longitudinal cutting, without the presence of cooling and lubricating agents was provided. Each field on workpiece was planned for one experimental point measurement.

Measuring the surface roughness parameters with the Talysurf 6 measuring device was done. After processing by a computer on the screen, was written or printed results. The personal computer was connected to the Talysurf-6 measuring device using a serial connection COM-3. Instead of the printer, a computer was connected with a special adapter with a measuring machine Talysurf-6. The basic parts of the measuring device Talysurf-6 are shown in Figure 2.

During study measured was the values of workpiece surface roughness parameters:  $R_a$ ,  $R_{max}$ . The measurement results of these parameters and estimated values by three factorial models are given in Table 2.



Figure 2. Surface roughness measurement system Talysurf-6 connected with computer

Table 2. The measurement and modeled results – Input parameters

No.	Factor			$R_i$ measured		$R_i$ Model	
	$v$ [m/min]	$f$ [mm/rev]	$a$ [mm]	$R_a$ [ $\mu$ m]	$R_{max}$ [ $\mu$ m]	$R_a$ [ $\mu$ m]	$R_{max}$ [ $\mu$ m]
1	90	0,05	0,10	0.51	3.2	0.47	2.81
2	160	0,05	0,10	0.53	2.8	0.50	2.76
3	90	0,20	0,10	1.17	4.8	1.26	5.10
4	160	0,20	0,10	1.2	4.8	1.32	5.01
5	90	0,05	0,50	0.75	6.2	0.63	4.20
6	160	0,05	0,50	0.85	6.1	0.66	4.13
7	90	0,20	0,50	2.01	7.6	1.66	7.63
8	160	0,20	0,50	2.1	7.6	1.74	7.49
9	120	0,10	0,22	0.93	4.5	0.91	4.57
10	120	0,10	0,22	0.77	4	0.91	4.57
11	120	0,10	0,22	0.91	4.4	0.91	4.57
12	120	0,10	0,22	0.76	4.3	0.91	4.57
13	80	0,10	0,22	0.69	3.56	0.88	4.63
14	180	0,10	0,22	0.71	4	0.94	4.51
15	120	0,045	0,22	0.43	2.4	0.52	3.24
16	120	0,25	0,22	1.91	8.01	1.73	6.78
17	120	0,10	0,07	1.06	6.6	0.74	3.43
18	120	0,10	0,70	0.98	5.5	1.11	6.11
19	80	0,10	0,22	0.65	3.93	0.88	4.63
20	180	0,10	0,22	0.7	3.5	0.94	4.51
21	120	0,045	0,22	0.39	2.5	0.52	3.24
22	120	0,25	0,22	1.82	8.3	1.73	6.78
23	120	0,10	0,07	1.04	2.8	0.74	3.43
24	120	0,10	0,70	1.38	6.2	1.11	6.11

### IMPLEMENTATION OF FACTORIAL EXPERIMENTAL PLAN

In the table 3 are given results data dispersion analyses, adequacy of models and significance of parameters.

Table 3. Adequacy of models and significance of parameters

Model adequacy	$R_a$ $F_a=4,33219$		$R_{max}$ $F_a=1,65230$	
	$F_{ro}$	16.62	1372,91	
Significance	Fr1(v)	0.66 (*)	0,03*	
	Fr2(f)	282.91	35,04	
	Fr3(a)	23.35	16,03	

For training the ANFIS during modeling was used "MatLab" software, which is the most powerful software for technical calculations [18].

Training and testing are the most important characteristics of ANFIS because just training and testing determine its characteristics. To create and train an ANFIS in the MATLAB is

used Fuzzy Logic Toolbox. Adaptive neuro–fuzzy inference system is an architecture which is functionally equivalent to a Sugeno type fuzzy rule base [19]. An ANFIS gives the mapping relation between the input and output data by using the hybrid learning method to determine the optimal distribution of membership functions [20]. Both artificial neural network (ANN) and fuzzy logic (FL) are used in ANFIS architecture [21]. In 1993, Jang first introduced the Adaptive Neuro–Fuzzy Inference System, which was reported as a very efficient system for solving the defined equations involving the automatic elicitation of knowledge expressed only by the if–then rules.

In our case ANFIS is a five–layer neural network that simulates the working principle of a fuzzy inference system. The ANFIS model generated from the membership functions and rules were data–driven by the process data for each mechanical property. Though there are many numbers of membership functions available like triangular, trapezoidal, Gaussian, etc. Each set of process data collected from the extrusions consisted of 30 data points from which 24 and 6 were selected randomly for training and testing, respectively. The models were developed and implemented using 100 epochs. The input and output data sets contained three inputs (cutting speed, feed rate and depth of cut) and one output (surface roughness Ra or Rmax).

**EXPERIMENTAL RESULTS AND ANALYSE**

Equations (1) and (2) for surface roughness parameters Ra and Rmax, modeled by design of central compositional experimental plan determined by software:

$$R_a = 2,8264 \cdot v^{-0.04471} \cdot f^{0.59975} \cdot a^{0.00716} \quad (1)$$

$$R_{max} = 9,0036 \cdot v^{-0.3717} \cdot f^{0.3739} \cdot a^{-0.6148} \quad (2)$$

As mentioned before, ANFIS modeling was used for analysis and optimization of surface roughness parameters in turning process. The obtained results of ANFIS model are given in the Table 4, side by side with the experimental results. For reduction of a model deviation, is needed to increase the number of experimental inputs trials.

Calculation of percental deviation for measured and model surface roughness parameters values was performed according next formula

$$E = \frac{|Ri_{exp} - Ri_m|}{Ri_{exp}} \cdot 100\% \quad (3)$$

where are: Riexp– experimental value, Rim– model value

Table 4. Experimental values and values of surface roughness obtained with percentage deviation

No.	Factor			R <sub>i</sub> – experimental roughness		R <sub>i</sub> – modeled roughness	
	v [m/s]	s [mm/rev]	a [mm]	R <sub>a</sub> [µm]	R <sub>max</sub> [µm]	R <sub>a</sub> [µm]	R <sub>max</sub> [µm]
1	81	0.1	0.22	0.7	3.93	0.99561	3.9245
2	182	0.1	0.22	0.65	3.5	0.74177	2.87921
3	121	0.045	0.22	0.39	2.5	0.42268	2.47317
4	122	0.25	0.22	1.82	8.3	1.85709	8.19655
5	123	0.1	0.07	1.04	2.8	0.97167	6.17389
6	119	0.1	0.7	1.38	6.2	0.84962	5.0787
Average deviation %						6.20950	8.8208

Figures 3 and 4 shows the correlation between the experimental and obtained values by factorial experimental design of surface roughness parameters (Ra, Rmax). From the diagram can be seen that the points are near regression line and correlation is good.

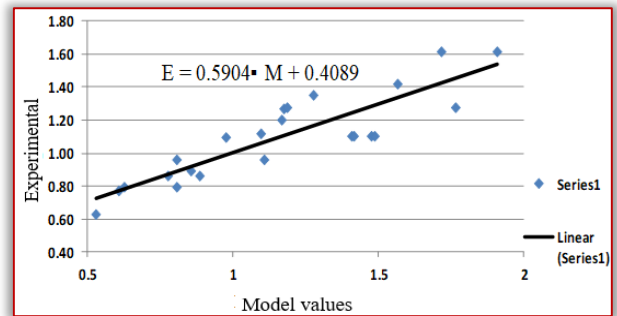


Figure 3. Correlation between experimental and obtained values of surface roughness– Ra

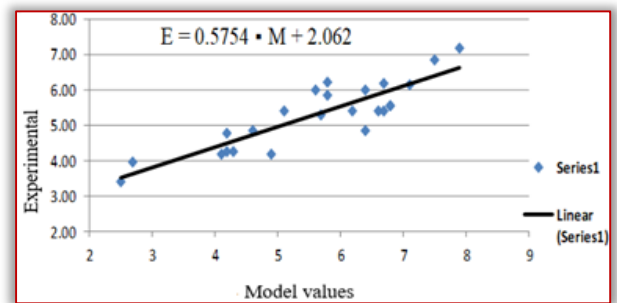


Figure4. Correlation between experimental and obtained values of surface roughness– Rmax

Deviation of experimental and model values of surface roughness is shown on Fig 5. Deviation of 6 testing numbers of ANFIS is on Fig 6.

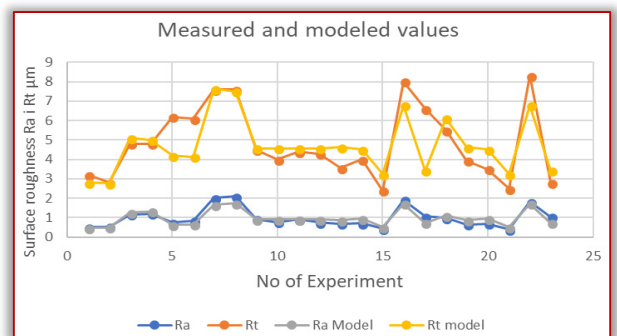


Figure 5. Deviation of experimental and model values of surface roughness

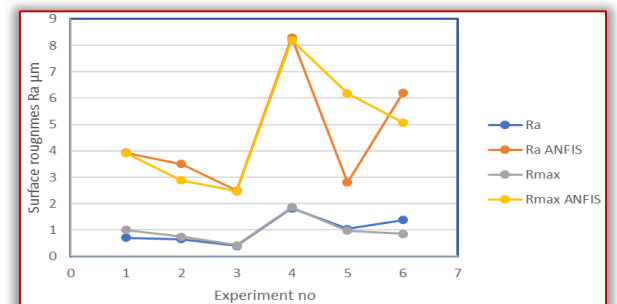


Figure 6. Deviation of 6 testing numbers of ANFIS

The surface roughness parameters ( $R_a$ ,  $R_{max}$ ) versus cutting speed is in Fig 7, versus feed in Fig. 8 and versus depth of cut in Fig 9.

Any change in the cutting speed leads to a slowly corresponding change in the value of surface roughness. The cutting speed has a small and decreasing effect Fig 7. Influence of feed on value surface roughness is higher than the cutting speed effect. Increasing feed increase surface roughness Fig 8.

Depth of cut at least influences the wear on the flank surface and surface roughness values slightly, Fig 9.

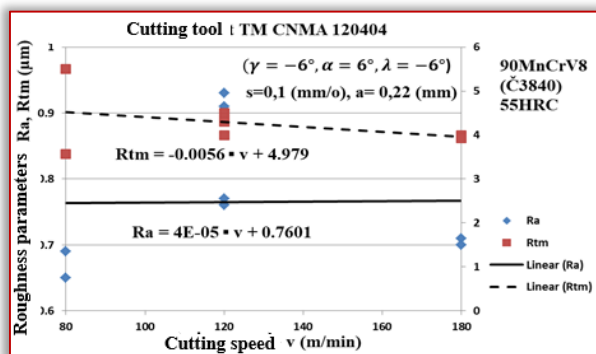


Figure 7. The surface roughness ( $R_a$ ,  $R_{max}$ ) versus cutting speed

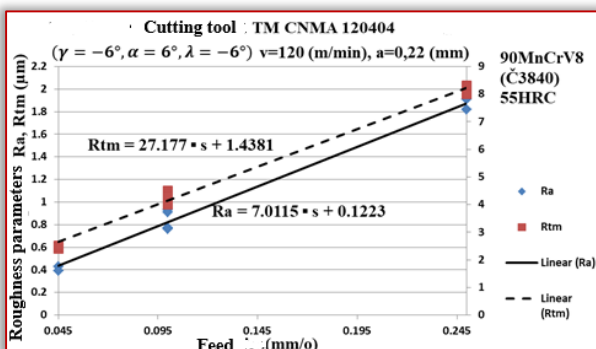


Figure 8. The surface roughness ( $R_a$ ,  $R_{max}$ ) versus feed per revolution

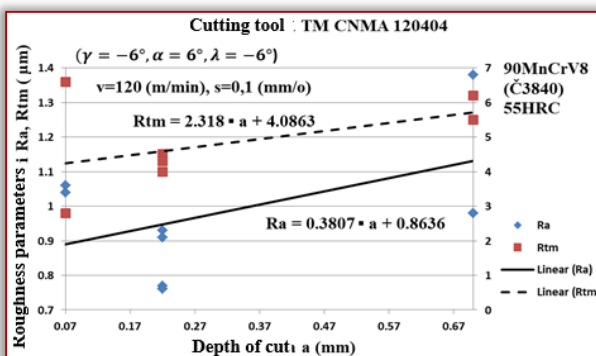


Figure 9. The surface roughness ( $R_a$ ,  $R_{max}$ ) versus the cutting depth

## CONCLUSION

Intelligent optimization techniques give the influence of cutting conditions on machining surface quality during turning hard material, are investigated through experimental verification. The investigation results confirm the highly consent of experimental research and intelligent techniques

modeling. The intelligent optimization techniques and experimental results show some good information which could be used by future researches for optimal control of machining conditions. This paper has successfully established ANFIS model, for predicting the workpiece surface roughness parameters. Figures 4 and 5 shows the compared predicted values obtained by experiment and estimated by ANFIS shows a good comparison with those obtained experimentally. The average deviations of models are checked and are found to be adequate. The model adequacy can be further improved by considering more variables and ranges of parameters.

## Acknowledgements

The paper is the result of the research within the project TR 35015 financed by the ministry of science and technological development of the Republic of Serbia SRB/SK bilateral project.

## Note

This paper is based on the paper presented at INTERNATIONAL CONFERENCE ON APPLIED SCIENCES – ICAS 2018, organized by UNIVERSITY POLITEHNICA TIMISOARA, Faculty of Engineering Hunedoara (ROMANIA) and UNIVERSITY OF BANJA LUKA, Faculty of Mechanical Engineering (BOSNIA & HERZEGOVINA), in cooperation with the Academy of Romanian Scientists, Academy of Sciences Republic of Srpska, Academy of Technical Sciences of Romania – Timisoara Branch and General Association of Romanian Engineers – Hunedoara Branch, in Banja Luka, BOSNIA & HERZEGOVINA, 9 – 11 May 2018.

## References

- [1] Chen J C, Savage M 2001 A Fuzzy–Net–Based Multilevel In–process Surface Roughness Recognition System in Milling Operations, The International Journal of Advanced Manufacturing Technology 17 670–676
- [2] Quintana G, Garcia–Romeu M L, Ciurana J 2009 Surface roughness monitoring application based on artificial neural networks for ball–end milling operations, Journal of Intelligent Manufacturing 22 607–617
- [3] Sivarao, Castillo, Taufik 2000 Machining Quality Predictions: Comparative Analysis of Neural Network and Fuzzy Logic, International Journal of Electrical & Computer Sciences IJES 9 451–456
- [4] Drégelyi–Kiss A, Horváth R, Mikó B 2013 Design of experiments (DOE) in investigation of cutting technologies, Development in Machining Technology DIM 2013, Cracow, Poland 20–34
- [5] Maňková I, Vrabel M, Beňo J, Kovač P, Gostimirovic M 2013 Application of Taguchi method and surface response methodology to evaluate of mathematical models for chip deformation when drilling with coated and uncoated twist drills, Manufacturing Technology 13(4) 492–499
- [6] Hadi Y, Ahmed S G 2006 Assessment of Surface Roughness Model for Turning Process. Knowledge Enterprise: Intelligent Strategies in Product Design, Manufacturing, and Management, in International Federation for Information Processing (IFIP) 207 152–158
- [7] Chen C C, Chiang K T, Chou C C, Liao Y C 2011 The use of D–optimal design for modeling and analyzing the vibration and surface roughness in the precision turning with a

- diamond cutting tool, International Journal of Advanced Manufacturing Technology 54 465–478
- [8] Choudhary A, Harding J, Tiwari M, Data mining in manufacturing: A review based on the kind of knowledge, Journal of Intelligent Manufacturing 20(5) 501–521
- [9] Grzenda M, Bustillo A, Zawistowski P 2012 A soft computing system using intelligent imputation strategies for roughness prediction in deep drilling, Journal of Intelligent Manufacturing 23 1733–1743
- [10] Balic J, Korosec M 2002 Intelligent tool path generation for milling of free surfaces using neural networks, International Journal of Machine Tools & Manufacture 42 1171–1179
- [11] Pe´rez C L J, 2002 Surface roughness modeling considering uncertainty in measurements, International Journal of Production Research, 40(10) 2245–2268
- [12] Azouzi R, Gullot M 1997 On–line prediction of surface finish and dimensional deviation in turning using neural network–based sensor fusion, International Journal of Machine Tools and Manufacturing 37(9), 1201–1217
- [13] Ho S Y, Lee K C, Chen SS, Ho S J 2002 Accurate modeling and prediction of surface roughness by computer vision in turning operations using an adaptive neuro–fuzzy inference system, International Journal of Machine Tools and Manufacture 42(13) 1441–1446
- [14] Zębala W, Gawlik J, Matras A, Struzikiewicz S, Ślusarczyk L 2014 Research of surface finish during titanium alloy turning, Key Engineering Materials 581 409–414
- [15] T. Rajasekaran, K. Palanikumar, B.K. Vinayagam 2011 Application of fuzzy logic for modeling surface roughness in turning CFRP composites using CBN tool, Production Process 5(2) 191–199
- [16] Savković B, Kovač P, Gerić K, Sekulić M, Rokosz K 2013 Application of neural network for determination of cutting force changes versus instantaneous angle in face milling, Journal of Production Engineering 16(2) 25–28
- [17] Kundrák J, Varga G 2013 Use of Coolants and Lubricants in Hard Machining, Technical Gazette 20(6) 1081–1086
- [18] Kovac P, Rodic D, Pucovsky V, Savkovic B, Gostimirovic M 2013 Application of fuzzy logic and regression analysis for modeling surface roughness in face milling, Journal of Intelligent Manufacturing 24(4) 755–762
- [19] Jang J S R, Sun C T 1995 Neuro–Fuzzy Modeling and Control, Proceedings of the IEEE 83 378–406
- [20] Ying L C, Pan M C 2008 Using adaptive network based fuzzy inference system to forecast regional electricity loads. Energy Conversation and Management 49 205–211
- [21] Avci E 2008 Comparison of wavelet families for texture classification by using wavelet packet entropy adaptive network based fuzzy inference system. Applied Soft Computing 8 225–231



ISSN: 2067–3809

copyright © University POLITEHNICA Timisoara,  
Faculty of Engineering Hunedoara,  
5, Revolutiei, 331128, Hunedoara, ROMANIA  
<http://acta.fih.upt.ro>

# Fascicule 4

## [October - December]

t o m e

# [2018] XI

**ACTA**Technica**CORVINIENSIS**  
BULLETIN OF ENGINEERING



**ISSN: 2067-3809**

copyright © University POLITEHNICA Timisoara,  
Faculty of Engineering Hunedoara,  
5, Revolutiei, 331128, Hunedoara, ROMANIA  
<http://acta.fih.upt.ro>

<sup>1</sup>O.A. ADETAYO, <sup>2</sup>O.A. BUCKNOR

# COMPARATIVE STUDY ON THE EFFECT OF GRINDED RICE HUSK AND RICE HUSK ASH ON COMPRESSIVE STRENGTH OF CONCRETE

<sup>1</sup>Department of Civil Engineering, Federal University Oye Ekiti, NIGERIA

<sup>2</sup>Department of Civil Engineering, University of Ibadan, NIGERIA

**Abstract:** Comparative study between Grinded Rice Husk (GRH) and Rice Husk Ash (RHA) effect on concrete performance were performed in this research. Ordinary Portland cement (OPC) cement was partially replaced by GRH at 5% and 10%, and RHA at 5%, 10%, and 20% by weight of cement for a specific water/cement ratio. Compressive strength for 7, 14, and 28 days were determined. The control mix at 28 days had a peak compressive strength of 49.07N/mm<sup>2</sup> while cement partially replaced by GRH at 5% and 10% were 47.84N/mm<sup>2</sup> and 45.47N/mm<sup>2</sup> respectively and cement partially replaced by RHA at 5%, 10%, 20% were 53.24N/mm<sup>2</sup>, 50.24N/mm<sup>2</sup>, and 46.53N/mm<sup>2</sup> respectively at 28 days. The results of the experiments showed that at 5% RHA partial replacement had the optimum compressive strength obtained at 28 days. Replacement of cement with GRH and RHA lead to improvement in the compressive strength of concrete and overall cost of construction.

**Keywords:** comparative study, grinded rice husk, rice husk ash, partial replacement, compressive strength

## INTRODUCTION

Recent work carried out on the formulation and manufacture of concrete has led to the development of various classes with improvement in its quality and properties. Typical concrete is a mixture of fine aggregate (sand), coarse aggregate (rock), cement, and water. The aggregate in the concrete is basically silica, but unfortunately it reacts too slowly, due to its reduced total surface area. Cement gives off lime as it hardens and this lime will inevitably react with silicates or alumino-silicates [1].

The use of pozzolans in concrete helps the lime produced in the hardening of the concrete to slowly react with the aggregate, producing gels. These gels are expansive, and they just fill the voids with a slight pressure thus avoiding water penetration and leaching. Concrete with sawdust ash as pozzolanic material gain strength rapidly at later stages, [2].

Rice plant is one of the plants that absorbs silica from the soil and assimilates it into its structure during the growth [3]. Rice husk is the outer covering of the grain of rice plant with a high concentration of amorphous silica, generally more than 80-85% [4]. It is responsible for approximately 30% of the gross weight of a rice kernel and normally contains 80% of organic and 20% of inorganic substances. Rice husk is produced in millions of tons per year as a waste material in agricultural and industrial processes.

Nigeria is the 19th largest producer of rice in the world with over 3.4 million metric tonnes of paddy rice produced annually and 63,400 metric tonnes of rice husk generated with a potential for production of at least 121,212 metric tonnes of rice husk ash from rice husk generated. This enormous waste is presently not being harnessed productively in the country other than burning, a major air

pollution activity and indiscriminate dumping that cause environmental hazard.

Rice husk in large quantities are grinded together to produce ground rice husk (GRH), and rice husk ash (RHA) is a byproduct of burned rice husk at higher temperature, it can contribute about 20% of its weight to RHA after incineration [5]. So for every 1000 kg of paddy milled, about 220 kg (22%) of grinded husk produced, and when this husk is burnt in the boilers, about 55 kg (25%) of RHA is generated. RHA is a highly pozzolanic material [6], the non-crystalline silica and high specific surface area of the RHA are responsible for its high pozzolanic reactivity. RHA has been used in lime pozzolana mixes and could be a suitable partly replacement for Portland cement (7, 8, 9, 10). RHA is also classified in the same category of highly active pozzolans as Silica Fume [11]. The mean particle size of RHA generally ranges from 5 to 10 µm. However, RHA has a very high specific surface area ranging from 20 to 260 m<sup>2</sup>/g [12] which is attributed to its porous structure [13, 14]. Mehta and Pirth [15], investigated the use of RHA to reduce temperature in high strength mass concrete and got result showing that RHA is very effective in reducing the temperature of mass concrete compared to OPC concrete. Mehta [16], later reported that ground RHA with finer particle size than OPC improves concrete properties, including that higher substitution amounts results in lower water absorption values and the addition of RHA causes an increment in the compressive strength.

This RHA in turn contains around 85%-90% amorphous silica. So for every 1000 kg of paddy milled, about 220 kg (22%) of husk is produced, and when this husk is burnt in the boilers, about 55 kg (25%) of RHA is generate [11].

## MATERIALS AND METHODS

The rice husk used in this work was collected from rice paddy industry in Ikole Ekiti, Ekiti State, Nigeria. Grinded rice husk (GRH) was obtained by milling rice husk inside milling machine (Figure 1).



Figure 1. Showing rice husk being milled to produce GRH  
Rice husk is burnt approximately 48 hours under controlled combustion process inside ferrous-cement furnace to produce rice husk ash (RHA). The burning temperature was within the range of 600°C to 850°C (Figure 2). The ash obtained is ground in a ball mill for 30 minutes and its color was seen as grey



Figure 2. Showing RHA being produce inside ferrous-cement furnace

Table 1. Quantities of Materials per Cubic meter of Concrete for various Batch

Mix No	Percentage Replacement (%)	Cement (kg)	GRH (kg)	RHA (kg)	Fine Aggregate (kn)	Coarse Aggregate (kn)	Water-Cement Ratio
1	0%	14.46	-	-	25.31	33.11	0.45
2	5% GRH	13.74	0.73	-	25.31	33.11	0.45
3	10% GRH	13.01	1.45	-	25.31	33.11	0.45
4	5% RHA	13.74	-	0.73	25.31	33.11	0.45
5	10% RHA	13.01	-	1.45	25.31	33.11	0.45
6	20% RHA	11.56	-	2.90	25.31	33.11	0.45

## MIX PROPORTIONS

The concrete mix design was done according to IS 456:2000 [17]. The traditional way of mix proportion in terms of fixed

ratios of Cement: Fine Aggregate: Coarse Aggregate (in general by volume). Ordinary Portland Cement (OPC) was used for the standard concrete production of grade M40 (1: 1.75: 2.29). The cement content was partially replaced by GHA at 5% and 10%, and RHA at 5%, 10%, and 20%, in addition with control mix as shown in Table 1.

## CASTING OF CONCRETE CUBES FOR CRUSHING

The concrete ingredients were thoroughly mixed and uniformly distributed within the concrete mass during various stages of handling. It was ensured that all the characteristics of concrete are in conformity with relevant codes of practice. The concrete was filled into the cube moulds of dimension 150 mm x 150 mm x 150 mm in layers of 50 mm thick. Each layer was compacted with not less than 35 strokes per layer using a tamping rod so as to avoid any voids.

The top surface was leveled and smoothed with a trowel. The specimens were marked for identification and stored in moist air for 24 hours and later removed from the moulds. Compressive strength test was performed after curing the samples for 7 days, 14 days and 28 days using compression testing machine (Figure 3).



Figure 3. The compression testing machine

The specimens were aligned centrally on the base plate of the machine and the movable portion of the machine was rotated gently by hand so that it touches the top surface of the specimen. Load was applied gradually without shock and continuously at the rate of 140kg/cm<sup>2</sup>/minute till the specimen fails. The maximum load was recorded and any unusual features in the type of failure were noted.

## RESULTS AND DISCUSSIONS

The results of the compressive strength obtained for M40 grade of concrete were shown in Table 2. It showed that as the age advances, the compressive strength and weight of concrete cubes increases.

The target mean compressive strength ( $f_t$ ) expected at 28 days is given by equation 1;

$$f_t = f_{ck} + 1.65 S \quad (1)$$

where  $f_{ck} = 40 \text{ N/mm}^2$  and

$S$  = standard deviation for each grade of concrete, taken as 5.0 for grade M40 obtained IS 456:2000

From equation 1, expected target compressive strength of concrete is given as;

$$f_t = 40 + 1.65 \times 5 = 48.25 \text{ N/mm}^2$$

The percentage change in compressive strength was less than 18% for all the partially replaced GRH and RHA in relation to the control mix. The control mix at 28 days had the highest weight of concrete cube at 84.07N and the lowest weight was 20% RHA partial replacement at 7 days having a weight of 67.00N.

The compressive strengths for 5% RHA partial replacement were more than the control mix at all age. At 10% RHA partial replacement, compressive strength was also higher than the control mix at 28 days. The maximum compressive strength recorded was 52.41 N/mm<sup>2</sup> for 5% RHA partial replacement, an increase of 6.81% over the control mix at 28 days.

The compressive strength of 5% GRH partial replacement was slightly decreased by 5.79% at 28 days, 9.25% at 14 days and 4.9% at 7 days. The minimum compressive strength results was 40.53 N/mm<sup>2</sup> at 28 days for 20% RHA partial replacement, a decreased of 17.40% compared with the control mix.

Table 2. Weight and Compressive Strength of Concrete Cubes at Grade M40

Replacement (%)	Weight (N)	Age (days)	Compressive Strength (N/mm <sup>2</sup> )	Percentage Change in Compressive Strength (%)	Change Indicator
0%	78.48	7	40.44	-	-
0%	81.62	14	43.02	-	-
0%	84.07	28	49.07	-	-
5% GRH	75.84	7	38.45	4.9	Negative
5% GRH	77.23	14	39.04	9.25	Negative
5% GRH	79.79	28	46.23	5.79	Negative
10% GRH	68.47	7	35.87	11.30	Negative
10% GRH	69.62	14	37.91	11.88	Negative
10% GRH	73.87	28	45.47	7.34	Negative
5% RHA	79.62	7	42.88	6.03	Positive
5% RHA	81.83	14	49.78	15.71	Positive
5% RHA	84.20	28	52.41	6.81	Positive
10% RHA	71.62	7	38.09	5.81	Negative
10% RHA	75.83	14	42.58	1.02	Negative
10% RHA	77.20	28	50.24	2.38	Positive
20% RHA	67.00	7	33.24	17.80	Negative
20% RHA	69.51	14	35.42	17.67	Negative
20% RHA	71.96	28	40.53	17.40	Negative

### COMPARISON OF COMPRESSIVE STRENGTH OF CONCRETE

Comparative results of the compressive strength obtained for the GRH partial replaced concrete and control mix were displayed in Figure 4, it indicated that at both 5% and 10% partial replaced GRH, the compressive strength were close to the results of the control mix as the coefficient of determination  $R^2 = 0.9492$  and  $0.9915$  respectively.

Figure 5 showed that the compressive strength results of the partial replaced RHA were compared well with the control mix, at  $R^2 = 0.7857$ ,  $0.9938$ , and  $1$ , for 5%, 10% and 20% RHA

respectively, and also indicated that RHA partial replaced concrete at 20% can be predicted without error from the control mix at  $R^2 = 1$ .

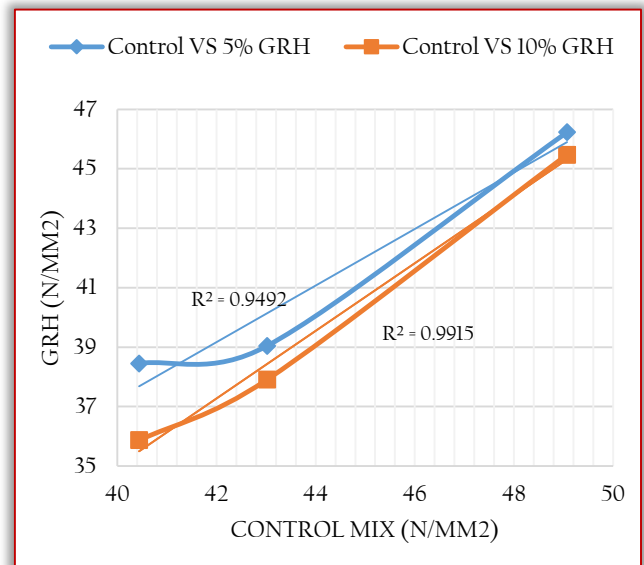


Figure 4. Comparative of Compressive strength (GRH vs. Control Mix)

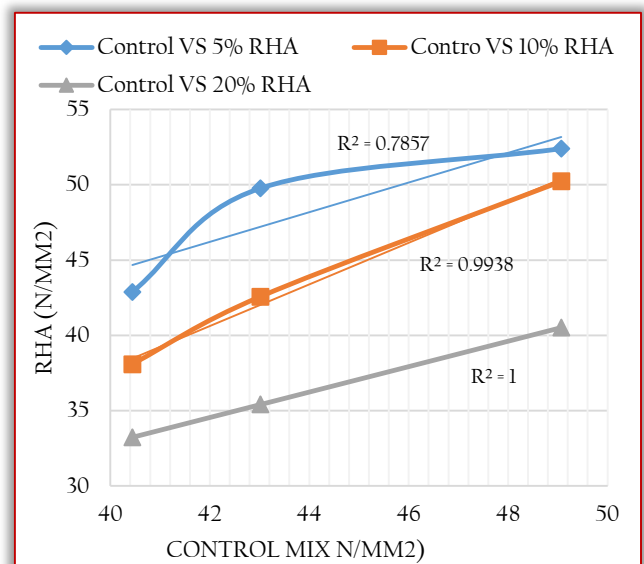


Figure 5. Comparative of Compressive Strength (RHA vs. Control Mix)

### CONCLUSION

Based on experiments and test results on fresh and hardened concrete the it was established that addition of GRH at 5% and RHA at 5% and 10% partial replacement of cement made concrete becomes cohesive and more plastic and thus permits easier placing and finishing of concrete. It also increases workability of concrete. The target compressive strength attained at 28 days for 5% and 10% RHA concrete cubes were above the target characteristic compressive strength of 48.25 N/mm<sup>2</sup> for M40 grade. Replacement of cement at 5% RHA gave the optimum compressive strength of 52.41 N/mm<sup>2</sup> at 28 days age. The utilization of RHA and GRH hold promising prospects in the country because it softens the impact on the environment and capital cost of the structure.

## References

- [1] Neville A.M., *Properties of Concrete*, 4<sup>th</sup> Edition, Asia, Person Education Pte. Ltd. 2006.
- [2] Udoeyo F.F., Sawdust Ash as Concrete Materials, *Journal of Material in Civil Engineering*, Vol. 14(2), pp. 173-176, 2002.
- [3] Smith R.G. and Kamwanja G.A., Baghdad. The Use of Rice Husk for Making a Cementitious Material, *Proc. Joint Symposium on the Use of Vegetable Plants and their Fibers as Building Material*, 1986.
- [4] Siddique R., Rice husk ash, In: *Waste materials and by-products in concrete*, Springer, pp.235-264, 2008.
- [5] Anwar M., Miyagawa T., and Gaweesh M., Using rice husk ash as a cement replacement material in concrete. In the *Proceedings of the 2001 first international Ecological Building Structure Conference*. pp. 671- 684, 2001.
- [6] Tashima G.A., *Brighter and brighter Picture of Agriculture. Vietnam Economy*, 2005.
- [7] Zhang M.H., and Mohan M.V., High-Performance Concrete Incorporating Rice Husk Ash as a Supplementary Cementing Material. *ACI Materials Journal*. Vol. 93(6): pp.629-636, 1996.
- [8] Nicole P.H., Monteiro P.J.M., and Carasek, H., Effect of Silica Fume and Rice Husk Ash on Alkali-Silica Reaction. *Materials Journal*. Vol.97 (4): pp. 486-492, 2000.
- [9] Sakr K., Effects of Silica Fume and Rice Husk Ash on the Properties of Heavy Weight Concrete. *Journal of materials in civil engineering*. Vol. 18 (3): pp.367-376, 2006..
- [10] Sata V., Jaturapitakkul C., and Kiattikomol K., Influence of pozzolan from various by-product materials on mechanical properties of high-strength concrete. *Construction and Building Materials*. Vol. 21(7): pp.1589–1598, 2007.
- [11] Mehta P.K., Pozzolanic and cementitious by-products as mineral admixtures for concrete - A critical review, *ACI Special Publication Vol.79*; pp.1-46, 1983.
- [12] Bui D.D., Rice husk ash as a mineral admixture for High Performance Concrete, PhD Thesis, Delft University of Technology, Delft, 2001.
- [13] Cook D., *Rice husk ash cements: their development and applications*, United Nations Industrial development organization, Vienna, 1984.
- [14] Mehta P.K., Rice husk ash - a unique supplementary cementing material, *Advances in Concrete Technology* (2nd edition), pp.419-444. CANMET, V.M. Malhotra (eds), 1994.
- [15] Mehta P. K., and Pirth, D., Use of rice husk ash to reduce temperature in high strength mass concrete. *ACI Journal Proceedings*, Vol.75: pp.60-63, 2000.
- [16] Mehta P.K., High performance, high volume fly ash concrete for sustainable development. In: *Proceedings of the International Workshop on Sustainable Development and Concrete Technology*, University of California, Berkeley, USA, 2004.
- [17] IS: 456. Indian Standard code book for RCC design guidelines, 4th Edition. Bureau of Indian Standards (BIS) New Delhi India, 2000



ISSN: 2067-3809

copyright © University POLITEHNICA Timisoara,  
Faculty of Engineering Hunedoara,  
5, Revolutiei, 331128, Hunedoara, ROMANIA  
<http://acta.fih.upt.ro>

<sup>1</sup>.P. Jaya PRAKASH, <sup>2</sup>.S. Sunil Kumar REDDY

# STUDY ON DI DIESEL ENGINE SUBSTITUTED WITH GROOVED PISTON AND POWERED USING NANO ADDITIVE BIODIESEL

<sup>1,2</sup>Department of Mechanical. Engineering, Siddharth Institute of Engineering & Technology, Puttur, AP, INDIA

**Abstract:** Economic and social transformation of people is leading to urbanization of a country. It becomes necessary to have good transportation facilities for a better life of the people in urban areas. Majority of transport vehicles in the transportation sector are equipped with the diesel engines due to their high efficiency. Dependency and utilization of these vehicles is increasing, as such the demand for petroleum products is also on high. On the other side because of high emissions from the diesel engines, strict regulations are laid by the governments to the engine manufacturers to reduce emissions and save the environment from the pollution. Researchers are always in the processes of finding a suitable alternate fuel such as biofuels produced from Jatropha oil, Pongamia oil, Rice bran oil, Corn oil, Neem oil etc. Jatropha biodiesel properties are near similar to that of diesel fuel. With or without minor changes in the diesel engine, Jatropha biodiesel can be used as an alternate fuel in existing diesel engine. One of the major drawbacks of Jatropha biodiesel is its flow characteristics, to overcome this problem nano additive (Aluminum oxide) is added to the Jatropha biodiesel to enhance the flow properties of the biodiesel. In the present work, the performance and emissions of diesel engine are investigated with biodiesel 20% by volume (B20) added with the Nano additive in quantities of 50 ppm, 100 ppm and 150 ppm. B20 biodiesel blend with 100 ppm nano additive showed better performance compared to diesel. Performance of the diesel engines depends upon the formation of homogeneous mixture and turbulence inside the combustion chamber. To investigate on this, engine is fitted with piston consisting of grooves that are created on its crown to enhance turbulence of biodiesel fuel in the combustion chamber. Diesel engine showed better performance fitted with rhombus grooved piston (RGP) fuelled with B20 blend biodiesel added with 100 ppm aluminum oxide Nano additive.

**Keywords:** Rhombus grooved piston (RGP), Jatropha biodiesel, Al<sub>2</sub>O<sub>3</sub> Nano additive, Brake thermal efficiency, Emissions

## INTRODUCTION

Diesel engines have been utilized as work horses for the industry from over a long period. This is due to their high torque output, durability, exceptional fuel economy and ability to provide power under a wide range of conditions. The consumption and demand of petroleum products are increasing day by day with increase in number of vehicles due to urbanization, the immediate effect of this change is leading to higher emissions of pollutants into the environment. To address this problem it becomes necessary to decrease the consumption and emissions of petroleum products. For this one solution is to substitute the petroleum products with the alternative fuels. The alternative fuels can be produced as per the demand and are environmental friendly. Current world energy dependency on fossil fuels is taking a gradual change and the situation is such where entire focus is on alternate methods of energy sources, one such source where more and more that is explored is on the usage of alternate fuels. On the other side which is hindering its dependability is lower heating value of alternative fuels so it is tried upon to overcome this by adding metal oxide Nano particles. With this biodiesel enhances the engine performance as well reduce the harmful gases from engine exhaust. Many researches had tried on Jatropha oil as a suitable substitute for diesel and confirmed that a slight increase in diesel engine efficiency with minor changes in diesel engine. Other issues like high viscosity of Jatropha oil affecting the flow capacity of oil is addressed by adopting blending process with diesel. It is also reported that adding aluminum oxide Nano particles to Jatropha biodiesel could enhance the ignition properties of biodiesel due to the heat buildup with in the fuel of sensitive

nature of aluminum Oxide Nanoparticles. Size of Nano particles may also affect the parameters like combustion process, ignition delay and burning rates of fuel.

## LITERATURE REVIEW

Considerable quantity and quality of research work has been done on diesel engines fuelled with biodiesels with minor engine modifications. Some of them are referred and their analysis and inference of their works are presented below.

S.Chiranjeeva Rao, et al. [1] examined the effect of diesel, M20 (20% Mahua Methyl Ester + 80% Diesel), M50 (50% Mahua Methyl Ester + 50% Diesel), M20+50CeO<sub>2</sub> (20% Mahua Methyl Ester + 80% Diesel+50 ppm of Cerium Oxide Nano additive) and M20+100CeO<sub>2</sub> (20% Mahua Methyl Ester + 80% Diesel+100 ppm of Cerium Oxide Nano additive). A single cylinder, four stroke, water cooled DI diesel engine is used for this experiment. The experiments are conducted at a constant speed of 1500 rpm by varying loads. From his findings it is noted that M20+50CeO<sub>2</sub> shows a better performance compared to diesel. The Brake thermal efficiency is increased up to 9% and SFC decreased compared to diesel at 12 Kg load. The emission NO<sub>x</sub> is increased and other emissions (HC, CO and Smoke) are decreased at full load condition (12 Kg). V.Karthickeyan, et al. [2] studied the influence of Diesel, B10 (10% Waste Cooking Palm oil+ 90% Diesel) and B20 (20% Waste Cooking Palm oil+ 80% Diesel) in single cylinder, four stroke, water cooled DI diesel engine. A thermal barrier with PSZ (partially stabilized zirconia) is coated in combustion chamber on piston crown, piston head, inlet valve and exhaust valve by using plasma spray coating technique. The experiment is carried at constant speed of 1500 rpm by varying loads. At full load condition results show

that brake thermal efficiency increased by 0.4% with B20 compared to diesel in coated engine. The Brake specific fuel consumption is increased in both the engines with B20 compared to diesel. The CO emissions are lower by 0.05% volume in coated engine with B20 compared to diesel. The HC emissions are lower by 8ppm with B20 compared to diesel in coated engine. The NO<sub>x</sub> emissions are higher in coated engine for diesel, B10 and B20 compared to uncoated engine. B.Dhinesh, et al. [3], Investigated the effect of diesel, B100 (100% Cymbopogon flexuosus), B20(20% Cymbopogon flexuosus + 80% Diesel), B20+10ppm (20% Cymbopogon flexuosus + 80% Diesel +10ppm of Cerium Oxide), B20 + 20ppm (20% Cymbopogon flexuosus + 80% Diesel + 20ppm of Cerium Oxide) and B20 + 30ppm (20% Cymbopogon flexuosus + 80% Diesel+30ppm of Cerium Oxide).

A single cylinder, four stroke, water cooled DI diesel engine is used for his investigation. The Investigation is carried at constant speed of 1500rpm by varying loads. From his findings at full load conditions it is noted that the Brake thermal efficiency is increased by 4.76% with B20+20ppm compared to B20. The Brake specific fuel consumption is lowered with B20+20ppm compared to B20. The CO and HC emissions are lower by 12.5% volume and 4ppm with B20+20ppm compared to B20. The NO<sub>x</sub> and smoke are reduced by 3% and 6.6% with B20+20ppm compared to B20. A.Prabhu, et al. [4], examined the effect of diesel, B20(20% Jatropha + 80% Diesel), B20+10A+10C (20% Jatropha + 80% Diesel +10ppm of Aluminum Oxide + 10ppm of Cerium oxide), B20+30A+30C (20% Jatropha + 80% Diesel +30ppm of Aluminum Oxide + 30ppm of Cerium oxide) and B20+60A+60C (20% Jatropha + 80% Diesel +60ppm of Aluminum Oxide + 60ppm of Cerium oxide). A single cylinder, four stroke, water cooled DI diesel engine is used for this experiment.

The experiments are conducted at a constant speed of 1500 rpm by varying loads. From his findings at full load conditions it is noted that the Brake thermal efficiency is nearer with B20+30A+30C compared to diesel. The Brake specific fuel consumption is lowered with B20+30A+30C compared to diesel. The CO, HC, NO<sub>x</sub> and smoke are reduced by 6%, 3.3%, 1.3% and 3.2% with B20+30A+30C compared to B20. Bhupendra Singh chauhan, et al. [5], observed the effect of diesel, B5 (5% Jatropha + 95% Diesel), B10 (10% Jatropha + 90% Diesel), B20 (20% Jatropha + 80% Diesel), B30 (30% Jatropha + 70% Diesel) and B100 (100% Jatropha). A single cylinder, four stroke, air cooled DI diesel engine is used for his experiment.

The experiments are conducted at a constant speed of 1500 rpm by varying loads. From his findings at full load conditions it is noted that the Brake thermal efficiency is lower in Jatropha biodiesel blends compared to diesel. The Brake specific fuel consumption is higher with Jatropha biodiesel blends compared to diesel. The CO, HC and Smoke emissions are lower with Jatropha biodiesel blends compared to diesel. The NO<sub>x</sub> emissions are increased with Jatropha biodiesel

blends compared to diesel. R.Vallinayagam, et al. [6], investigated the effect of diesel and Pine oil in characteristics study of pine oil in a single cylinder, four strokes, and water cooled DI diesel engine. The investigations are carried out at constant speed of 1500rpm by varying loads. From the results at full load conditions, they observed that HC, CO and Smoke emissions are reduced by 30%, 65% and 70%. M.J. kao, et al. [7], studied the effect of the diesel and addition of Aluminum nanoparticle to diesel along with 3-6% volume of water.

A single cylinder, four stroke, water cooled DI diesel engine is used for his experiment. The experiments are conducted at a constant speed of 1500 rpm by varying loads. From his findings at full load conditions it is noted that there is significant improvement in brake thermal efficiency and also reduction in smoke and nitrous oxide. Arockiasamy, et al. [8], conducted an experimental analysis using diesel, alumina nanoparticle with jatropha biodiesel in single cylinder, four strokes, water cooled DI diesel engine. The experiments are conducted at a constant speed of 1500 rpm by varying loads. From his analysis at full load conditions it is noted the HC, CO, NO<sub>x</sub> and smoke are reduced.

#### PRODUCTION OF JATROPHA OIL

The Jatropha plant is known for its adaptability to different climatic conditions and the oil productivity of the Jatropha seeds. Preparation of Jatropha oil is shown with the flow chart diagram in Figure 1 below.

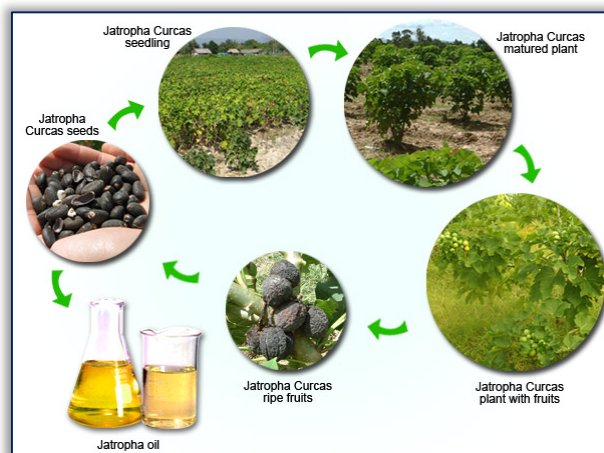


Figure 1. Flow chart for production of Jatropha oil

#### EXPERIMENTAL WORK

In the present experimental work, four stroke single vertical cylinder type, water cooled, constant speed diesel engine is equipped with AVL flue gas analyzer system and smoke meter is used. Aluminum oxide nano particle powder is the additive mixed in Jatropha blended biodiesel. Engine operated at a constant speed of 1520 rpm, fuel injected at 23.4° before TDC (Top Dead Centre), and a continuous load tests were carried out for different loads. To measure its output, belt type brake dynamometer is fitted to engine. Data was collected under steady state conditions and results were evaluated for analyzing performance and emission characteristics of the diesel engine with modified piston fuelled with biodiesel mixed with additive. The investigation setup for experimental

tests is shown in below Figure 2. The specifications of the engine and properties of fuel and Nano additive is shown in the below Tables 1,2& 3.



Figure2. Experimental Setup

Table 1. Technical Specifications of the Engine

Make	Kirloskar
Type	Four-stroke, Single cylinder diesel engine (Water cooled)
Rated power output	5HP,1500 RPM
Bore & Stroke	80mm x 110mm
Compression Ratio	16.5:1
Dynamometer	Belt brake
Emissions	AVL Gas analyzer

Table 2. Properties of Diesel and Jatropa biodiesel

Sl.No	Properties	B20	Jatropa	Diesel
1	Density (Kg/m <sup>3</sup> )	856	880	850
2	Viscosity (mm <sup>2</sup> /s)	3.0	4.8	2.6
3	Flash Point (°C)	73.4	127	60
4	Fire Point (°C)	77.4	131	64
5	Calorific Value (MJ/Kg)	41.5	39.2	43

Table 3. Properties of Al<sub>2</sub>O<sub>3</sub> powder

S. No.	Properties	Aluminum oxide
1	Density (Kg/m <sup>3</sup> )	3900
2	Molecular Weight (g/mol)	101.96
3	Appearance	White solid
4	Melting Point (°C)	2000

Biodiesel is a mixture of Jatropa oil mixed with diesel in different proportions. Magnetic stirrer is used for uniform mixing of both the oils.

Next step in this process is addition of Nano additive to the biodiesel. For this Ultrasonication process is employed. Ultrasonicator is a device known for fast agitation and homogeneous mixing of particles with help of sound waves. Ultrasonicator is set to a frequency of 40 kHz and 120W and operated for a period of 60 minutes so that Aluminum oxide nano powder is thoroughly mixed with Jatropa biodiesel to form very small clusters in a selected sample. This process is utilized to prepare different B20 blends of biodiesel with mass fractions of 50 ppm, 100 ppm and 150 ppm of Aluminum oxide nano particles. Finally engine fuel is a B20blend (80% diesel+20% Jatropa biodiesel ) added with aluminum oxide nano powder in the quantity fraction of 50 ppm, 100 ppm and 150 ppm. Performance and emission characteristics of diesel engine fuelled with these fuels are compared with diesel. B20 blend with 100ppm proved with better a result which was further investigated with modified piston.

## — Replacement of Piston in the Engine

In-cylinder air motion in internal combustion engines has its own significance which shows its influence on the combustion process. It governs the fuel-air mixing and burning rates in diesel engines. To obtain a better combustion with lesser emissions in diesel engines, it is necessary to reach a good longitudinal distribution of the injected fuel throughout the full space of chamber. This requires matching of the fuel sprays with combustion chamber geometry. In other words, the combustion chamber geometry, fuel injection and gas flows are the most critical factors for getting a better combustion.

In DI diesel engines compression induced squeeze flow increases turbulence which in turn increases the rate of fuel-air mixing ultimately reducing the combustion spell. Since the flow in the combustion chamber develops from interaction of the intake flow with the in-cylinder geometry, the goal of this work is to characterize the role of combustion chamber geometry on in-cylinder flow, fuel-air mixing and combustion processes. For this six rhombus grooves were created on the crown of the piston to vary the air turbulence in the engine cylinder.

Performance parameters such as brake power, specific fuel consumption and thermal efficiency are calculated based on experimental results.

## — Rhombus Grooved Piston (RGP):

Dimensions of rhombus groove machined on the piston crown are given below and modified piston is shown in the Figure 3 below:

- Length of the diagonal 1 = 10mm
- Length of the diagonal 2 = 5mm
- Depth of the groove = 2mm
- Number of grooves to be made = 6 No's
- Angle between consecutive grooves = 60°



Figure 3.Top view of the Rhombus Grove Piston Crown

## RESULTS AND DISCUSSIONS

### — Performance Characteristics

Performance and emissions data of the diesel engine fitted with normal aluminum piston and RGP of aluminum material fuelled with both diesel and B20 blend biodiesel added with 100ppm aluminum oxide nano powder are collected and compared. Based on data at full load conditions, graphs are plotted for analysis.

### » Brake Thermal Efficiency

The variation of brake thermal efficiency with brake power is given in figure 4. The brake thermal efficiency of the diesel engine fitted with RGP increased by 1.72% compared to normal piston when fuelled with diesel. In the other case brake thermal efficiency of the diesel engine fitted with RGP increased by 3.7% compared to normal piston when fuelled with B20 blend Jatropha biodiesel with 100ppm  $Al_2O_3$  nano additive.

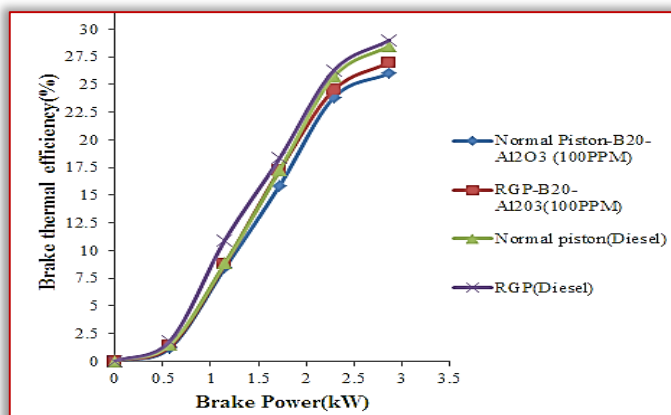


Figure 4. Variation of Brake thermal efficiency with B.P

Turbulence characteristics improved with the RGP due to presence of grooves on piston crown that enhances the combustion with the formation of homogeneous mixture and oxygen content in biodiesel compared to normal piston.

### » Specific Fuel Consumption

The variation of Specific fuel consumption with brake power is given in figure 5. The Specific fuel consumption of the diesel engine fitted with RGP decreased by 1% compared to normal piston when fuelled with diesel. In the other case Specific fuel consumption of the diesel engine fitted with RGP decreased by 3.2% compared to normal piston when fuelled with B20 blend Jatropha biodiesel diesel with 100ppm  $Al_2O_3$  Nano additive. Grooved piston enhances fuel combustion releasing more power that is less fuel more power so this reduces specific fuel consumption. Additionally with the grooved piston the weight of the piston is reduced which adds to decrease in the specific fuel consumption.

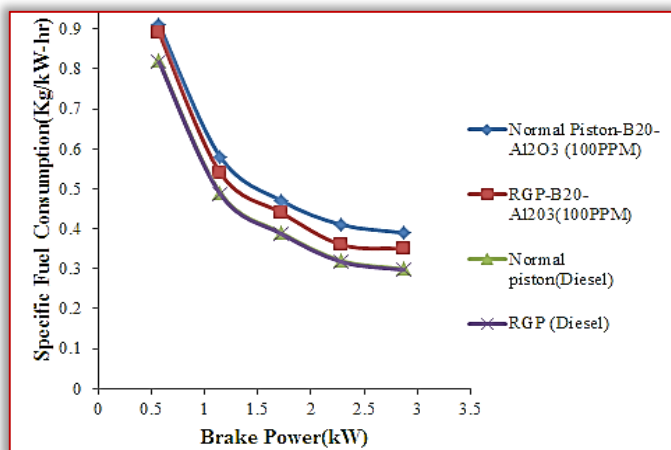


Figure 5. Variation of Specific fuel consumption with B.P

### » HC Emissions

The variation of HC emissions with brake power is shown in figure 6.

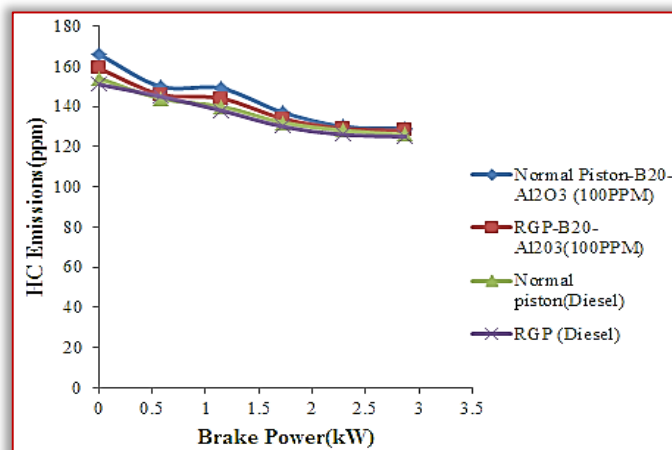


Figure 6. Variation of HC Emissions with B.P

The creation of HC emissions is due to the wall quenching, inappropriate mixing and incomplete combustion. With the turbulence in the combustion chamber standardized mixture forms which leads for the complete combustion and higher temperatures in the chamber.

As more oxygen content is available with the diesel in RGP, the HC emissions are decreased by 0.79% in grooved piston compared to normal piston with diesel.

### » CO Emissions

CO emissions with brake power are detailed in figure 7. The formation of CO emissions is due to the incomplete combustion and lack of sufficient oxygen content with the fuel. With the higher inherent oxygen content in the diesel, the carbon monoxide emissions formed will be oxidized and converts into carbon dioxide gas. Hence the CO emissions are decreased by 6.7% with grooved piston compared to normal piston with diesel. In grooved piston the air fuel ratio is equal to the stoichiometry air fuel ratio and also due to presence of grooves on piston crown the air gets turbulence throughout the combustion chamber, the complete combustion takes place in the combustion chamber. So the CO emissions are decreased in RGP compared to normal piston.

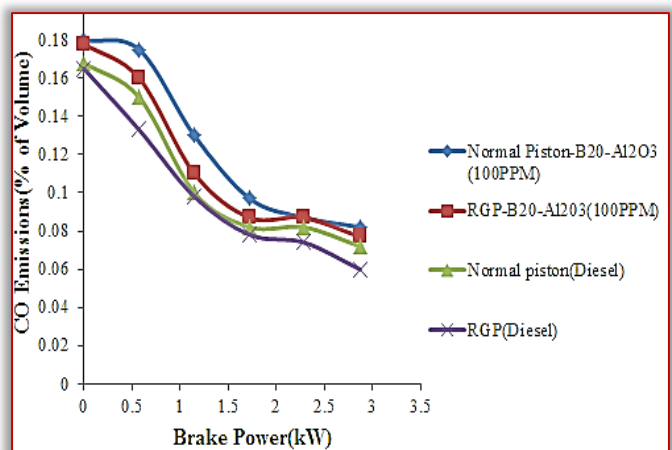


Figure 7. Variation of CO Emissions with B.P

### — NO<sub>x</sub> Emissions

NO<sub>x</sub> emissions with brake power are shown in figure 8.

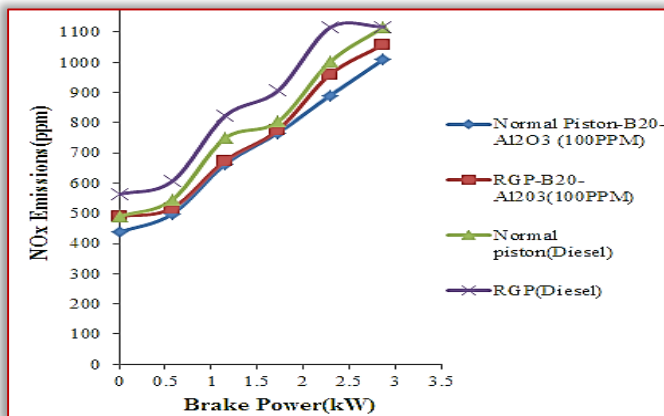


Figure 8. Variation of NO<sub>x</sub> Emissions with B.P

At lower temperatures nitrogen acts as an inert gas and will be active at higher temperatures. With the grooved piston, there is good turbulence and homogeneous mixture formation in the combustion chamber. Hence the heat produced is more and with the higher oxygen content the NO<sub>x</sub> emissions are increased by 0.13% in grooved piston compared to normal piston with diesel.

### CONCLUSIONS

The performance and emission characteristics of diesel engine with normal piston fuelled with diesel and also with B20 blend Jatropha biodiesel added with Al<sub>2</sub>O<sub>3</sub> Nano additive are investigated in the first phase. Later similar procedure is adopted with rhombus grooved piston (RGP) and further investigations are carried out. The conclusions are as follows.

- Brake thermal efficiency of diesel engine fitted with RGP is more because of complete combustion in the chamber compared to normal piston.
- The Specific fuel consumption of diesel engine fitted with RGP decreased compared to normal piston.
- HC emissions of diesel engine fitted with RGP decreased compared to normal.
- CO emissions also decreased when normal piston is replaced by RGP.

With the higher temperature in chamber, the NO<sub>x</sub> emissions increased in case of RGP compare to normal piston.

### References

- [1] S. Chiranjeeva Rao, et al., Influence of Nano added MME blends on CI engine based on DOE concept, IJMET, Volume 8, issue 7, July 2017, PP 860-868.
- [2] V. Karthickeyan, et al., Environmental effect of thermal barrier coating with waste cooking palem oil methyl ester blends in a diesel engine, Biofuels, April 2017, PP. 1759-7269.
- [3] R. Dhinesh, et al., An experimental analysis on the influence of fuel borne additives on the single cylinder diesel engine powered by cymbopogon flexuosus biofuel, Journal of Energy Institute, April 2016, PP. 1-12.
- [4] A. Prabhu, et al., Emission control strategy by adding Alumina and Cerium oxide Nano particle in biodiesel,

Journal of Energy Institute, March 2015, PP. S1743-9671(14) 20316-3.

- [5] Bhupendra Singh chauhan, et al., A study on the performance and emission of a diesel engine fuelled with Jatropha biodiesel oil and its blends, Journal of Energy Institute, Volume 37, November 2011, PP. 616-622.
- [6] R. Vallinayagan, et al., Combustion Performance and Emission characteristics study of Pine oil in a diesel engine, Renewable Energy, volume 57, 2013, PP. 344-355.
- [7] M.J. Kao, et al., Aqueous Aluminum Nano fluid combustion in diesel fuel, J. Test Evaluation, Volume 36, 2008, PP. 1-5.
- [8] Prabhu Arackiasamy, et al., Performance, combustion and emission characteristics of a DI diesel engine fuelled with Nano particle blended Jatropha biodiesel, Polytechnic Mechanical Engineering, volume 59, issue 2, 2015, PP.88-93



ISSN: 2067-3809

copyright © University POLITEHNICA Timisoara,  
Faculty of Engineering Hunedoara,  
5, Revolutiei, 331128, Hunedoara, ROMANIA  
<http://acta.fih.upt.ro>

# Fascicule 4

## [October - December]

t o m e

# [2018] XI

**ACTA**Technica**CORVINIENSIS**  
BULLETIN OF ENGINEERING



**ISSN: 2067-3809**

copyright © University POLITEHNICA Timisoara,  
Faculty of Engineering Hunedoara,  
5, Revolutiei, 331128, Hunedoara, ROMANIA  
<http://acta.fih.upt.ro>

<sup>1</sup>B.S. LUKA, <sup>2</sup>J.A. JAPHET, <sup>3</sup>P.A. DAUDA

## SINGLE LAYER DRYING CHARACTERISTICS OF HOSPITAL TOO FAR LEAVES (*JATROPHA TANJORENSIS*) UNDER OPEN SUN AND IN SOLAR DRYER

<sup>1</sup>Department of Food Science and Technology, Federal University Wukari, Taraba State, NIGERIA

<sup>2</sup>Department of Mechanical Engineering, University of Jos, Plateau State, NIGERIA

<sup>3</sup>Department of Agricultural and Bioresource Engineering, Taraba State University Jalingo, Taraba State, NIGERIA

**Abstract:** The desire for cheap and proper drying methods, the need to obtain quality dried products and understanding of drying parameters of leafy vegetables have necessitated the evaluation of drying methods. In this study, Hospital too far leaves were obtained and cleaned with distilled water. The leaves were divided in two samples each weighing 20grams. The first sample was spread in a single layer on a mesh wire attached to a rack under open sun and the second sample was also spread in single layer on drying mesh of a solar dryer. The drying starts from 8:00 am to 4:30pm. Weights of the samples were measured after every 30 minutes. Ambient air temperature and drying chamber temperature were also measured. Moisture diffusivity coefficient was found to vary from  $3.55 \times 10^{-8}$  to  $4.22 \times 10^{-7}$  and  $3.55 \times 10^{-8}$  to  $3.94 \times 10^{-7}$  for open sun dried sample and solar dried samples respectively. The experimental drying curves exhibit only falling drying rate period. Solar drying method has shorter drying time against open sun drying method. Nine mathematical models were fitted to the experimental drying curves. The Page model was found to decently describe both open sun drying curve and solar drying curve.

**Keywords:** drying curves, effective moisture diffusivity, mathematical drying models

### INTRODUCTION

Hospital too far belongs to the family Euphrobiaceae and show physical appearance akin to *Jatropha Gossypifolia* and *Jatropha Curcas* (Parabakan and Siyatha, 1999). The plant originates from Central America and is very popular in Mexico, it has been introduced in the United State of America as potential leafy vegetable and or as medicinal plant (Kuti, 1996). In Nigeria, the leaf is popularly called 'Ugu oyibo' in the east and 'lyana ipaja' in the west, predominantly consumed as leafy vegetable and medicament for diabetes mellitus, treatment of malaria, blood building herb, antioxidant and supports spermatogenesis (Olayiwola *et al.*, 2004; Mordi and Akanji, 2012; Gilbert, 2017; Omigie *et al.*, 2013; Osuchukwu *et al.*, 2016).

Drying increases the shelf life of farm produce by reducing the moisture content to a safe level. In Nigeria, fruits and vegetables are largely dried under open sun to harness the abundant solar radiation, however, open sun drying predisposes food to potential contaminant, rain damage and characterised by variation in drying time (Werner and Josef, 2012) and is not suitable for vegetables at temperatures below 30°C because they contain lower sugar and acid; this increases the risk for food spoilage (Naseer *et al.*, 2013), solar dryers made up the shortcomings of open sun by providing increased drying temperature and lower humidity at the drying chamber thus providing more marketable products and efficient drying alternative to open sun (Werner and Josef, 2012) however, the geometry of the product also affects its drying rate (Lewicki, 2006) thus, vegetables and fruits are better dried in thin layer or single layer (Mursalim and Dewi, 2002). During crude organic compounds extraction from leaves especially for medicinal purposes, the

leaves need to be dried for easy pulverization to obtain larger surface area and to obtain compounds in their natural and unaltered state due to inhibited biochemical reaction (Ravi, 2015).

Some studies carried out on the drying behaviour of some leaves under different drying conditions are documented in the literature: Vernonia amygdalina leaves (Alara, Abdulrahman and Olalere, 2017) Mint, Parsely and Basil leaves (Akpınar, 2006), Coriander leaves (Ahmed and Singh, 2001), Peppermint leaves (Alireza, 2016). Aramant leaves (Papu *et al.*, 2014) and red chilly leaves (Subahana *et al.*, 2014) However, no study was reported on the drying characteristics of hospital too far leaves, thus the experimental investigation of the effective moisture diffusivity coefficient, drying curve and mathematical modelling of drying curves of hospital too far leaves forms the objectives of this study.

### MATERIALS AND METHOD

Hospital too far leaves were detached from the plant, the leaves were then washed with distilled water to rid it of any dust or dirt and were allowed to rid off the water under ambient condition. The leaves' thickness was measured using SONGQI SQ-SXQFC25 digital micrometer screw gauge at different locations and the average was computed. The leaves were detached from the stalk and were divided into two samples weighing 20 grams each. The first sample was spread on mesh wire fixed to a rack forming single layer under open sun, the second sample was placed in a natural draft solar dryer chamber forming single layer on a mesh wire rack as well. The experiment started around 8:00 am and the mass of the leaves were measured after every 30 minutes till no further change in mass of the leaves was recorded, the air drying temperature under open sun and in the drying

chamber were measured using MexTech digital multi-thermometers and the changes in mass of the leaves were measured using KERRO BL3002 electronic compact scale with precision of  $\pm 0.01g$ .

The moisture content was computed using eq. 1 on wet basis

$$M_C = \frac{M_i - M_f}{M_i} \times 100 \quad (1)$$

$M_i$  is the mass of sample before drying;  $M_f$  is the mass of sample after drying

For the purpose of performing mathematical modelling to obtain model equation(s) that best describe the drying characteristics of hospital too far leaves, the moisture ratio was computed using eq. 2

$$MR = \frac{M_t - M_e}{M_o - M_e} \quad (2)$$

The drying rate was estimated using eq. 3:

$$\frac{dR}{dt} = \frac{M_t + dt - M_t}{dt} \quad (3)$$

$M_t$  is the moisture content at a particular drying time (%);  $M_e$  is the equilibrium moisture content (%);  $M_o$  is the initial moisture content (%);  $dt$  is the change in drying time;  $M_{t+dt}$  is the instantaneous moisture content as the drying time changes.

Nine (9) single layer drying models presented in Table 1 were fitted to the moisture ratio drying curves using MATLAB R2009b. Highest  $R^2$  and lowest MSE and RMSE values were used as the performance function of the models.

Table 1: Single layer mathematical models for describing drying characteristics

S/N	Model name	Model equation
1	Newton	$MR = \exp(-kt)$
2	Page	$MR = \exp(-kt^n)$
3	Henderson and Pabis	$MR = a \exp(-kt)$
4	logarithmic	$MR = a \exp(-kt) + b$
5	Approximation of difussion	$MR = a \exp(-kt) + (1-a) \exp(-kbt)$
6	Modified Henderson and Pabis	$MR = a \exp(-kt) + b \exp(-k_o t) + c \exp(-k_1 t)$
7	Midilli-Kucuk	$MR = a \exp(-kt^n) + bt$
8	Wang and Singh	$MR = 1 + at + bt^2$
9	Verma et al.	$MR = a \exp(-kt) + (1-a) \exp(-k_o t)$

## RESULT AND DISCUSSION

### – Drying Curves

For open sun and solar dried samples, as the drying temperature increases, the drying rate also increases and consequently the moisture content and moisture ratio decreases (Figs. 1, 2, 3, 5 and 6). It was observed that solar dried samples have shorter drying time compared to open sun dried sample, this was further substantiated by Midilli (2001) and Belghit *et al.*, (2000) with the explanation that this could be possible owing to higher drying chamber temperature and lower relative humidity (Fig. 3). The two samples reached their maximum drying rate at 43.64% (Open sun) and 27.76% (Solar dryer) moisture level at 270th minute drying time which was succeeded by falling drying rate period (Figs. 5 and 6), according to Earle and Earle (1966) at

the point of maximum drying rate followed by falling drying rate period, the water stops behaving as if it was a free water due to changes in energy binding pattern between the water molecules, thus negates a predominantly temperature controlled water diffusion to the surface of the leaves, hence, moisture content changes controls the drying rate. A similar drying result was reported by (Akpinar, 2011) for drying Parsley leaves under open sun and in solar dryer.

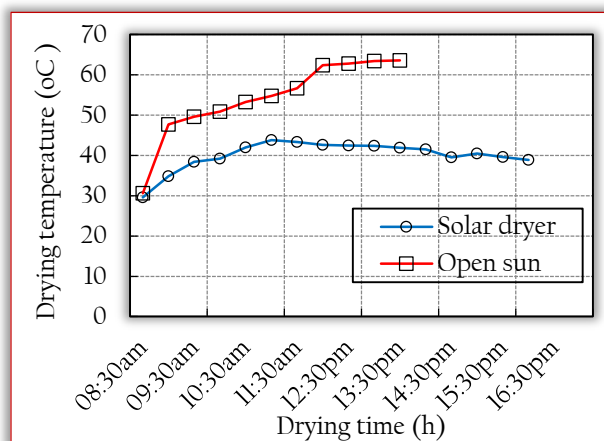


Figure 1. Variation of drying temperature with drying time

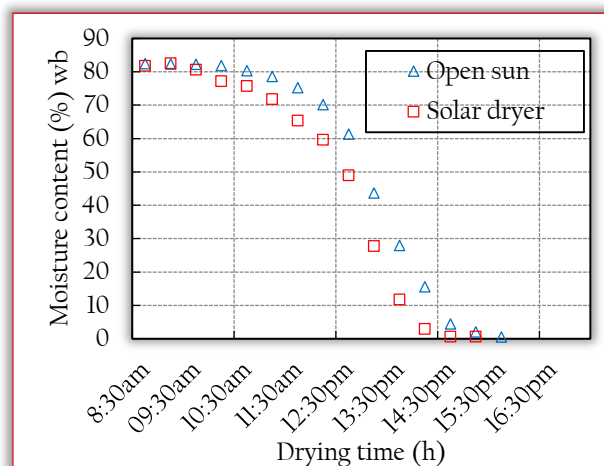


Figure 2. Variation of moisture content with drying time

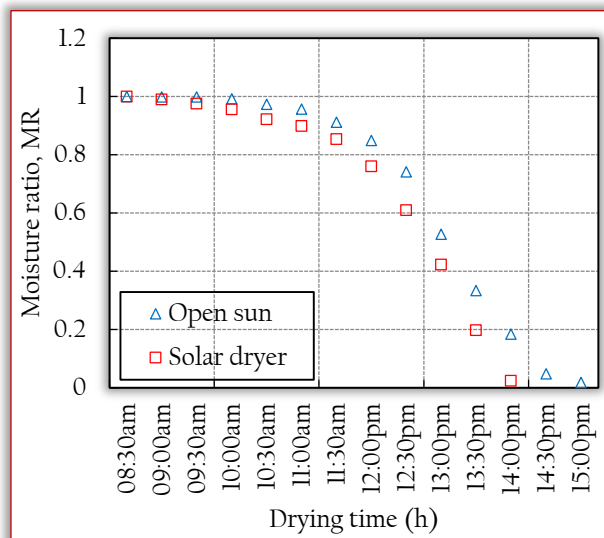


Figure 3. Variation of moisture ratio with drying time

It can also be seen from Figs. 5 and 6 that the drying rate curve of solar dried sample exhibits multiple negative and positive gradient at the early stage as moisture escapes the surface of the leaves, Keey (2011) imputed such behaviour to periodic discontinuities in drying causing selective moisture evaporation as the leaves' composition alters and also the build-up and cracking of the leaves' surface crust caused by disturbances (temperature changes during removal of samples from drying chamber) during sample weighing. The solar dried leaves appear greener to the eye against the open sun dried sample, this inferred superior product quality as more chlorophyll is retained in the leaves.



(a)



(b)



(c)

Figure 4. Fresh and dried hospital too far leaves: (a) fresh leaves sample; (b) open sun dried sample; (c) solar dried sample

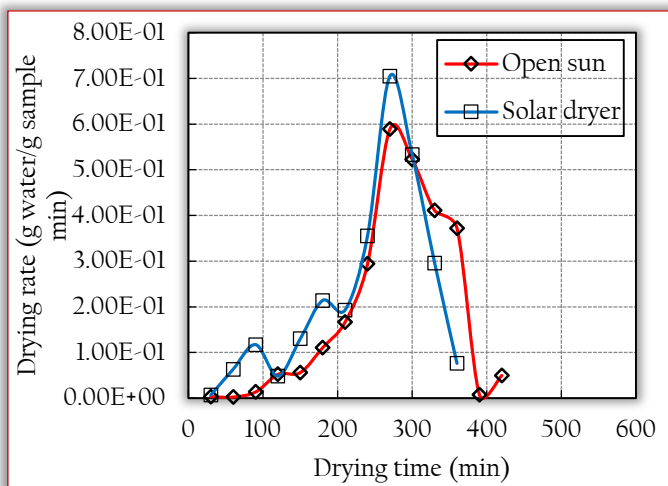


Figure 5. Plot of drying rate with changes in drying time

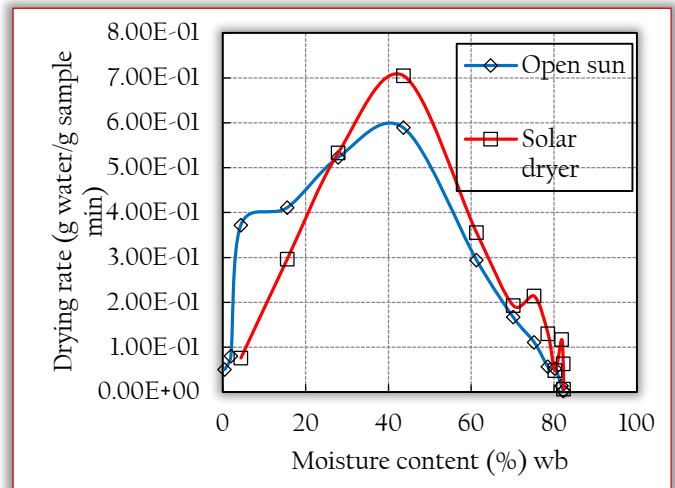


Figure 6. Variation of drying rate with changes in moisture content

#### — Effective Moisture Diffusivity ( $D_{eff}$ )

During food drying, drying takes place in either falling rate period or constant rate period and it is govern by heat and mass transfer. During falling drying period, the rate of moisture migration in hygroscopic and isentropic matters could be represented by effective moisture diffusivity (Wang *et al.*, 2007). Moisture diffusivity can be explained in terms of the magnitude of the molar flux through the surface of the drying material per unit moisture concentration gradient away from the plane geometry (COMSOL, 2017). Effective moisture diffusivity is dependent on temperature, moisture content, porosity of material and pressure (Abe and Afzal, 1997; COMSOL, 2017). However, explaining how mass transfer occur in fruits and vegetables is quite difficult hence, Fick's second law expressed in eq. 1 (Crank, 1975) is widely adopted to best describe the drying kinetics.

$$MR = \frac{8}{\pi^2} \sum_{n=1}^{\infty} \frac{1}{(2n+1)^2} \exp \left[ -\frac{(2n+1)^2 \pi^2 D_{eff} t}{4l^2} \right] \quad (4)$$

MR is the dimensionless moisture ratio,  $D_{eff}$  is the effective moisture diffusivity ( $m^2/s$ ),  $l$  is half the slab thickness of the material (m),  $t$  is the drying time (s) and  $n$  is the number of terms taken. Effective moisture diffusivity is determined by taking the slope of the plot of  $\ln MR/t$ , the slope is presented in eq. 5 (Lamharrar *et al.*, 2017).

$$K_o = \frac{\pi^2 D_{eff}}{4l^2} \quad (5)$$

In this study, the effective moisture diffusivity was estimated at a given moisture ratio, drying time and drying air temperature neglecting shrinkage in the leaves thickness. The leaves were assumed to be infinite slabs.

It can be seen in Figure 7, that the effective moisture diffusivity of Hospital too far leaves ranges from  $3.55 \times 10^{-8}$  to  $4.22 \times 10^{-7}$  and  $3.55 \times 10^{-8}$  to  $3.94 \times 10^{-7}$  for open sun dried sample and solar dried sample respectively. The values fall between  $10^{-7}$  to  $10^{-12}$  for food materials as reported in Ashton (2013), Dincer and Hussain (2002) and Hosain *et al* (2014). From Figures 8 and 9, at the initial stage, as drying temperature increases, the effective moisture diffusivity of both open sun dried sample and solar dried sample gradually increases, however, toward the end of the drying time, when drying

temperature changes was minimal and moisture content is low, diffusion coefficient increases sharply, this may signify that moisture content decrease results in vapour permeability increase (Hosain *et al.*, 2013).

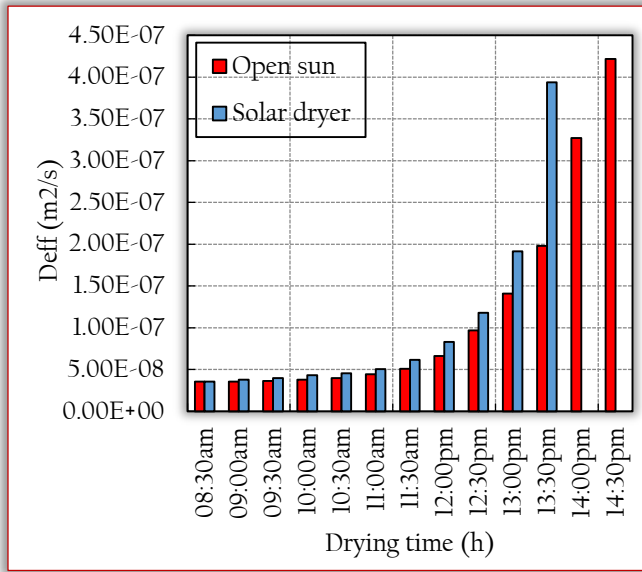


Figure 7. Plot of effective moisture diffusivity versus drying time

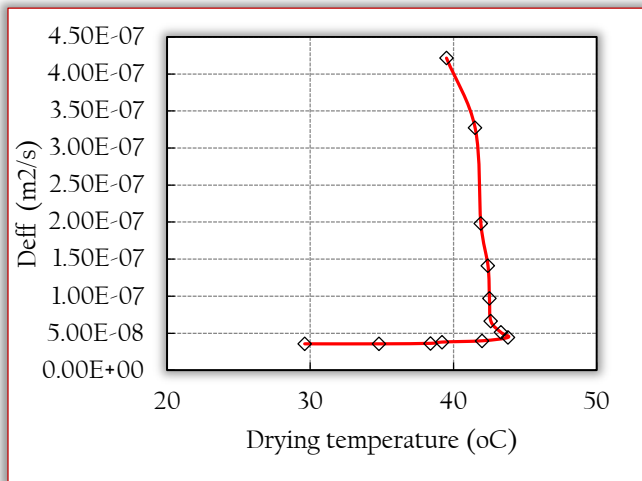


Figure 8. Variation of effective moisture diffusivity of open sun drying method with drying temperature

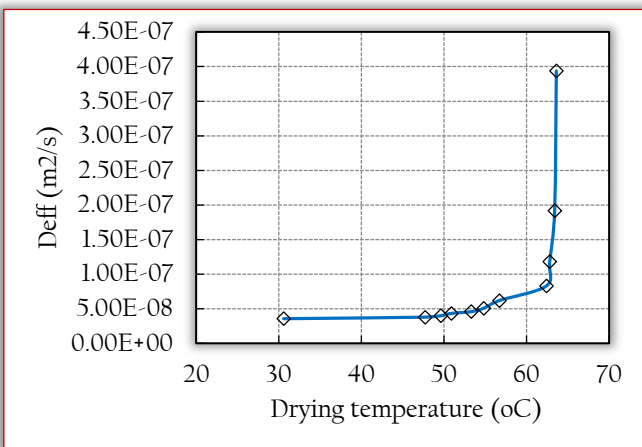


Figure 9. Variation of effective moisture diffusivity of solar drying method with drying temperature

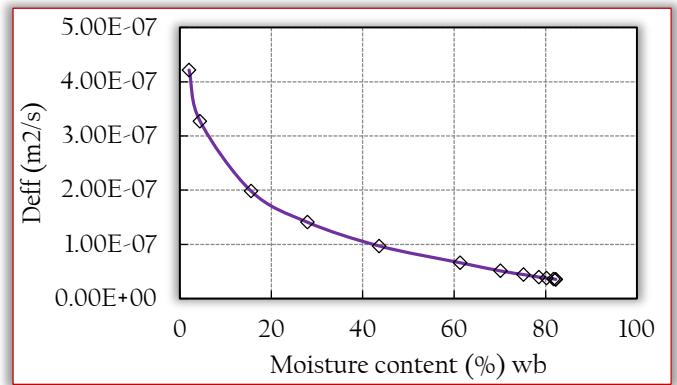


Figure 10. Variation of effective moisture diffusivity of open sun drying method with changes in moisture content

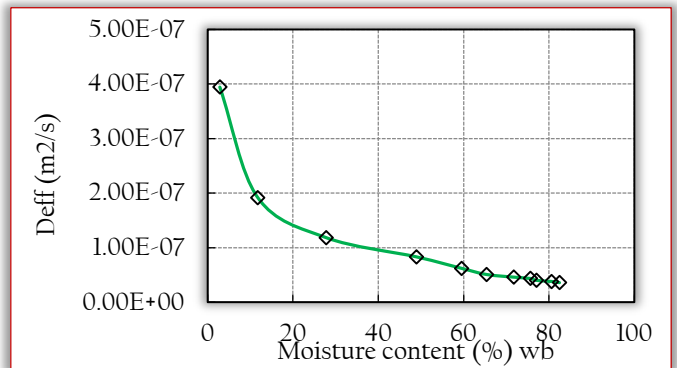


Figure 11. Variation of effective moisture diffusivity of solar drying method with changes in moisture content

From Figs. 10 and 11, the plot of  $D_{eff}$  against moisture content gave an exponential curve. Similar result was reported by Jen *et al.* (2001) and Hosain *et al.* (2013) with the explanation that it implies that effective moisture diffusivity is dominantly a function of moisture content of the leaves. Curve fitting was carried out using MATLAB R2009b and correlation equation was obtained for estimating moisture content dependent moisture diffusivity for both drying methods and is presented in eq. 6 below:

$$D_{eff} = 2.245 \times 10^{-7} \exp(-0.1817MC) + 2.245 \times 10^{-7} \exp(-0.0243MC) \quad (6)$$

MC is the moisture content, (wb).

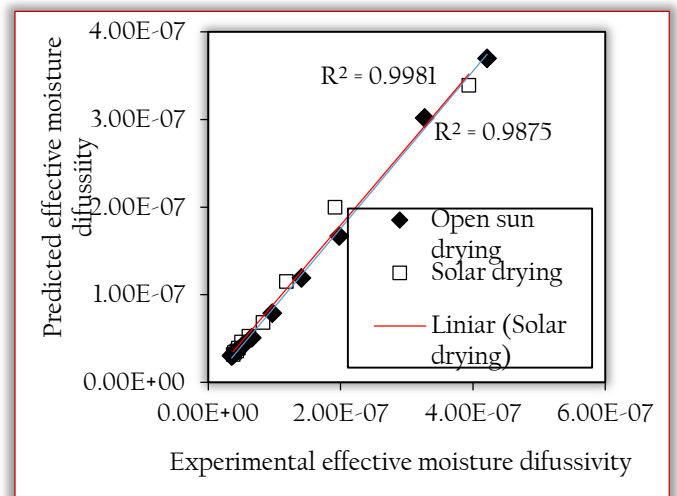


Figure 12. Experimental and predicted moisture diffusivity coefficient

— Fitting drying curves to mathematical drying models

Modelling is the most appropriate tool used in describing the drying characteristics and drying curves of fruits and vegetables. The results of fitted drying models presented in Tables 2 and 3 show that the Page model best describes the drying performance of both open sun and solar dried hospital too far leaves samples with  $R^2=0.9989$ ,  $SSE=0.001879$  and  $RMSE=0.01251$  and  $R^2=0.9901$ ,  $SSE=0.01214$  and  $RMSE=0.03484$  respectively.

Table 2: Open sun drying statistical parameters for each drying model

S/N	Model name	Coefficient	R <sup>2</sup>	SSE	RMSE
1	Newton	k=0.06438	0.5695	0.8093	0.2495
2	Page	k=9.27x10 <sup>-7</sup> n= 5.821	0.9989	0.001879	0.01251
3	Henderson and Pabis	a= 1.359; k=0.1003	0.7028	0.5587	0.2158
4	Logarithmic	a= 369.7; k= 0.0002; b= -368.5	0.8338	0.3124	0.1685
5	Midilli-Kucuk	a= 239.8; k= 5.363; b=-0.2039; n=-0.07199	0.9533	0.06757	0.0822
6	Wang and Singh	a=0.0376; k=0.008227	0.9749	0.04715	0.06268
7	Approximation of diffusion	a= -169.7; k= 0.2357; b= 0.9899	0.8357	0.3089	0.1676
8.	Modified Henderson and Pabis	a= 54.54; k <sub>0</sub> = 0.1659; k <sub>1</sub> = 0.8834; b= 0.9842; c= -24.26	0.8666	0.2507	0.177
9	Verma et al.	a= 54.54; k= 0.2289; k <sub>0</sub> = 0.2362	0.8355	0.3092	0.1676

Table 3: Solar drying statistical parameters for each drying model

S/N	Model name	Coefficient	R <sup>2</sup>	SSE	RMSE
1	Newton	k= 0.06331	0.5710	0.5269	0.2189
2	Page	k=3.293e-006; n= 5.457	0.9901	0.01214	0.03484
3	Henderson and Pabis	a= 1.302; k= 0.0986	0.6995	0.3691	0.1921
4	Logarithmic	a=327.1; k=0.0002318; b= -326	0.8149	0.2274	0.1589
5	Midilli-Kucuk	a= 45.76; k= 3.7; b= -0.2079; n= -0.1035	0.9493	0.0235	0.0882
6	Wang and Singh	a=0.04133; c=-0.01001	0.9809	0.04715	0.04847
7	Approximation of diffusion	a= -1.131; k= 0.06314; b=0.9794	0.571	0.5269	0.242
8.	Modified Henderson and Pabis	a= 1.897; k <sub>0</sub> = 0.001765; k <sub>1</sub> = 0.2876; k <sub>2</sub> = 0.4087; b= - 1.098; c= 0.3376	0.9490	0.06269	0.1022
9	Verma et al.	a= 127.9; k= 0.2034; k <sub>0</sub> = 0.2056	0.8019	0.2433	0.1644

CONCLUSION

Study on drying characteristics of hospital too far leaves has been carried out, the experimental drying curves exhibit only falling drying rate period and solar drying method has shorter drying time against open sun drying method hence the advantage of solar drying approach against open sun drying. The effective moisture diffusivity coefficient of hospital too far leaves ranges from 3.55x 10<sup>-8</sup> to 4.22x 10<sup>-7</sup> and 3.55x10<sup>-8</sup> to 3.94x10<sup>-7</sup> for open sun dried sample and solar dried samples respectively. The Page model was found to decently describe both open sun drying curve and solar drying curve.

References

- [1] Ahmed J., Singh G: Drying characteristics and product quality of coriander leaves. Food and bio products processing. Vol. 79, Issue 2, 103-106, 2001.
- [2] Akpina, E. K.: Drying of parsley leaves in a solar dryer and under open sun: Modelling, energy and exergy aspects. Journal of food process engineering. 77-67, 2011.
- [3] Ashton, A.: Issues in general food research. Scholarly Editions, Atlanta, Georgia. ISBN: 978-1-490-10951-0, 279-282, 2013.
- [4] Alizera S., Seyed-Hassan, M. A., Mahmood R. G.: Comparison of drying characteristics of peppermint using different drying methods. Journal of Food Processing and Preservation. Vol. 41, Issue 3, 2016.
- [5] Alara O. R., Abdulrahman O. A., Olalere O. A.: Mathematical modelling and morphological properties of thin layer oven drying of Vernonia Amygalina leaves. Journal of the Saudi Society of Agricultural Science. 2017.
- [6] Akpinar, E. K.: Mathematical modelling of thin layer drying process under open sun of some aromatic plants. Journal of Food Engineering. 77, 864-870, 2006.
- [7] Abe, T., Afzal, T. M.: Thin-layer infrared radiation drying of rough rice. Journal of Agricultural Engineering Research 67, 289-297, 1997.
- [8] Belghi, A, Kouhila, M., Bouteleb, B, C.: Experimental study of drying kinetics by forced convection of aromatic plants. Energy Conservation and Management. Vol. 44, 1303-1321, 2000.
- [9] COMSOL: Multiphysics Cyclopedia, available at <http://www.comsol.com/multiphysics/diffusion-coefficient>, 2017.
- [10] Crank, J.: The mathematics of Diffusion (2<sup>nd</sup> ed.). Oxford, UK, Clarendon Press, 1975.
- [11] Dincer, I. & Hussain, M. M.: Development of a new bi-di correlation for solid drying. International Journal of Heat and Mass Transfer, Vol. 45, No.15, 3065-3069, 2002.
- [12] Earle, R. L., Earle, M. D.: Unit operation in food processing. NZIFST (inc), 1966.
- [13] Giulbert, E.: Jathropher tanjorensis ("hospital too far"), Ugu-Oyibo, lyana-lpaja; an underutilized medicinal plant. Health bubbles, available at <http://healthbubbles.com/gb///?p=3534>, 2017.
- [14] Hosain, D., Abbas R. S., Ali, A., Mohsen A., Gholamhasan N., Jalaj, K.: Study of the drying kinetics of pepper. Journal of the Saudi Society of Agricultural Science. 13, 130-138, 2014.

- [15] Jen, Y. L., William, T. S., Steve P. V.: An Inverse Moisture Diffusion Algorithm for the Determination of Diffusion Coefficient. *Drying Technology*, 19(8), 1555-1568, 2001.
- [16] Keey, R. B.: Drying. *Thermopedia*. Available at [www.thermopedia.com/content/711/](http://www.thermopedia.com/content/711/). 2011.
- [17] Lamharrar A., Idlimam A., Alouani A., Kouhila M.: Modelling of thin layer solar drying kinetics and effective diffusivity of *Urtica dioica* leaves. *Journal of Engineering Science and Technology*. Vol. 12, no. 8, 2141-2153. 2017.
- [18] Lewicki, P. P.: Design of hot air dryer for better foods. *Trends in food science and technology*, 17, 153-163, 2006.
- [19] Kuti, J. O., Torres E. S.: Potential nutritional benefit of tree spinach in: progress in new crops, J. Janick (Ed), Arlington V. A., ASHS Press, 516-520, 1996.
- [20] Mursalim, S. and Dewi, Y S.: Drying of cashew nut in shell using solar dryer, *science and technology*, 3(2), 25-30, 2002.
- [21] Mordi, J. C., Akanji M. A.: Phytochemical screening of the dried leaf extract of *snidoscolus aconitefolius* and associated changes in lower enzymes induced by its administration in winstar rats. *Curr. Res. Journ. Biol. Sci.* 4(2), 153-158, 2012.
- [22] Midilli A.: Determination of Pistachio Drying Behaviour and Condition in a Solar Drying Systems. *International Journal of Energy Research*, Vol. 25 No8, 715-725, 2001.
- [23] Naseer A., Jagmohan S., Harmeet C., Prerna G., Anisa A., Harleen K.: Different drying methods: Their application and recent advances. *International Journal of Food Nutrition and Safety*. 4(1), 34-42, 2013.
- [24] Omigie, M. I., Agoreyo, F. O., Edobor, E. V.: The effect of jatropher *tanjorensis* on homoglobin concentration and parcked cell volume of winstar rats. *Jos Journal of Medicure*. 7,1, 2013.
- [25] Olayiwola, G. E. O, Iwalewa E. O., Omobuwajo, A. A., Verspohi, E. J.: The anti-diabetic potential of *Jatropher Tanjeronis* leaves. *Nigerian Journal of Natural Medicine*. 8, 55-58, 2004.
- [26] Osuchukwu I. W., Sakpa C. L., Ekezie J., Okeke C. U., Eke C. C., Ezejindu D. N.: Effect of leave extract of *Jatropha Tanjeronis* on the testis of wistar rats. *Journal of Medical and Dental Science*. Volume 15, Issue 4, Ver. IV, 66-71, 2016.
- [27] Prabakaran, A. J., Sujalha M.: *Jatropher Tanjeronis* Ellis and Saroja, a natural interspecific hybrid occurring in Tamil Nadu, India. *Gen. Res. Crop Evol.*, 46:213-218, 1999.
- [28] Ravi K. Why do we extract dried, ground plant material instead of fresh ones? Available at [www.researchgate.net](http://www.researchgate.net), 2015.
- [29] Subahana K. R. R., Natarajan A., Melvin M., Muralidharan N. G.: The thin layer drying characteristics of chilly leaf under open sun and in solar dryer. *ARPN Journal of Engineering and Applied Sciences*. Vol. 9, No. 11, 2158-2167, 2014.
- [30] Werner W., Josef B. *Solar Drying: Establishment of a production, sales and consulting infrastructure for solar thermal plant in Zimbabwe*. Training Course, 2012.
- [31] Wang, Z., Sun, J., Chen, F., Liao, X., Hu, X.: Mathematical modelling of thin layer microwave drying of apple pomace with and without hot-air pre drying. *Journal of Food Engineering*. 80(2), 536-544, 2007.



ISSN: 2067-3809

copyright © University POLITEHNICA Timisoara,  
Faculty of Engineering Hunedoara,  
5, Revolutiei, 331128, Hunedoara, ROMANIA  
<http://acta.fih.upt.ro>

<sup>1</sup>Iliia ZUMBILEV, <sup>2</sup>Angel ZUMBILEV

# STUDYING THE POSSIBILITY THE ACOUSTIC EMISSION TO BE APPLIED IN THE PROCESSES OF MATERIALS DESTRUCTION

<sup>1-2</sup>Technical University of Sofia – Branch Plovdiv, BULGARIA

**Abstract:** The aim of the present paper is to study the possibility to use acoustic emission for studying the processes of microcracking and fracture of thermally and chemical-thermal treated materials. The obtained results show that the acoustic emission can be used as an indicator of pre-destructive processes for thermally treated and nitrided materials. It has been established that the values of  $K_{\sigma}$  (AE), defined for a material in a non-destructive way in laboratory conditions, can well serve in production as a criterion of forthcoming brittle fracture.

**Keywords:** acoustic emission, fracture, thermally treated steels, nitriding

## INTRODUCTION

Reliability and exploitation life of tools and details depends mainly on origination and propagation of cracks, expressed by the following characteristics – fracture toughness  $K_{Ic}$  and critical opening of the crack banks  $\delta_{Ic}$  [4, 5, 6, 9].

In addition to wear at high contact loads and high temperatures, resistance against formation of cracks on the surface is essential for tools for hot working.

Tool steels for hot working, being not very plastic, are very sensitive to brittle fracture. About 70% of the reasons for failure of the molds for casting nonferrous alloys under pressure are due to magistral and thermal cracks [4,5].

A number of methods for studying the processes of formation and development of cracks in multi-layer systems have been described in [1,2,1-13]. Common disadvantage of most of these methods is that they are applied after completion of the fracture. One of the most modern methods for studying the processes of microcracking and fracture in the matrix and its adjacent thin layers is acoustic emission.

The acoustic emission (AE) is based on physical phenomena, related to radiation of acoustic impulses in the material. The sources of AE can be divided into two groups. The first one characterizes the phenomena, related to plastic deformation: twinning of the crystals, slipping along the grain boundaries and, most of all, own motion of the dislocations [1,2,11]. The phenomena, related to the motion of the dislocations are less energetic. They are registered by a continuous AE. The second group consists of the more pronounced energetic phenomena, accompanying the mechanisms of fracture: formation and propagation of the micro-crack, intercrystalline and transcrystalline fracture, phase transformations etc. These phenomena are registered by an impulse AE.

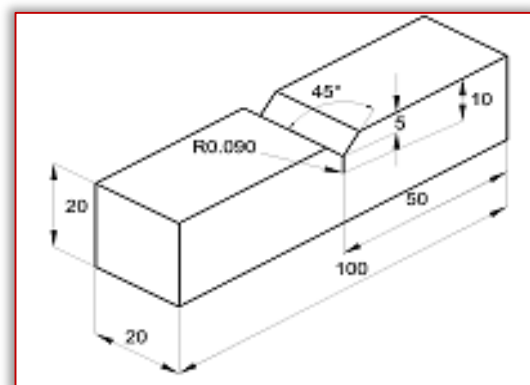
The impulse type acoustic emission is observed in materials when suddenly mechanical energy of elastic deformation is released, at the moment of microcracking or propagation of cracks. Energy release in the deformed material goes discreetly as a series of individual acts, registered as AE-impulse and AE-phenomena (events) in a minor volume of

the material. Then they propagate in the form of waves of elastic deformation (stress waves, AE-waves) throughout the volume. Registration of the spectrum and the parameters of AE, radiated by a material, subjected to deformation, gives significant information about the mechanisms of the process of crack formation and fracture.

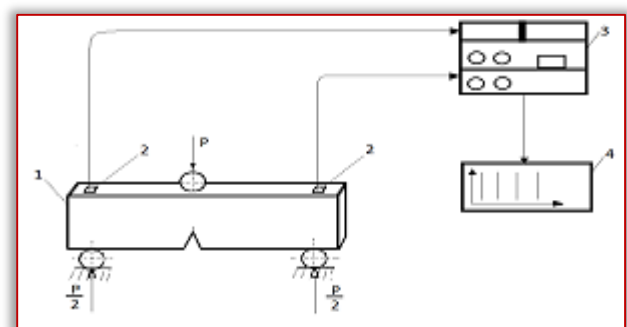
The aim of the present paper is to study the possibility to use acoustic emission for studying the processes of microcracking and fracture in thermally treated materials.

## METHODOLOGY OF STUDY

Experiments were conducted with steel BH11 BS4659 (4X5MΦC - ΓOCT), from which standard samples with a notch for three-point bending were produced [7,8] – Figure 1.



a)



b)

Figure 1 - a - sample, b – block-scheme of the experiment  
1- sample, 2- sensors, 3- AE systems, PAC 3000/3104, 4-printer

The spherical waves, emitted by the source, were transformed into surface AE-waves (stress waves), and registered by the sensor (2), attached to the sample (1). The mechanical energy of the acoustic-emission impulse was converted into an equivalent electrical signal. After filtration it was fed into the pre-amplifier and from there – into the analogue part for additional amplification and processing by the computer block of the AE-equipment PAC 3000/3104(3). The processing of the characteristics of the AE-signal (duration, rise time, impulses, amplitude, energy etc.) was carried out by the microcomputer of the AE-system and could be printed by a printing machine (4). The experiments were conducted at room temperature.

The samples were thermally treated in a vacuum furnace VKUQ -Degussa, and then part of them were subjected to ion nitriding in the installation ION-20. After the thermal treatment the samples were grinded at  $R_a = 0,32\mu\text{m}$ . The modes of thermal treatment and ion nitriding are given in Table 1.

Table 1 - Modes and results from the ion nitriding of steel BH11

No of the sample	$t_{\text{hard}}$ , °C	$t_{\text{temp.}}$ , °C	HRC	$t_{\text{nitrid.}}$ , °C	$P_{\text{NH}_3}$ , Pa	$\tau$ , h	HV <sub>0,1</sub>	$\delta_{\text{tot.}}$ , $\mu\text{m}$	$\delta_{\text{cz.}}$ , $\mu\text{m}$
215	1040	600	51	530	300	7	1168	240	6
249	1040	650	46	530	300	10	1100	270	8

It was proved by metallographic and fractographic analysis that the tip of the notch was not nitrided after nitriding. The resistance against crack propagation was defined for three-point bending of the samples by means of a universal testing machine INSTRON 1343 at velocity of loading 0,5mm/min. The motion of the crack banks ( $V_g$ ) was registered at room temperature by a console tenso-resistive perceiver with sensitivity 2,5  $\mu\text{V}/\text{mm}$ , base 10 mm and step 2 mm, having the diagram force (P) – crack banks motion recorded at the same time ( $V_g$ ).

For studying the AE-activity in three-point bending and fracture of the samples a four-channel AE-system PAC 3000/3104 (USA) with wide-band sensors Wd was used – Figure 1. The sensors were placed on a sample, locally doped with silicon paste, and fastened by special springs, providing constant pressure. The sensitivity of the sensors was controlled by the imitator of Hsu. At total amplification of 80 dB (40 dB pre-amplification) and constant threshold of 1V, a registered signal of 98 dB from the imitator was taken as good sensitivity.

For clearing out and correct interpretation of the results from the acoustic-emission (AE) tests, calibration curves were obtained based on metallographic and fractographic analyses, concerning the different structural states. The obtained graphical and tabular AE-information was cleared at

the maximum from the influence of noises by appropriate conduction of the experiments and consequent analysis of the data.

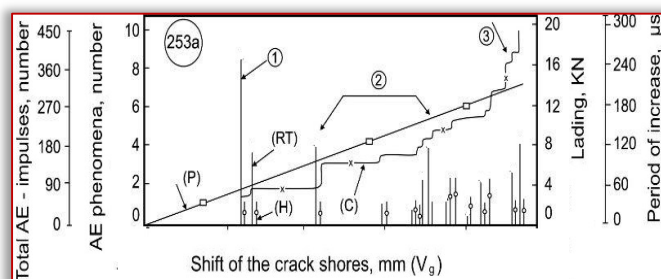
## EXPERIMENTAL RESULTS AND ANALYSIS

### Thermal threaded simple bodies

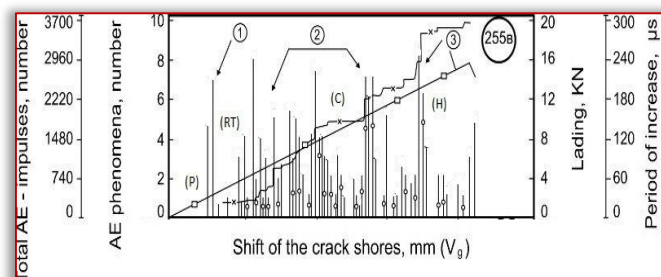
The acoustic-emission parameters: number of AE-events (H), AE-impulses (C), rise time (RT), AE-energy (E), AE-amplitude (A) and pressure (P) are shown in dependence on the displacement of the crack banks ( $V_g$ ) – Figure 2.

The experimental results from the acoustic-emission activity of the vacuum-thermally treated samples (№ 253 и № 255) speak of brittle fracture with clearly expressed character.

The fracture is in the linear (elastic) zone of the curve “pressure – displacement (opening) of the crack banks” without any signs of stable growth of the crack in microscopic aspect. The differences in the slopes P –  $V_g$  for the two samples (Figure 2) are due to structural distinctions – grain structure, distribution, size and shape of the carbides.



(a)



(b)

Figure 2 - Change of the AE-parameters and the load in dependence on the displacement of the crack banks for the thermally treated samples

AE-phenomena with low energy, amplitude and impulses but with sufficient rise time were observed even at the lowest values of the load. They are denoted in Figure 2, zone ① and indicate the beginning of formation of a new zone of plastic deformation in front of the crack tip. In this zone from 20 to 60% of the load AE-phenomena with increased number of AE-impulses, energy and amplitude are observed but with shorter rise time, what is an evidence of the beginning of a brittle micro-cracking.

Such AE-signals of brittle materials are related to fracture or to de-cohesion of the carbides and the intergranular brittle fracture at micro-level. Most probably fracture of the carbides begins, together with microcracking in local areas, near the crack tip [3,4]. Low-energetic AE-signals are also observed,

which are due to the fracture of most of the disperse carbides (Figure 2a, zone ②). A common feature of the samples in this series is the appearance of signals with high amplitudes and energy, with very short rise time and duration under a load, close to the fracture load. These AE-signals can be taken as a harbinger of the end of the unstable brittle fracture. In Figure 2 they are separated in zone ③ of the AE-tests.

These signals are due to the growth of microcracks and the formation of the facets, observed at the fractures of the samples by means of a scanning electronic microscope (SEM) – Figure 3.

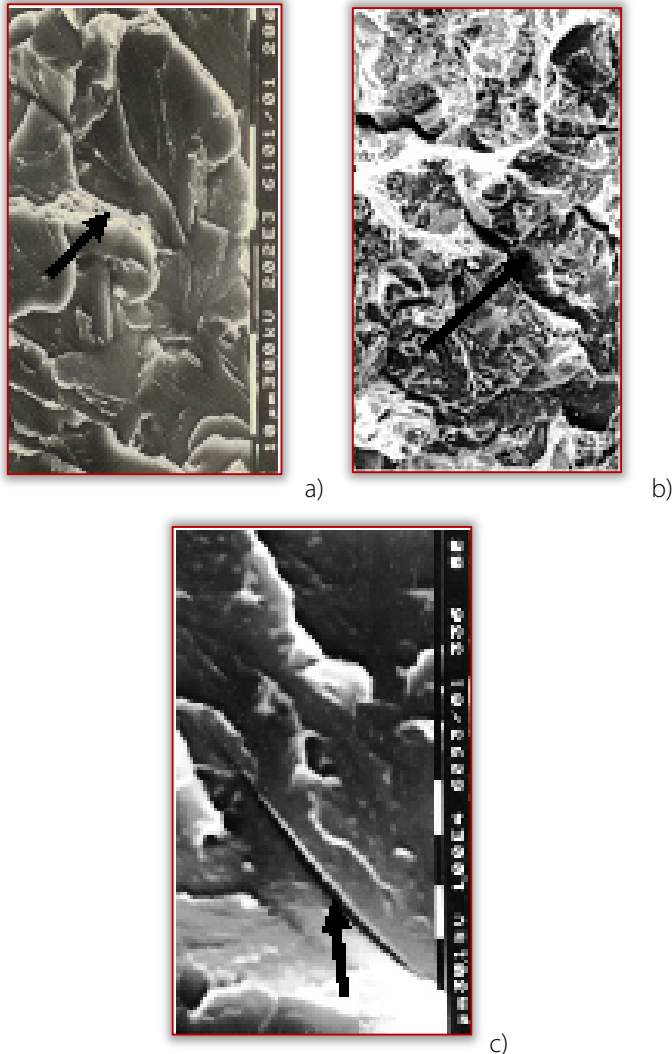


Figure 3 - Fractographs of thermally treated samples after tempering at: a, c - 600°C; b- 650°C

Isolated carbides were observed by means of SEM in the vicinity of the crack tip at the possible boundary of the zone of micro-plastic deformation, and they are sources of AE-signals. Zones of blunting the crack tip and its successive unstable growth after reaching the critical micro-stresses for initiating the unstable brittle fracture were also observed. Facets with big areas, free of micro-pores, prevail in these zones. Together with the increase of the temperature of tempering, sections of micro ductile fracture are observed around the facets – Figure 4.

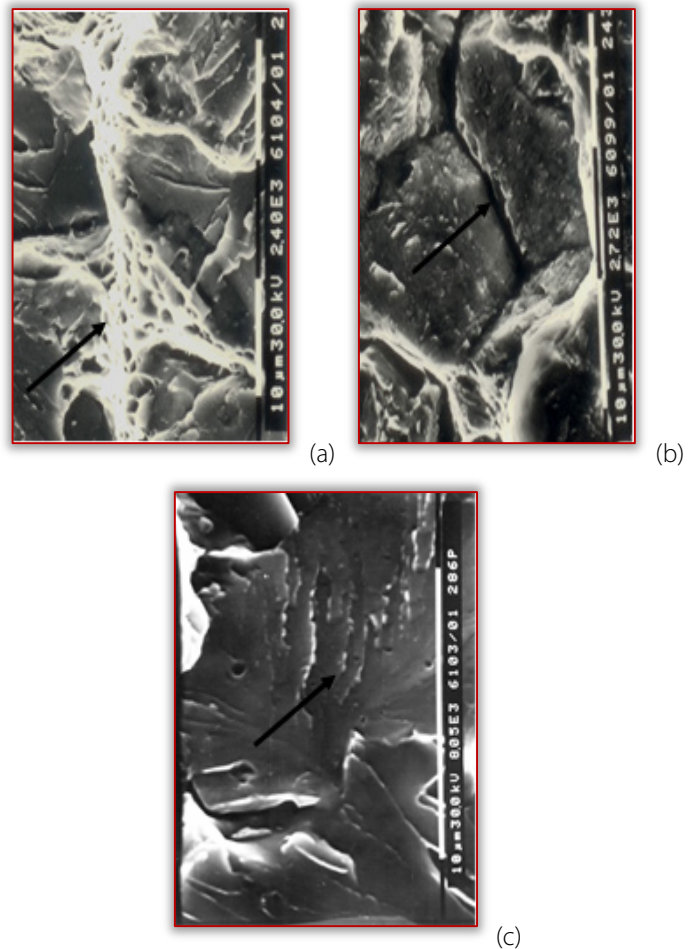


Figure 4 - Fractographs of thermally treated samples after annealing at: a, c - 600°C; b- 650°C

These sections, in addition to the increased content of carbides, are the reason for the increased AE-activity in the sample, tempered at 923K (650°C). The inter-crystalline cracks prevail in this sample and contribute to emitting high-energy AE-signals both in zone ② and ③ - Figure 4b. It can be confidently asserted that all processes of internal and inter-crystalline brittle structure emit AE-signals, which can be registered.

Together with the increase in the temperature of tempering, overall increase of AE-activity is observed, which is best expressed in graphical representation of the total (cumulative) AE-energy depending on the load – Figure 5.

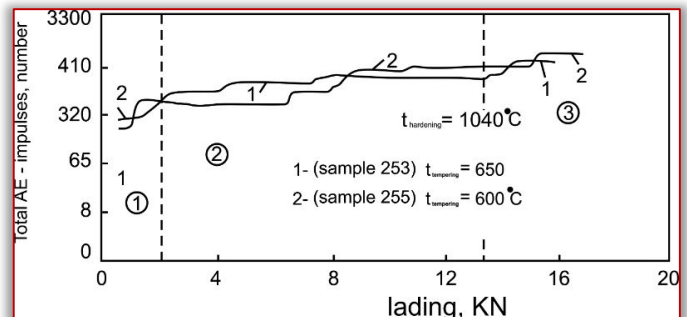


Figure 5 - Change of the total energy with respect to the load of the studied samples

The increase in plasticity of the material leads to an increase in the AE-activity at the low values of loading, due to the larger zone of micro-plastic deformation in front of the crack tip – zone ①. Zone ② is characterized for all samples by comparatively uneven frequency of appearance of high energy AE-phenomena. In zone ③ the AE-phenomena with high energy for samples, tempered at 873 K and 923 K, are an excellent indicator of the end of the brittle fracture. The quantitative characteristics of the fracture of the thermally treated samples is made by means of the parameter “total (cumulative) energy” and expressed in Figure 6.

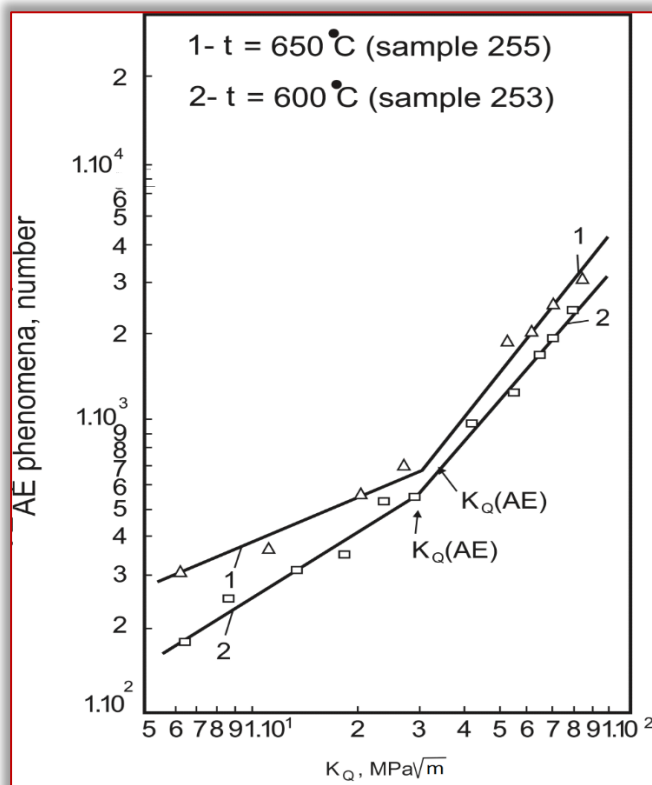


Figure 6 - Change of the total energy with respect to  $K_Q$

From Figure 6 it can be seen that at temperature of tempering the steel 923 K (650°C), the value of  $K_Q$  (AE) is the highest, what shows that the number of sources of AE is bigger.

The points of breakage on the graphs, denoted by  $K_Q$  (AE), are the beginning of unstable fracture. Reaching this moment of loading, value of  $K_Q$  and total AE, unsteadily growing “quasi brittle” crack starts developing in the material.

The values of  $K_Q$  (AE), defined in a non-destructive way in laboratory conditions for the material, can serve well in production as a criterion of its forthcoming brittle fracture.

#### — Nitrided simple bodies

The acoustic-emission parameters: AE-impulses (C), rise time (RT) and pressure (P) are shown in dependence on the displacement of the crack banks ( $V_g$ ) – Figure 7.

The experimental results from the acoustic-emission activity of the ion nitride samples (215, 249) speak of brittle fracture with clearly expressed character and are presented in Figure 7 and Figure 8.

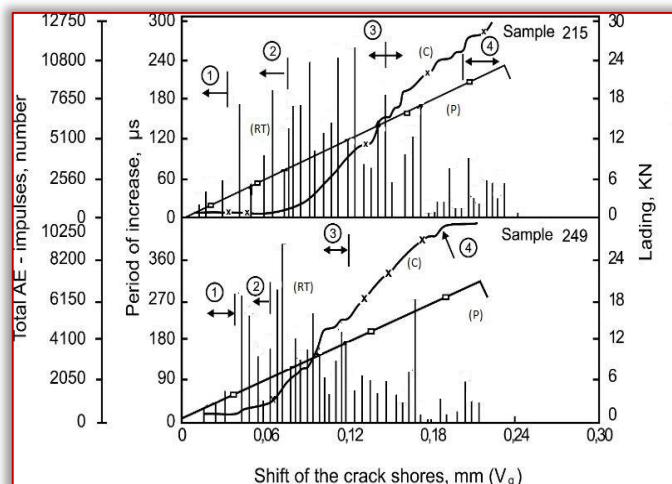


Figure 7 - Change of the AE-parameters and the load with respect to the displacement of the crack banks for the ion-nitrided samples 215 and 249

The fracture of the ion-nitrided samples is in the linear elastic zone of the curve P- $V_g$ . The AE-activity of the samples is with considerably lowered AE-parameters at low loads. Figure 7, number ① denotes this zone of low AE activity, in which the rise time of the registered AE phenomena is below 60 $\mu$ s, and the AE-impulses are with low intensity. The AE-phenomena, registered in zone ① are due to premature microcracking of the layer, when the deformation at small loads is sufficient to achieve the critical destructive stresses for the imperfect (defective) micro-sections of the layer [14,15]. This confirms the assumption that these stresses do not necessarily lead to microcracks in the matrix. The assumed micro-cracking in the defective sections of the layer is also supported by the fact that the layer has a significantly higher modulus of elasticity and it will crack before the tensile strength of the matrix is reached.

In the three-point bending processes of reduction of the residual compressive stresses occur. This is also accompanied by plastic deformation of the layer. The formation of a zone of plastic deformation in front of the crack tip and in the layer is the reason for the observed AE-activity in zone ② Figure 7. It is with comparatively high values of rise time. In the third zone ③, characterizing mainly the processes of brittle fracture of the matrix, linear rise of the total number of AE-impulses is observed.

This type of distribution of the AE-impulses is characteristic of the processes of fracture, evenly distributed in time or with respect to the load and containing elements of ductile fracture. It is possible to isolate a fourth zone ④ in the studied samples, where the AE-activity is with lowered parameters again. It corresponds to the final brittle micro-cracking of the layer and the fracture of the whole sample.

For the cumulative distribution of the AE-energy four zones can also be distinguished, what confirms the assumed behavior at fracture, causing the corresponding AE-activity – Figure 8.

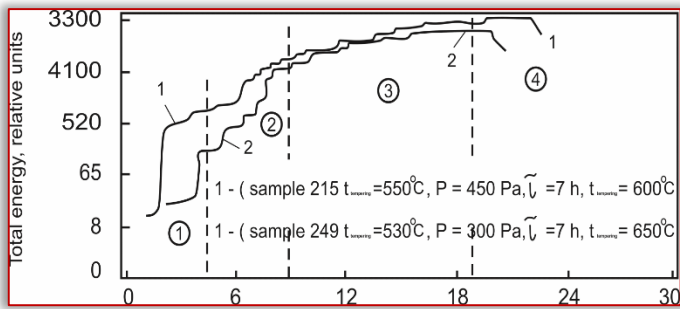


Figure 8 - Total energy change with respect to the load for the nitrided samples

It can be noted in conclusion that two types of AE-activity are observed in the studied samples. They are characterized by four zones of AE-activity: zone of premature microcracking of the layer; zone of plastic deformation in front of the notch tip; zone of brittle fracture of the matrix and zone of final microcracking and fracture of the sample.

The AE-activity can be used as an indicator of pre-fracture processes in nitride details and tools. Based on the carried acoustic-emission and fractographic analysis, the following probable mechanism of fracture of a nitrided body, subjected to static loads, is suggested.

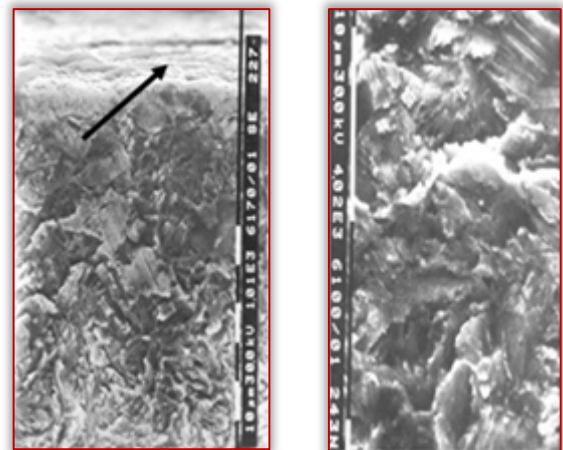
At low initial pressure (P) of the ion-nitrided sample - up to 6 kN - in front of the notch tip at both its ends, where a nitride layer is present, processes of reduction of the residual compressive stresses occur, on the one hand, and, on the other hand, premature deformation of the layer and its microcracking occurs due to its high modulus of elasticity – Figure 7, zone ①. Microcracks are formed first in the combined (white) zone and then in the diffusion zone (Figure 9a).

This is due to the higher brittleness of the combined zone. For these loads the micro-deformations in the diffusion zone are sufficient for achieving the critical destructive stresses in the imperfect (defective) sections of the layer, primarily the areas with high density of dislocations around the nitride (carbonitride) depositions [14,9].

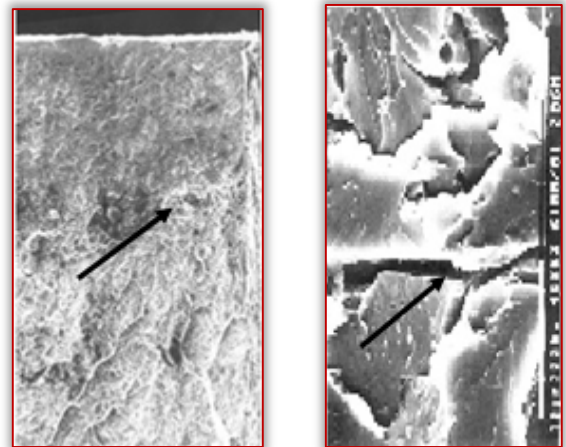
At these initial loads micro-cracks are not formed in the non-nitrided matrix, what is due to the lower modulus of elasticity and the arising (because of that) lower stresses in it at the same levels of deformation. On the other hand, the matrix is much more plastic than the nitrided layer.

Only at heavier loads plastic deformation occurs in front of the notch in the matrix – Figure 7, ②. This causes microcracking of the biggest carbide particles, having the highest density, which are located in the plastic zone or in closest proximity to it, which leads to appearance of microcracks in the matrix as well [4,5,9]. The closest to the layer newly formed microcracks do not propagate in it, since the diffusion zone prevents from plastic deformation occurrence at these stresses.

The propagation of the microcracks in the layer is also impeded by the residual compressive stresses and the higher hardness of the layer.



a) b)



c) d)

Figure 9 - Fractographs of the ion-nitrided samples

After certain level of loading, conditions arise for propagation of the formed micro-cracks both in the layer (combined zone and diffusion zone) and in the matrix. Some microcracks in the matrix and the layer move and merge to form a larger (magistral) crack, which propagates along the boundary between the diffusion zone and the matrix – Figure 9c,d – most probably where the compressive stresses are very low or change their sign. The crack develops unsteadily after reaching the critical micro-stresses for initiating brittle fracture (Figure 7), zone ③. This magistral crack, located at the boundary between the layer and the matrix obviously has the greatest contribution to the process of splitting off the layer and fracture of the nitrided body. Naturally, the other cracks in the layer and the matrix also have their influence on this process. The nitrided layer breaks last - (Figure 7), zone ③.

## CONCLUSIONS

Acoustic emission can be used for studying pre-fracture processes, going on in thermally treated and nitrided materials.

The values of  $K_0$  (AE), defined in a non-destructive way in laboratory conditions for the material, can serve well in production as a criterion of forthcoming brittle fracture.

## References

- [1] Lozev, M., Application of the acoustic emission for non-destructive control of vessels, working under pressure,

- Mechanical Engineering, 11, 1984, pp.507-509 (In Bulgarian)
- [2] Khan M. A., Shoji T., Takahashi B., Acoustic Emission from cleavage microcracking in alloy steels, *Metals Science*, Vol.16, 1982, pp. 118-126.
- [3] Grunling H. W., Schneider K., Singheiser L., Mechanical Properties of Coated Systems, *Materials Science and Engineering*, 88, 1987, pp 177-189.
- [4] Okuno T., Effect of microstructure on the toughness of hot work tools, *Steel AINI*, H13, H10, H11, *Transactions ISIY*, Vol.27, 1987, pp.51-55.
- [5] Qamar S., Sheikh A., Arif A., Pervez, Siddiqui R., Heat treatment of a hot work die steel, *Archives of Materials Science and Engineering*, Volume 28, Issue 8, August 2007, pp. 503-508.
- [6] Toshkov V., A. Zumbilev and M. Lozev, On Some Aspects of the Fracture of Heat Treated and Ion Nitrided Steels, *Proceed, of 5th International Seminar on "Heat Treatment and Surface Engineering"* 26-29, IX, 1995, Isfahan, Iran, pp. 265-270.
- [7] BS 5447-1977. Methods of test for plane strain fracture toughness ( $K_{Ic}$ ) of metallic materials.
- [8] BS 5762-1979. Methods for crack opening displacement (COD) testing.
- [9] Zumbilev A., About the influence of heat treatment over the resistance against fragile destruction of BH21 steel, *Technical University Journal "Annals of the faculty of engineering Hunedoara"*, Tome VIII, Fascicle 1 (ISSN1584/2665), Romania, 2010, pp.21-24.
- [10] Acoustic emission in the diagnostics of pre-fracture state and forecasting fracture of welded constructions, *Papers, International School*, 1986, p146 (In Russian)
- [11] Lozev M. Acoustic evaluation of austenitic welded joints. *Chimmash, Informa, Sofia*, 1990, p.44
- [12] Mihovski M., M. Lozev, Non-destructive control in chemical machine building, *Techniques*, 1987, p 159 (In Bulgarian)
- [13] Bunina, N., Studying plastic deformation of metals by the method of acoustic emission, *Leningrad University*, 1990, p 156 (In Russian)
- [14] Maksimovich, G, Shatynskij V., Kopilov V., Physical and chemical processes in plasma dusting and destruction of coated materials, *Kiev, Naukovadumka*, 1983, p.260
- [15] Lozev M., Zyumbyulev A., Toshkovand V., Boev L., Fracture mechanics of ion-nitrided steel, *Materials Science*, Volume 28, Number 2, March, 1993, pp. 116-119



ISSN: 2067-3809

copyright © University POLITEHNICA Timisoara,  
Faculty of Engineering Hunedoara,  
5, Revolutiei, 331128, Hunedoara, ROMANIA  
<http://acta.fih.upt.ro>

# OPTIMIZATION OF PROCESS PARAMETERS IN TREATMENT OF BREWERY EFFLUENT

<sup>1-2</sup>Department of Chemical Engineering, Faculty of Engineering, University of Benin, PMB 1154, Benin City, Edo State, NIGERIA

**Abstract:** A three– variable Box–Behnken design (BBD) coupled with response surface methodology (RSM) was employed to optimize and evaluate the effect of adsorbent dose, contact time and temperature on percentage reduction of BOD, COD and TDS in brewery effluent. Adsorbent was prepared from coconut shell, which was carbonized at temperature of 600°C for 2 hours and thereafter activated. The effluent was treated with the adsorbent by varying three variables: adsorbent dosage (1–5 g), contact time (40–180) and temperature (30–40°C). Statistical analysis of the results showed that all the factors, except the temperature, had significant effect on the responses. Quadratic models were developed for percentage reduction of (biological oxygen demand) BOD, chemical oxygen demand (COD) and total dissolved solids (TDS). The models were significant with  $p < 0.0001$  and showed a good fit to the experimental data. The percentage reduction of BOD, COD and TDS were positively influenced by adsorbent dose and contact time. The temperature range used for this study did not have so much effect on the responses. The optimum conditions for BOD, COD and TDS reduction of 75.268%, 69.865% and 69% respectively were adsorbent dosage of 5g, contact time of 180 minutes and temperature of 34.4°C.

**Keywords:** brewery effluent; BBD; adsorbent; optimization

## INTRODUCTION

The industrialization of developing countries has led to increased industrial activities. A major source of pollution in developing countries is industrial activities and this has gradually increased the problem of waste disposal (Alao *et al.*, 2010). The emerging industries include metal plating, mining, painting, and brewery.

Brewery wastes are composed mainly of liquor pressed from the wet grain and wash water from the various departments (Noorjahan and Jamuna, 2012). Untreated wastes from processing factories located in cities are usually discharged into inland water bodies. The resultant water pollution poses demonstrated risks to aquatic ecosystems, human health and productive activities (UNEP, 2016). The Biochemical oxygen demand levels of brewery effluents are quite high, as are the total solids; typically about half the BOD and over 90% of the suspended solids are generated in the brewing operation (Noorjahan and Jamuna, 2012). Disposal of such effluent without any prior treatment into water courses causes serious pollution problems (Ninnekar, 1992).

A number of treatment methods for industrial effluents have been reported, which includes, ion exchange, electrodialysis, electrochemical precipitation, evaporation, solvent extraction, reverse osmosis, chemical precipitation and adsorption (Gupta *et al.*, 2009). Most of these methods suffer from drawbacks such as high capital and operational costs or the disposal of the residual sludge. Due to its simplicity and easy operational conditions, adsorption is a widely–used process (Mabrouk *et al.*, 2009).

In studying the individual and interactive effects of the selected effluent parameters on the chosen responses, a statistical design of experiments is employed as against the

traditional one–factor–at–a–time experiment which is time–consuming (Carmona *et al.*, 2005; Huang *et al.*, 2008). Response surface methodology based on statistically designed experiments has been found to be very useful in optimising multivariable processes.

The aim of this study was to optimise the effect of adsorbent dose, contact time and temperature on the percentage reduction of COD, BOD and TDS of brewery effluent. A three variable BBD was adopted to design the percentage reduction of the selected effluent physicochemical parameters.

## METHODOLOGY

### — Preparation of Activated Carbon and Carbonization

The coconut shells were obtained waste bins at Uselu market in Benin City, Edo state. Coconut fibre and sand were removed from the shells and washed with water, to remove dust and other impurities, sun dried and were pulverised. The pulverized coconut shells was carbonized at 600°C for 2 hours and allowed to cool. It was then impregnated in 100 mL 20% (v/v) concentration of phosphoric acid for 24 hours. The sample was washed with distilled water until a pH of 6–7 was obtained and then the sample was dried to remove moisture at 85°C for 2 hours in the oven. The dried activated carbon was crushed with a mortar and sieved using a 35 mesh size to obtain a particle size of 0.45 mm or less.

### — Effluent Collection

Samples of effluents were collected at point of discharge from a brewery in Benin City, Nigeria. They were collected in 2 L sterile glass bottles and transported to the laboratory at 4°C for analysis.

### — Effluent Characterization

The TDS of effluents was determined by using ELICO EC–TDS meter (CM 183) where electrode was directly dipped into the respective solutions to display result on a digital scale. Biochemical oxygen demand (BOD) was determined according to standard Methods for the examination of water and waste water (APHA, 2005).

COD determination was carried out with dichromate reflux method with the addition of 10 ml of 0.25 N potassium dichromate (K<sub>2</sub>Cr<sub>2</sub>O<sub>7</sub>) and 30 ml H<sub>2</sub>SO<sub>4</sub>+Ag<sub>2</sub>SO<sub>4</sub> reagent in 20 ml diluted sample. The mixture was refluxed for 2 h and was cooled to room temperature. The solution was then diluted to 150 ml by using distilled water and excess K<sub>2</sub>Cr<sub>2</sub>O<sub>7</sub> remained was titrated with ferrous ammonium sulphate (FAS) using ferroin indicator.

$$\text{COD} = \frac{(A-B) \cdot N \cdot 1000 \cdot 8}{\text{volume of sample}} \quad (1)$$

where *A* is the ml of FAS used for blank; *B* is the ml of FAS used for sample, *N* is the normality of FAS and 8 is milliequivalent weight of oxygen.

### — Experimental Design

A three variable Box–Behnken design (BBD) for response surface methodology was used to develop a statistical model for the reduction of BOD, COD and TDS of effluent. The ranges of the variables that were optimized are as shown in Table 1. The experimental design made up of 17 runs was developed using Design Expert 7.0.0 (Stat–ease, Inc. Minneapolis, USA). The levels of the independent variables as shown in Table 1 were selected based on preliminary experiments. The relation between the coded values and actual values are described as follows:

$$x_i = \frac{X_i - X_0}{\Delta X} \quad (2)$$

where *x<sub>i</sub>* and *X<sub>i</sub>* are the coded and actual values of the independent variable respectively. *X<sub>0</sub>* is the actual value of the independent variable at the centre point and Δ*X<sub>i</sub>* is the step change in the actual value of the independent variable.

Table 1: Experimental range and levels of independent variables

Independent Variables	Symbols	Coded and Actual Levels		
		-1	0	+1
Adsorbent dose (g)	X <sub>1</sub>	1	3	5
Contact time (min)	X <sub>2</sub>	40	110	180
Temperature (°C)	X <sub>3</sub>	30	35	40

## RESULTS AND DISCUSSION

Experiment was conducted at different levels of combination of factors that affect adsorption (adsorbent dose, contact time and temperature), using statistically designed experiment. The data obtained was analyzed by RSM (response surface methodology), and the results were presented using suitable graphs.

Linear, cubic and quadratic models were investigated by the software to select the statistically significant model for determining the relationship between the responses and the input variables. The statistics of the models summaries for the four responses are given in Table 3–5.

Table 2: Three level factorial Box–Behnken design matrix and the experimental responses

Run No.	Factors			Responses		
	X <sub>1</sub>	X <sub>2</sub>	X <sub>3</sub>	BOD (Y <sub>1</sub> ) Actual	COD (Y <sub>2</sub> ) Actual	TDS (Y <sub>3</sub> ) Actual
1	3	110	35	73.082	66.335	66.257
2	1	180	35	52.899	59.605	54
3	5	110	30	74.995	69.084	69
4	1	110	30	51.761	57.554	53.333
5	3	180	40	73.785	68.667	67
6	1	40	35	50.1	57.081	53.333
7	3	180	30	72.586	68.751	67.289
8	3	40	40	69.348	66.297	65.425
9	3	110	35	72.264	67.899	66.667
10	3	40	30	69.995	64.775	64.235
11	5	40	35	73.998	68.1	68.085
12	3	110	35	71.896	68.364	65
13	3	110	35	72.002	67.096	65.25
14	5	110	40	74.005	68.995	67
15	1	110	40	52.387	57.005	54
16	3	110	35	72.347	67.45	63.333
17	5	180	35	75.028	69.125	68.5

Table 3: Model summary statistics for BOD

Source	Std. dev	R–Squared	Adjusted R–Squared	Predicted R–Squared	F Value	
Linear	5.06	0.7588	0.7031	0.5673	13.63	
2FI	5.75	0.7605	0.6167	0.0693	0.023	
Quadratic	0.59	0.9982	0.9960	0.9810	316.10	Suggested
Cubic	0.47	0.9994	0.9975		2.40	Aliased

Table 4: Model summary statistics for COD

Source	Std. Dev	R–Squared	Adjusted R–Squared	Predicted R–Squared	F Value	
Linear	2.38	0.7760	0.7243	0.5973	15.01	
2FI	2.69	0.7799	0.6478	0.1438	0.058	
Quadratic	0.85	0.9847	0.9650	0.8606	50.02	Suggested
Cubic	0.78	0.9927	0.9707		1.46	Aliased

Table 5: Model summary statistics for TDS

Source	Std. Dev	R–Squared	Adjusted R–Squared	Predicted R–Squared	F–Value	
Linear	2.86	0.7998	0.7536	0.6264	2.893	
2FI	3.22	0.8043	0.6868	0.1831	0.563	
Quadratic	1.13	0.988	0.9612	0.9124	45.05	Suggested
Cubic	1.3	0.9873	0.949		1.06	Aliased

From Tables 3–5, it is seen that the suggested quadratic model is satisfactory since it has the highest F values of 316.10, 50.02 and 45.05 for BOD, COD and TDS respectively. As shown in a related study (Yi *et al.*, 2010), the larger the magnitude of the F–value and correspondingly the smaller the ‘Prob. > F’ value, the more significant is the corresponding coefficient.

Regression analysis was performed to fit the response. Regression models were developed for each response, BOD ( $Y_1$ ), COD ( $Y_2$ ) and TDS ( $Y_3$ ), as a function of  $X_1$ ,  $X_2$  and  $X_3$  as shown in Equations (1)–(3).

$$Y_1 = 16.77376 + 20.53151X_1 + 0.00898969X_2 + 0.83339X_3 - 0.00315893X_1X_2 - 0.0404X_1X_3 + 0.00131857X_2X_3 - 2.18168X_1^2 - 0.000119434X_2^2 - 0.012179X_3^2 \quad (1)$$

$$Y_2 = 28.24171 + 8.58117X_1 + 0.065582X_2 + 0.98606X_3 - 0.00267679X_1X_2 + 0.0115X_1X_3 - 0.00114714X_2X_3 - 0.98926X_1^2 + 0.00000121939X_2^2 - 0.012491X_3^2 \quad (2)$$

$$Y_3 = 46.06836 + 13.10999X_1 + 0.029843X_2 - 0.45001X_3 - 0.00045X_1X_2 - 0.066675X_1X_3 - 0.00105643X_2X_3 - 1.18449X_1^2 + 0.0000849082X_2^2 + 0.010792X_3^2 \quad (3)$$

Statistical testing of the models was executed with analysis of variance (ANOVA) and the results are given in Tables 6–8.

Table 6: Analysis of variance of model developed for BOD

Source	Sum of squares	DF	Mean square	F-Value	P-Value	
Model	1377.52	9	153.06	442.35	< 0.0001	Significant
$X_1$	1032.37	1	1032.37	2983.67	< 0.0001	
$X_2$	14.73	1	14.73	42.58	0.0003	
$X_3$	$4.42 \cdot 10^{-3}$	1	$4.42 \cdot 10^{-3}$	0.013	0.9132	
$X_1X_2$	0.78	1	0.78	2.26	0.1764	
$X_1X_3$	0.65	1	0.65	1.89	0.2119	
$X_2X_3$	0.85	1	0.85	2.46	0.1606	
$X_1^2$	320.66	1	320.66	926.73	< 0.0001	
$X_2^2$	1.44	1	1.44	4.17	0.0805	
$X_3^2$	0.39	1	0.39	1.13	0.3234	
Residual	2.42	7	0.35			
Lack of Fit	1.56	3	0.52	2.4	0.2086	not significant
Pure Error	0.87	4	0.22			
Cor Total	1379.94	16				

The model Fisher F-tests of 442.35, 50.02 and 45.05 with low probability value ( $p < 0.0001$ ) show a high statistical significance for the regression models as shown in Table 6–8[10]. The "Lack of Fit F-values" of 2.4, 1.46 and 0.44 and P-values of 0.2086, 0.3521 and 0.7355 imply the Lack of Fit is not significant relative to the pure error.

A non-significant lack of fit is desirable as it implies that the model could be used for theoretical prediction of the reduction of BOD, COD and TDS (Vazquez *et al.*, 2011). The  $R^2$  values of 0.9960, 0.9650 and 0.988 imply that the predicted values were found to be in good agreement with

experimental values (Khataee *et al.*, 2010). A regression model is well defined if  $R^2$  value is higher than 0.80 (Sin *et al.*, 2006). Response surface curves were generated from the statistical models to examine the interactions between the independent variables and to determine the optimum levels of the variables.

The effects of adsorbent dosage, contact time and temperature on BOD reduction, COD reduction and TDS reduction as responses are shown in the response surface graphs given in Figure 1–9.

Table 7: Analysis of variance of model developed for COD

Source	Sum of squares	DF	Mean square	F Value	P-Value	
Model	323.53	9	35.95	50.02	< 0.0001	Significant
$X_1$	242.65	1	242.65	337.64	< 0.0001	
$X_2$	12.24	1	12.24	17.03	0.0044	
$X_3$	0.08	1	0.08	0.11	0.7484	
$X_1X_2$	0.56	1	0.56	0.78	0.406	
$X_1X_3$	0.053	1	0.053	0.074	0.794	
$X_2X_3$	0.64	1	0.64	0.9	0.3751	
$X_1^2$	65.93	1	65.93	91.74	< 0.0001	
$X_2^2$	$1.5 \cdot 10^{-4}$	1	$1.5 \cdot 10^{-4}$	$2.09 \cdot 10^{-4}$	0.9889	
$X_3^2$	0.41	1	0.41	0.57	0.4744	
Residual	5.03	7	0.72			
Lack of Fit	2.63	3	0.88	1.46	0.3521	not significant
Pure Error	2.4	4	0.6			
Cor Total	328.56	16				

Table 8: Analysis of variance of model developed for TDS

Source	Sum of squares	DF	Mean square	F Value	P-Value	
Model	520.41	9	57.82	45.05	< 0.0001	Significant
$X_1$	419.33	1	419.33	326.67	< 0.0001	
$X_2$	4.08	1	4.08	3.18	0.1179	
$X_3$	0.023	1	0.023	0.018	0.8966	
$X_1X_2$	0.016	1	0.016	0.012	0.9146	
$X_1X_3$	1.78	1	1.78	1.39	0.2777	
$X_2X_3$	0.55	1	0.55	0.43	0.5348	
$X_1^2$	94.52	1	94.52	73.63	< 0.0001	
$X_2^2$	0.73	1	0.73	0.57	0.4757	
$X_3^2$	0.31	1	0.31	0.24	0.64	
Residual	8.99	7	1.28			
Lack of Fit	2.24	3	0.75	0.44	0.7355	not significant
Pure Error	6.75	4	1.69			
Cor Total	529.39	16				

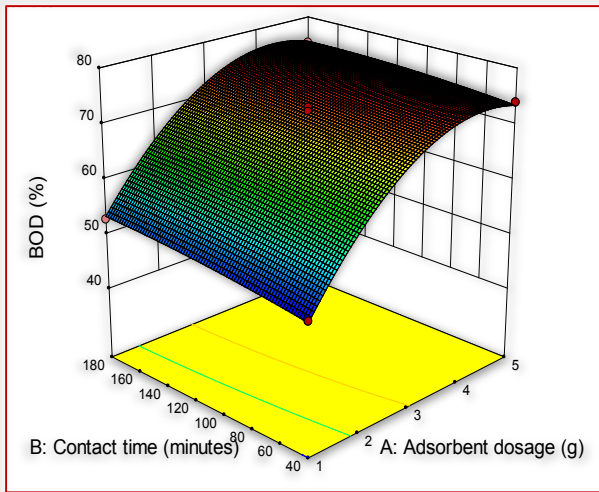


Figure 1: Response surface plot showing predicted BOD reduction as a function of adsorbent dosage and contact time with temperature fixed at 35°C.

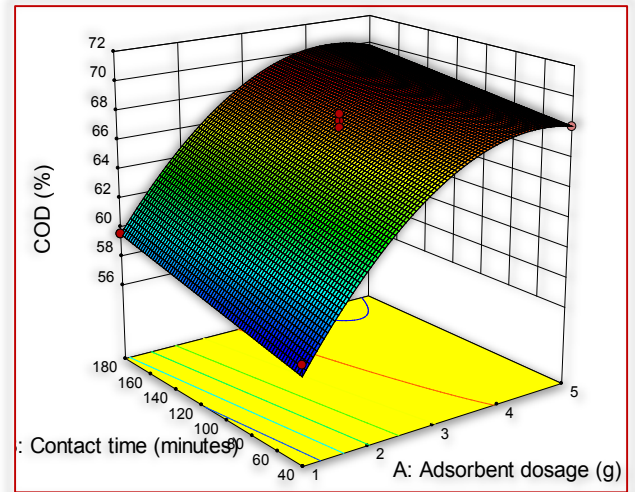


Figure 4: Response surface plot showing predicted COD reduction as a function of adsorbent dosage and contact time with temperature fixed at 35°C.

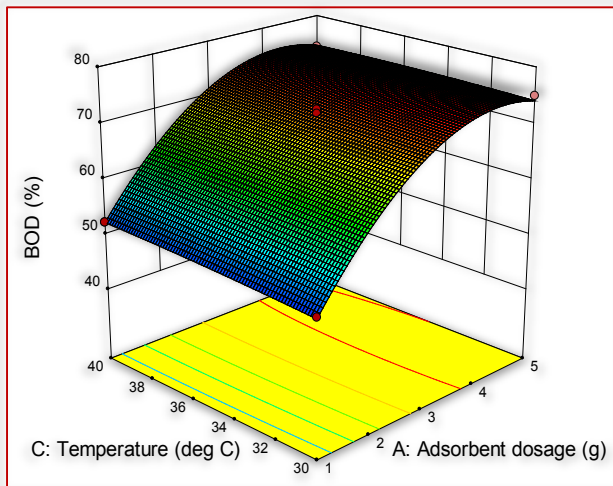


Figure 2: Response surface plot showing predicted BOD reduction as a function of adsorbent dosage and temperature with contact time fixed at 110minutes.

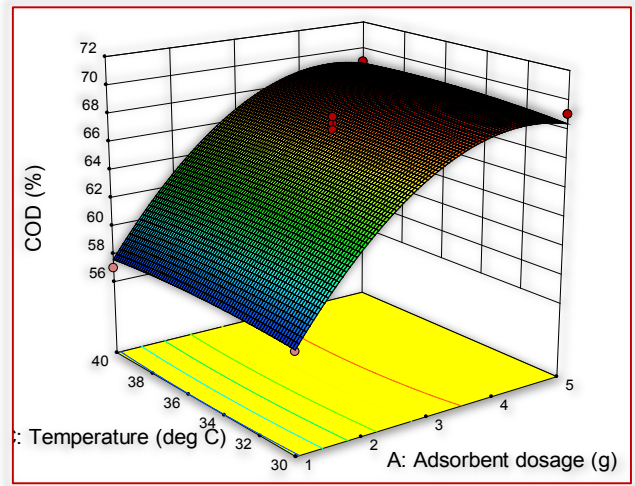


Figure 5: Response surface plot showing predicted COD reduction as a function of adsorbent dosage and temperature with contact time fixed at 110minutes.

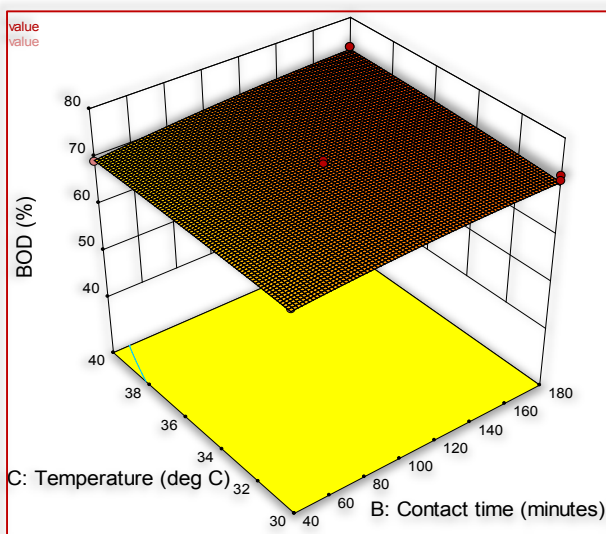


Figure 3: Response surface plot showing predicted BOD reduction as a function of contact time and temperature with fixed adsorbent dosage at 3g.

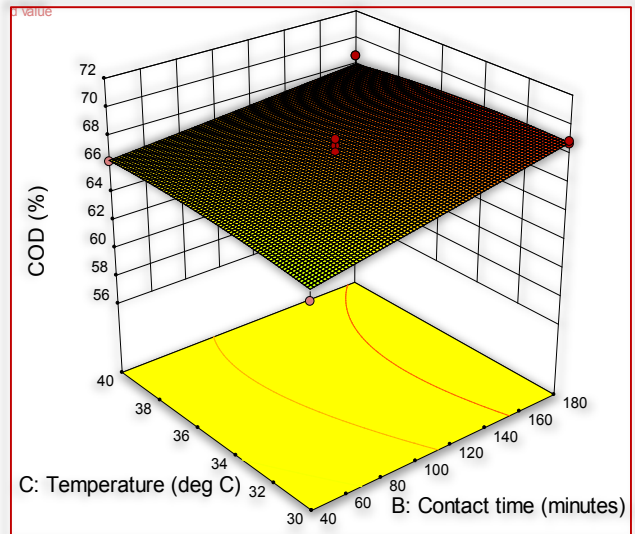


Figure 6: Response surface plot showing predicted COD reduction as a function of temperature and contact time with adsorbent dosage fixed at 3g.

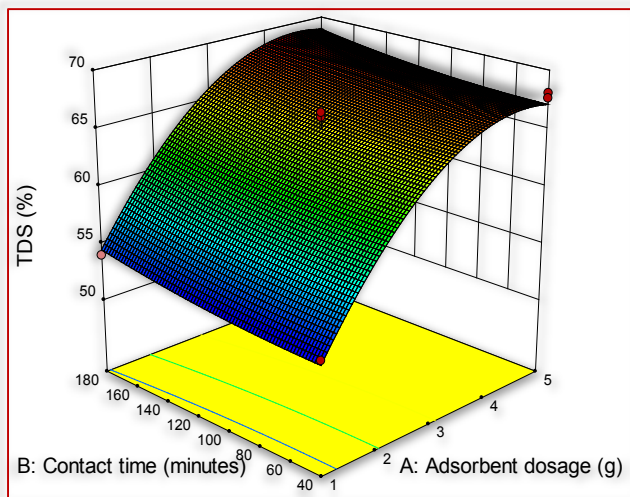


Figure 7: Response surface plot showing predicted TDS reduction as a function of adsorbent dosage and contact time with temperature fixed at 35°C.

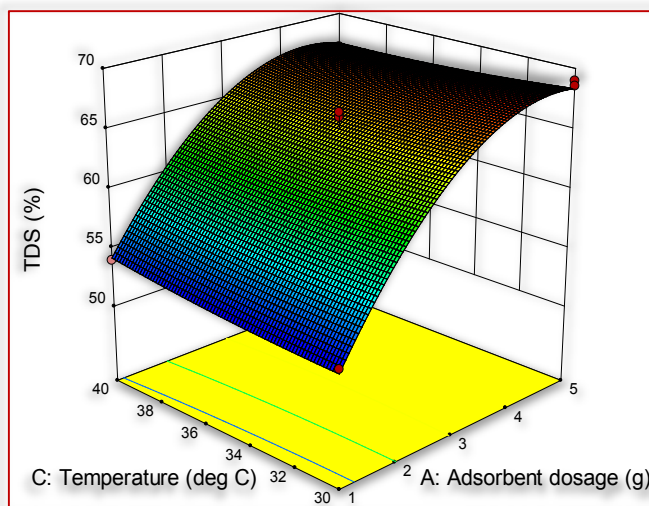


Figure 8: Response surface plot showing predicted TDS reduction as a function of adsorbent dosage and temperature with contact time fixed at 110 minutes

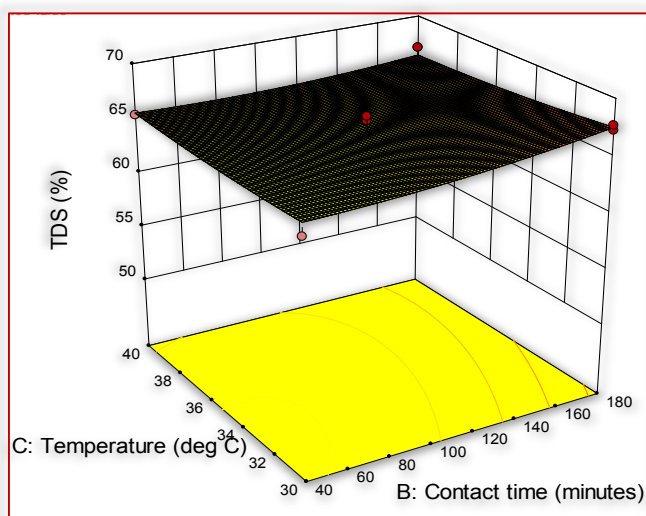


Figure 9: Response surface plot showing predicted TDS reduction as a function of contact time and temperature with adsorbent dosage fixed at 3g

From Figures 1–3 BOD removals increased as adsorbent dose, contact time and temperature increased. There was a high statistical influence of adsorbent dose on BOD reduction compared to contact time. Also BOD reduction was more affected by contact time than temperature. This is also corroborated by the fact that adsorbent dose had a much smaller p value ( $<0.0001$ ) than contact time, which had a smaller p value than temperature as shown in Table 6.

From Figures 4–6, COD removal increased as adsorbent dose, contact time and temperature increased. There was a high statistical influence of adsorbent dose on COD reduction compared to contact time. Also COD reduction was more affected by contact time than temperature. This is also corroborated by the fact that adsorbent dose had a much smaller p value ( $<0.0001$ ) than contact time, which had a smaller p value than temperature as shown in Table 7.

From Figures 7–9 TDS removal increased as adsorbent dose, contact time and temperature increased. There was a high statistical influence of adsorbent dose on TDS reduction compared to contact time and temperature. Also TDS reduction was more affected by contact time than temperature. This is also corroborated by the fact that adsorbent dose had a much smaller p value ( $<0.0001$ ) than contact time, which had a smaller p value than temperature as shown in Table 8. As shown in Figures 2, 3, 5, 6, 8 and 9, generally temperature did not have any significant effect on BOD, COD and TDS reduction. This is corroborated by the fact that temperature had high p-values of 0.9132, 0.7484 and 0.8966 as shown in Tables 6–8.

The values of adsorbent dose, contact time and temperature were optimized based on the statistical models. The highest BOD, COD and TDS percentage reduction of 75.268%, 69.865% and 69% respectively at optimum adsorbent dose of 5 g, contact time of 180 min and temperature of 34.4°C.

The validity of the results predicted by the regression models, were confirmed by carrying out triplicate experiments under optimal conditions (that is adsorbent dose of 5 g, contact time of 180 min and temperature of 34.4°C).

The results obtained from three replications demonstrated that the average of percentage reductions of 74.98%, 69.78% and 68.99% for BOD, COD and TDS respectively were close to the predicted percentage reduction values of 75.268%, 69.865% and 69% for BOD, COD and TDS respectively. The excellent correlation between the predicted and measured values after optimization justified the validity of response models.

## CONCLUSION

In this study the reduction of BOD, COD and TDS of brewery effluent using activated carbon from coconut shell as adsorbent was investigated. A three-variable Box-Behnken design was used to study the simultaneous effects of adsorbent dose, contact time and temperature on reduction of BOD, COD and TDS of brewery effluent. The models developed to describe relationship among reduction of BOD, COD and TDS and the chosen independent variables were

statistically significant ( $p < 0.0001$ ). From the RSM, the optimum values of variables were: 5 g for adsorbent dose, 180 min for contact time of 180 min and 34.4°C for temperature. The reduction of BOD, COD and TDS were generally favoured by increased adsorbent dose, contact time and, not so significantly, by temperature.

#### References

- [1] Alao, O., Arojojoye, O., Ogunlaja, O. and Famuyiwa, A: Impact assessment of brewery effluent on water quality in Majawe, Ibadan, southwestern Nigeria, *Researcher*, vol. 2(5), pp. 21–28, 2010.
- [2] American Public Health Association–APHA .Standard methods for the examination of water and waste, 20th ed., Washington, D.C USA, APHA –AWWA– WPCF, 2005.
- [3] Carmona, M.E.R., da Silva, M.A.P. and Leite, S.G.F: Biosorption of Chromium using Factorial Experimental Design, *Process Biochemistry*, vol. 40, pp. 779–788, 2005.
- [4] Gupta, N., Prasad, M., Singhal, N. and Kumar, V: Modeling the Adsorption Kinetics of Divalent Metal Ions onto Pyrophyllite Using the Integral Method, *Industrial and Engineering Chemistry Research*, vol. 48(4) pp. 2125–2128, 2009
- [5] Huang, W., Zhenshan, L., Niu, H., Li, D. and Zhang, J : Optimization of Operating Parameters for Supercritical Carbon Dioxide Extraction of Lycopene by Response Surface Methodology, *Journal of Food Engineering*, vol. 89, pp.298–302, 2008.
- [6] Khataee, A. R., Gholamreza, D., Elahe, E. And Minoo, P : Central Composite Design Optimization of Biological Dye Removal in the Presence of Macroalgae *Chara* sp. *Clean, Soil, Air, Water*, vol. 38 (8), pp.750–757, 2010.
- [7] Mabrouk, E., Ikram, J. and Mourad, B :Adsorption of Copper Ions on Two Clays From Tunisia: pH and Temperature Effects, *Applied Clay Science*, vol. 46, pp. 409–413, 2009
- [8] Maiti, S.K. *Handbook of Methods in Environmental Studies* (1 and 2) ABD Publishers, Jaipur, 2004.
- [9] Ninnekar, H.Z: Purification and properties of 2,3–dihydroxy–p–cumate–3,4–dioxygenase from *Bacillus* species, *Biochemistry international*, vol. 28, pp. 97–103, 1992.
- [10] Noorjahan, C.M. and Jamuna, S: Physico–Chemical Characterisation of Brewery Effluent and Its Degradation using Native Fungus – *Aspergillus Niger*, *Aquatic Plant – Water Hyacinth– Eichhornia sp* and Green Mussel – *Pernaviridis*, *Journal of Environment and Earth Science*, vol. 2 (2), pp.31–40, 2012
- [11] Sin, H. N., Yusof, S., Hamid, N. S. A. and Rahman, R. A: Optimization of enzymatic clarification of sapodilla juice using response surface methodology, *Journal of Food Engineering*, vol. 73, pp. 313–319, 2006.
- [12] United Nations Environment Programme (UNEP). A snapshot of the world's water quality: towards a global assessment. Nairobi, 2016.
- [13] Vazquez, M., Delgado, R. and Castro, A.J: Modelling of the enzymatic hydrolysis of potato (*Solanum tuberosum*) using response surface methodology, *Starch*, vol. 61, no. 10, pp. 601–609, 2009.
- [14] Yi, S., Su, Y., Qi, B., Su, Z. and Wan, Y: Application of response surface methodology and central composite rotatable design in optimization; the preparation condition of vinyltriethoxysilane modified silicalite/polydimethylsiloxane hybrid pervaporation membranes, *Separation and Purification Technology*, vol.71, pp.252–262, 2010.



ISSN: 2067–3809

copyright © University POLITEHNICA Timisoara,  
Faculty of Engineering Hunedoara,  
5, Revolutiei, 331128, Hunedoara, ROMANIA  
<http://acta.fih.upt.ro>

<sup>1</sup>Irena Barbara JAŁMUŻNA, <sup>2</sup>Jan KRÓLIKOWSKI, <sup>3</sup>Justyna SAŁATA

## METHODOLOGY OF RAPID VERIFICATION OF WORK STANDARDS

<sup>1-3</sup>Lodz University of Technology, Faculty of Organization and Management, Lodz, POLAND

**Abstract:** The paper presents the use of properly selected research methods allowing for quick verification of the operator's labour standards for workstations. It concerns the evaluation and improvement of work method on the examined assembly station. The method used the principles of TQM, Lean Thinking, TOC, Kaizen, standardisation of time and ergonomics. The result of this approach was the rapid evaluation of the operator's labour standards and identification of the personalised standard that allows to work specific operators within acceptable deviations from the assumed normative.

**Keywords:** efficiency, lean, standardization of work, rapid evaluation, statistical tests

### INTRODUCTION

Any company, both manufacturing type and service type, want to improve their processes. They always reach for the work optimization tools. But before the company will develop practical solutions it has to often go through the tedious process of collecting and processing data. Therefore, it becomes essential to reduce test time and data analysing time. Hence important is the adoption of appropriate research methods for a rapid, but simultaneously complex operation.

In this study, the authors tried to show how to deal with the problem in the standardization of working time in the development of labour standards in the assembly station with a high degree of employee fluctuation, where the collection of multiple measures is often very limited due to the limited time that can be allocated for the measurement process. Attention was also drawn to the tools of statistical inference, so that the analysis of these data is appropriate and allows for the proper conduct of inference.

### PREMISES OF LITERATURE

Looking through the eye of the management concept and the production control concepts [12; 14-20; 23; 25-29] it should be noted that each of them points to the need for optimal process management. Each of the concepts indicates the direction of the appropriate action, as many authors write [12; 14-20; 23; 25-29], the managers may freely choose the appropriate set of tools to evaluate appearing enterprise specific problems. There are a number of different publications, in which there are shown different methodologies used in processes [1-3;5-11;13;15-17;19-21;23-29] and application in case studies [2; 7; 9-10; 13; 19; 22; 27; 29], on the basis of which the persons managing and improving the different processes can freely implement various methods in their processes on the basis of benchmarking.

Considering the number of different approaches to process improvement [12; 14-20; 23; 25-29] and a variety of case studies [1-3;5-21; 23-29], it should be noted that each of the organizations using known management principles must develop its own model of process improvement. This applies

both to process management and organization of work stations [12; 14-20; 23; 25-29]. Selection of the appropriate methodology for the procedure is closely connected with the knowledge of managers and their knowledge of the methods, and management techniques.

Following the literature [1-29], one can assume that there is no universal solution for any given problem, therefore, in this paper, based on the presented references a new approach to the problem is presented, taking into account the needs of the enterprise concerned.

### RESEARCH METHODOLOGY

For the investigation, the authors adopted the appropriate research methodology, which uses the principles of production management concept, as the philosophy of TQM, Lean Thinking, TOC and Kaizen [1-29].

The main objective of the study was to optimize of the work on the assembly station of the examined production process. In connection with the adoption of this objective thought was given to the two key problems.

1. How can you quickly evaluate initial research sample for the possibility of limiting the number of future measurements?
2. What factors influence the standards of work performed on the surveyed assembly station?

In accordance with a first research question, the following hypotheses were developed:

- H<sub>0</sub>: it is possible to quickly verify of the existing standards on the tested production line based on a small number of measurements;
- H<sub>1</sub>: lack of the quick verification of the existing standards on the tested production line based on the small number of measurements.

Accordingly, for the designated assembly station the test methodology consist of 7 stages:

1. observation of the operators using tools of time standardization and statistical data verification,
2. study the movements of hands on assembly station based on the techniques of Work Measurement to assess the standards of the operators,
3. identification of the losses the operators work,

4. assessment of takt time,
5. quick assessment of the accuracy of current standard of work on the assembly station,
6. brainstorming in order to identify the most important changes,
7. develop a new standard.

Because of the complexity of the methodology assumed in this study it will be short presentation of all the points from the above list and the following chapter tries to answer the first research question.

#### EVALUATION OF OPERATORS WORK USING TOOLS OF TIME STANDARDIZATION AND STATISTICAL DATA VERIFICATION

##### — Characteristics of the research sample

Due to the lack of permission of the Management Board of the company to disclose its name, in this study it will be determined by description "manufacturing company with foreign capital." Examined company is a Polish subsidiary of German company which employs nearly 39,000 workers in 43 factories around the world, including Belgium, China, the United States, Canada, Turkey, Holland, Italy, Portugal, Germany, Poland, Russia, Slovakia or France. The company is the largest manufacturer in Europe in its sector and one of the leaders in the sector. The company sells its products under many brand names, fifty-four brand-names in total.

The company started its activity in 1993 in the central part of the Poland, in city of Lodz in 1999. They created a modern production plant, which now has two factories, due to the fact that six years later they expanded as the investment in the Lodz Special Economic Zone. Currently both plants are producing more than 3 million units per year.

Divisions of company in central Poland are certified according to ISO 9001, ISO 14001, OHSAS 18001. The company works mainly with local suppliers of raw materials and semi-finished products, putting the supply within the Just-in-Time system. Among the suppliers there are also the company divisions from three other counties. Analysed company is also a supplier within the Group. The Customers of products manufactured by the company are primarily large retail chains, as well as individual consumers, both in Poland and around the world. Analysed company also runs a number of investments at national and global levels.

##### — The analysed process of working on workstations

In the analysed company the production staff work three shifts. In addition, every two hours, every shift is obligatory rotation of employees at workplaces.

The analysis covers the work of assembly station fitting engines in final products. The engines are subjected to a process of sub-assembly in the area of picking. The employee has the task of completion of the transportation carriage consisting of 30 pieces sub assembled equipment and 30 pieces of pulleys and in addition a proper quantity of seals. Preparation of carriages is driven by a sequential plan delivered from the production area by e-mail.

After preparing a set of two carriages the "milkrun" driver moves them to the appropriate assembly line every 30 minutes. On the production floor take place the actual process of engine assembly and fitting pulley to the manufactured product. The employee gets from the carriage a pulley and mount it on the spindle, fitting tanks and engine. During installation, the employee performs the control of a serial number of the engine.

In the assembly station the flow of the engine ends as a single component. In further processes, it is present as a subcomponent of another level in Bill of Material.

##### — Observation of operator using tools of time standardization and statistical data verification

Due to the fact that it was found that one of the main problems in the process is the lack of standardized work in the assembly of the engine, researches carried out their own observation on this position using the method of timing. As is known the success of this method depends on the right amount of data, the collection of which often have time limits, and from the other hand operators are reluctant to agree to the filming and often one should perform this type of observation from the hide. In the analysed company is a serious aspect of the high rotation of employees in positions, which further is reflected in the difficulty in collecting a large number of measurements.

Table 1 – Timing the assembly operations

Operations	Results						
	1	2	3	4	5	6	7
Pick screw	1	1,4	1	1,3	1,4	2	1,1
Pick and fitting pulleys	2	2	2,8	2,5	2,6	2,5	2
Placing screw	1,5	1,2	1,8	1,3	1,2	1,8	1,3
Pick screw gun and transfer to right hand	1,5	1,5	1,3	1,3	1,1	1,5	1,3
Screwing the first screw	2	1,4	1,7	2	1,7	2	1,6
Screwing the second screw	2	1,9	1,3	1,7	1,8	2	1,8
Screwing the third screw	2	1,6	2	1,9	1,8	2	1,8
Screwing the fourth screw	2	1,4	2	1,6	2	1,8	2
Pick foil and fit on engine	3,5	2,7	4	3,5	3,5	3,3	4
Engine assembly	3,5	3,9	3	3,2	3	3	3
Picking two screws and assembly	2	2,5	2,3	2	2,3	2,3	2
<b>Total</b>	<b>23</b>	<b>21,5</b>	<b>23,2</b>	<b>22,3</b>	<b>22,4</b>	<b>23,9</b>	<b>21,8</b>

Accordingly, statistical tools were used with the highlight on statistical Ryan-Joiner test appropriate for the small samples [4] test that helps determine the sample size for a reliable analysis of the time distribution operations. This test involves checking the strength of the correlation between the data

from the sample and the normal distribution for the data. If the correlation coefficient (1) is close to 1, it is presumed that the data are normally distributed. However, if the ratio is below the critical level, then one must reject the null hypothesis  $H_0$ . Determination of distribution of test data is necessary for the selection of appropriate statistical methods in further stages of research.

$$R = \frac{\sum_{i=1}^n b_i y_i}{\sqrt{\sum_{i=1}^n (y_i - \bar{y})^2 \cdot \sum_{i=1}^n b_i^2}} \quad (1)$$

where:  $y_i$  - sample data,  $b_i$  - percentage point from the normal distribution

Therefore, for the investigated process, researchers initiated two hypotheses: the null and alternative which reads as follows:

$H_0$ : Time distribution of operation is a normal distribution

$H_1$ : Time distribution of operation is not a normal distribution

In order to verify the hypotheses were made observation of the variation of the operation for the worker and the results are shown in Table 1. On the basis of the data contained in it started to test for normality Ryan-Joiner time distribution operations. The results obtained are shown in Figure 1.

» **Interpretation of results:**

The analysis of the parameters shown in Figure 1 shows that if the critical level P. Value is greater than 0.1 then there is no reason to reject the null hypothesis. Therefore, it is assumed that the distribution operation time in the assembly of the engine is normally distributed.

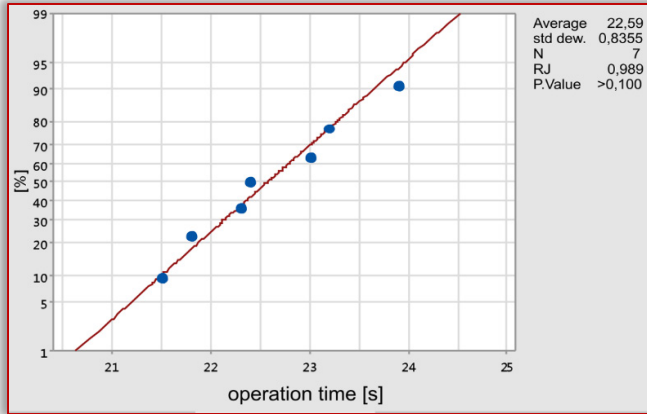


Figure 1 – Test Ryan-Joiner to prove normal distribution of operation time in the assembly line (Source: own study based on calculations in Minitab)

Referring to the result obtained in the test Ryan-Joiner, assuming that the operation time in the assembly the engine has a normal distribution, Minitab software application determined the required minimum number of measurements.

If the population has a normal distribution  $N(\mu, \sigma)$ , where  $\sigma^2$  is unknown, and value  $\hat{s}^2$  obtained from initial small trials with a number of  $n_0$  elements, the necessary population size was determined in the Formula 2 [4]:

$$n = \frac{t_{\alpha}^2 \cdot \hat{s}^2}{d^2} \quad (2)$$

where:  $t_{\alpha}$  - the value of the variable t-Student read from the statistical tables for  $n-1$  degrees of freedom and  $1-\alpha$  ( $t_{\alpha} = 2,4469$ ); is to  $P\{-t_{\alpha} < t < t_{\alpha}\} = 1 - \alpha$ ,  $\hat{s}$  - the standard deviation of the initial sample;  $d$  - margin of error (0,5s).

As a result of the program analysis it was obtained that at the 95% confidence level it is necessary to perform fourteen motion measurements of engine assembly for one workers according to individual movement patterns Figure 2.

Table 2 summarizes the average results and deviations of the cycle time of observed 5 employees. The analysis of the data shows that there is a difference in the meantime operations by employees, as well as their volatility. The histogram of processing time – Figure 3 it can be seen that the operators the third and fifth workers have the shortest average assembly times, and the first worker have the highest average installation time.

Sample Size for Estimation	
<b>Data</b>	
Parameter	Mean
Distribution	Normal
Standard deviation	0.84
Confidence level 95%	
Confidence interval	Two- sided
<b>Results</b>	
Margin of Error	0.5 s
Sample Size	14

Figure 2 – Determination of sample size

(Source: own calculations in Minitab)

Table 2 – Summary installation times for different labour standards

Cycle times in the assembly of the engine [s]						
Indicator	Small sample	1st person	2nd person	3rd person	4th person	5th person
$\bar{x}$	22,59	22,51	21,04	19,51	20,85	19,72
S(x)	0,84	0,66	0,71	0,63	0,73	0,79

In order to choose the best variant of work appropriate statistical tests were performed to determine whether the differences in times are random or are statistically significant and are based on different standards of work. It was assumed that all tests will be performed at the level of significance  $\alpha = 0,05$ .

It was assumed that the assembly times for individual operators are adequate to the pre-test, are normally distributed, therefore, to verify the equality of variances in the population has benefited from the Bartlett test. To perform the test was the following hypotheses:

- $H_0$ : Variances of operation time are the same for each individuals
- $H_1$ : Variances of operation time are the different for each individuals

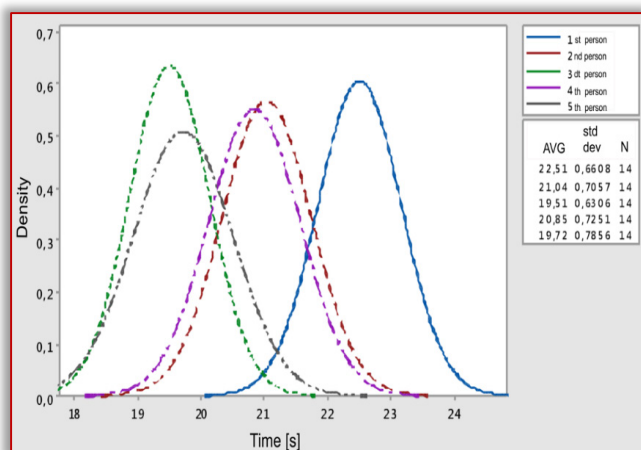


Figure 3 – Histogram of engine assembly time depending on the operator (Source: own calculations in Minitab)

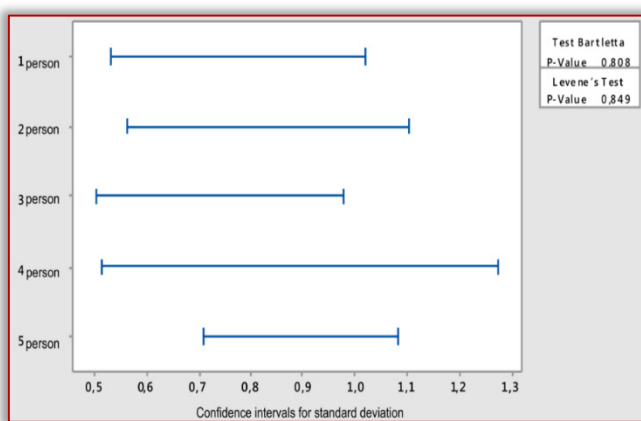


Figure 4 – Bartlett's test for equality of variances for the time of operation the successive operators (Source: own calculations in Minitab)

» Interpretation of the result:

Due to the fact that the critical level is 0.808 and is higher than the target level of confidence ( $0,05 \leq p \leq 0,808$ ) there is no reason to reject the null hypothesis, and therefore it is assumed that the variances of operation time for individuals are the same.

Due to the fact, that it was assumed that the analysed times are normally distributed and have the same variance it is possible to perform the test ANOVA. This test allows to indicate one of the surveyed methods that holds the best average results.

The test ANOVA undertakes two hypotheses regarding the equality of average time of operations for individual employees:

- $H_0$ : All average times of operations for individuals are the same
- $H_1$ : All average times of operations for individuals are not the same

» Interpretation of the result:

Due to the fact that the value of the critical level is lower than the target level of confidence ( $p \leq 0,05$ ) the null hypothesis must be rejected. The null hypothesis assumes that the average times of operation are the same.

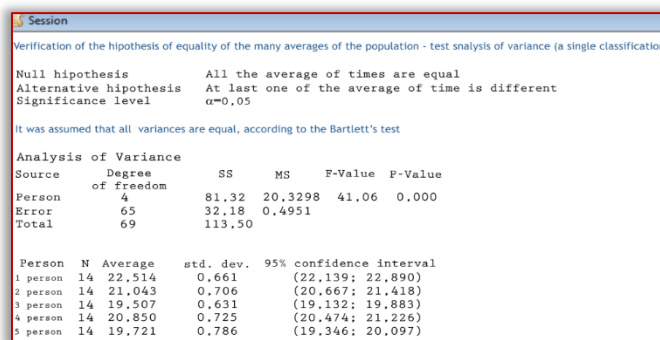


Figure 5 – The ANOVA test for equality of averages in the population (Source: own calculations in Minitab)

Consequently with the obtained result of the ANOVA Figure 5 it is necessary to analyse the confidence interval for average assembly times for operators. Based on Figure 6 it concluded that the best methods are applied by operator 3 and operator 5 because of the shortest duration.

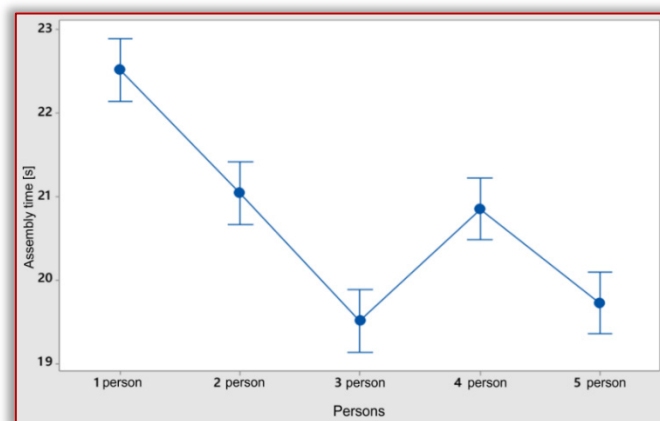


Figure 6 – 95% confidence intervals for the average assembly times

The next step of choosing the best variant from among the designated two is to perform the Student test (3). This test checks whether the average assembly times for these operators are the same or different.

$$t = \frac{\bar{X}_1 - \bar{X}_2}{\sqrt{\frac{n_1 \cdot s_1^2 + n_2 \cdot s_2^2}{n_1 + n_2 - 2} \cdot \left(\frac{1}{n_1} + \frac{1}{n_2}\right)}} \quad (3)$$

Following hypotheses were posed:

- $H_0$ : Both average times of operations for individuals 3, 5 could be treated as identical
- $H_1$ : the two average times of operations for individuals 3, 5 could not be treated as identical

Result of simulation performed in Minitab software are shown on Figure 7.

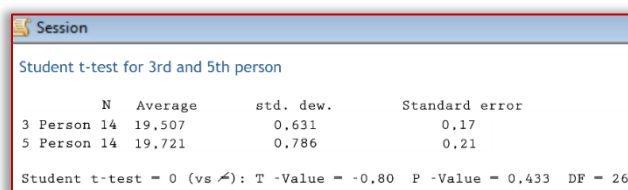


Figure 7 – Student's test for equality of two means in the population (Source: own calculations in Minitab)

» **Interpretation of the result:**

Due to the fact that the value of the critical level is above a predetermined level of confidence ( $0,05 \leq p \leq 0,433$ ) there are no grounds to reject the null hypothesis.

As a result of conducted statistical tests, it was found that among work standards carried out by operators of engine assembly line two out of five operators deserve attention, because they do not have significant differences in the speed of operations performed, but only in the way they perform. Therefore, it was assumed that the standards of the third operator, and a fifth became the basis for the development of the applicable work standard.

**CONCLUSIONS**

The adopted research methodology allowed for the rapid assessment of collected data based on a small number of measurements, which allowed to carry out the speedy verification of existing labour standards in workplaces on the assembly line. At the same time research confirmed the validity of tested research hypothesis about the possibility of a rapid verification of the work standards on the designated production line based on a small number of measurements.

**Note**

This paper is based on the paper presented at 9th International Conference "Management of Technology – Step to Sustainable Production" – MOTSP 2017, organized by Faculty of Mechanical Engineering and Naval Architecture of the University of Zagreb, CROATIA and University North, Varaždin, CROATIA, in Dubrovnik, CROATIA, 5 – 7 April 2017.

**References**

[1] Czerska, J., Pozwól płynąć swojemu produktowi, Wydawnictwo PLACET, Warszawa, 2011.

[2] Dennis, P., Lean Production Simplifies: A Plain Language Guide to the World's Most Powerful Production System, Productivity Press, New York, 2007.

[3] Domagała, W., Badania metod pracy, TWWP, Warszawa, 1971.

[4] Domański, C., Metody statystyczne. Teoria i zadania, Wydawnictwo UŁ, Łódź, 2001

[5] Imai, M.: Gemba Kaizen: zdroworoządkowe, niskokosztowe podejście do zarządzania, MT Biznes, Warszawa 2006.

[6] Jordan, J., Michel, F.: The Lean company making the right choices, Society of Manufacturing Engineers, Michigan, 2001.

[7] Kubik, Sz., Gniazdo produkcyjne. Przepływ jednej sztuki dla zespołów roboczych, ProdPublishing, Wrocław, 2010.

[8] Kubik, Sz., Kornicki, L.: 5S dla operatorów. 5 filarów wizualizacji miejsca pracy, ProdPress.com, Wrocław, 2008.

[9] Kubik, Sz., Kornicki, L.: Identyfikacja marnotrawstwa na hali produkcyjnej, ProdPublishing.com, Wrocław, 2008

[10] Kubik, Sz., Kornicki, L.: Standaryzacja pracy na hali produkcyjnej, ProdPress.com, Wrocław 2008.

[11] Kubik, Sz., Wąsiel, M.: Kanban na hali produkcyjnej, ProdPublishing, Wrocław, 2015.

[12] Lewandowski, J., Antosiak, M., Production planning and control, Wyd. Politechniki Łódzkiej, Łódź, 2012.

[13] Lewandowski, J., Jałmużna, I.: Contemporary problems in managing production and services supporting manufacturing processes, Wydawnictwo Politechniki Łódzkiej, Łódź, 2009.

[14] Lewandowski, J., Organizacja systemów produkcyjnych, PWE, Warszawa, 2014.

[15] Lisiński, M., Martyniak, Z., Potocki, A.: Techniki organizatorskie: badanie pracy, Akademia Ekonomiczna, Kraków 1985.

[16] Maciak, J.: Klasyfikacja metod, koncepcji, technik i narzędzi zarządzania, Ekonomia i organizacja przedsiębiorstwa, 4(2009), 711.

[17] Michłowicz, E.: Metody i techniki Lean Management jako ważny element logistyki produkcji w małych firmach, Gospodarka Materiałowa i Logistyka, 1 (2011).

[18] Mikołajczyk, Z.: Techniki organizatorskie w rozwiązywaniu problemów zarządzania, PWN, Warszawa, 2002.

[19] Monden, Y.: Toyota Production System: An Integrated Approach to Just- In- Time, 4<sup>th</sup> edition, Industrial Engineering and Management Press, Michigan University, 1993.

[20] Nicholas, J.: Lean Production for competitive advantage: A comprehensive guide to Lean methodologies and management practices, CRC Press, New York, 2010.

[21] Rother, M., Harris, R.: Creating continuous flow: an action guide for managers, engineers and production associates, Lean Enterprise Institute, Cambridge, 2003.

[22] Rother, M., Harris, R.: Creating continuous flow: an action guide for managers, engineers and production associates, Lean Enterprise Institute, Cambridge, 2003.

[23] Rother, M., Harris, R.: Tworzenie ciągłego przepływu, Lean Enterprise Institute Polska, Wrocław, 2004.

[24] Rother, M., Shook, J., Womack, J., Jones, D.: Learning to see: Value Stream Mapping to add value and eliminate MUDA, Lean Enterprise Institute, Cambridge, 2003.

[25] Szymonik, A.: Transport economics for logistics and logisticians: theory and practice, Lodz University of Technology Press, Łódź, 2013.

[26] Womack, J., Jones, D.: Odchudzanie firm. Eliminacja marnotrawstwa – kluczem do sukcesu, Centrum Informacji Menedżera, Warszawa, 2001.

[27] Womack, J. P., Jones, D. T.: Lean Thinking: Banish waste and create wealth in your corporation, Free Press, New York, 2003.

[28] Womack, J. P., Jones, D. T., Ross, D.: The machine that changed the world: The story of Lean Production, HarperCollins, California, 1991.

[29] Womack, J. P.: Lean Solutions: How companies and customers can create value and wealth together, Simon and Schuster, New York, 2009.



ISSN: 2067-3809

copyright © University POLITEHNICA Timisoara,  
Faculty of Engineering Hunedoara,  
5, Revolutiei, 331128, Hunedoara, ROMANIA  
<http://acta.fih.upt.ro>

# Fascicule 4

## [October - December]

t o m e

# XI

[2018]

**ACTA**Technica**CORVINIENSIS**  
BULLETIN OF ENGINEERING



**ISSN: 2067-3809**

copyright © University POLITEHNICA Timisoara,  
Faculty of Engineering Hunedoara,  
5, Revolutiei, 331128, Hunedoara, ROMANIA  
<http://acta.fih.upt.ro>

<sup>1</sup>Mihai–Paul TODOR, <sup>2</sup>Ciprian BULEI, <sup>3</sup>Imre KISS

# AN OVERVIEW ON KEY TRENDS IN COMPOSITE MATERIALS CONTINUOUS INNOVATION AND IMPROVEMENTS WITH FOCUS ON COMPOSITES BASED ON CELLULOSE FIBERS

<sup>1-2</sup>University Politehnica Timisoara, Faculty of Engineering Hunedoara, Doctoral School, Timisoara / Hunedoara, ROMANIA

<sup>3</sup>University Politehnica Timisoara, Faculty of Engineering Hunedoara, Dept. Engineering & Management, Hunedoara, ROMANIA

**Abstract:** The composite materials have shown improved properties compared to those of metal and polymeric materials, which made the composites being used as structural parts. On the other hand, fiber reinforced polymers are predominantly made of synthetic fibers, such as glass or carbon, and a petro–chemically sourced thermosetting resin or thermoplastic matrix. In this context, an emerging field of high–performance natural fibers, especially bast fibers (which include flax, hemp and jute), is gaining interest and are immediately attractive. Therefore, the industry includes many significant innovations at every stage of the manufacturing of composites, which is extends from the fibers and their precursors or preforms through to the manufacturing processes and their associated industries. Lots of innovations are taking place in the market across the value chain, most innovations being focusing on performance improvement and cost benefits in composites industry. This paper is an overview on key trends in composite materials continuous innovation and improvements with focus on composites based on cellulose fibers.

**Keywords:** composite materials, cellulose fibers, naturally–derived fibres, innovation and improvements, trends

## INTRODUCTORY NOTES

Many composites used today are at the leading edge of materials technology, with performance and costs appropriate to ultra–demanding applications and conquered different sectors such aerospace industry, aeronautics, automotive industry, manufacturing industries, construction and the marine sector. Moreover, increasing usage of composite applications are emerging.[1–18] This highly competitive market continues to evolve, with the major emphasis in the past being to produce materials with adequate strength, and high wear resistance. [1,7,8]

For a long time, composites enabled us to make remarkable products with exceptional capacities, but often they are being made in a unique or small series production. Today, the end–use sectors, particularly the aeronautics and automobile industries, require a large–scale production. Therefore, the composites industry must meet the specifications of a large series production which is need for the innovative industries. This is an unprecedented opportunity for the composites industry which has grown rapidly thanks mainly to innovation that has created new applications for users and improved on existing applications. In the future, the industry’s growth will depend on other capabilities.[1–18]

Composites becoming the material of choice for various industries due to its cost–performance benefits. Moreover, significant innovations in the area of composites in the next years are expected, having in view that the composites industry must meet the specifications of large series production to increase large penetration in several advanced industries. The weight reduction and improved mechanical property are one of the prime factors to develop new materials for automotive and other means of transportations.

Composite materials have thus become the most attractive candidate due to their excellent property and light weight. In particular, fiber reinforced polymer (FRP) composite materials have been used as an alternative to metals.[1–18] The composite materials have shown improved properties compared to those of metal and polymeric materials, which made the composites being used as structural parts. [1–18] On the other hand, fiber reinforced polymers are predominantly made of synthetic fibers, such as glass or carbon, and a petro–chemically sourced thermosetting resin or thermoplastic matrix.

In this context, an emerging field of high–performance natural fibers, especially bast fibers, is gaining interest. [1–18] These bast fibers include flax, hemp and jute and are immediately attractive as they provide comparable or improved tensile strength and stiffness to that of glass fiber, as well as contain favorable vibration dampening and non–abrasive properties.[7–18] However, natural fibers and resins are on the rise because of their beneficial properties, competitive cost, legislative drivers, and consumer preferences. There are some key innovations for these types of fiber composites.[1]

The industry sectors, users of natural fibers, are now engaged in an eco–design approach. The main goal is to upgrade the knowledge of fibers and preforms (materials for matrix and for reinforcements – matt, long or short fibres, woven and non–woven fabrics –, manufacturing technologies, prepreg composites, compounds, hybrid association of materials etc.) and attract new industries. [4, 5]

## KEY TRENDS IN COMPOSITE MATERIALS

The industry includes many significant innovations at every stage of the manufacturing of composites, which is extends

from the fibers and their precursors or preforms through to the manufacturing processes and their associated industries. These innovations are not only providing opportunities for a wide-range of companies at each step of the part production, but are also developing both improved and new materials which are taking this market into expanding and emerging applications.[1–8]

Lots of innovations are taking place in the market across the value chain, most innovations being focusing on performance improvement and cost benefits in composites industry. Innovation creates “business value”, where value can be derived from a combination of: [1–8]

- meeting functional needs in target markets, and/or
- meeting existing needs better or more economically

All these needs highlight the importance of an open-innovation approach in order to meet the need of the industry for the medium and long term.

Nowadays, key trends in composite materials continuous innovation and improvements are as follows:

- continued light weighting of automotive, aerospace and industrial parts
- enhanced higher performance of reinforcement (fiber, fabric or particulate) and matrix (resin) systems to meet higher mechanical and chemical requirements;
- cost reduction in various composite parts;
- faster and more predictable technologies, applicable of large series production;
- reduction in number of part counts in many applications, developing one-piece or modular products technologies;
- environmentally friendly reinforcement (fiber, fabric or particulate) and matrix (resin) systems, with focus on development of high strength green materials

The usages of the composite materials range from simple household to light-to-heavy industrial purposes. Therefore, composite materials are playing an increasing role in various industry segments like aerospace, automotive, defense and space, marine, consumer products due to desirable characteristics of lightweight, corrosion resistance, high strength, and design flexibility among many others.[1–18] Albeit it continues to replacing traditional materials in several industries, composites are underrepresented in many markets and potential applications.

The above mentioned innovations trend will enable composite materials to increase penetration across different industries. Therefore, aerospace, automotive, transportation, wind sectors and construction segments are expected to grow at a higher rate in the next years. Continuous innovation is expected in development of higher performance glass fibers to meet higher mechanical and chemical requirements. Also, improvement in stiffness and strength along with development of low-cost carbon fiber or particulate composite parts for different applications in automotive, wind, and industrial applications are the major innovation trends. Relative to the core materials in the layered composites, the emerging innovations are conducted for

improvement in strength and stiffness for automotive and other applications and obtaining the lower density to meet end use industries demand. Therefore, light weighting and cost reduction are the major trends in various application segments, such as automotive, aerospace, or wind energy.

### FOCUS ON GREEN MATERIALS

The evolution of composite materials has given an opportunity to use new and better materials resulting in cost reduction, increase in efficiency and better utilization of available resources.[1–8] Moreover, the focus on green materials would give momentum to development of high strength natural fibers to increase penetration in automotive, construction and other industries. Durability, compatibility, affordability and sustainability, including resource availability, land use, biodiversity, environmental impact, are the challenges for converting renewable resources into industrial materials.[1–8] In this sense, the emerging innovations in composite materials relative to the natural fibers, are:

- improvement in strength and stiffness to compete with glass fiber;
- finding new application areas to expand the footprints in different industries;
- improvement in strength and stiffness for automotive applications;
- improvement in impact resistance and aesthetic properties;
- expect the advanced and innovative industries to use new reinforced composites to replace parts currently made with other materials or other types of composites.

Environmental concern has resulted in a renewed interest in bio-based materials. Among them, plant fibers are perceived as an environmentally friendly substitute to glass fibers for the reinforcement of composites, particularly in automotive engineering. Due to their wide availability, low cost, low density, high-specific mechanical properties, and eco-friendly image, they are increasingly being employed as reinforcements in polymer matrix composites. [2,7,8]

Increasing environmental concerns and depletion of petroleum resources calls for new green eco-friendly materials. Among various natural materials, cellulosic natural fibers or fabrics are envisioned as the most suitable ways to solve these problems especially environment related issues. The potential of cellulosic fibers as reinforcement in composite materials have been well recognized, but the renewed interest in the natural fibers resulted in a large number of modifications in order to bring it equivalent and even superior to synthetic fibers.

After tremendous changes in the quality of natural fibers, they emerged as a substitute for the traditional materials, being an environment friendly material for the future. Considering the high performance standard of composite materials in terms of durability, maintenance and cost effectiveness, applications of natural fiber reinforced composites as a substitute for the synthetic fiber reinforced composites is an emerging trend.

Due to the disadvantage of the synthetic and fiber glass as reinforcement, the use of natural fiber reinforced composite gained a great attention. With the advancement of science and technology the new means of characterization and evaluation of physico–chemico–thermo–mechanical properties of the composite have been used that have explored the new horizon of utilizing them for various applications.

Natural fiber reinforced polymer matrix got considerable attention in numerous applications because of the good properties and superior advantages of natural fiber over synthetic fibers in term of its relatively low weight, low cost, less damage to processing equipment, good relative mechanical properties such as tensile modulus and flexural modulus, improved surface finish of molded parts composite, renewable resources, being abundant, flexibility during processing, biodegradability, and minimal health hazards.

Global awareness of environmental issues has resulted in the emergence of economically and environmentally friendly bio–based materials free from the traditional side effects of synthetics. With scopes for the utilization of natural resources–based materials as potential replacements for traditional petroleum products, more researchers are exploring new composite materials based on biorenewable resources. Also, the development of polymers from renewable resources has received considerable attention in recent years, in particular due to volatility of crude oil prices and the desire to avoid landfill disposal.[1–18]

Natural fiber composites from renewable resources offer significant sustainability. Industrial ecology, eco–efficiency, and green chemistry are guiding the development of the next generation of materials, products, and processes. Considerable growth has been seen in the use of natural fiber composites in many industrial applications over the past decade and many types of natural fibers have been investigated with polymer matrices to produce composite materials that are competitive with the synthetic fiber composites.[3] Therefore, the increased focus on green technology will result in high strength fibers to increase penetration in manufacturing. Resins, together with natural fibers, have sustainability.[1–18] They can create lightweight components for interior/exterior structural components. Moreover, in the future, bioinspired materials may replace traditional composites and come to dominate the industry.

#### FOCUS ON COMPOSITES BASED ON CELLULOSE FIBERS

Natural fiber reinforced polymers have been identified as a potential low impact alternative to glass– and carbon–fiber reinforced polymers. Although the replacement of glass– and carbon–fiber with natural fibers for reinforcement in polymer composites appears to be a modern phenomenon, the natural fiber reinforced polymers are not strictly modern by invention. However, the large environmental concern has resulted in a renewed interest in this bio–based materials.

In this sense, composites based on cellulose fibers from wood and plants constitute a relatively new and promising class of

composite materials. They are environmentally friendly, and they offer good technical performance. The use of cellulose fibers as reinforcement in composite materials has increased in recent years as a response to the increasing demand for developing biodegradable, sustainable, and recyclable materials. For several load–carrying applications, where glass or carbon fiber composites are conventionally used, cellulose fiber composites can be a worthwhile alternative. This is particularly the case for applications where the green advantages (renewability, biodegradability) play an important role, and top–end mechanical properties are not the primary motivation.

Composite materials derived from natural, renewable sources have received significant interest in recent years, in particular due to the increased awareness of and drive towards more environmentally sustainable technologies. This innovation in the composite industry, dictated by new environmental directives, depends on both the ecological performances of the raw materials and their technical performances. With their strong double bonus – ecological and technological – flax, jute and hemp fiber uses in thermoplastic and thermoset composites have imposed themselves in the industry. In many cases bio–based materials offer weight reduction, added functionality (e.g. damping / impact absorption) and occupational health benefits. A significant market driver for high volume applications is the potential to disassociate material costs from the fluctuating price of oil and energy.

The most interesting fibers for composite reinforcements are from plants, in particular bast, leaf and wood fibers. Bast fibers, such as flax, hemp, jute and kenaf, are taken from the stem of the plant and are most commonly used as reinforcements because they have the longest length and highest strength and stiffness. Natural fibers, such as hemp, flax, jute and kenaf, have good strength and stiffness, whilst being significantly lighter than conventional reinforcements such as glass fibers, and they are relatively low cost and biodegradable.

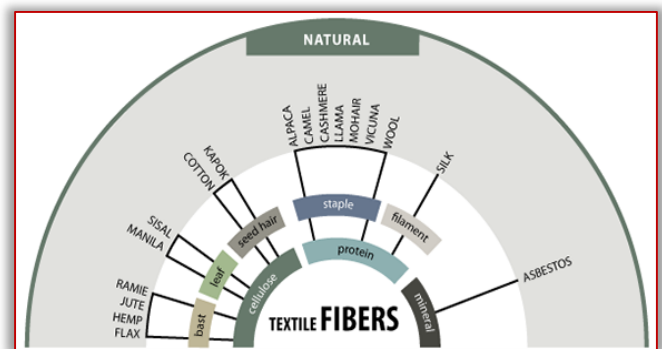


Figure 1. Classes of textile fibres

Natural fibers are currently used in significant quantities, in particular in automotive interior components, to reinforce synthetic polymers. More recently, combinations of these natural fibers and bio–based polymers have been shown to have appealing composite properties, offering the enticing prospect that fully bio–based composites are an increasing commercial reality.

Bast fibers (flax, jute and hemp) solutions meet not only the technical requirements of composite manufacturers in terms of innovative and high-performance reinforcements, but also societal expectations in terms of fiber traceability. Furthermore, the use of these fibers helps to reduce the environmental impacts of composites and provides a view on sustainability through life cycle analyses. Many research in this field, focuses on the flax, jute and hemp reinforcements available on the market, confirms that these fibers provide efficient solutions for the composite industry, due to the remarkable properties besides the fibers' excellent mechanical performance, as added value for composite products.

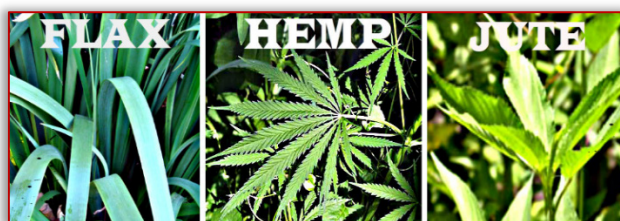


Figure 2. Bast fibers (flax, jute and hemp)

The ecological properties of the bast fibers put these natural fibers to be increasingly used in various, innovative sectors of the industry which are today obliged to take into account sustainable development in their production methods. Flax, jute and hemp fibers, with their specific mechanical properties also bring performance and competitiveness to the new materials used. All specialists from industries, technical institutes and universities now see natural vegetation fibers as an alternative solution to synthetic fibers as they develop composite materials. Today, the entire flax, jute and hemp industry is focusing its research on a new generation of materials which guarantee protection of the environment all the way to their end-of-life cycle. A necessary advance dictated by environmental questions and the oil crisis.

Thanks to the weak density of these natural fibers in relation to glass fibers (~40%), composite materials using flax, jute and hemp prove interesting for those applications where light weight is a defining element. Flax, jute and hemp fibers' mechanical properties offer characteristics comparable to glass fibers because of their characteristics. Natural fibers offer several advantages over glass fibers:

- plant fibers are renewable and their availability is unlimited.
- when natural fiber reinforced plastics are subjected to combustion or landfill at the end of their life cycle, the released amount of carbon dioxide is less with respect to that assimilated during its life cycle.
- natural fibers are less abrasive and can be easily processed as compared to glass fiber.
- natural fiber reinforced in biodegradable polymer matrix are environment friendly and can be composted easily.

After the fibers have been extracted from the plants – by a retting process, followed by a series of mechanical processes –, the fibers can be converted into non-woven mats or into

a continuous plant fiber yarn, which can be used directly to produce composites using a yarn preform or can be used as woven fabrics preform. In fact, the natural fibers can be used in their loose form (as non-woven mats) or can be spun into yarns and woven into textiles. The types of plant fiber preforms available for composites are shown in Figure 3. The long fibers tend to be used for higher quality applications (e.g. cloth for apparel and furnishings) and therefore command high prices, whilst the short fibers are less valuable and are used in ropes, carpets and insulation. Both types can be used for composite reinforcements, although it is usually only economically viable to use the cheaper short fibers. Whilst many natural fiber yarns and textiles are commercially available, in particular for carpet backing, bags, upholstery, clothing etc., these are generally unsuitable for composite reinforcement. A number of woven and unidirectional / biaxial flax and jute fabrics are now commercially available.

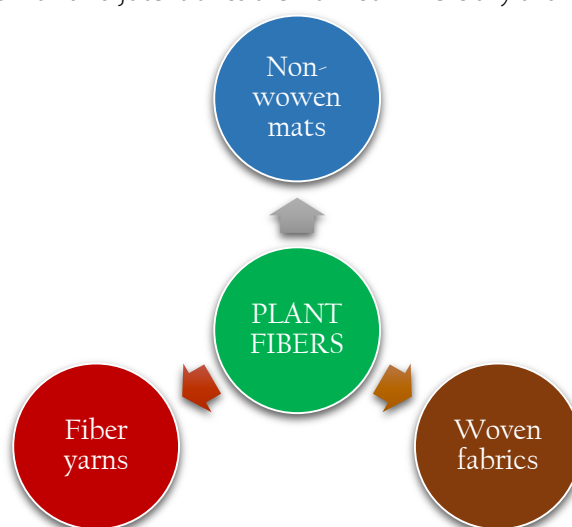


Figure 3. Types of plant fiber preforms available for composites



Figure 4. Bast fibers (flax, jute and hemp) solutions for non-woven mats



Figure 5. Bast fibers (flax, jute and hemp) solutions for yarns



Figure 6. Bast fibers (flax, jute and hemp) solutions for woven fabrics

Woven fabrics are fabricated with a range of weaving patterns, such as plain, twill and satin weave, in which the yarns are differently interlaced in the two main, orthogonal, planar directions. The yarns in the two directions can have different linear densities, and they can be placed with different distances to each other. The woven fabrics offer the possibility of having a planar yarn configuration in two dimensions designed to meet the loading profile of a given composite application. Woven fabrics of flax, jute and cotton fibers are widely available, but they are most often tailored for textile applications, and not for composite applications.

#### CONCLUSIONS

Composite materials can offer significant environmental benefits because of their characteristically low weight, good mechanical properties, excellent resistance to corrosion and the possibility of being sustainably sourced. However, although the in-service environmental benefits of composites are known, there is far less understanding of the environmental and social implications associated with the manufacture of composite materials and products, and the options at end-of-life. Natural materials and technologies have been developed, in part, to help address these problems, but to date there has still been confusion within the industry as to the detailed benefits of these alternatives. Generally, naturally-derived fibres and polymers are perceived as being 'greener' than their synthetic alternatives, but in some instances this has been proven to not be the case.

Also, the recovery of the housing market is likely to drive the construction market in coming years. To meet market expectations of low cost composite a natural-based fiber or particulate made from recycled materials has the ability to replace glass fibers in high-performance composites used in cars and airplanes. Also, it is more sustainable and environmentally friendly unlike the traditional composites. From a waste point of view new polymer matrices will need to be developed that can either be recycled or degraded at the end of life for those composites in order to recover the expensive fillers and reduce overall costs.

Trends in sustainability, recycling and the circular economy require greater focus on minimizing waste and environmental impacts.

Composites have attractive mechanical and physical properties that are now being utilized on a grand scale

world-wide. New fibers, polymers, and processing techniques for all classes of composites are constantly being developed. Research is also ongoing to improve repair techniques, recyclability, and the bonding between fibres and matrix materials.

The increase in environmental consciousness and community interest, the new environmental regulations, led to thinking of the use of environmentally friendly materials. In this sense, the natural fibers are getting attention to use in polymer composites due to their ecofriendly nature and sustainability. Natural fiber is considered one of the environmentally friendly materials which have good properties compared to synthetic fiber. Therefore, the use of natural fiber from resources such as flax, sisal, hemp and jute to produce composite materials, gained considerable attention in the last decades.

There is no doubt that, if processing costs can be substantially reduced, composite materials will be increasingly employed in applications that require light weight in addition to toughness and wear- and abrasion-resistant properties. The new applications that are being found on an almost daily basis, and the continuous reporting of company investments into the manufacture of composite parts, tend to indicate that important progress has been made towards the reduction of processing and manufacturing costs.

However, it is important to realize that the use of composites requires an integrated approach between user and designer/manufacturer to ensure functionality. This entails a knowledge of the structural efficiency of the material, its isotropic or anisotropic behaviour, environmental effects, and its manufacturing requirements, assembly, and repair.

#### References

- [1] Richard Collins, Composites 2017–2027: Innovations, Opportunities, Market Forecasts Complete supply chain analysis and emerging market applications of both synthetic and natural fibre reinforced composite material (FRP, CMC, MMC) <https://www.idtechex.com/research/reports/>
- [2] Amandine Céline, Sylvain Fréour, Frédéric Jacquemin, Pascal Casari, The hygroscopic behavior of plant fibers: a review, *Frontiers in Chemistry*, 2014, 1, 1–12
- [3] Kurki Nagaraj Bharath and Satyappa Basavarajappa, Applications of biocomposite materials based on natural fibers from renewable resources: a review, *Science and Engineering of Composite Materials*, 23, 2, 2016
- [4] Chokri Cherif (2016) Textile materials for lightweight constructions: Technologies – Methods – Materials – Properties, Chapter: Introduction, 1–7
- [5] Jan Hausding, Olaf Diestel (2016) Textile materials for lightweight constructions: Technologies – Methods – Materials – Properties, Chapter: Pre-impregnated Textile Semi-finished Products (Prepregs), 361–379
- [6] Malgorzata Zimniewska, Jerzy Myalski, Mateusz Koziol, Jerzy Mankowski and Edyta Bogacz, Natural Fiber Textile Structures Suitable for Composite Materials, *Journal of Natural Fibers*, 9(4), 2012

- [7] Todor M–P, Bulei C, Heput T and Kiss I (2018) Researches on the development of new composite materials complete / partially biodegradable using natural textile fibers of new vegetable origin and those recovered from textile waste, IOP Conference Series: Materials Science and Engineering, 294, 1–9
- [8] Todor M–P, Bulei C and Kiss I (2018) Composite materials manufacturing using textile inserts with natural origins fibres, IOP Conference Series: Materials Science and Engineering, 393, 1–6
- [9] Pickering KL, Efendy MGA and Le TM (2016) A review of recent developments in natural fiber composites and their mechanical performance Composites Part A, 83, 98–112
- [10] Faruk O, Bledzki A, Fink H and Sain M (2014) Progress report on natural fiber reinforced composites Macromolecular Materials and Engineering 299(1) 9–26
- [11] Faruk O, Bledzki A, Fink H and Sain M (2012) Biocomposites reinforced with natural fibers: 2000 – 2010 Progress in Polymeric Science 37 1552–1596
- [12] Bledzki A K and Gassan J 1999 Composites reinforced with cellulose based fibres Progress in Polymer Science 24 221–274
- [13] Summerscales J, Dissanayake NPJ, Virk AS and Hall W 2010 A review of bast fibers and their composites. Part 1 – Fibers as Reinforcements Composites Part A 41 1329–1335
- [14] Summerscales J, Dissanayake NPJ, Virk AS and Hall W (2010) A review of bast fibers and their composites. Part 2 – Composites, Composites Part A 41 1336–1344
- [15] Sen T and Reddy HN (2011) Various industrial applications of hemp, kenaf, flax and ramie natural fibers International Journal of Innovation, Management and Technology 2 192–198
- [16] Dicker M, Duckworth P, Baker A, Francois G and Hazzard M (2014) Green composites: a review of material attributes and complementary applications, Composites Part A 56 280–289
- [17] Elisa Zini E and Scandola M (2011) Green composites: An overview Polymer Composites 32(12) 1905–1915
- [18] Saxena M, Pappu A, Sharma A, Haque R and Wankhede S (2011) Composite materials from natural resources: Recent trends and future potentials, advances in composite materials – Analysis of natural and man–made materials, InTech, <http://www.intechopen.com/>



ISSN: 2067–3809

copyright © University POLITEHNICA Timisoara,  
Faculty of Engineering Hunedoara,  
5, Revolutiei, 331128, Hunedoara, ROMANIA  
<http://acta.fih.upt.ro>

<sup>1</sup>Ishaque KHAN, <sup>2</sup>Lalsingh KHALSA, <sup>2</sup>Vinod VARGHESE

# UNSTEADY-STATE HEAT CONDUCTION PROBLEM ON A THICK CIRCULAR PLATE AND ITS ASSOCIATED THERMAL STRESSES

<sup>1-3</sup>Department of Mathematics, Mahatma Gandhi Science College, Armori, Gadchiroli, INDIA

**Abstract:** In this paper, an attempt has been made to determine and discuss the quasi-static transient thermal stresses on a thick circular plate subjected to arbitrary heat supply [i.e.  $f_1(r)$  on the upper face and  $f_2(r)$  on the lower face], while the circular curved surface is thermally insulated. The results are obtained in a series form in terms of Bessel's functions. Some numerical results for the displacement, change in temperature and the stress distributions are shown in figures.

**Keywords:** temperature distribution, heat conduction, thermal stresses, thick circular plate

## INTRODUCTION

The interest on thermal stress problems has grown considerably due to the increased usage of industrial and construction materials. Hence, some concerned been reported the theoretical studies in this regard so far. However, to simplify the analyses, almost all the studies were conducted on the assumption that heat is impacted moreover on the upper face or lower face of the plate, or it is kept insulated, or heat was dissipated with uniform heat transfer coefficients throughout the surfaces. For example, Nowacki [1] has determined the steady-state thermal stresses on a thick circular plate subjected to an axisymmetric temperature distribution on the upper face with zero temperature on the lower face and the circular edge respectively. Sugano [2] analysed the unsteady thermal stress in an infinite thick plate with an axisymmetric heat generation on both of its surfaces using generalised finite Fourier transformation and the Hankel transformation based on Weber-Orr development. Noda et al. [3] investigated the two-dimensional transversely isotropic thick circular plate by applying integral transform technique. Sansalone and Carino [4] used finite element method to study the transient response of thick circular plates and different geometries subjected to point impact of different duration in both the time and the frequency domains. Ootao and Tanigawa [5] considered the theoretical treatment of a two-dimensional coupled thermal stress problem of an orthotropic material using a perturbation technique for temperature and thermoelastic fields. Sherief and Hamza [6] derived two-dimensional problem of a thick plate whose lower and upper surfaces are traction free and subjected to a given axisymmetric temperature distribution considered within the context of the theory of generalized thermoelasticity with one relaxation time using Laplace and Hankel transform techniques. Sharma et al. [7] have developed a mathematical model for predicting the response of a thick thermoelastic axisymmetric solid plate subjected to sudden lateral mechanical and thermal loads. The governing equations of motion and heat conduction have been solved by using

Laplace and Fourier transform methods to predict the response of the plate in the physical time domain. The model is also formulated and solved with the help of the finite element method (FEM). Nasser [8, 9] investigated problems due to heat sources in the generalised thermoelastic body. Kulkarni and Deshmukh [10,11] determined quasi-static thermal stresses in a thick annular disc subjected to arbitrary initial temperature on the upper face with the lower face at zero temperature for a steady and unsteady state using the classical method. Recently, Varghese and Khalsa [12,13] have investigated the thermoelastic problem for thick plates with boundary conditions of radiation type, in which sources are generated according to the linear function of the temperatures, which will also satisfy the time-dependent heat conduction equation. Kedar and Deshmukh [14] studied the temperature distribution and thermal stresses on a thick circular plate wherein the arbitrary initial heat flux is provided on the upper surface whereas, the lower and the curved surfaces are kept at zero temperature. The temperature distribution in the plate is determined by solving heat conduction equation using variable separation technique. Very recently, thermoelastic analysis of a thick plate with radiation conditions on its curved surfaces was studied by Kumar et al. [15]. Khan et al. [16] investigated steady state heat conduction problem and its associated stress on a thick annular disc due to arbitrary axisymmetric heat flux based on classical method. Most of the researches carried out by previous authors have not considered any thermoelastic problem for thick plates on which sectional heat is impacted from both sides of the faces. The present investigation deals specifically with the practical problem on a thick circular plate affected by sectional heat supply on its upper face and lower face, whereas, the curved surfaces are kept insulated. In this paper, heat conduction differential equation has been solved at the first instance by using an unconventional classical method. The thermoelastic stresses are determined with the help of suitable Love's function and Goodier's thermoelastic displacement potential function. The results presented here will be more beneficial in engineering problems particularly

in thermally induced stress analysis and in determining the state of strain on a thick plate constituting foundations for reactors, pressure vessels, furnaces, etc.

### STATEMENT OF THE PROBLEM

Consider a thick circular plate of radius  $a$  and thickness  $h$  defined by  $0 \leq r \leq a$ , and  $-h/2 \leq z \leq h/2$ . Let the plate be subjected to the arbitrary initial temperature over the upper and lower surface (i.e.  $z = \pm h/2$ ). The fixed circular edge ( $r = a$ ) is thermally insulated as shown in Figure 1.

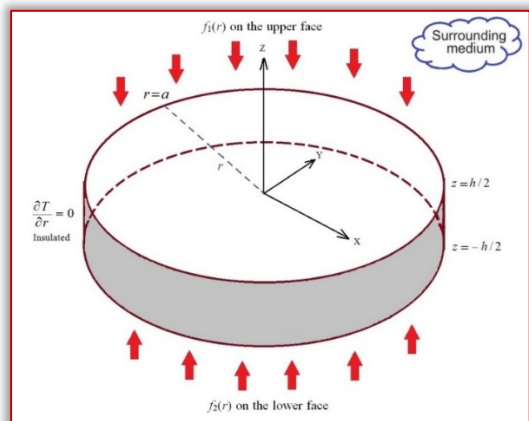


Figure 1. Plate physical configuration

It is assumed that the circular boundary of the thick circular plate is free from traction under considered prescribed conditions. The quasi-static thermal stresses are required to be determined.

### — Temperature distribution

The temperature of the plate at time  $t$  satisfy the heat condition equation

$$\frac{\partial^2 T}{\partial r^2} + \frac{1}{r} \frac{\partial T}{\partial r} + \frac{\partial^2 T}{\partial z^2} = \frac{1}{\kappa} \frac{\partial T}{\partial t} \quad (1)$$

subjected to the initial and boundary conditions

$$T \neq 0 \text{ at } t = 0 \quad (2)$$

$$T = f_1(r) \text{ at } z = h/2 \quad (3)$$

$$T = f_2(r) \text{ at } z = -h/2 \quad (4)$$

$$\frac{\partial T}{\partial r} = 0 \text{ at } r = a \quad (5)$$

in which thermal diffusivity of the material of the plate is denoted as  $\kappa = \lambda / \rho C$ ,  $\lambda$  being the thermal conductivity of the material,  $\rho$  is the density and  $C$  is the calorific capacity, assumed to be constant.

### — Thermal displacements and thermal stress

The Navier's equations in the absence of body forces for axisymmetric two-dimensional thermoelastic problem can be expressed as [17]

$$\left. \begin{aligned} \nabla^2 u_r - \frac{u_r}{r} + \frac{1}{1-2\nu} \frac{\partial e}{\partial r} - \frac{2(1+\nu)}{1-2\nu} \alpha_t \frac{\partial T}{\partial r} &= 0 \\ \nabla^2 u_z - \frac{1}{1-2\nu} \frac{\partial e}{\partial z} - \frac{2(1+\nu)}{1-2\nu} \alpha_t \frac{\partial T}{\partial z} &= 0 \end{aligned} \right\} \quad (6)$$

where  $u_r$  and  $u_z$  are the displacement components in the radial and axial directions, respectively and the dilatation  $e$  as

$$e = \frac{\partial u_r}{\partial r} + \frac{u_r}{r} + \frac{\partial u_z}{\partial z} \quad (7)$$

The displacement function in the cylindrical coordinate system is represented by the Goodier's thermoelastic displacement potential  $\phi$  and Love's function  $L$  as

$$u_r = \frac{\partial \phi}{\partial r} - \frac{\partial^2 L}{\partial r \partial z}, \quad (8)$$

$$u_z = \frac{\partial \phi}{\partial z} + 2(1-\nu) \nabla^2 L - \frac{\partial^2 L}{\partial z^2} \quad (9)$$

in which Goodier's thermoelastic potential  $\phi$  must satisfy the equation

$$\left( \frac{\partial^2}{\partial r^2} + \frac{1}{r} \frac{\partial}{\partial r} + \frac{\partial^2}{\partial z^2} \right) \phi(r, z, t) = K\tau \quad (10)$$

with

$$\phi = 0 \text{ at } t = 0 \quad (11)$$

whereas, the Love's function  $L$  must satisfy the equation [18]

$$\left( \frac{\partial^2}{\partial r^2} + \frac{1}{r} \frac{\partial}{\partial r} + \frac{\partial^2}{\partial z^2} \right)^2 L(r, z, t) = 0 \quad (12)$$

where  $K = (1+\nu)\alpha / (1-\nu)$  is the resistance coefficient,  $\tau = T - T_i$ ,  $T_i$  is the initial temperature condition,  $\tau$  is the temperature change to be determined from the heat conduction differential equation (1).

The component of the stresses are represented by the use of the potential  $\phi$  and Love's function  $L$  as

$$\sigma_{rr} = 2G \left\{ \frac{\partial^2 \phi}{\partial r^2} - K\tau + \frac{\partial}{\partial z} \left( \nu \nabla^2 L - \frac{\partial^2 L}{\partial r^2} \right) \right\}, \quad (13)$$

$$\sigma_{\theta\theta} = 2G \left\{ \frac{1}{r} \frac{\partial \phi}{\partial r} - K\tau + \frac{\partial}{\partial z} \left( \nu \nabla^2 L - \frac{1}{r} \frac{\partial L}{\partial r} \right) \right\}, \quad (14)$$

$$\sigma_{zz} = 2G \left\{ \frac{\partial^2 \phi}{\partial r^2} - K\tau + \frac{\partial}{\partial z} \left( (2-\nu) \nabla^2 L - \frac{\partial^2 L}{\partial z^2} \right) \right\}, \quad (15)$$

and

$$\sigma_{rz} = 2G \left\{ \frac{\partial^2 \phi}{\partial r \partial z} + \frac{\partial}{\partial r} \left( (1-\nu) \nabla^2 L - \frac{\partial^2 L}{\partial z^2} \right) \right\} \quad (16)$$

in which  $G$  is the shear modulus,  $\nu$  is the Poisson's ratio, and the Laplacian operator presented as

$$\nabla^2 = \frac{\partial^2}{\partial r^2} + \frac{1}{r} \frac{\partial}{\partial r} + \frac{\partial^2}{\partial z^2} \quad (17)$$

The boundary condition on the traction free surface stress functions are

$$\sigma_{zz} = \sigma_{rz} = 0 \text{ at } z = -h/2 \quad (18)$$

Equations (1) to (18) constitute the mathematical formulation of the problem.

### SOLUTION TO THE PROBLEM

#### — Solution of temperature change

We assume that the expression for temperature distribution as

$$T(r, z, t) = \cosh(z + h/2) \sum_{n=1}^{\infty} f_n(t) J_0(\alpha_n r) \quad (19)$$

where  $f_n(t)$  will be determined from heat conduction equation,  $J_1(\alpha_n, a)$  is the Bessel function of the first kind of order one, and  $\alpha_1, \alpha_2, \dots$  are the roots of the equation  $J_1(\alpha_n, a) = 0$  respectively.

Using equation (19) in (1) and integrating, one obtains

$$f_n(t) = A_n \exp[\kappa(1 - \alpha_n^2)t] \quad (20)$$

in which the constant  $A_n$  can be determined from the nature of temperature prescribed on the lower and upper faces.

Taking into account the boundary conditions (3) and (4), the assumed temperature equation (19), and equation (20), we have

$$f_1(r) + f_2(r) = [\cosh(h) + 1] \sum_{n=1}^{\infty} A_n J_0(\alpha_n r) \exp[\kappa(1 - \alpha_n^2)t] \quad (21)$$

By using the theory of Bessel's function, we arrive at a constant value as

$$A_n = \frac{2}{a^2 (\cosh h + 1) J_0(\alpha_n a)} \int_0^a r [f_1(r) + f_2(r)] J_0(\alpha_n r) dr \quad (22)$$

Using equations (19) and (20), we arrive at the solution of the temperature distribution stated above as

$$T = \cosh(z + h/2) \sum_{n=1}^{\infty} A_n J_0(\alpha_n r) \exp[\kappa(1 - \alpha_n^2)t] \quad (23)$$

Now the initial temperature  $T_i$  is given by  $t = 0$  as

$$T_i = \cosh(z + h/2) \sum_{n=1}^{\infty} A_n J_0(\alpha_n r) \quad (24)$$

Taking into account the equations (23) and (24) in the expression  $\tau = T - T_i$ , the temperature change is finally represented by

$$\tau = \cosh(z + h/2) \sum_{n=1}^{\infty} A_n J_0(\alpha_n r) \{ \exp[\kappa(1 - \alpha_n^2)t] - 1 \} \quad (25)$$

### — Solution of the thermal stress problem

Referring to the fundamental equation (1) and its solution (25) for the heat conduction problem, the solution for the displacement function are represented by the Goodier's thermoelastic displacement potential governed by equation (10) represented by

$$\phi = D_n \cosh(z + h/2) \sum_{n=1}^{\infty} A_n J_0(\alpha_n r) \{ \exp[\kappa(1 - \alpha_n^2)t] - 1 \} \quad (26)$$

Using equation (26) in equation (10), one attains

$$D_n = K / \alpha_n^2 \quad (27)$$

Substituting equation (27) into equation (26), the displacement potential  $\phi$  is indicated by

$$\phi(r, z, t) = K \cosh(z + h/2) \sum_{n=1}^{\infty} A_n J_0(\alpha_n r) \{ \exp[\kappa(1 - \alpha_n^2)t] - 1 \} / \alpha_n^2 \quad (28)$$

Similarly, the solution for Love's function  $L$  are assumed so as to satisfy the governed condition of equation (12) as

$$L(r, z, t) = \sum_{n=1}^{\infty} A_n J_0(\alpha_n r) \{ H_n \cosh[\alpha_n(z + h/2)] + R_n \alpha_n z \sinh[\alpha_n(z + h/2)] \} \{ \exp[\kappa(1 - \alpha_n^2)t] - 1 \} / \alpha_n^2 \quad (29)$$

In this manner, two displacement functions in the cylindrical coordinate system (i.e.  $\phi$  and  $L$ ) are fully formulated. Now, in order to obtain the displacement components, we substitute

the values of thermoelastic displacement potential  $\phi$  and Love's function  $L$  in equations (8) and (9) and we get

$$u_r = \sum_{n=1}^{\infty} A_n \alpha_n J_1(\alpha_n r) \{ -K \cosh(z + h/2) + \alpha_n \{ H_n \sinh[\alpha_n(z + h/2)] + R_n \alpha_n z \cosh[\alpha_n(z + h/2)] + \sinh[\alpha_n(z + h/2)] \} \} \times \{ \exp[\kappa(1 - \alpha_n^2)t] - 1 \} / \alpha_n^2, \quad (30)$$

$$u_z = \sum_{n=1}^{\infty} A_n J_0(\alpha_n r) \{ K \sinh(z + h/2) - H_n \alpha_n^2 \cosh[\alpha_n(z + h/2)] + R_n \alpha_n^2 \{ 2(1 - \nu) \cosh[\alpha_n(z + h/2)] - \alpha_n z \sinh[\alpha_n(z + h/2)] \} \} \times \{ \exp[\kappa(1 - \alpha_n^2)t] - 1 \} / \alpha_n^2 \quad (31)$$

In this manner, the stress components can be evaluated. By substituting the values of thermoelastic displacement potential  $\phi$  from equation (33) and Love's function  $L$  from equation (34) in equations (13), (14), (15) and (16), one acquires

$$\sigma_{rr} = 2G \sum_{n=1}^{\infty} \{ K(-\alpha_n) \{ J_0(\alpha_n r) - J_1(\alpha_n r) / r \} \cosh(z + h/2) - K \cosh(z + h/2) \alpha_n^2 A_n J_0(\alpha_n r) + H_n A_n \alpha_n^2 \{ \alpha_n J_0(\alpha_n r) \times J_1(\alpha_n r) / r \} \sinh[\alpha_n(z + h/2)] + R_n A_n \alpha_n^2 \{ \alpha_n 2\nu J_0(\alpha_n r) \times \sinh[\alpha_n(z + h/2)] + (\alpha_n J_0(\alpha_n r) - J_1(\alpha_n r) / r) \times \sinh[\alpha_n(z + h/2)] + \alpha_n z \cosh[\alpha_n(z + h/2)] \} \} \times \{ \exp[\kappa(1 - \alpha_n^2)t] - 1 \} / \alpha_n^2, \quad (32)$$

$$\sigma_{\theta\theta} = 2G \sum_{n=1}^{\infty} \{ A_n J_0(\alpha_n r) \sinh(z + h/2) / r - K \cosh(z + h/2) \times A_n J_0(\alpha_n r) + H_n A_n \alpha_n^2 J_1(\alpha_n r) / r \} \sinh[\alpha_n(z + h/2)] + R_n A_n \alpha_n^2 \{ \alpha_n 2\nu J_0(\alpha_n r) \sinh[\alpha_n(z + h/2)] + (J_1(\alpha_n r) / r) \times \sinh[\alpha_n(z + h/2)] + \alpha_n z \cosh[\alpha_n(z + h/2)] \} \times \{ \exp[\kappa(1 - \alpha_n^2)t] - 1 \} / \alpha_n^2, \quad (33)$$

$$\sigma_{zz} = 2G \sum_{n=1}^{\infty} \{ K A_n J_0(\alpha_n r) \cosh(z + h/2) / r - K \cosh(z + h/2) \times A_n J_0(\alpha_n r) + H_n A_n \alpha_n^3 J_0(\alpha_n r) \sinh[\alpha_n(z + h/2)] + R_n A_n \alpha_n^3 J_0(\alpha_n r) \{ (1 - 2\nu) \sinh[\alpha_n(z + h/2)] - \alpha_n z \cosh[\alpha_n(z + h/2)] \} \} \times \{ \exp[\kappa(1 - \alpha_n^2)t] - 1 \} / \alpha_n^2, \quad (34)$$

$$\sigma_{rz} = 2G \sum_{n=1}^{\infty} \{ K A_n (-\alpha_n) J_1(\alpha_n r) \sinh(z + h/2) + H_n A_n \alpha_n^3 J_1(\alpha_n r) \cosh[\alpha_n(z + h/2)] + R_n A_n \alpha_n^3 J_1(\alpha_n r) \{ 2\nu \cosh[\alpha_n(z + h/2)] + \alpha_n z \sinh[\alpha_n(z + h/2)] \} \} \times \{ \exp[\kappa(1 - \alpha_n^2)t] - 1 \} / \alpha_n^2 \quad (35)$$

### — Determination of unknown arbitrary function

In order to satisfy the condition (18) solving the equation (34) and (35) for  $H_n$  and  $R_n$  we arrive at

$$H_n = 4\nu K / \alpha_n^2 h, \quad R_n = -2K / \alpha_n^2 h \quad (36)$$

Using these values of equation (36) in equations (30)-(35), the expression for displacement and stresses are obtained. The equations of stresses are rather lengthy. Consequently, the same have been omitted here for the sake of brevity, but have been considered during graphical discussion using MATHEMATICA software.

### — Special case

Assume that point impulsive heat source impacts the thick plate as

$$f_1(r) = Q_1 \delta(r - a), f_2(r) = Q_2 \delta(r - a) \quad (37)$$

in which  $Q_0$  is constant heat flux and  $\delta(r - b)$  is the Dirac delta function.

Using (37), equation (22) yields

$$A_n = \frac{2(Q_1 + Q_2)}{a(\cosh h + 1)J_0(\alpha_n a)} \quad (38)$$

For the sake of simplicity, we will set  $A = 2(Q_1 + Q_2)/ah$ ,  $B = 2K(Q_1 + Q_2)/ah$  and  $C = 4KG(Q_1 + Q_2)/ah$  in expressions (30)-(35) during the graphical presentation.

#### NUMERICAL RESULTS, DISCUSSION AND REMARKS

Numerical calculations have been carried out for Aluminum metal plate with physical parameters as  $a = 1$  cm,  $b = 0.5$  cm,  $h = 0.25$  cm, wherein, mechanical material properties are considered as Modulus of Elasticity  $E = 6.9 \times 10^6$  N/cm<sup>2</sup>, Shear modulus  $G = 2.7 \times 10^6$  N/cm<sup>2</sup>, Poisson's ratio  $\nu = 0.281$ , Thermal expansion coefficient,  $\alpha = 25.5 \times 10^6$  cm/cm-°C, Thermal diffusivity  $\kappa = 0.86$  cm<sup>2</sup>/sec, Thermal conductivity  $\lambda = 0.48$  cal sec<sup>-1</sup>/cm °C with  $\alpha_n = 3.8317, 7.0156, 10.1735, 13.3237, 16.4701, 19.6159, 22.7601, 25.9037, 29.0468, 32.1823$  are the positive & real roots of the transcendental equation  $J_1(\alpha_n, a) = 0$ . In order to examine the influence of heating

on the plate, numerical calculation for all variables was performed. Numerical calculations are depicted in the following figures with the help of MATHEMATICA software. Figures 2–4 illustrate the numerical results of temperature distribution, displacements, and stresses of thick circular plate impacted by two sources of sectional heat supply on opposite faces.

Figure 2(a) indicates the temperature distribution along the  $r$ -direction of the thick plate. The maximum value of temperature magnitude occurs at the outer edge due to additional heat supply. The distribution of the temperature gradient at each instance decreases towards inner edge along the radial direction but is again restricted to finite value due to another sectional heat supply.

As expected, in Figure 2(b), with an increase of time in small values along the  $z$ -direction, the temperature increases due to thermal deformation occurring with additional sectional heat.

Figure 2(c) illustrates the temperature profile along the time line for different values of  $r$ . At the center of the core, temperature fluctuation is high compared to the inner and outer edge. This may be due to the accumulation of more heat energy and hence thermal expansion increases giving high tensile force which later stabilises by converging at a particular point.

At first glance, as shown in Figure 2(d), graph follows an exponential curve (increasing form) where temperature grows rapidly at the initial stage, then levels out to some limiting value along  $t$ -direction for different values of  $z$ .

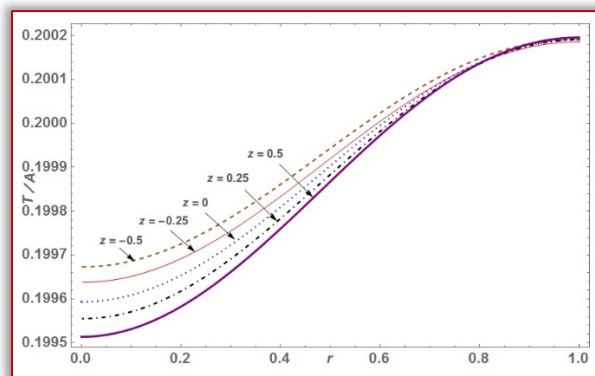


Figure 2(a). Temperature distribution along  $r$  for different values of  $z$

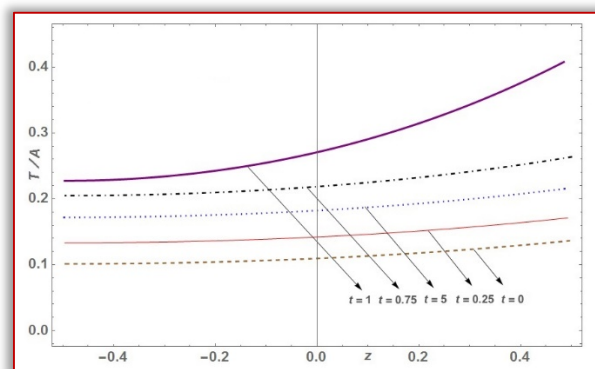


Figure 2(b). Temperature distribution along  $z$  for different values of  $t$

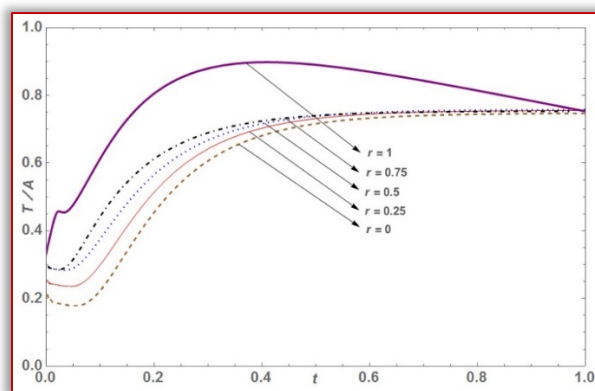


Figure 2(c). Temperature distribution along  $t$  for different values of  $r$

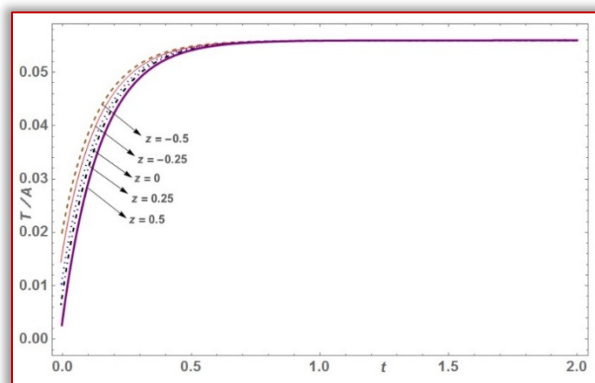


Figure 2(d). Temperature distribution along  $t$  for different values of  $z$

Figures 3(a) and 3(b) describe the radial and axial displacement profile along  $r$ - and  $z$ -directions. Figure 3(a) indicates that  $u_r$  curves were in increasing trend, wherein the curves for  $u_z$  are decreasingly stiffer. Thus both displacement profiles have an opposite characteristic, but combined effect nullifies their magnitude variation effects. In Figure 3(b),  $u_r$  curves are mostly following a bell-shaped curve (i.e. zero at both the extreme ends and having maximum magnitude at the center) and  $u_z$  curves are sinusoidal in nature along the radial direction.

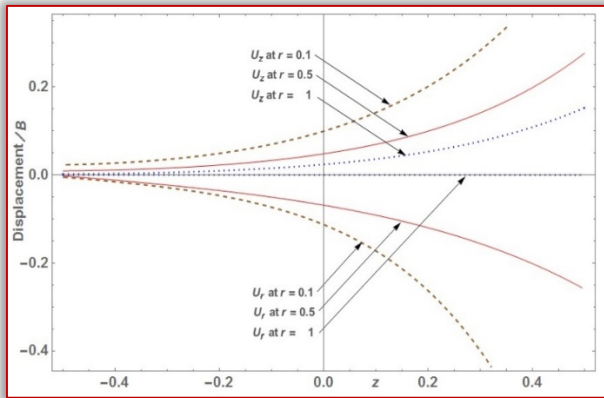


Figure 3(a). Displacement profile along  $z$  for different values of  $r$

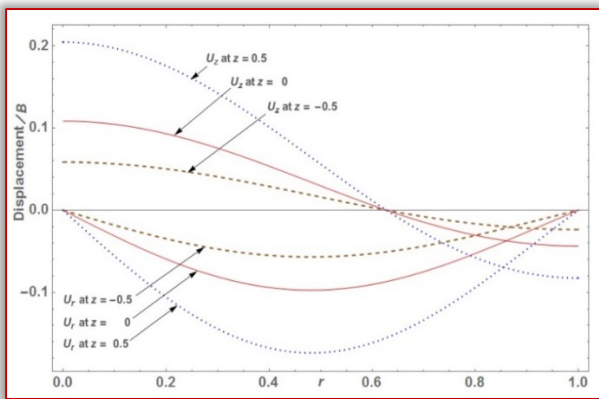


Figure 3(b). Displacement profile along  $r$  for different values of  $z$

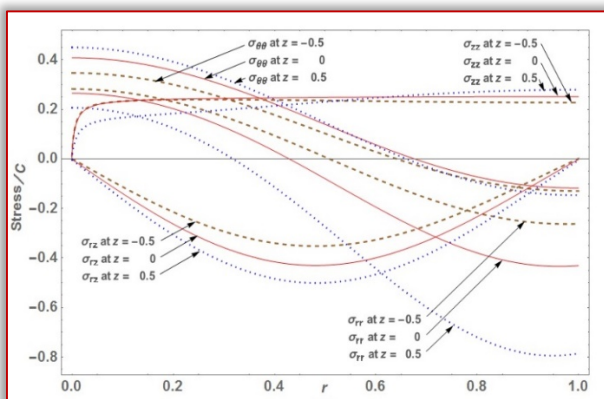


Figure 4(a). Stresses profile along  $r$ -direction for different values of  $z$

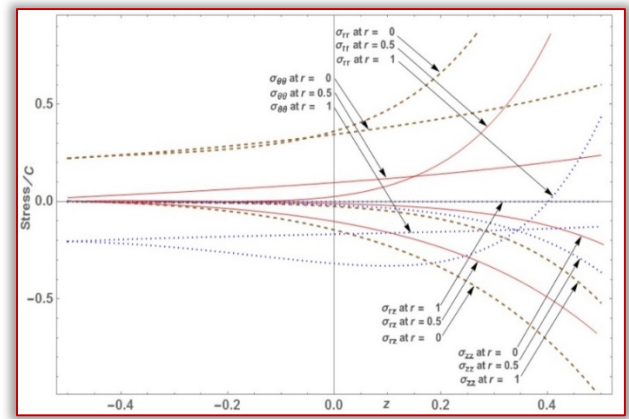


Figure 4(b). Stresses profile along  $z$ -direction for different values of  $r$

Figures 4(a) and 4(b) depicts the combined graphs of radial, circumferential, axial and shear thermal stresses to view at a single glance.

In Figure 4(a), the radial and tangential stress curves are following a decreasing trend, that is, initially stresses are at a higher absolute value which gradually drops along the radial direction. It could be due to compressive forces existing within the concentric region. The axial stress rapidly takes increasing exponential nature which later on stabilises itself along the radial direction at different  $z$ . The variation of shear stresses response is maximum at the end points through-the-radial direction, while the thermal stress response is minimum on the interior so that the outer edge tends to expand more under tensile stress than the inner part being under tensile stress. In Figure 4(b), almost all stresses gradually increase along  $z$ -direction for values of  $r$ .

The  $\sigma_{rr}$  and  $\sigma_{\theta\theta}$  curves are similar in nature. It was observed that initially stresses are minimum, but as it approaches towards the outer edge, it gradually increases due to the sources of heat. Stresses  $\sigma_{rz}$  and  $\sigma_{zz}$  initially attains zero at the inner boundary, but increases towards the outer edge along the  $z$ -axis for different values of  $r$ . This could owe due to thermal expansion due to external heat supply.

### CONCLUDING REMARKS

In this problem, a thick circular plate has been considered for theoretical investigation for determining the expressions for temperature change, displacements and stress functions. As a particular case, the mathematical model is composed of two different sectional heat sources that were impacted on the lower and upper faces. The numerical calculations were performed and plotted graphically.

From the graphs, it is evident that there is a significant impact on the deformation of various components of stresses, displacement, conductive temperature and temperature change in the thick circular plate when impacted with two separate heat supplies. The following results were obtained while carrying out the research work:

- » The advantage of this method is its generality and its mathematical power to handle different types of mechanical and thermal boundary conditions.
- » Comparing the corresponding results by noting the asymptotic behaviour  $\cosh(z+h/2)/\cosh(\alpha_n h) \approx \exp[-\alpha_n(-z+h/2)]$ , it is observed that the expressions for stress functions are more rapidly convergent.
- » The results obtained here are useful in engineering problems, particularly, in determining the state of strain on a thick circular plate. Any particular case of special interest can be derived by assigning appropriate values to parameters and functions involved in the general solution given with the help of equations (32)-(35).

#### References

- [1] W. Nowacki, The state of stresses in a thick circular disk due to temperature field, *Bull. Acad. Polon. Sci., Ser. Sci. Techn.*, 5, 227, 1957.
- [2] Y. Sugano, Transient thermal stresses in a transversely isotropic thick plate with a circular hole due to axisymmetric heat generations on the upper and lower surfaces, *Nippon Kikai Gakkai Ronbunshu*, 47(419), 730-739, 1981.
- [3] N. Noda, Y. Takeuti, K. Uemura, Transient thermal stress problem in a transversely isotropic thick plate with a stationary heat supply on its surfaces, *Transactions of the Japan Society of Mechanical Engineers Series A*, 48(436), 1536-1543, 1982.
- [4] M. Sansalone, N.J. Carino, Transient impact response of thick circular plates, *Journal of Research of the National Bureau of Standards*, 92(6), 355-367, 1987.
- [5] Y. Ootao, Y. Tanigawa, Two-dimensional coupled thermal stress analysis of an orthotropic thick plate due to symmetrical heating, *Transactions of the Japan Society of Mechanical Engineers Series A*, 55 (511), 530-537, 1989.
- [6] H.H. Sherief, F.A. Hamza, Generalized thermoelastic problem of a thick plate under axisymmetric temperature distribution. *Journal of Thermal stresses*, 17(3), 435-452 1994.
- [7] J.N. Sharma, P.K. Sharma, R.L. Sharma, Behavior of thermoelastic thick plate under lateral loads, *Journal of thermal stresses*, 27, pp 171-191, 2004.
- [8] M.E. Nasser, Two dimensional problems with heat sources in generalized thermoelasticity, *J. Therm. Stresses*, 27, 227-239, 2004.
- [9] M.E. Nasser, Two dimensional problems for a thick plate with heat sources in generalized thermoelasticity, *J. Therm. Stresses*, 28: 1227-1241, 2005.
- [10] V.S. Kulkarni, K.C. Deshmukh, Quasi-Static Thermal Stresses in a thick circular plate, *Applied Mathematical Modeling*, Elsevier Publication, 31(8), 1479-1488, 2007.
- [11] V.S. Kulkarni, K.C. Deshmukh, Quasi-static thermal stresses in steady state thick circular plate, *Journal of Brazilian Society of Mechanical Sciences and Engineering*, XXX, (2) 175, 2008.
- [12] V. Varghese, V., L. Khalsa, Two-Dimensional transient problem for a thick disc with internal heat source, *FME Transactions*, Vol. 38, 173-180, 2010.
- [13] V. Varghese, L. Khalsa, Transient thermoelastic problem for a thick annular disc with radiation, *International Journal of Applied Mathematics and Mechanics*, 7 (7), 57-73, 2011.
- [14] G.D. Kedar, K.C. Deshmukh, Estimation of temperature distribution and thermal stresses in a thick circular plate, *African Journal of Mathematics and Computer Science Research*, 4(13), 389-395, 2011.
- [15] R. Kumar, N.K. Lamba, V. Varghese, Analysis of thermoelastic disc with radiation conditions on the curved surfaces, *Materials Physics and Mechanics*, 16, 175-186, 2013.
- [16] I.A. Khan, L. Khalsa, V. Varghese, A steady state heat conduction problem in a thick annular disc due to arbitrary axisymmetric heat flux, *Nonlinear Analysis and Differential Equations*, 4(3), 121-131, 2016
- [17] N. Noda, R.B. Hetnarski, Y. Tanigawa, *Thermal stresses* 2<sup>nd</sup> Ed., pp 259-261, Taylor and Francis New York, 2003.
- [18] A.E.H. Love, *A treatise on the mathematical theory of elasticity*, 4<sup>th</sup> Ed, Dover Publications Inc., New York N.Y., 1944.



ISSN: 2067-3809

copyright © University POLITEHNICA Timisoara,  
Faculty of Engineering Hunedoara,  
5, Revolutiei, 331128, Hunedoara, ROMANIA  
<http://acta.fih.upt.ro>

<sup>1</sup>M.A. BODUDE, <sup>2</sup>R.N. NNAJI, <sup>3</sup>L.O. OSOBA

## COMPARATIVE STUDIES ON THE HIGH TEMPERATURE OXIDATION BEHAVIOUR OF HAYNES 282 AND INCONEL 718 NICKEL–BASED SUPERALLOYS

<sup>1-3</sup>Department of Metallurgical and Materials Engineering, University of Lagos, Akoka, Lagos, NIGERIA

**Abstract:** Nickel-based superalloys are heat-resistant metallic materials used in the fabrication of hot-section components of aero- and land-based gas turbine engines. At high temperatures in oxidizing environments, gas turbine superalloy components depend on the formation of stable, compact, and adherent oxide layers on their surfaces for protection against high temperature oxidation. However, at temperatures above 1000°C, certain protective oxides become volatile, thereby limiting the protective properties of such oxides. In this present investigation, the high temperature oxidation behaviour of Haynes 282 and Inconel 718 nickel-based superalloys were examined under isothermal conditions through gravimetric experimental study, microscopic observation of the morphology of the surface oxides formed, and elemental composition of the formed-oxides at 1050 °C and 1100°C for a maximum exposure period of 10 hours. The morphology and elemental compositions of the surface oxides formed after the oxidation experiments were assessed using Scanning Electron Microscopy (SEM) and X-ray Energy Dispersive Spectroscopy (EDS). The isothermal oxidation rate constant,  $k_p$  was calculated from the gravimetric data analysis for the superalloys at both test temperatures and found to be  $k_p = 1.87 \text{ (mg}^2/\text{cm}^4 \cdot \text{h)}$  and  $8.24 \text{ (mg}^2/\text{cm}^4 \cdot \text{h)}$  for Haynes 282; and  $k_p = 0.49 \text{ (mg}^2/\text{cm}^4 \cdot \text{h)}$  and  $7.70 \text{ (mg}^2/\text{cm}^4 \cdot \text{h)}$  for Inconel 718 at 1050 and 1100 °C test temperatures respectively. Haynes 282 had an overall higher weight gain and higher  $k_p$  than Inconel 718 at both test temperatures as obtained from the oxidation kinetics. After 10 hours' exposure at 1050°C and 1100°C, the surface SEM image of Haynes 282 specimen showed crystal-like oxides structures, while Inconel 718 showed amorphous oxide clusters with pores. EDS results suggested presence of titanium and chromium oxides for Haynes 282 and predominantly chromium oxide for Inconel 718.

**Keywords:** Haynes 282, Inconel 718, Oxidation kinetics, Oxides, Superalloys

### INTRODUCTION

Superalloys are heat-resistant multi-component metallic materials designed for high temperature applications such as jet engines and power-generation gas turbines. Intensive superalloy development and processing over the past few decades have resulted in nickel-based superalloys that can tolerate average temperatures of 1050°C with occasional short trips (near airfoil tips) to temperatures as high as 1200°C. The popularity of nickel-based superalloys in high-temperature applications is largely due to their high-temperature oxidation and creep resistance (Pérez-González *et al.*, 2014; Pollock and Tin, 2006; Wu *et al.*, 2010). Superalloys premier introduction into military gas turbine engines in the second quarter of the 20<sup>th</sup> century (during World War II) led to significant improvement in jet engine production technology in the modern aerospace industry (Barbosa *et al.*, 2005). The largest application of superalloys is in the gas turbine industry, where good mechanical strength and thermal stability at service temperatures are required (Shukla *et al.*, 2013).

Improved efficiency is the requirement for all types of modern gas turbines and this often happens with increase in operating temperature, which also increases the risk of high-temperature oxidation in the material components. Gas turbine blades are one of the most critical aircraft engine components affected by high-temperature oxidation. For best performance of the engine, the combustion temperature should be the maximum obtainable from the complete combustion of the oxygen and the fuel (Eliaz *et al.*,

2002). The total power produced as well as the engine efficiency often depend on the condition of individual turbine blade. In attempts to generate more power with improved efficiency, gas turbine engines have steadily become bigger and more sophisticated over the past twenty years. Therefore, the turbine blades must also be capable of operating in more demanding environments. These environments typically include but not limited to high centrifugal stresses and very high temperatures (surpassing 1500°C), which lead to fast degradation of the turbine blades and ultimately weakens overall engine performance through mechanisms such as high-temperature oxidation (Saravanamutto *et al.*, 2009; Caron and Khan, 1999; Smith, 2013).

At temperatures above 1000°C high-temperature oxidation becomes a very significant problem and most nickel-based superalloys are used at such temperatures in service. Above this temperature, the oxidation resistance of gas turbine superalloy components reduces rapidly (Mahobia *et al.*, 2013; Zitnansky *et al.*, 1998). The service environment of the gas turbine is highly oxidizing; therefore, hot-gas-path components depend on formation of compact oxide layers to provide protection against high-temperature oxidation. However, a stable and protective oxide may crack, spall or even form volatile compounds above a certain temperature point under high-temperature exposures leading to loss in oxidation resistance (Ahlatci, 1991). For instance, the rate of formation of chromium oxides is quick in comparison with aluminium oxides. Therefore, chromium oxide is often

preferred to aluminium oxide given that it will form quickly to protect the base material, and will also repair itself quickly if the oxide layer spalls or becomes damaged by foreign object fragments. However, chromium oxide becomes volatile at temperatures above 1000°C, therefore requiring the formation of more stable oxides, like aluminium oxide, for operating temperatures exceeding 1000°C (ASM, 1997; Pomeroy, 2005; Smith, 2013).

Regardless of the advancements in superalloy compositions and microstructure through manufacturing processes, working temperatures in excess of 70–90% melting temperature of the material are pushing the limits of even the most resilient superalloys. Due to the presence of several alloying elements in superalloys (as many as 10 to 15 different elements or more), their reactions with different environments encountered in practice can result in rather complex processes. Superalloys are classified into three main groups namely, iron-based, cobalt-based, and nickel-based (Pollock and Tin, 2006; Pérez-González *et al.*, 2014; Barbosa *et al.*, 2005).

### MATERIALS AND METHODS

Rectangular specimens were prepared from as-received bars of Haynes 282 and Inconel 718 superalloys. Each sample of both Haynes 282 and Inconel 718 superalloys was cut to an approximate dimension of 1.06 cm x 0.8 cm x 0.4 cm (length x width x thickness). Samples were ground using 600, 800, and 1,200 grit in succession (to remove all surface oxides). The samples were then cleaned by immersing them in methylated spirit for 10 minutes and thereafter, washed with hot water to remove any possible oil or residue contaminants deposited on the sample during the cutting and grinding processes.

Samples in this set were prepared following the procedure outlined in Section 3.1 for isothermal oxidation test at 1050°C. Samples and the crucibles were weighed before the oxidation experiments using a digital weighing scale (Shimadzu UW1020H) sensitive to 0.001g. Afterwards, the samples were placed in specific arrangements in the crucibles and then on a stainless-steel plate (secondary plate) and held in place by a mild steel plate (primary plate) as shown in Plates 3(a) and (b) and, subsequently placed inside the furnace. The samples were placed in the furnace at ambient temperatures and heating continued until the furnace temperature stabilized at 1050°C.

The samples and crucibles were oxidized at 1050°C for different exposure times ranging from 4 to 10 hours for either of both superalloys. Upon removal from the furnace, the oxidized weights of the samples and crucibles were taken using the same digital scale as above and weight gain was calculated. The oxidized samples after the weight gain calculations were wrapped in aluminium foil and labelled accordingly for further analyses.

Oxidation tests at 1100°C for Haynes 282 and Inconel 718 superalloy samples followed the same procedure above as described for the 1050°C test temperature.

Samples used in this work were created from the same as-received Haynes 282 and Inconel 718 superalloy bars respectively. Rectangular specimens were prepared from as-received bars of of 1.06 cm x 0.8 cm x 0.4 cm for both Haynes 282 and Inconel 718 superalloys. Each sample were placed in specific arrangements in the crucibles and then on a stainless steel plate (secondary plate) and held in place by a mild steel plate (primary plate) as shown in Figure 1(a) and, subsequently placed inside the furnace. The arrangement had Haynes 282 alloy samples on the left side of the plate and Inconel 718 alloy samples on the right side inside the furnace [Figure 1(b)].



(a)



(b)



(c)



(d)

Figure 1. Experimental Setup: (a) sample arrangement inside the crucible; (b) crucible arrangement in the furnace; (c) furnace stability at first test temperature; (d) furnace environment before samples were retrieved

The samples and crucibles were oxidized at 1050°C for different exposure times between 4 to 10 hours for either of both superalloys [Figure 1 (c)]. Upon removal from the

furnace [Figure 1 (d)], the oxidized weights of the samples and crucibles were taken using the same digital scale as above and weight gain was calculated. Oxidation tests at 1100°C for both superalloy samples followed the same procedure outlined above.

— Light Optical Microscopy (LOM)

The test samples were carefully sectioned along their lengths using a fresh hardened-steel hack-saw blade one at a time for each sample and the cross sections were mounted in epoxy (resin). Sample surface grinding was conducted with successive finer wet silicon carbide papers from 220 to 1200 grit. The edges were properly chamfered and rounded to ensure a proper flat surface of the specimens during the grinding operations.

The samples were then polished using 0.3 μm and 0.05 μm alumina slurries sequentially. The samples were properly washed under running water and dried using hot air. Samples were chemically etched and once again properly washed under running water and dried using hot air. The longitudinal cross-sectional areas of the oxidized specimens were examined using light optical microscope type [CETI] fitted with digital camera (5 Mega Pixels resolution) in the Laboratory at the Department of Metallurgical and Materials Engineering, University of Lagos.

Samples of the as-received Haynes 282 and Inconel 718 superalloys were also subjected to the above metallographic procedures and etched for Light Optical Microscopy. To visualize the thickness of the oxide film, optical micrographs of the boundaries between the oxidized specimens' cross-sections and the epoxy were taken.

— Scanning Electron Microscopy (SEM) and Energy Dispersive X-ray Spectroscopy (EDS)

To further examine the morphology and composition of the surface oxides formed, SEM (Scanning Electron Microscopy) and EDS (X-ray Energy Dispersive Spectroscopy) were used. EDS was used to identify the elemental composition of the oxides on the surface of the samples. For this investigation, the Phenom Desktop SEM machine with Phenom ProX software attached, in Covenant University, Ota, Ogun State, Nigeria was used.

RESULTS AND DISCUSSION

— Results

The average nominal compositions of the as-received Haynes 282 and Inconel 718 superalloys given by the PMI (Positive Material Identification) machine at Midwal Engineering and Testing Laboratory, Lekki, Lagos, Nigeria are shown in Table 1.

Table 1: Average Nominal Composition of As-Received Haynes 282 and Inconel 718 Superalloys (wt. %)

Element	Ni	Cr	Fe	Nb	Mo	Ti	Al	
Haynes 282	57.96	18.03	2.81	–	8.62	1.97	ND	
Inconel 718	50.08	18.98	18.95	5.03	3.14	1.00	ND	
Element	Co	C	Mn	Si	P	S	B	Cu
Haynes 282	9.40	ND	0.13	ND	–	–	–	ND
Inconel 718	0.24	ND	0.09	ND	ND	ND	ND	ND

ND = Not Determined

Three locations on each alloy sample were x-rayed using the PMI machine and the averages were calculated as shown in the table.

— Oxidation Performance and Weight Change

The entire surface area was used for the calculation of the weight change per area, which was approximately 0.85 cm<sup>2</sup> for both superalloy test samples. Most of the oxidation observed took place on the top surface exposed to the oxidizing environment as shown in the sample arrangement in Plate 3(a) and therefore, contributed the most to the weight gain of each sample (Olivares *et al.*, 2013; Smith, 2013). Observations from the weight change measurements show that both superalloy samples gained weight at both test temperatures at all oxidation times except for Haynes 282 sample oxidized for 4 hours at 1050°C.

Haynes 282 had a sharp weight gain between 4–6 hours' exposure-time at 1050°C, followed by a drop-in weight gain between the 6–8 hours' exposure-time. However, there was further gain in weight between the 8–10 hours' exposure-time. Inconel 718 superalloy displayed a steady increase in weight gain between the 4–8 hours' exposure-time. There was a drop-in weight gain between the 8–10 hours' exposure time at 1050°C.

Similarly, the weight gain calculations and plot for both superalloys at the 1100°C test temperature are shown in Table 5 (A and B) and Figure 5 respectively.

At 1100°C, Haynes 282 showed an almost linear increase in weight gained by the samples across the length of the exposure time. Inconel 718 showed increase in weight gained by the samples between 4–8 hours' exposure-time, with equal weight gain at 8 and 10 hours exposure time (Figure 5). Weight change during an isothermal oxidation process has been reported to follow a relationship of the form:

$$\Delta W = k_p \times t^{0.5} \tag{1}$$

where, ΔW represents the weight gain per unit area in mg/cm<sup>2</sup>, k<sub>p</sub> the isothermal oxidation rate constant in mg<sup>2</sup> cm<sup>-4</sup> h<sup>-1</sup>, and t is the oxidation time at a particular temperature in hours. Equation (1) implies that weight gain, (ΔW), is proportional to the square root of time (t<sup>0.5</sup>). (Pérez-González *et al.*, 2014; Olivares *et al.*, 2013; Sinharoy and Narasimhan, 2004).

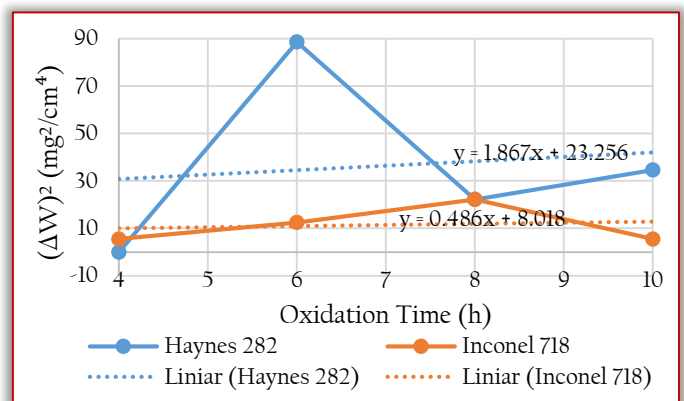


Figure 2. Isothermal rate constant for oxidation of Haynes 282 and Inconel 718 superalloys at 1050°C

By approximating the oxidation kinetics to Equation (9), a plot of the square of weight gain versus time ( $\Delta W^2 = k_p \times t$ , allows for the estimation of the isothermal oxidation rate constant,  $k_p$  (Olivares et al., 2013).

By plotting the square of weight gain versus time and ignoring scatter, an overall isothermal oxidation rate constant,  $k_p$ , is approximately determined from the slope of the best-fit straight line as shown in Figures 2 and 3 for 1050 and 1100°C test temperatures respectively.

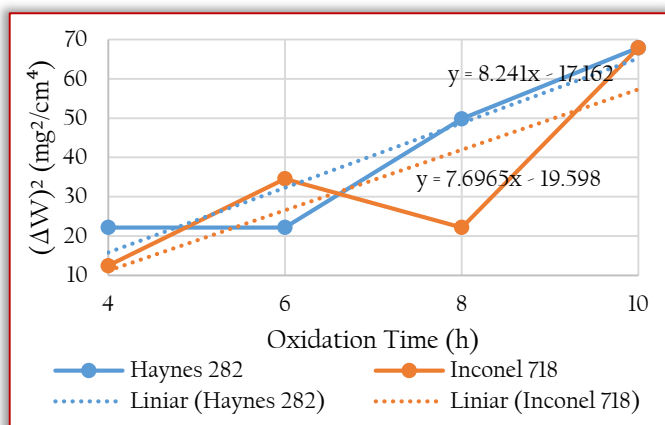


Figure 3. Isothermal rate constant for oxidation of Haynes 282 and Inconel 718 superalloys at 1100°C

### — Summary of Oxidation Tests

Weight gain as well as the isothermal oxidation rate was observed to increase with temperature for both Haynes 282 and Inconel 718 at the 1050 and 1100°C test temperatures. The oxidation rate constant of Haynes 282, the slope of the fitted straight line, is about 3.8 times higher (1.87 mg<sup>2</sup>/cm<sup>4</sup>. h) than that of Inconel 718 (0.49 mg<sup>2</sup>/cm<sup>4</sup>. h) at 1050°C.

At 1100°C, the oxidation rate of Haynes 282, the slope of the best-fit straight line, is approximately 1.1 times more (8.24 mg<sup>2</sup>/cm<sup>4</sup>. h) than that of Inconel 718 (7.70 mg<sup>2</sup>/cm<sup>4</sup>. h).

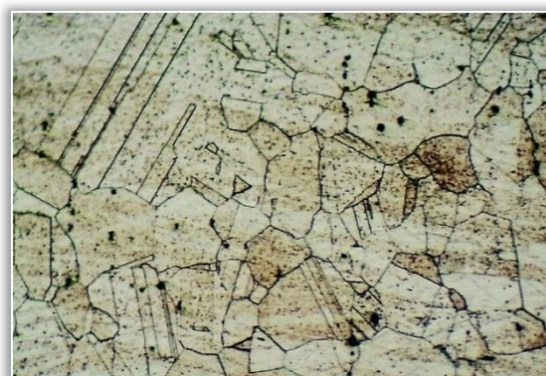
Table 2: Summary of high temperature oxidation of Haynes 282 and Inconel 718 superalloys at 1050 and 1100 °C test temperatures

Alloy type	1050°C		1100°C	
	Total wt. gain, 10 h (mg/cm <sup>2</sup> )	Isothermal oxidation rate (mg <sup>2</sup> /cm <sup>4</sup> . h)	Total wt. gain, 10 h (mg/cm <sup>2</sup> )	Isothermal oxidation rate (mg <sup>2</sup> /cm <sup>4</sup> . h)
Haynes 282	20.00	1.87	24.72	8.24
Inconel 718	12.94	0.49	22.36	7.70

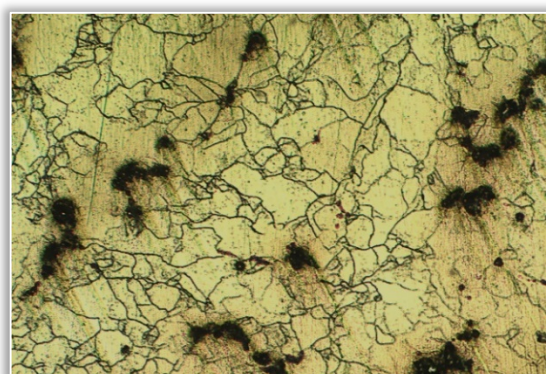
### — Light Optical Microstructural Analysis

Light optical microstructural analysis of cross-sections of the oxidized samples of both superalloys was carried out in an attempt to determine the thickness of the formed-surface-oxides (Plates 2–9).

The micrographs were observed at the boundary between the epoxy mount and the samples cross sections at 100x magnification. Microstructure of the as-received superalloy samples were also examined (Plate 1 a, and b).



(a)

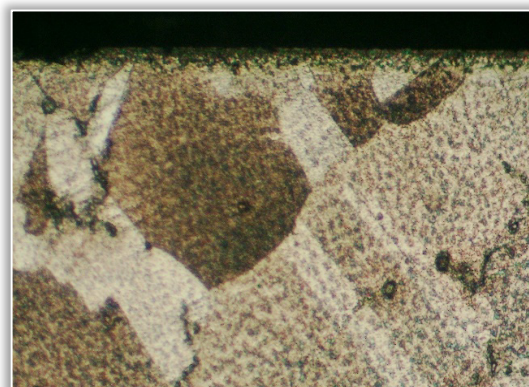


(b)

Plate 1. Optical micrographs of (a) As-Received Haynes 282 (100x), (b) As-Received Inconel 718 (100x)

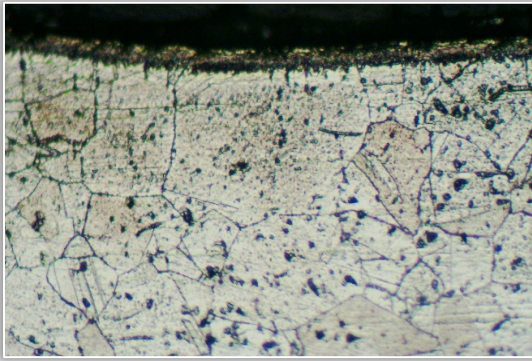


(a)



(b)

Plate 2. Optical micrographs of samples oxidized at 1050°C for 4 hours (a) Haynes 282 Sample 1 (100x), (b) Inconel 718 Sample A (100x)

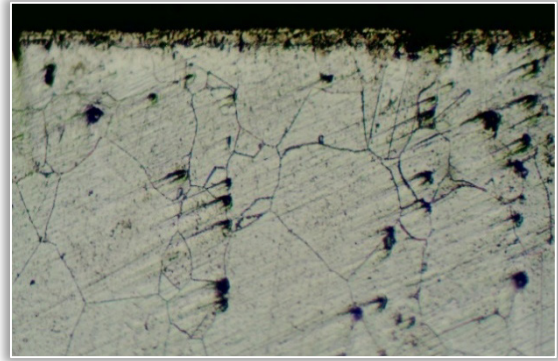


(a)

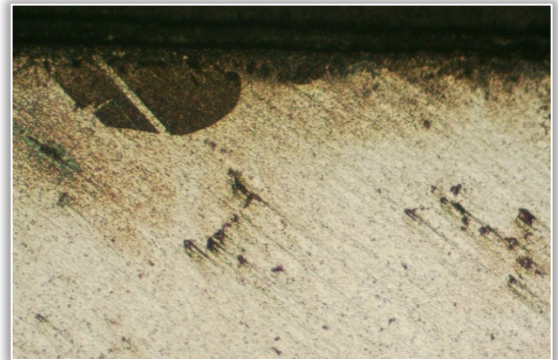


(b)

Plate 3. Optical micrographs of samples oxidized at 1050°C for 6 hours (a) Haynes 282 Sample 2 (100x), (b) Inconel 718 Sample B (100x)

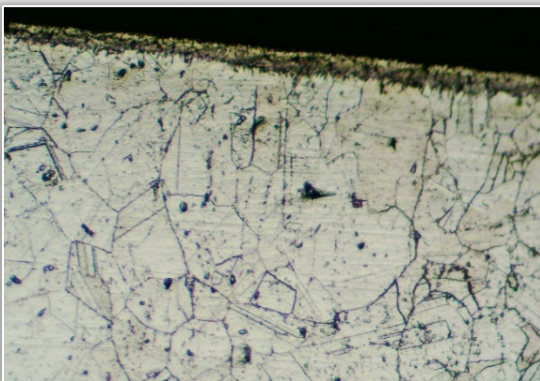


(a)

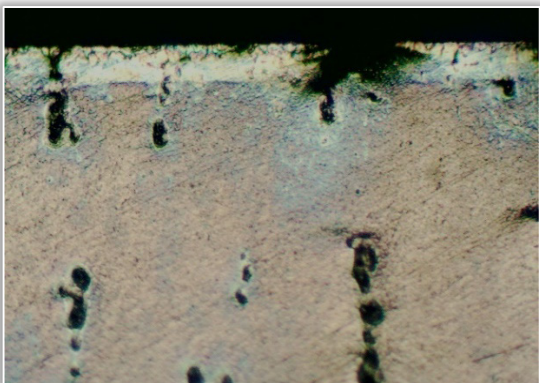


(b)

Plate 5. Optical micrographs of samples oxidized at 1050°C for 10 hours (a) Haynes 282 Sample 4 (100x), (b) Inconel 718 Sample D (100x)

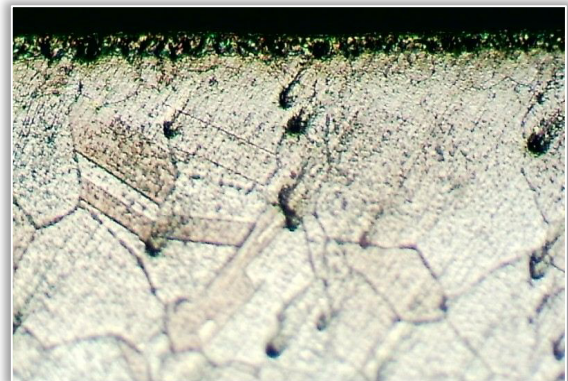


(a)



(b)

Plate 4. Optical micrographs of samples oxidized at 1050°C for 8 hours (a) Haynes 282 Sample 3 (100x), (b) Inconel 718 Sample C (100x)

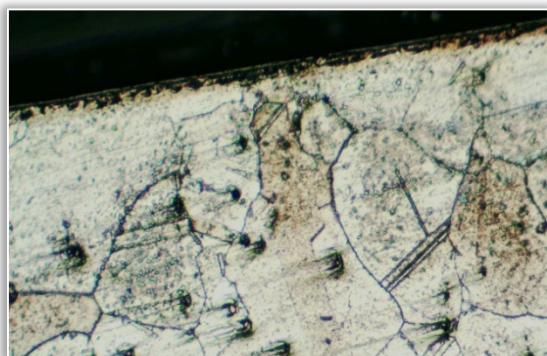


(a)

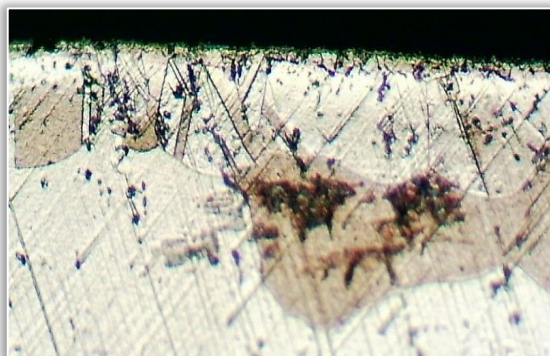


(b)

Plate 6. Optical micrographs of samples oxidized at 1100°C for 4 hours (a) Haynes 282 Sample 5 (100x), (b) Inconel 718 Sample E (100x)

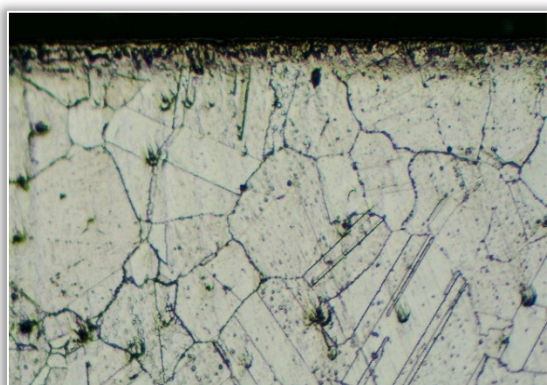


(a)



(b)

Plate 7. Optical micrographs of samples oxidized at 1100°C for 6 hours (a) Haynes 282 Sample 6 (100x), (b) Inconel 718 Sample F (100x)

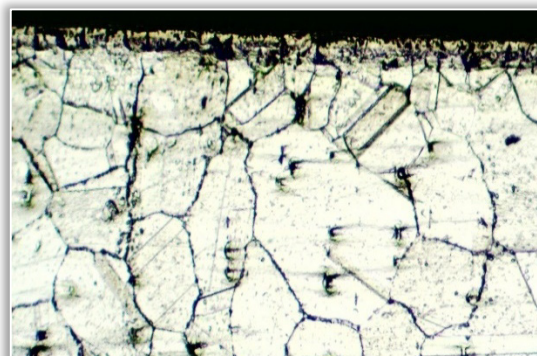


(a)

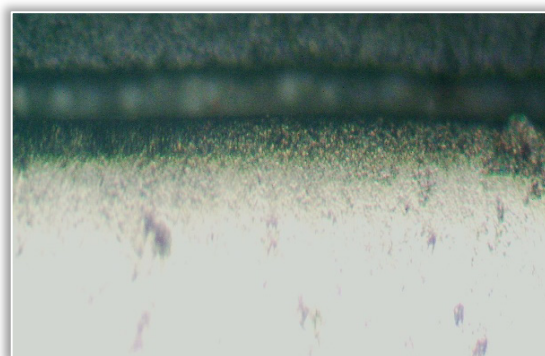


(b)

Plate 8. Optical micrographs of samples oxidized at 1100°C for 8 hours (a) Haynes 282 Sample 7 (100x), (b) Inconel 718 Sample G (100x)



(a)



(b)

Plate 9. Optical micrographs of samples oxidized at 1100°C for 10 hours (a) Haynes 282 Sample 8 (100x), (b) Inconel 718 Sample H (100x)

All examined cross sections of both superalloys' oxidized samples showed distinctly oxidized regions at the top exposed surfaces. However, the thickness of the formed-oxide film was not readily determinable from the light optical microscope used. This could have been due to software limitations. Therefore, measurement of the oxide layer thickness in this present study was not performed using light optical microscopy to prevent inconsistency of results in oxide thickness determination.

#### SEM and EDS Analyses

In order to characterize the oxide morphology, the top surfaces of oxidized samples were examined using SEM. Elemental composition of the formed-surface-oxides was analysed using EDS. For this investigation, the Phenom Desktop SEM machine with Phenom ProX software attached, in Covenant University, Ota, Ogun State, Nigeria was used.

#### Oxidized Haynes 282 superalloy

Figures 4 and 5 show the external surface SEM image and spot EDS analysis of Haynes 282 samples oxidized at 1050 and 1100°C for 10 hours.

#### Oxidized Inconel 718 superalloy

Figures 6 and 7 show the external surface SEM image and spot EDS analysis of Inconel 718 samples oxidized at 1050 and 1100°C for 10 hours each.

SEM surface oxide morphologies of Inconel 718 samples oxidized for 10 hours at 1050 and 1100°C, as observed show cluster-like oxide structures. EDS elemental composition at both test temperatures as observed, was predominantly Cr, and O; suggesting presence of a chromium oxide film.

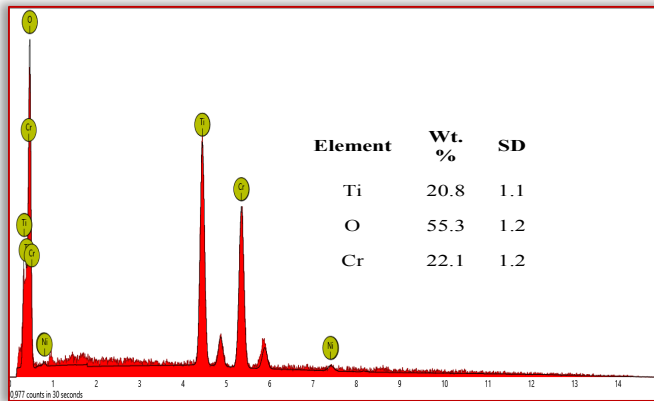
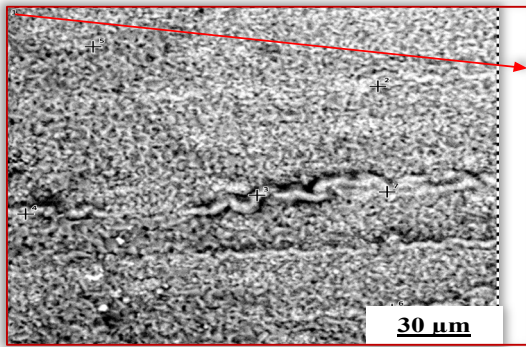


Figure 4. External surface SEM image of Haynes 282 sample oxidized at 1050°C for 10 hours (2,500x) with EDS spectrum of spot 1 attached

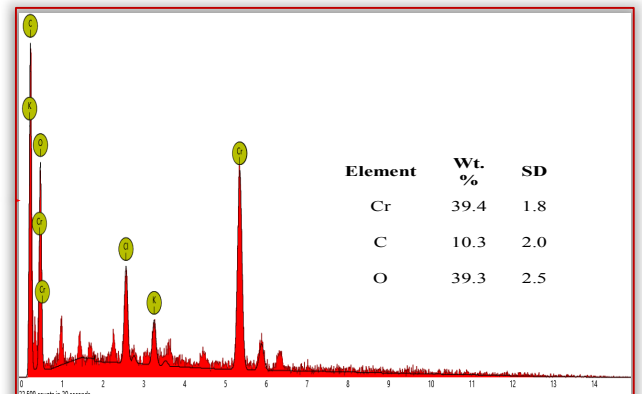
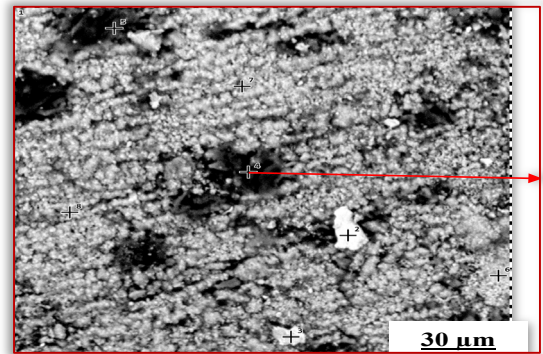


Figure 6. External surface SEM image of Inconel 718 sample oxidized at 1050°C for 10 hours (2,500x) with EDS spectrum of spot 4 attached

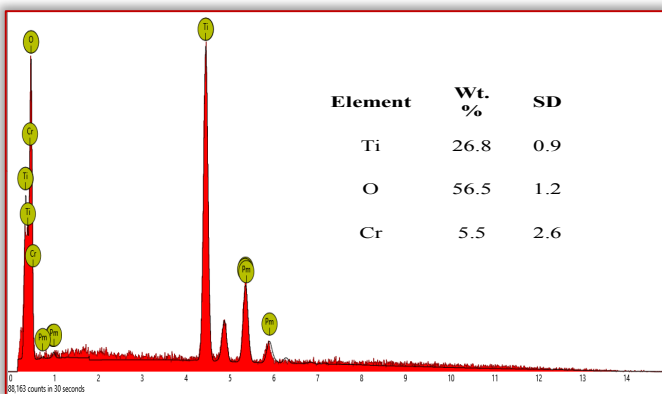
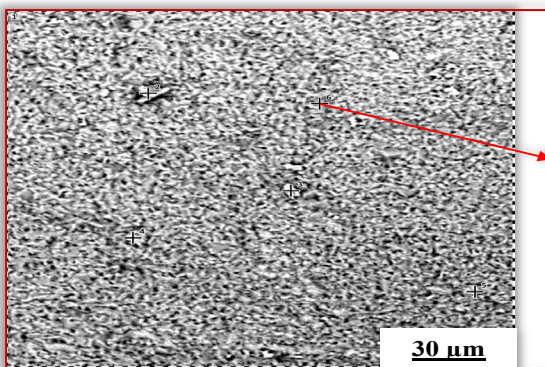


Figure 5. External surface SEM image of Haynes 282 sample oxidized at 1100°C for 10 hours (2500x) with EDS spectrum of spot 6 attached.

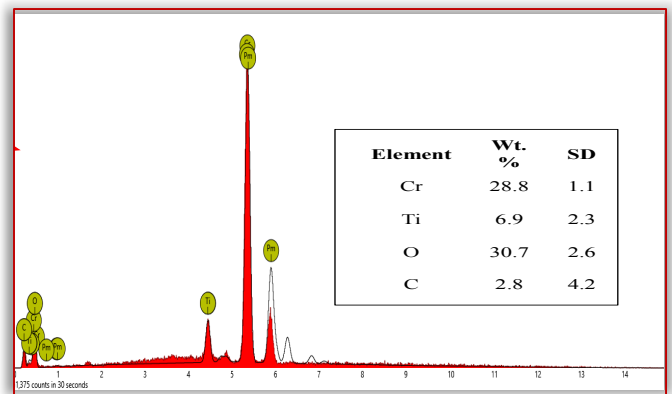
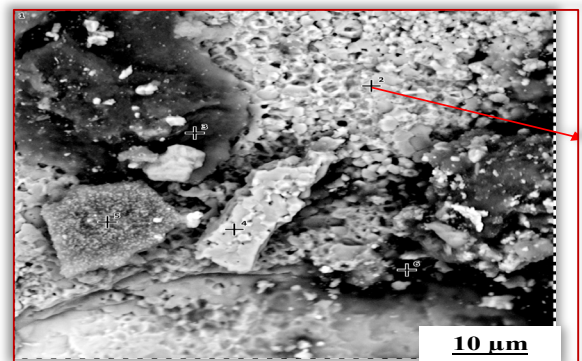


Figure 7. External surface SEM image of Inconel 718 sample oxidized at 1100°C for 10 hours (5000x) with EDS spectrum of spot 2 attached

## DISCUSSIONS

Oxidation resistance of superalloys is fundamentally due to the formation of adherent oxide layers. These oxides are formed by a selective oxidation of the elements in the alloy, which is affected by a number of factors including relative concentration of reactive elements, cracking behaviour of the oxide scale, and an upper-temperature limit for oxide failure (Pérez-González et al., 2014; Smith, 2013).

Typically, nickel-based superalloy gas turbine components form protective oxides such as Cr<sub>2</sub>O<sub>3</sub> (chromia) when exposed to oxidizing environments at high temperatures. Often, the rate of formation of chromium oxides is quicker in comparison with other protective oxides. This makes chromium oxide a preferred oxide since it will form quickly to protect the alloy, and will repair itself quickly in the event of oxide layer spallation. However, chromium oxide may lose its protective properties at temperatures above 1000°C, leading to formation of volatile CrO<sub>3</sub>. Consequently, Cr<sub>2</sub>O<sub>3</sub> alone may not provide sufficient oxidation protection at very high temperatures (Cottis et al., 2010; Smith, 2013)

## CONCLUSIONS

This study has shown that:

- At temperatures of 1050 and 1100°C, a thin protective oxide film was developed on the surfaces of both Inconel 718 and Haynes 282 superalloys.
- Haynes 282 has significantly higher isothermal oxidation rate,  $k_p$  than Inconel at 1050°C but a slightly higher  $k_p$  than Inconel at 1100°C.
- At both temperatures the elemental composition of the oxide film observed on Haynes 282 suggested presence of chromium oxide containing some titanium oxide-film at both temperatures, while elemental composition of Inconel 718 suggested presence of chromium oxide.

## Acknowledgements

Test materials for this work were received through the kind assistance of Prof. A. O. Ojo of the department of Mechanical and Production Engineering, University of Manitoba, Canada. Special thanks to the Management of MIDWAL ENGINEERING (Metallurgical Engineers and Testing Laboratory), Lekki, Lagos, Nigeria.

## References

- [1] Ahlatci, H. (1991). The use of coatings for hot corrosion and Erosion protection in turbine hot section components. *Journal of Engineering Sciences*, 5(1), 885–892.
- [2] ASM International, *ASM Metals Handbook Special Volume: Heat Resistant Materials*. ASM International, 1997.
- [3] Barbosa, C., Nascimento, J. L., Caminha, I.M. V., and Abud, I. C. (2005). Microstructural aspects of the failure analysis of nickel base superalloys components. *Elsevier, Engineering Failure Analysis*, 12, 348–361.
- [4] Caron, P. and Khan, T. (1999). Evolution of Ni-based superalloys for single crystal gas turbine blade applications. *Aerospace Science Technology*, 3, 513–523.
- [5] Eliaz, N., Shemesh, G. and Latanision, R. M. (2002). Hot corrosion in gas turbine components. *Pergamon, Engineering Failure Analysis*, 9, 31–43.
- [6] Mahobia, G. S., Sudhakar R.G., Antony, A., Chattopadhyay, K., Srinivas, N. C. S. and Singh, V. (2013). Effect of Salt Coatings

- [7] on Low Cycle Fatigue Behavior of Nickel-base Superalloy GTM-SU-718. Elsevier, *Procedia Engineering*, 55, 830–834.
- [8] Olivares, R. I., Stein, W., and Marvig, P. (2013). Thermogravimetric study of oxidation-resistant alloys for high-temperature solar receivers. *Journal of The Minerals, Metals & Materials Society (JOM-TMS)*, 65(12), 1660–1669.
- [9] Pérez-González, F. A., Garza-Montes-de Oca, N. F., Colás, R. (2014). High Temperature Oxidation of the Haynes 282 Nickel-based Superalloy. *Springer, Oxidation of Metals*, 82, 145–161.
- [10] Pollock, T M. and Tin, S. (2006). Nickel-based superalloys for advanced turbine engines: Chemistry, microstructure and properties. *Journal of Propulsion and Power*, 22(2), 361–374.
- [11] Pomeroy, M. J. (2005). Coatings for gas turbine materials and long-term stability issues," *Materials and Design*, 26(3), 223–231.
- [12] Saravanamuttoo, H., Rogers, G., Cohen, H., and Straznicky, P. (2009). *Gas Turbine Theory*, Sixth Edition ed. Edinburgh Gate, Harlow, England: Pearson Education Limited.
- [13] Shukla, V. N., Jayaganthan, R., and Tewari, V. K. (2013). Oxidation and Hot Corrosion Behaviour of Ni-based Superalloy Inconel 718 in Na<sub>2</sub>SO<sub>4</sub>–75%V<sub>2</sub>O<sub>5</sub> Environment at Elevated Temperature. *International Journal of Surface Engineering & Materials Technology*, 3(1), 20–24. ISSN: 2249–7250.
- [14] Sinharoy, S. and Narasimhan, S. L. (2004). Oxidation behaviour of two nickel-base superalloys used as elevated temperature valves in spark ignited engines and diesel exhaust recirculation (EGR) applications. *Superalloys 2004*, Edited by K. A. Green, T. M. Pollock, H.
- [15] Harada, T. E. Howson, R. C. Reed, J. J. Schirra, and S. Walston. *TMS (The Minerals, Metals & Materials Society)*, 623–626.
- [16] Smith, M. M. (2013). Comparative Oxidation Study of Uncoated and coated CMSX-4 and CMSX-486 Single Crystal Superalloys. Masters' Thesis, University of Manitoba, Winnipeg, Canada.
- [17] The University of Manchester, Shreir's Corrosion, 4th ed., R. A. Cottis et al., Eds. Amsterdam, Netherlands: Elsevier Ltd., 2010, Vol. 1.
- [18] Wu, Y., Li, X. W., Song, G. M., Wang, Y. M., and Narita, T. (2010). Improvement of the oxidation resistance of the single-crystal Ni-based TMS-82+ superalloy by Ni-Al coatings with/without the diffusion barrier. *Springer, Oxidation of Metals*, 74, 287–303. DOI 10.1007/s11085-010-9211-9.



ISSN: 2067-3809

copyright © University POLITEHNICA Timisoara,  
Faculty of Engineering Hunedoara,  
5, Revolutiei, 331128, Hunedoara, ROMANIA  
<http://acta.fih.upt.ro>

# REINTRODUCTION OF IRON-CONTAINING WASTE AND STEEL ALLOYING ELEMENTS INTO THE ECONOMIC CIRCUIT

<sup>1</sup>University Politehnica Timișoara, Faculty of Engineering Hunedoara, ROMANIA

**Abstract:** As a result of the activity in the metallurgical and anti-corrosion industries, there is an important mass of waste, for which there are still no efficient recovery solutions. Besides environmental issues, this waste is enormous and consumes significant amounts of money, as it could be valuable sources of recyclable material in the steel industry and beyond. The main object of the researched theme was the identification of the technological systems / processes approached both at the theoretical and practical / experimental level, regarding the utilization of the waste resulting from the corrosion coatings and those resulted from the steel fluxes. The proposed recovery procedure is a complex one and covers the following aspects: quantitative and qualitative determinations of waste used for experiments performed; their physico-chemical characterization; performing laboratory experiments on pelleting and briquetting processes; establishing their own recipes for these experiments; mathematical correlation to optimize the best results (using Excel, Matlab, DataFit); establishing optimal areas of variation of different technological parameters of waste processing; the interpretation and scientific substantiation of the results obtained; developing strategies for the implementation of the results obtained in industrial practice. The relevance of the paper is the contribution made to the solution of some pressing environmental problems regarding environmental pollution, as well as the concern for the production of new materials with an economic and technological role.

**Keywords:** waste treatment & recovery, ferrous concentrates, galvanic waste recovery, waste management and treatment.

## GENERAL CONSIDERATIONS

The development of technologies and methods of waste treatment and recovery and their implementation is an important environmental and applicative issue. The studies carried out have shown that using the proposed recovery technologies there are obtained ferrous concentrates containing at least 85% metallic iron, the recovery of these concentrates in the furnace and steelmaking sectors and the improvement of the environmental conditions in the areas where they are currently stored waste. From an ecological point of view, the implementation of the galvanic waste recovery process allows to reduce the environmental pollution hazard with the listed metal compounds.

Studies on waste management and treatment in Romania are carried out under the European Union Framework Directive 2008/98/EC on waste. The aim of this directive is to protect the environment and human health by emphasizing the importance of proper waste management and the use of recovery and recycling techniques to reduce resource pressures and improve them. The legislative act establishes the waste hierarchy: prevention, reuse, recycling, recovery for other purposes – such as energy and disposal.

The environmental aspects of waste management, in accord with the waste hierarchy concept, are:

- reduction of waste volume and their environmental impact through rational use and minimization of their quantity;
- reducing the consumption of natural resources and its impact on the balance and status of ecosystems by making full use of waste as a secondary raw material (energy source, fertilizers, building materials, etc.);
- recovery, use, neutralization and disposal of waste, through environmentally friendly and human health procedures.



Figure 1. The waste hierarchy concept

Galvanic enterprises are the most uneconomic by their harmful working conditions and large amounts of waste generated. It is considered that in enterprises where galvanic sections operate, the waste water produced by these sections accounts for 30–50 % of their total volume. The average waste water of an enterprise with a galvanic section is 600–800 m<sup>3</sup>/24 hours. Galvanic waste is formed in the galvanic sections of machine building machinery, machinery and apparatus in the metal pickling process. Galvanic waste is high in metals, such as Cu, Ni, Mn, Pb, Sn and W. Moreover, about 1 km<sup>3</sup> of toxic waste water, containing heavy metals, acids and bases, is discharged annually, and 25–30 % of these waters are deposited in aquatic basins.

The purpose of this paper is to establish the reintroduction in the economic circuit of iron-containing wastes and elements for alloying steel, expressed by ecological, chemical-technological and economic aspects. Ensuring the presence of environmental and chemical-technological aspects provides for modern approaches such as minimizing the impact of waste using the pollution prevention principle,

which consists in implementing technologies that generate a minimum volume of waste.

In the present paper the ecological and chemical-technological aspects foresee the use of advanced production technologies, which ensure obtaining products with a net technical characteristics superior to the previous ones. The approach, solving and implementation of the proposed technologies depend to a large extent on the nature of the materials subject to processing, namely waste as secondary materials to be recycled, as well as the shape of the finished product under which these materials are processed. The study of waste recovery experiments is essential both for the understanding of the recovery process and the reintroduction into the economic circuit of solid waste, as well as for the development of some theoretical and practical analyzes in this field.

### MATERIALS AND METHODS

The waste used in the experiments came from different points: pulverulent iron powder (dust) from ponds and industrial waste dumps, agglomeration and iron fluxes, steel production in arc furnaces and oxygen converters, continuous casting, rolling mills, etc. It is necessary that in the supply of raw materials / waste they are stored in well-defined spaces so that they do not mix or impregnate them with earth, concrete, refractory materials. We considered it of interest to use in pelletizing and briquetting recipes, waste from ArcelorMittal Hunedoara, Cemtrade Oradea, Galvano Alco Oradea, IUS Braşov.

Under laboratory conditions, the waste was stored in plastic containers both before processing (grinding, volumetric classification) for pelletisation/briquetting, and after this processing, mentioning the name of the waste and its quality characteristics. Experimental determinations were carried out at Hunedoara Faculty of Engineering/Polytechnic University of Timișoara, CEMS – Politehnica University of Bucharest (Special Materials Research and Expertise Center) and at ArcelorMittal Hunedoara. These three institutions have laboratories equipped with installations and equipment that have been used to carry out the experiments.

The proposed experimental technological solutions (pelletizing and briquetting) aimed at capitalizing the secondary materials, consisting of small and powdered waste such as: blast furnace dust, red mud, corrosion protection sludge, as well as some basic additions (lime, bentonite). Experiments were carried out on the granulometric class of blast furnace dust, steel dust, gut (originated from ArcelorMittal Hunedoara), red mud (from Oradea), anticorrosive protective sludge (originating from Oradea and Brasov), weighing 10 kg of these types of waste.

For the production of raw pellets and briquettes, the used waste (composition of recipes) and their chemical composition are presented in the Tables 1–5. The granulometric composition of the mixture obtained from all these components is influenced by the weight of each waste

in the recipe, determining the quality of the recyclable product, namely a more uniform particle size distribution.

Table 1. Composition for each recipe (pellets): PO – steel dust; PAF – agglomerating-furnace dust; NR – red sludge; NG – galvanically sludge; G – graphite; B – bentonite; V – lime; T – thermal power plant ash

NUMBER RECIPE	WASTES TYPE							
	P.O.	P.A.F.	N.R.	N.G.	G	B	V	C.T
R1	37	28	14	9	4	6	2	–
R2	18	45	7	18	5	5	2	–
R3	29	29	10	20	5	4	3	–
R4	32	32	10	10	4	4	4	–
R5	21	42	11	11	–	5	4	5
R6	11	53	11	11	–	5	5	4
R7	57	11	11	11	–	3	3	2
R8	72	–	12	12	–	4	–	–
R9	–	72	12	12	–	4	–	–
R10	72	–	–	24	–	4	–	–
R11	–	72	–	24	–	4	–	–
R12	69	–	–	23	1	3	2	–
R13	69	–	23	–	2	5	2	–

Table 2. Composition for each recipe (briquettes): PAF – agglomerating-furnace dust; PO – steel dust; NR – red sludge; NGO – galvanically sludge Oradea; NGB – galvanically sludge Braşov; G – graphite; B – bentonite; V – lime

NUMBER RECIPE	WASTES TYPE						
	P.O.	P.A.F.	N.R.	N.G.	G	B	V
R1	32	38	5	11	8	–	5
R2	27	43	3	14	8	–	5
R3	52	16	5	11	11	–	5
R4	40	20	15	10	10	–	5
R5	55	–	15	15	10	–	10
R6	–	–	–	84	10	10	–
R7	–	42	–	43	9	10	–
R8	–	84	–	–	9	10	–
R9	–	–	–	84	10	6	–
R10	–	–	–	81	9	9	–

Table 3. Chemical composition for red sludge

Fe <sub>2</sub> O <sub>3</sub>	Al <sub>2</sub> O <sub>3</sub>	CaO	SiO <sub>2</sub>	TiO <sub>2</sub>	Na <sub>2</sub> O	Cr <sub>2</sub> O <sub>3</sub>	ZnO	Altele
36.63	27.22	16.35	8.31	5.12	3.77	0.250	0.112	1.10

Table 4. Chemical composition for the galvanically sludge from Brasov

CaO	Al <sub>2</sub> O <sub>3</sub>	Fe <sub>2</sub> O <sub>3</sub>	SiO <sub>2</sub>	S	Na <sub>2</sub> O	Ni	Cr <sub>2</sub> O <sub>3</sub>	MgO
63.25	7.72	6.75	5.07	3.86	3.05	2.75	1.77	1.58

Table 5. Chemical composition for the galvanically sludge from Oradea

ZnO	Fe <sub>2</sub> O <sub>3</sub>	Na <sub>2</sub> O	NiO	P <sub>2</sub> O <sub>5</sub>	SiO <sub>2</sub>	Al <sub>2</sub> O <sub>3</sub>	CaO	Altele
24.43	21.59	12.33	7.73	5.56	5.44	3.52	1.72	8.02

## THE EXPERIMENTAL DATA PROCESSING

### – Mathematical correlations

The character of the optimization of the metallurgical processes is largely influenced by their complex particularities, which take place within a large number of variables (parameters) that act independently or intercondition over time. For this reason, for the analysis of metallurgical processes and for the establishment of double correlation equations between the technological factors and the compressive strength of the raw pellets and the briquettes, the data were processed in the Matlab computing program and the results are presented both graphically and analytically.

The experimental data were modeled in the form of the equation (1).

$$z(x,y) = ax^2 + by^2 + c \cdot xy + d \cdot x + e \cdot y + f \quad (1)$$

where the  $a, b, c, d, e$  and  $f$  are regression coefficients

The equations of the regression hyper-surface are in the form of the above equation, for which there is a correlation coefficient  $R^2$  and a deviation from the regression surface.

In the experimental data processing it was envisaged to obtain some correlations expressed by polynomial functions and the selection of those having representative values for the regression coefficient on the one hand, and on the other hand it was considered that the analytical expression had a shape as much as possible simple. For each correlation, we determined the expression of the functions that limit the upper and lower domains respectively.

It was intended to determine the form of mathematical functions linking dependent variables of the technological process to independent variables, based on experimental determinations, after a correlation analysis of these data was performed.

The resulted regression equations, with the multiply determination coefficients ( $R^2$ ), are presented in eq. (2)–(10).

$$z = -0.0050x^2 - 0.0430y^2 + 0.0037xy - 0.2944x - 1.6302y + 232.8057 \quad (2)$$

$$R^2 = 0.8742$$

$$z = 0.0173x^2 - 0.4860y^2 - 0.0193xy + -1.9154x + 12.2658y + 165.8485 \quad (3)$$

$$R^2 = 0.8652$$

$$z = -0.0124x^2 + -0.0420y^2 + 0.0007xy + 1.3304x - 1.5737y + 194.9876 \quad (4)$$

$$R^2 = 0.8967$$

$$z = -0.0109x^2 - 0.1750y^2 - 0.0055xy + 1.2592x + 5.8883y + 128.1288 \quad (5)$$

$$R^2 = 0.9389$$

$$z = -0.0002x^2 + 0.0075y^2 - 0.0014xy + 0.0399x - 0.0270y - 0.2477 \quad (6)$$

$$R^2 = 0.9858$$

$$z = -0.0002x^2 + 0.0061y^2 - 0.0003xy + 0.0309x - 0.0573y - 0.1376 \quad (7)$$

$$R^2 = 0.9990$$

$$z = -0.0003x^2 - 0.0001y^2 - 0.0001xy + 0.0373x + 0.0190y - 0.3511 \quad (8)$$

$$R^2 = 0.9852$$

$$z = -0.0001x^2 + 0.0009y^2 + 0.0003xy - 0.0080x - 0.0159y + 0.9344 \quad (9)$$

$$R^2 = 0.9973$$

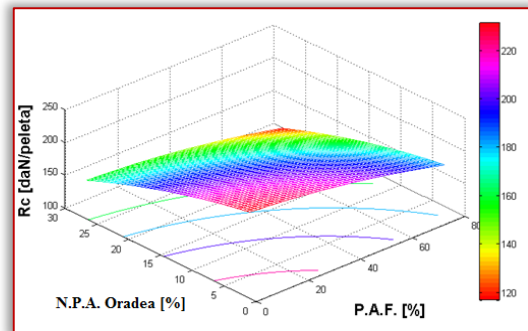
$$z = -0.0003x^2 + 0.0011y^2 + 0.0003xy - 0.0060x - 0.0137y + 0.7364 \quad (10)$$

$$R^2 = 0.9854$$

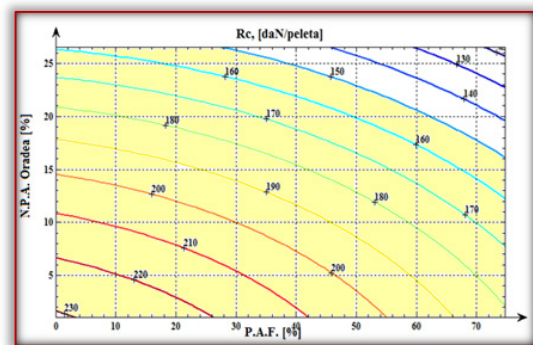
### — Graphical interpretations

In graphical form is presented the regression surface, which has either a maximum/minimum point (a paraboloid shape)

or a stationary point, so that it is a surface type. On the basis of the level curves, the limits of variation of the independent parameters (of the influence factors) can be determined on the dependent parameter, in this case the compressive strength of the raw pellets.

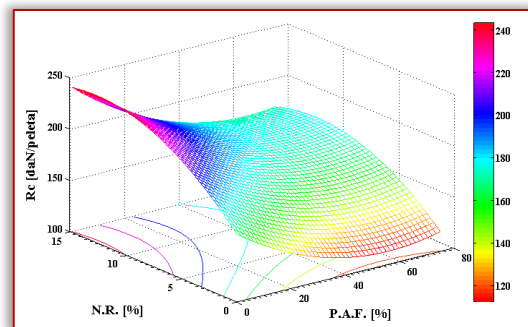


(a)

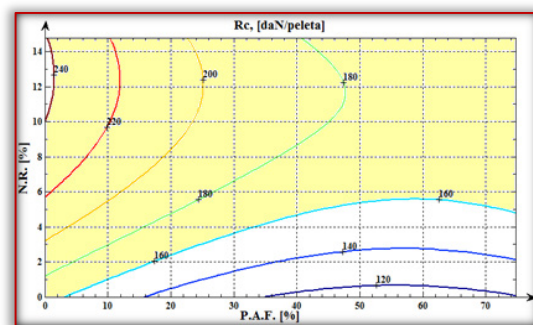


(b)

Figure 2. Compressive strength of pellets according to the percentage of agglomeration dust-furnaces (%) and the proportion of galvanically sludge Oradea (%): (a)–spatial representation; (b)–horizontal level projection curves

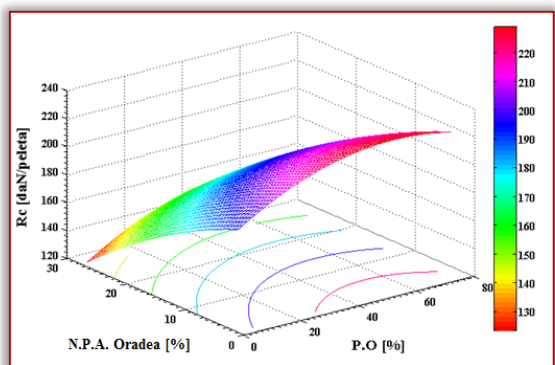


(a)

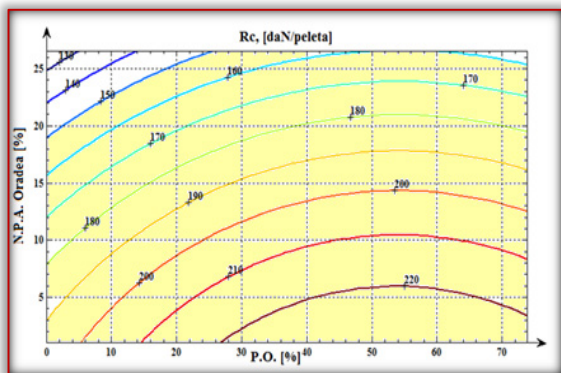


(b)

Figure 3. Compressive strength of pellets according to the proportion of agglomeration dust-furnaces (%) and the proportion of red sludge (%): (a) –spatial representation; (b)–horizontal level projection curves

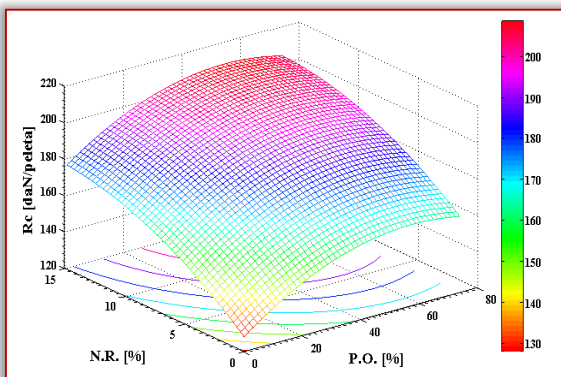


(a)

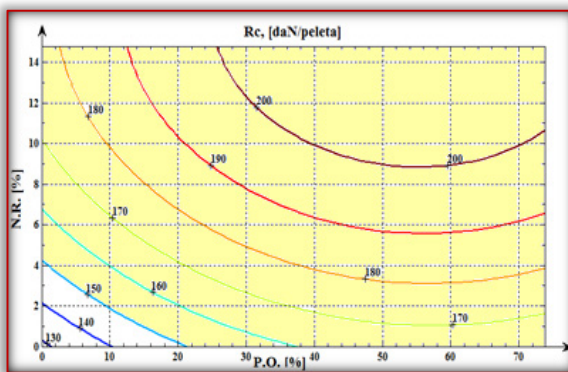


(b)

Figure 4. Compressive strength of pellets according to the percentage of steel dust (%) and the proportion of galvanically sludge Oradea (%): (a)–spatial representation; (b)–horizontal level projection curves

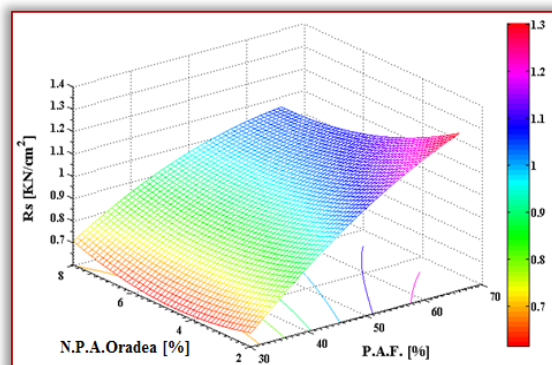


(a)

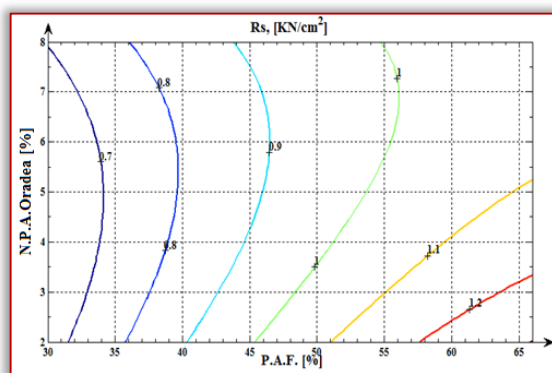


(b)

Figure 5. Compressive strength of pellets according to the proportion of steel dust (%) and the proportion of red mud (%): (a)–spatial representation; (b)–horizontal level projection curves

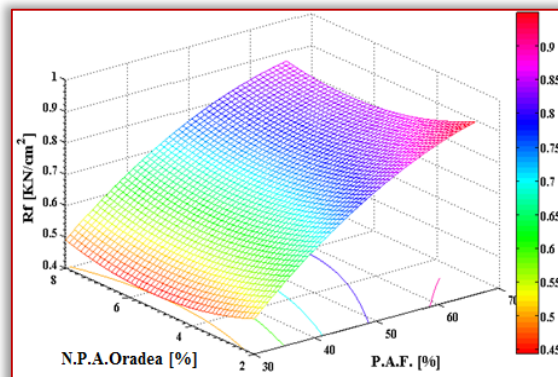


(a)

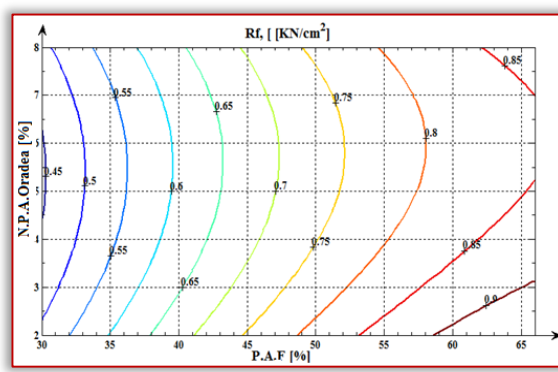


(b)

Figure 6. Crushing resistance of lighters according to the percentage of agglomeration dust (%) and the proportion of galvanically sludge Oradea (%): (a)–spatial representation; (b)–horizontal level projection curves

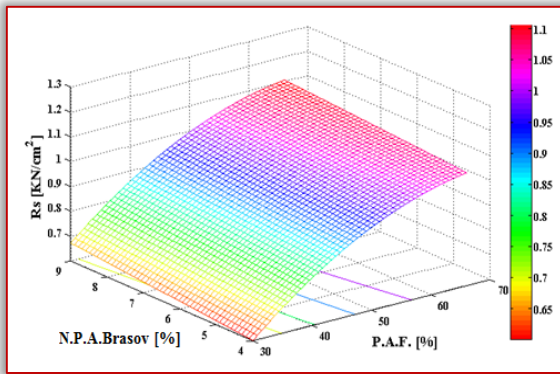


(a)

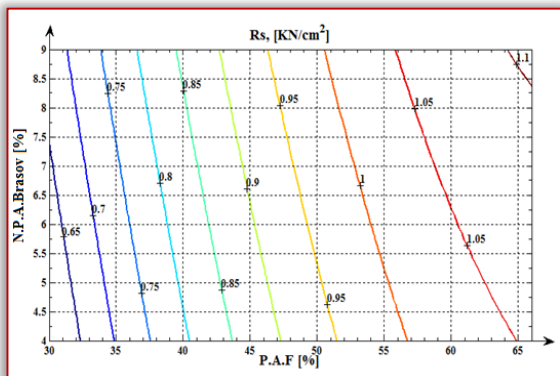


(b)

Figure 7. Crack resistance of the briquettes according to the percentage of agglomeration dust (%) and the proportion of the galvanically sludge Oradea (%): (a)–spatial representation; (b)–horizontal level projection curves

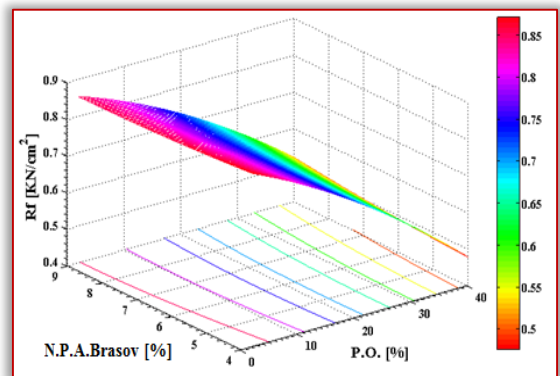


(a)

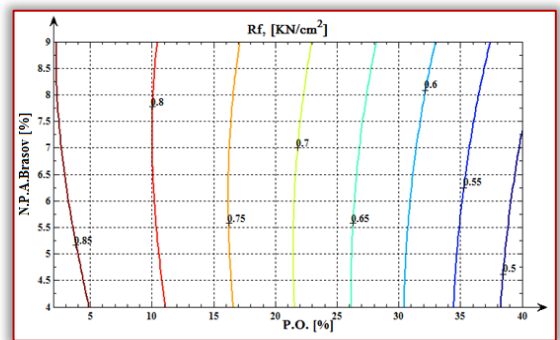


(b)

Figure 8. Briquette crushing resistance according to the percentage of agglomeration dust (%) and the proportion of galvanically sludge Braşov (%): (a)–spatial representation; (b)–horizontal level projection curves

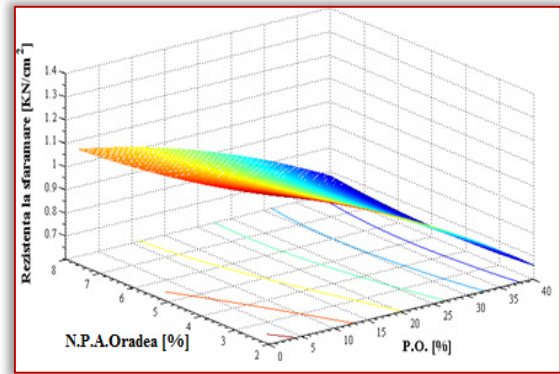


(a)

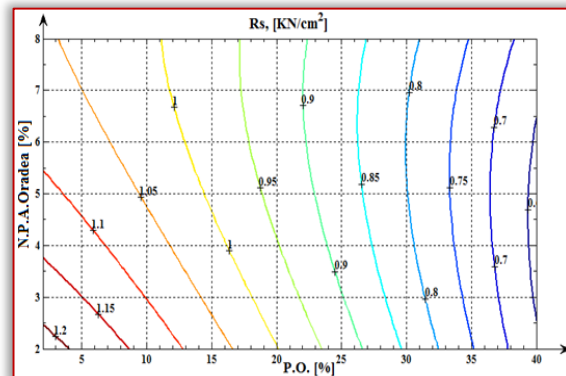


(b)

Figure 9. Crack resistance of the briquettes according to the proportion of steel dust (%) and the proportion of galvanically sludge Braşov (%): (a)–spatial representation; (b)–horizontal level projection curves



(a)



(b)

Figure 10. Crushing resistance of briquettes according to the percentage of steel dust (%) and the proportion of galvanically sludge Oradea (%): (a)–spatial representation; (b)–horizontal level projection curves

## DISCUSSIONS

The analysis carried out shows the following:

- as far as the influence of the red sludge is concerned, increasing its proportion leads to an increase in the compressive strength, the technological explanation being that it has a high content of  $Al_2O_3$  and  $SiO_2$ , which also serves as a binder. In this respect, it can be used in a concentration of 10–12 %, with the mention that compared to other assortments of this material, it (deposited in the ponds in Oradea) has very low content of As on the one hand, and on the other part is currently not recycled;
- it can be seen that although the compressive strength decreases with increasing the proportion of sludge from the anticorrosive protection, it can be used without restrictions up to about 12 % in the pelleting batch. In fact, considering the quantities of about 20–25 tons/year resulting in the corrosion protection process, the waste pelleting waste recyclers can use this waste in smaller proportions depending on the destination of the product obtained;
- in the case of the use of the corrosion protection sludge together with the agglomeration dust–furnaces it is found that higher values for the compressive strength are obtained at their lower proportions in the pelleting batch. High quality pellets can be obtained with agglomeration–blasting dust within the maximum 50%

limit and 10–15 % anti-corrosion protection sludge, with the values for  $R_c$  in the hauling area;

- Figure 6 shows the positive influence of red sludge acting as a binder, basically a 14–16 % red slurry adds good value for pellets even if the agglomeration–baking dust content exceeds 50 %. In the assessments made it is considered that in the majority of cases the pellets are destined for recovery in the steel works;
- Figure 4 shows that an increase in the proportion of steel powder has a positive influence on the compressive strength of the pellets, and the anti-corrosion protection sludge has a negative influence (lower bonding capacity) but within the limits used to ensure the achievement of the required values for resistance (it is clearly seen in the hatched subdomains);
- Figure 5 shows that an increase in compressive strength occurs with the increase in the proportion of red mud and steel powder, the best values being obtained for the upper limits of the two components of the recipe. The technological explanation lies in the high finesse of both material assortment and the content of  $Al_2O_3$  in the red mud. Depending on the availability of waste, it would be preferable to place their proportion to values for  $R_c$  above 140 daN / pellet, especially in the upper right corner;
- analyzing the correlations shown in Figure 7 it is deduced that the correlation surface has a point. For example, at 45% agglomeration dust and 5% corrosion protection mud from Oradea, crack resistance  $R_f = 0.657$  KN/cm<sup>2</sup> (Figure 7); in order to obtain a crush resistance  $R_s = 1$ KN/cm<sup>2</sup>, at a 50% agglomeration dust content, the anti-corrosion protection sludge must have a 3,5 % share. At 50 % agglomeration dust and 4 % corrosion protection sludge from Oradea, crack resistance  $R_f = 0.75$  KN/cm<sup>2</sup> (Figure 7).
- the level curves of these dependencies can be considered as correlation–correlation diagrams of the chemical composition and can guide the conduction of a process for optimizing the chemical composition.

## CONCLUSIONS

Following the analysis carried out on the processing of the secondary materials from the areas mentioned in the paper, the following conclusions can be drawn:

- analysing the pelletization process, it results that the metal coating (chrome and nickel) from GALVAN ALCO Oradea can be utilized by pelletizing;
- it was considered that for the recovery of sludge from S.C. IUS Braşov, the cold hardening variant is the most suitable, CaO having a binding character;
- the pellets obtained (metallised as a result of autoreduction) can be used in the alloyed load of the arc electric furnaces;
- it is apparent from the graphical representation that within the limits of variation of the waste used in the experiments it is ensured that the lighters with the

qualitative characteristics necessary in the process of their utilization are obtained.

Experiments on the possibilities of capitalizing on small and pulverous ferrous waste have led to the obtaining of graphical and analytical correlations that allow the optimal domains of variation of the technological parameters and the qualitative characteristics of the resulting products.

The obtained products, usable as raw material or auxiliary material in the steel processes, contribute to the reduction of the costs for the ferrous raw materials and bring technological, economic and ecological benefits, namely: increasing productivity, reducing the specific energy consumption and increasing the iron recovery rate.

The reintroduction into the economic circuit of small and pulverous ferrous waste, both of those resulting from current production flows as well as those deposited on dumps or ponds, leads to the reduction of the level of water–air–soil pollution in the areas generating such of waste.

## References

- [1] \*\*\* Strategia Națională pentru Dezvoltare Durabilă a României. Orizonturi 2013–2020–2030, Programul Națiunilor Unite pentru Dezvoltare, Centrul Național pentru Dezvoltare Durabilă, Guvernul României, Ministerul Mediului și Dezvoltării Durabile, București, 2008
- [2] Jones, J., The future of Hot Metal Use in EAF Steelmaking, Atlanta, Georgia, USA, 2000
- [3] Heino, J., Recycling or utilisation of dust, scales and sludge from steel industry, [www.ce.jyn.fi/helsie/pdf/heino.pdf](http://www.ce.jyn.fi/helsie/pdf/heino.pdf)
- [4] Constantin, N., Nicolae, M., Geantă, V., Butnariu, I., Processes and alternative technologies in steel, Printech, Bucharest, 2009
- [5] Constantin, N., Nicolae, M., Rucai, V., Research regarding the physical and chemical characteristics of pre-reduced iron area steel analysis of the possibilities of their use in their on and steel elaborating process, International Conference – Prereduced products and Europe, Milano, Italy (1996), p.230–239.
- [6] Ciocan, A., Turning waste generated in small and powder metallurgy, National Publishing Group, Bucharest, 2003
- [7] Hepuț, T., Socalici, A., Ardelean E., Ardelean M., Constantin N., Buzduga R., Utilization of small and pulverulent ferrous waste, Politehnica Publishing House Timisoara, 2011
- [8] Șerban, S., Hepuț, T., Kiss, I., Recovery possibilities through pelletizing of the pulverous wastes stored in the regional ponds, The VI<sup>th</sup> International Conference Industrial Engineering and Environmental Protection (IIZS 2016), Zrenjanin, Serbia, p.116–122.
- [9] Șerban, S., Hepuț, T., Ferrous wastes recovery possibilities in the area of steel industry–experiments in the laboratory phase on the briquettes production from fine and pulverous wastes, Acta Technica Corviniensis – Bulletin of Engineering, Fascicule 3 (2015), p.49–56.
- [10] Socalici A., Hepuț T., Ardelean E., Ardelean M., Ferrous waste processing by peletizing, briquetting and mechanically mixed, International Journal of Energy and Environment, 4(5),2011, pp.532–540

copyright © University POLITEHNICA Timisoara,  
Faculty of Engineering Hunedoara,  
5, Revolutiei, 331128, Hunedoara, ROMANIA  
<http://acta.fih.upt.ro>

<sup>1,2</sup>Samir REMLI, <sup>3</sup>Aissa BENSELHOUB, <sup>1</sup>Issam ROUAIGUIA

# EXPERIMENTATION OF A BLASTING THEORY FOR THE DIGGING OF AN UNDERGROUND HORIZONTAL EXCAVATION FROM BOUKHADRA IRON MINE (EASTERN ALGERIA)

<sup>1</sup>. Laboratory of Mining Resources Valorization and Environment, Badji Mokhtar University, Annaba, ALGERIA

<sup>2</sup>. Mining Engineering Department, Larbi Tebessi University, Tebessa, ALGERIA

<sup>3</sup>. State Agrarian and Economic University, Dnipro, UKRAINE

**Abstract:** The digging of horizontal mining excavations where the rock is hard requires an appropriate blasting plan. Thus the recognition of all the parameters that affect the latter including section, advancement and stability of the structure. to do this, a test of a theory at the level of the iron mine of Boukhadra, based on the assurance of creation for another liberation surface inside the front to be cut down; in order to improve the progress of the construction site due to the reduction of the specific explosive consumption, also in order to avoid the back effect after blasting which negatively influences the desired section shape.

**Keywords:** Algeria, mining, civil engineering, tunnels, rock fragmentation, blasting, demolition, underground excavation

## INTRODUCTION

The main technological process in underground ore body development is the blasting process. During development and sloping processes, drilling and blasting operations take up 50-70% of all the process and volume. The quality and the cost of development depend on the effectiveness of the drilling and blasting operation. The duration and laboriousness of drilling-blasting operations mainly depends on the physical and the mechanical properties of the blasted rock, the cross-section of the development, the blasting parameters and the blast hole and hole charge construction (Raskildinov B., U., 2001).

Good blast design and execution are essential ingredients for successful underground mining. Poor blasting practices can have a severely negative impact on the economics of mining. Military blasting, rather than precision blasting, can result in dilution of high-grade ores. Military blasting can damage sensitive or tender rock structures that make up the hanging wall or footwall so unwanted caving occurs with the possibility/probability of ore loss and/or dilution. Poor design and execution when ring drilling can mean that succeeding rings are damaged ailure to complete undercuts can mean the transmission of very high loads to the underlying structures and their subsequent failure. The results are lost revenues and added costs.

Good drilling and good blasting go hand in hand. If the drilling is poor, there is little one can do to correct the rest of the job. It is similar to building a house. If the foundation is poorly done, there are major problems along the rest of the way. A discussion of drilling practices is beyond the scope of this chapter, but the blast design must begin there. Prior to designing the blasting, one must be sure that the miners have the machines and the capabilities to build the design. If the design cannot be built with the tools at hand, then it is no design. Hence, one starts the design process by carefully

examining the drilling capabilities (Roger H., William H., et Claude C., 2014).

Drilling and blasting method (DBM) is globally used for rock excavation due to low investment, cheap explosive energy, easy acceptability among the stakeholders, possibility of dealing with different shapes and sizes of openings and reasonably faster rate of advancement in a suitable geotechnical mining condition. This makes DBM a preferred method of rock excavation (Innaurato N., Mancini R. et Cardu, M., 1998). The drill and blast method is characterized by operations that occur in a repeated cyclic sequence. The level of automation and mechanization of these tasks is low and there is a high degree of hard manual labor involved. During temporary support installation and mucking, worker safety is a serious issue. This is because immediately after blasting there can be a high degree of risk from rock falls in the unsupported section of tunnel. The drill and blast excavation method is a very adaptable and flexible process in regard to the excavation of any tunnel cross section or intermediate section, and it allows for the installation of various kinds of temporary rock support. Further, the drill and blast method is characterized by a short mobilization time requirement due to the use of standard equipment (Gerhard G., Cliff S., et Asce, F., 2002).

Duvall and (Duvall, W.I., et Fogelson, D.E., 1962); Langefors U., et Khilstrom, B., 1973) and others, have published blast damage criteria for buildings and other surface structures. Almost all of these criteria relate blast damage to peak particle velocity resulting from the dynamic stresses induced by the explosion. While it is generally recognized that gas pressure assists in the rock fragmentation process, there has been little attempt to quantify this damage. The blasting sequence in a tunnel or drift always starts from the "cut", a pattern of holes at or close to the center of the face, designed to provide the ideal line of deformation. The placement, arrangement and drilling

accuracy of the cut is crucial for successful blasting in tunneling. A wide variety of cut types have been used in mining and construction, but basically they fall into two categories: cuts based on parallel holes, and cuts that use holes drilled at certain angles.

The most common types of cut today is the parallel and V cut. The V cut is the older of the two and is still widely used in construction. It is an effective type of cut for tunnels with a fairly large cross-section and requires fewer holes than a parallel cut. The parallel cut was introduced when the first mechanized drilling machines came on the market making accurate parallel drilling possible.

When developing an underground mining project (Babyouk G., et Chaib R, 1988), one of the main operations is the establishment of a favorable blasting plan for the digging of the underground excavation. This is normally determined by a more rational method.

This paper is intended to ensure the creation of another liberation surface during digging of horizontal excavations, by the exact arrangement of the empty holes and that of cut from a mathematical theory based on the coefficient of expansion of the rock, in order to optimize the blasting process by improving the progress of the construction site due to the reduction of the specific explosive consumption.

## MATERIALS AND METHOD

### — Theoretical Calculation

#### » Elastic Models of Explosive–Rock

Detonation of an explosive charge in rock results in dynamic loading of the walls of the borehole and generation of a stress wave, which transmits energy through the surrounding (Brady B. H. G., Brown E.T., 2005). The generation of fractures can be assumed to be related in some way to the magnitudes of the transient stresses associated with the passage of the wave.

The most important solution for the stress distribution around an explosive source is that due to Sharpe (1942) for a spherical charge. The charge is detonated in a spherical cavity of radius  $a$ , generating a spherically divergent P wave.

The transient cavity pressure is taken to be represented by the expression (1):

$$p = p_0 e^{-\alpha t} \quad (1)$$

where;  $p_0$  is the peak wall pressure, and  $\alpha$  is decay constant.

#### » Phenomenology of Rock Breakage by Explosive

Explosive attack on rock is an extremely violent process, and experimental attempts to define the mechanics of rock breakage by explosives have not been highly successful. The following qualitative account of explosive interaction with rock is based mainly on the accounts by Duvall and Atchison (1957), and Kutter and Fairhurst (1971). In the period during and following the passage of a detonation wave along an explosive charge, the rock around the blast hole is subjected to the following phases of loading:

- dynamic loading, during detonation of the explosive charge, and generation and propagation of the body wave in the medium;
- quasi-static loading, under the residual blast area pressure applied by the detonation product gases;
- release of loading, during the period of rock displacement and relaxation of the transient stress field.

#### » Dynamic Load

Three zones of material response to the impulsive loading and high-intensity stress wave are recognized in the medium. In the immediate vicinity of the blast hole, the high stress intensity results in the generation of a shock wave in the rock. In this so-called shock zone, the rock behaves mechanically as a viscous solid.

Passage of the stress wave causes the rock to be crushed or extensively cracked, and the intensity of the wave is reduced by viscous losses. The attenuation process also results in reduction of the wave propagation velocity to the acoustic velocity. For a blast hole of radius  $r_h$ , the radius  $r_s$  of the shock zone may be about  $2r_h$ . In some cases, superficial observation may not, in fact, reveal a crushed zone around a blast hole.

The domain immediately outside the shock zone is called the transition zone. In this region, the rock behaves as a non-linear elastic solid; subject to large strain (i.e. the small strain elastic theory developed in this text is inadequate to describe rock behavior in this zone). New fractures are initiated and propagated in the radially compressive stress field, by wave interaction with the crack population. Crack development is in the radial direction, resulting in a severely cracked annulus, called the rose of cracks. Generation of the radial cracks extracts energy from the radial P wave, resulting in reduction in the stress intensity. The radius,  $r_t$ , of the transition zone is about  $4-6r_h$ .

In the transition zone, the intensity of the state of stress associated with the radial wave is reduced to a level at which the rock behaves linearly elastically. The behavior of the rock in this domain, called the seismic zone, although new cracks may be initiated in this region, crack propagation occurs exclusively by extension of the longest cracks of the transition zone. Thus, a short distance outside the transition zone, a few cracks continue to propagate, at a velocity of about  $0.20-0.25C_p$ . The P wave therefore rapidly outruns the crack tips, and propagation ceases. It appears that at a radius of about  $9r_h$ , macroscopic crack generation by the primary radial wave ceases.

However, during transmission of the wave towards the free face, fractures may be initiated at the Griffith cracks. The process may be considered as one of conditioning the rock mass for subsequent macroscopic rupture, or of an accumulation of damage in the rock fabric.

When the radial compressive wave is reflected at a free face, a tensile wave, whose apparent source is the mirror image of the blast hole reflected in the free face, is generated. It is possible that, in massive rock, surface will occur at the free face, although there is no convincing evidence for this.

In the interior of the medium, crack extension may be promoted by the more favorable mechanical environment of the tensile stress field, resulting in further accumulation of damage. In a jointed rock mass, the role of the reflected tensile pulse is limited, due to joint separation, trapping the wave near the free face.

» **Quasi-Static Load**

The dynamic phase of loading is complete when the radial wave propagates to the free face, is reflected, and propagates back past the plane of the blast hole. For an average rock mass ( $C_p = 4000 \text{ m s}^{-1}$ ), this process is complete within 0.5 ms/m of burden. Because mass motion of the burden does not occur for an elapsed time much greater than the dynamic load time, it appears that pressure exerted in the blast hole by the detonation product gases may exercise a significant role in rock fragmentation.

Sustained gas pressure in the blast hole increases the borehole diameter, and generates a static stress field around the blast hole. Gas may also stream into the fractures formed by dynamic loading, to cause fracture extension by pneumatic wedging.

In the following discussion, the effect of field stresses on the quasi-static stress distribution is neglected. The simplest case of quasi-static loading involves a pressurized hole, of expanded radius  $a$ , subject to internal pressure  $p_0$ . If the region around the hole boundary is not fissured, the state of stress at any interior point, of radius is given by equation (2):

$$\sigma_{rr} = p_0 a^2/r^2, \sigma_{\theta\theta} = -p_0 \frac{a^2}{r^2}, \sigma_{r\theta} = 0 \quad (2)$$

Then, the hole boundary stresses are given by equation (3):

$$\sigma_{rr} = p_0, \sigma_{\theta\theta} = -p_0 \quad (3)$$

Thus, if the state of stress represented by equation (3) is incapable of generating fractures at the hole boundary, that represented by equation (2) cannot generate fractures in the body of the medium. This suggests that the pattern of cracks produced during the dynamic phase may be important in providing centers from which crack propagation may continue under gas pressure.

Quasi-static loading may occur in the presence of radial cracks, with no gas penetration of the cracks. The presence of radial cracks means that no circumferential tensile stresses can be sustained in the cracked zone.

At any point within the cracked zone of radius  $r_c$ , the state of stress at any point  $r$  is defined by equation (4):

$$\sigma_{rr} = p_0 a/r, \sigma_{\theta\theta} = 0 \quad (4)$$

Moreover, at the perimeter of the cracked zone by:

$$\sigma_{rr} = p_0 a/r_c, \sigma_{\theta\theta} = -p_0 a/r_c \quad (5)$$

The implication of these last equations is that existing radial cracks around a hole may extend so long as the state of stress at the boundary of the cracked zone satisfies the macroscopic failure criterion for the medium.

A third possible case of quasi-static loading involves radial cracks, but with full gas penetration. If the volume of the cracks is negligible, the state of stress at the boundary of the cracked zone is given by equation (6):

$$\sigma_{rr} = p_0, \sigma_{\theta\theta} = -p_0 \quad (6)$$

In practice, the degree of diffusion of gas into the fractures is likely to lie somewhere between the second and third cases, described by equations (5) and (6). In any event, the existence of circumferential tensile stresses about the blast hole provides a satisfactory environment for radial fracture propagation.

— **Proposed Solution**

the creation of another clearance surface is ensured by the determination of the expansion coefficient of the rock  $K_e$ , thus empty holes are drilled in the center of the section (or a single hole with a large diameter) and the volume of the empty created by that, the latter will occupy by the excess of expanded volume resulting after blasting of the section located between the cut holes. The arrangement of these that empty is parallel to this last.

The coefficient of expansion is determined by the ratio between the volume of the blasted rocks  $V_{ab}$  and that of the rocks in place  $V_{bb}$  (equation 7):

$$K_e = V_{ab}/V_{bb} \quad (7)$$

Knowing that these volumes have the same length, so just do the calculations using the surfaces if all. So we have the equation (8):

$$S_{ab} = \frac{K_e}{S_{bb}} \quad (8)$$

To determine the four cut holes around the first surface, we assume a square area value  $S_{bb}$  around the empty holes; then we check the condition  $S_{eh} \geq S_{ab} - S_{bb}$ . who says: the excess of expanded surface ( $S_{ab} - S_p$ ) less than or equal to the surface of the voids generated by the uncharged holes by explosive  $S_{eh}$ .

Where the latter is determined by the calculation relation of the surface of the circle, and multiplied by the number of empty holes (equation 9):

$$S_{eh} = \pi D^2 / 4 \cdot N_{eh} ; \text{cm}^2 \quad (9)$$

where:  $D$  is the diameter of the hole (cm),  $N_{eh}$  is the number of empty holes.

Besides, to solve  $S_{ab}$ , we can express it from the equation (8), so we get the equation 10:

$$S_{ab} = K_e \cdot S_{bb} ; \text{cm}^2 \quad (10)$$

If the condition mentioned above is not verified (figure 1), we redo another supposition of the surface and then we check it until the optimum value is reached, the sides of which represent the cut holes. Therefore, the square root of the optimal surface  $S_{bb}$  gives the length of each side of square by the formula (11):

$$L = \sqrt{S_{bb}} \quad ; \text{ cm} \quad (11)$$

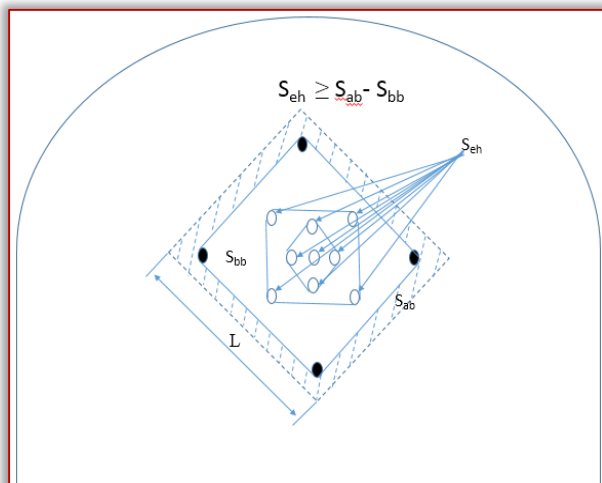


Figure 1: Schema of disposition of the empty holes and that of cut

To facilitate the work of the supposition buckle of the surface  $S_{bb}$ , it can be translated into a flowchart (figure 2) that can be used in a computer program, so it is as follows:

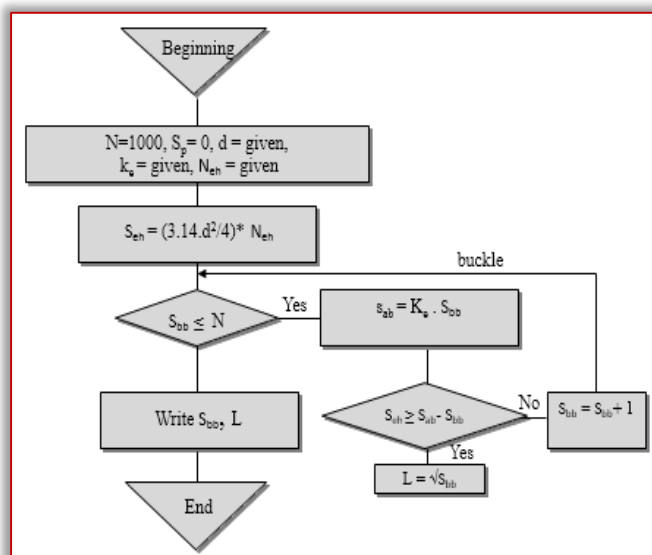


Figure 2: Flowchart of calculation a surface of cut holes

### — Stop Hole

The holes surrounding the cut are called stop holes. The diameter of a stop hole is typically between 41 - 51mm. Holes smaller than 41mm may require drilling an excessive number of holes to ensure successful blasting. Holes bigger than 51mm can result in excessive charging and an uncontrolled blast.

Holes are placed around the cut section in an evenly distributed pattern using a space/burden ration of 1:1.1. If hole size is between 45 - 51mm, typical spacing and burden are both between 1.0m - 1.3m. Actual rock conditions and ability to drill in the required positions are factors that can reduce or add to the number of holes needed. The design of the drilling pattern can now be carried out and the cut located in the cross section in a suitable way.

### — Contour Hole

Floor holes have approximately the same spacing as stop holes, but the burden is somewhat smaller; from 0,7m to 1,1m. Inaccurate or incorrect drilling and charging of the floor holes can leave not blasted bumps, which are difficult to remove later. The contour holes lie in the perimeter of the drilling pattern. In smooth blasting, contour holes are drilled closer to each other and are specially charged for smooth blasting purposes. Spacing is typically from 0.5m to 0-7m and burden varies between 1 and 1.25 times the space. This type of layout makes it possible to use special smooth blasting explosives, which limits the width and depth of the fracture zone in the walls and roof caused by blasting. In special circumstances, two or more smooth blasting rows can be used.

Rock hardness is occasionally incorrectly considered to be the only dominant factor when optimizing the drilling pattern. The change from very hard rock to soft rock therefore causes a change in the drilling pattern. Rocks that are hard but abrasive are easily blasted, whereas the blast ability of rocks such as some limestone, although relatively soft, is poor. However, it is beneficial to redesign and optimize the drilling pattern long before this stage is reached and, more important still, to consider rock blast ability.

### — EXPERIMENTATION: Geographical and Geological Location of the Experimental Site

We tried this theory at the iron mine of Boukhadra Tebessa Algeria in the main horizontal gallery that gives access to the iron deposit of which a section of 12 m<sup>2</sup>, its shape is vaulted. The drill chariot used is MERCURY (1FP) with a diameter of hole 65 mm, the rock is a mineralized marl.

The Jebel Boukhadra (Gadri L., 2012) is located in the east of Algeria 45 km north of the wilaya of Tebessa, 47 km from the mine of Ouenza, 13 km from the Algerian-Tunisian borders, and 190 km south of the steel complex of El Hadjar (wilaya of Annaba). The Jebel of Boukhadra is an isolated massive that rises above the Morsott valley from 700 to 800 m of altitude. With a climax of 1463m. The deposit is between the meridians 8°- 01'and 8°-04' East and the parallels 35°- 40'et 35°- 50' North. The Boukhadra area consists of Mesozoic sediments and with a part of Tertiary and Quaternary for Mesozoic, formed by Triassic and Cretaceous sediments.

### RESULTS AND DISCUSSION

The parameters of the blasting plan were calculated for a progression gallery (figure 3 and 4) using the above-mentioned theory, therefore the summary results were found in table 1. While the operation of loading the holes, the type of the explosive material used is the Marmanit I which has a detonation speed of 4000 m/s, a density of 0.95 and a diameter of cartridge of 50mm, the priming is in electric with a schema of the blasting order (figure 5) as follows:

- The four cut holes: instantaneous electric detonators N°0.
- The four stop holes: micro-delay electric detonators N°3.
- The eight contour holes: micro-delay, electric detonators N°5.

Table 1: Blasting Plan Parameters

Number of empty holes	09 holes
Number of cut holes	04 holes
Number of stopholes	04 holes
Number of contour holes	08 holes
Number of total holes	25 holes
Depth of the hole	1.2 m
Number of holes loaded	16 holes
The amount of the explosive charge	24,50 kg
Volume of rocks blasted	12,96 m <sup>3</sup>
Average explosive consumption per hole	1.53 g/m <sup>3</sup>



Figure 3: Photo gallery of holes disposition



Figure 4: Blasting result in the gallery

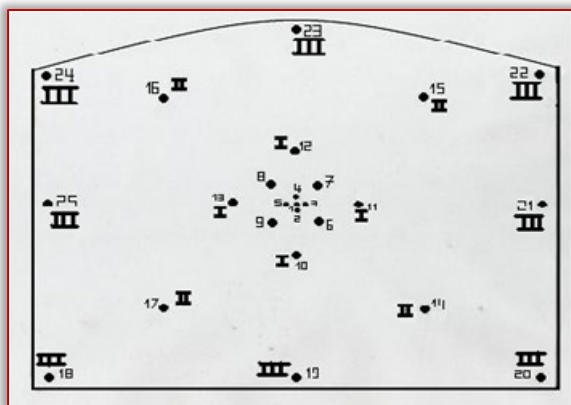


Figure 5: Schema of the blasting order

From the figure 4, we notice that the form of the gallery is well formed in comparison with that old, which is among the problems of the company for the guarded, the deformation of the form generates auxiliary work during a digging of the gallery which is the void filling created between the support and the wall of it, and this is mandatory to ensure the stability of the structure. So the void created by the holes not loaded with explosive material allowed us to ensure another liberation surface inside the massive to be fragmented, which

in turn to avoid the fragmentation clamping of the rocks and also to avoid the back effect of blasting due to the deformation of the gallery form.

### CONCLUSION

This theory of digging horizontal mining excavations based on the real disposition of the cut holes, suggests that there is a good blasting process running in the rock massive, a good advancement of the front of the gallery and also a good form of its section which consequently to a reduction of the specific consumption of explosives.

This theory did not take into account the voids of the discontinuities, cracks ... etc which are in the interval of the cut holes, because it is difficult to quantify their volume in the massive, in any case it is an advantage for the existence of these because it will increase the void more than the empty holes which in turn will also create another liberation surface.

### Bibliography

- [1] Babyouk G., Chaib R, (1988). Creusement des excavations minières, pp. 10.
- [2] Brady B. H. G., Brown E.T. (2005). Rock Mechanics for underground mining, third edition, pp. 519-521.
- [3] Raskildinov B., U., (2001). Increasing the Effectiveness of Blasting in Underground Mines. 17<sup>th</sup> International Mining Congress and Exhibition of Turkey- IMCET, pp. 313.
- [4] Duvall, W.I., Fogelson, D.E. (1962). Review of criteria for estimating damage to residences from blasting vibrations. U.S, pp. 19.
- [5] Gadri L. (2012). Etude de la déformation et de la rupture des massifs fissurés par la méthode des éléments finis (Cas de la mine souterraine de Boukhadra), Thèse de doctorat, pp. 172.
- [6] Gerhard G., Cliff S., Asce, F., (2002). Drill and Blast Tunneling Practices, Practice periodical on structural design, pp. 125-133
- [7] Innaurato N., Mancini R., Cardu, M., (1998). On the influence of rock mass quality on the quality of blasting work in tunnel driving, Tunneling and Underground Space Technology vol. 13 (1), pp. 81 - 89.
- [8] Langefors U., Khilstrom, B. (1973). The modern technique of rock blasting. 2<sup>nd</sup> edition. New York: Wiley, pp. 405.
- [9] Roger H., William H., Claude C. (2014), Blast Design for Underground Mining Applications, pp. 79.



ISSN: 2067-3809

copyright © University POLITEHNICA Timisoara,  
Faculty of Engineering Hunedoara,  
5, Revolutiei, 331128, Hunedoara, ROMANIA  
<http://acta.fih.upt.ro>

# Fascicule 4

## [October - December]

t o m e **XI**

### [2018]

**ACTA**Technica**CORVINIENSIS**  
BULLETIN OF ENGINEERING



**ISSN: 2067-3809**

copyright © University POLITEHNICA Timisoara,  
Faculty of Engineering Hunedoara,  
5, Revolutiei, 331128, Hunedoara, ROMANIA  
<http://acta.fih.upt.ro>

<sup>1</sup>S.I. ADEDOKUN, <sup>2</sup>M.A. ANIFOWOSE, <sup>3</sup>S.O. ODEYEMI

# ASSESSMENT OF STEEL SLAG AS REPLACEMENT FOR COARSE AGGREGATE IN CONCRETE: A REVIEW

<sup>1</sup>Department of Civil Engineering, Ladoke Akintola University of Technology, Ogbomoso, NIGERIA

<sup>2</sup>Department of Civil Engineering, Federal Polytechnic, Offa, NIGERIA

<sup>3</sup>Department of Civil Engineering, Kwara State University, Malete, NIGERIA

**Abstract:** This study presents a review on the utilization of steel slag as replacement for coarse aggregate in concrete. Merits and demerits of steel slag in concrete as well as its physical properties and chemical compositions of steel slag are also presented. It has been reported that it is economical to use steel slag, as the costs of steel slag are just about 50% of that of conventional aggregates. However, the optimum replacement of coarse aggregate with steel slag that gives better mechanical properties (compressive strength, tensile strength and flexural strength) than conventional concrete is found to be between 30 and 60%. In South Western part of Nigeria, there are numbers of steel/iron producing company with large deposits of steel slag. Therefore, there is need for the utilization of this by-product (steel slag) in concrete production in Nigeria as cost of natural aggregates (fine and coarse aggregate) is becoming higher.

**Keywords:** steel slag, coarse aggregate, compressive strength, tensile strength, flexural strength

## INTRODUCTION

Concrete is one of the most widely used construction material in the world. It can be cast in diverse shapes. Concrete is a composite material formed by the combination of cement, sand, coarse aggregate and water in a particular proportion in such a way that the concrete produced meets the needs as regards its workability, strength, durability and economy (Abdul Kadar and Dhanalakshmi, 2016). The aggregates typically account for about 75% of the concrete volume and play a substantial role in different concrete properties. Conventional concrete consists of sand as fine aggregate and gravel, limestone or granite in various sizes and shapes as coarse aggregate. There is a growing interest in using waste materials as alternative aggregate materials and significant research is made on the use of many different materials as aggregate substitutes (Ravikumar *et al.*, 2015). Industrial waste materials such as coal ash, blast furnace slag and steel slag and agricultural waste materials such as coconut shell, palm kernel shell etc. have been used by many researchers in replacement of aggregate in concrete for the purpose of recycling industrial and agricultural waste materials.

Steel slag (SS) is a by-product from steel production. It can be categorized as carbon steel slag and stainless steel slag according to the type of steel, and as pre-treatment slag, basic oxygen furnace slag (BOFS), electrical arc furnace slag (EAFS), ladle refining slag (LFS) and casting residue according to the steelmaking process (Yi *et al.*, 2012). The molten liquid is a complex solution of silicates and oxides that solidifies on cooling and forms steel slag. However, steel slag is defined by the American Society for Testing and Materials (ASTM) as a non-metallic product, consisting essentially of calcium silicates and ferrites combined with fused oxides of iron, aluminium, manganese, calcium and magnesium that are

developed simultaneously with steel in basic oxygen, electric arc, or open hearth furnaces (Sharma *et al.*, 2015). Use of more and more environmentally friendly materials in any Industry in general and construction industry in particular, is of paramount importance. Steel slag aggregates are already being used as aggregates in asphalt paving road mixes due to their mechanical strength, stiffness, porosity, wear resistance and water absorption capacity. Also, steel slag could be used as a partial replacement for coarse aggregate (Padmapriya *et al.*, 2015).

Utilization of steel slag is economical because the costs of steel slag are just about 50% of that of conventional aggregates (Tiwari *et al.*, 2016). It does not contain materials such as chlorides, organic impurities, clay and shells (Tarawneh *et al.*, 2014). It leads to increased strength as materials age (Tarawneh *et al.*, 2014). According to Abrol *et al.* (2016), steel slag has longer life span and durability than the natural aggregates, and when used in asphalt layer in the laying of roads, steel slag offers a better non-skid-able surface (Tarawneh *et al.*, 2014). The use of slag promotes the conservation of natural resources (Kothai and Malathy, 2014). The disadvantage of steel slag is that it will lead to social and environmental problem if not properly disposed (Kumar and Kumar, 2016). However, Palod *et al.* (2017) reported that steel slag possess high mineralogical composition and has higher density than other binders.

Several studies proved that the use of steel slag in concrete as aggregate improves its mechanical and durability properties (Sekaran *et al.*, 2015). Subramani and Ravi (2015), also reported that when steel slag is used in concrete, it acts as filler and as a strengthening material. According to Sezer and Gulderen (2015), its high density makes its use advantageous in some constructions such as foundations, retaining walls, breakwater blocks, noise barriers, radiation

insulators etc. Tran *et al.* (2014) also noted that steel slag aggregates improve the compressive strength, tensile strength, flexural strength and modulus of elasticity of concrete.

In Nigeria and many countries of the world, steel is mainly produced from smelting of metal scrap metals and hundreds of tonnes of steel slag are produced every year. And most often, steel slag are disposed around the steel producing centres posing environmental threats. However, not much research work has been reported on the use of steel slag produced from scrap metals, as produced in Nigeria (Olonade *et al.*, 2015).

### PHYSICAL PROPERTIES OF STEEL SLAG AND GRANITE

Some selected physical properties of steel slag and coarse aggregate (granite); Specific Gravity, Aggregate Impact Value (AIV), Aggregate Crushing Value (ACV) and Los Angeles Abrasion Value (LAAB) from some previous research work are presented in Table 1.

Table 1: Physical Properties of Steel Slag and Granite

Source	Aggregate Type	Specific Gravity	AIV (%)	ACV (%)	LAAB (%)
Priya <i>et al.</i> (2017)	Steel Slag	2.97	40	21.73	23.7
	Granite	2.93	28.9	12.4	13.4
Yi (2008)	Steel Slag	-	17.2	26.05	9.80
	Granite	-	20.54	26.10	9.80
Abrol <i>et al.</i> (2016)	Steel Slag	3.2-3.6	-	-	-
	Granite	-	-	-	-
Sekaran <i>et al.</i> , (2015)	Steel Slag	2.9	24.93	19.25	16.4
	Granite	2.75	28	26	18.6
Khafaga <i>et al.</i> (2014)	Steel Slag	3.48	6.6	11.4	13.5
	Granite	2.65	10.00	22.00	18.50
Olonade <i>et al.</i> (2015)	Steel Slag	2.63	-	-	-
	Granite	2.71	-	-	-
Warudkar & Nigade (2015)	Steel Slag	2.61	-	-	-
	Granite	2.673	-	-	-
Tran <i>et al.</i> (2014)	Steel Slag	-	-	16.83	6.03
	Granite	-	-	13.65	4.24
Tarawneh <i>et al.</i> (2014)	Steel Slag	-	6.31	-	20.26
	Granite	-	23.13	-	23.06
Kothai and Malathy (2014)	Steel Slag	2.95	-	-	-
	Granite	2.75	-	-	-

As observed from Table 1, steel slag possesses higher specific gravity value than coarse aggregate (Priya *et al.*, 2017; Sekaran *et al.*, 2015; Khafaga *et al.*, 2014 and Kothai and Malathy, 2014) but the value of specific gravity reported by Olonade *et al.*, (2015) and Warudkar & Nigade (2015) have lower specific gravity compare to coarse aggregate. Although, these values are relatively close implying that steel slag can perform as substitutes for coarse aggregates. The Aggregate Impact Value (AIV) indicates that coarse aggregate possesses higher values than steel slag except from that of Priya *et al.*, (2017). Similarly, the Aggregate Crushing Value (ACV) possesses similar properties except from the one reported by Priya *et al.*, (2017), Sekaran *et al.*, (2015) and Khafaga *et al.*, (2014). Nonetheless, Los Angeles Abrasion Value (LAAB) also

indicates that steel slag possesses similar properties to coarse aggregate except from those reported by Priya *et al.*, (2017) and Khafaga *et al.*, (2014). This shows that steel slag has relatively similar physical properties to coarse aggregates, which is an indication that slag can relatively perform as substitutes for coarse aggregates in concrete production. This will thereby reduce the environmental pollution caused by the heaps of steel slag, improve the properties of concrete and minimize the cost of concrete production.

### Chemical composition of steel slag

Both Basic-Oxygen- Furnace (BOF) and Electric-Arc-Furnace (EAF) slag are formed during basic steelmaking operations, as explained above. Therefore, in general, the chemical and mineralogical compositions of BOF and EAF slag are similar. Calcium oxide and iron oxide are the two major chemical constituents of both EAF and BOF slag. Ladle slag is generated during the steel refining processes in which several alloys are added to the ladle furnace to produce different grades of steel. For this reason, the chemical constituents of ladle slag differ from those of BOF and EAF slag (Yildirim and Prezzi, 2011). However, chemical compositions of steel slag from previous research work are provided in Table 2.

Table 2: Chemical Compositions of Steel Slag

Source	SiO2	Al2O3	Fe2O3	CaO	MgO	K2O	MnO	TiO2	P2O5
Sezer and Gulderen (2015)	17.79	7.82	35.22	24.62	-	-	-	-	-
Abrol <i>et al.</i> , (2016)	10-19	1-3	-	40-52	-	-	5-8	-	0.5-1
Khafaga <i>et al.</i> (2014)	13.10	5.510	36.80	33.0	5.030	-	4.180	-	0.598
Gokul <i>et al.</i> , (2012)	12.5	2.4	31.2	41.3	4.3	-	6.1	0.8	1.1
Olonade <i>et al.</i> , (2015)	42.40	15.00	31.90	5.00	-	2.05	-	-	-
Tran <i>et al.</i> , (2014)	16.3	6.07	39.2	28.9	1.68	-	4.02	1.02	0.36
Tarawneh <i>et al.</i> , (2014)	9-11	1.4-0.7	10-13	50-57	1-2	0.04-0.01	4-5	-	3.2-2.3
Kothai and Malathy (2013)	10-19	1-3	20-30	40-52	5-10	-	5-8	-	0.5-1
Kothai and Malathy (2014)	10-19	1-3	20-30	40-52	5-10	-	5-8	-	0.5-1
Subramani and Ravi (2015)	10-19	1-3	10-40	40-52	5-10	-	5-8	-	-

The steel slag chemical compositions results of Khafaga *et al.*, (2014) and Gokul *et al.*, (2012) falls within the acceptable limits reported by Abrol *et al.*, (2016), Kothai and Malathy (2013), Kothai and Malathy (2014) and Subramani and Ravi (2015) as contain in Table 2. It is observed from the Table that SiO<sub>2</sub>, Fe<sub>2</sub>O<sub>3</sub>, CaO and MgO are the major constituents of steel slag.

### EFFECT OF STEEL SLAG ON THE PROPERTIES OF CONCRETE

#### — Compressive Strength

Khafaga *et al.* (2014) investigated twenty-four normal, high and ultra-high strength concrete mixtures with replacement percentages 0, 33.33, 66.67 and 100% by weight of the coarse aggregate with two cement contents (450 and 600 kg/m<sup>3</sup>) and three silica fume percentages (0, 10 and 20%). Their results indicated that the optimum concrete compressive strength was obtained for the mixtures with a percentage of 66.67% steel slag aggregates as a replacement of the coarse aggregate. Qurishee *et al.* (2016) in their experimental study on the use of slag as coarse aggregate and its effect on mechanical properties of concrete. It was reported that compressive strength of concrete made by replacing coarse aggregate with slag is higher than normal conventional concrete. However, the compressive strength for concrete made with partial replacement of coarse aggregate by slag is observed to increase up to replacement level of 40% but decreases afterwards. Kothai and Malathy (2013) in their study concluded that workability of concrete containing steel slag does not have any major change while the compressive strength of different mixes shows reasonable improvement of about 10%.

Gokul *et al.* (2012) investigated the use of mild steel slag as a potential replacement for concrete aggregate. It was concluded from the study that compressive strength and the other tests showed that mild steel slag is superior to the natural aggregates (Figure 1). As observed from the Figure, the 28 days result shows compressive strength increase of the concrete from 0 to 60% replacement of coarse aggregate with steel slag, but later reduced with 80% steel slag in both mixes but increase at 100% replacement of coarse aggregate.

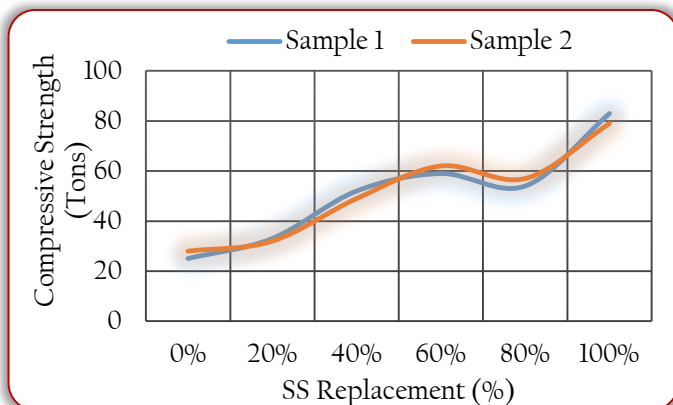


Figure 1: Effect of Steel Slag on the Compressive Strength at 28 day curing (Gokul *et al.*, 2012)

Kumar and Kumar (2016) replaced coarse aggregate with 25, 30 and 35% steel slag and 1% of polypropylene fibre. Results

as presented in Figure 2 showed an increase in compressive strength with increasing steel slag, with the partial replacement of coarse aggregate with iron slag containing 35% steel slag and 1% of polypropylene fibre exhibited the highest strength. The results of all the replacements were higher than that conventional concrete. This is an indication that steel slag is good substitute for coarse aggregate in concrete.

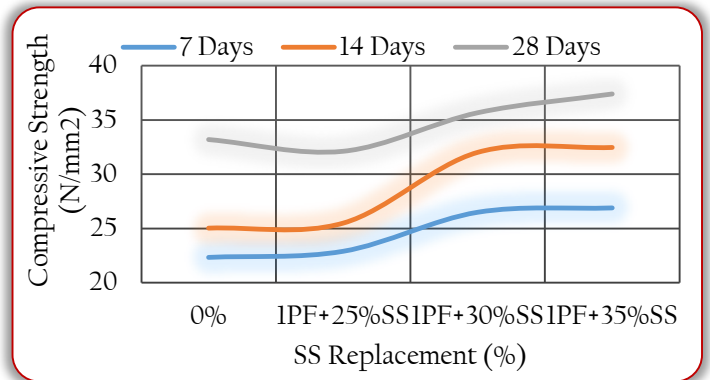


Figure 2: Compressive Strength of Concrete Grade 30 (Kumar and Kumar, 2016)

Raza *et al.* (2014) investigated the strength analysis of concrete by using iron slag as a partial replacement for coarse aggregate in concrete. In this study, coarse aggregate (CA) were partially replaced with iron slag aggregate (ISA) at different proportions of 0, 10, 20, 30, 40 and 50%. The result (Figure 3) shows that 30% replacement of coarse aggregate with iron slag aggregate gives optimum compressive strength.

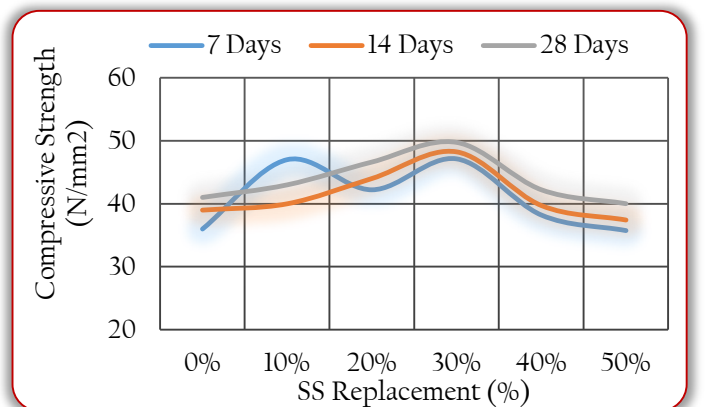


Figure 3: Steel Slag Compressive Strength (Raza *et al.*, 2014)

The research conducted by Thangaselvi (2015) as seen in Figure 4 shows that the compressive strength of concrete increases up to 60% (with an increment of 9.70%) replacement of coarse aggregate with steel slag but the strength decrease at 80% replacement. This is quite in agreement with the previous study conducted by Gokul *et al.* (2012).

Subramani and Ravi (2015) studied the replacement of coarse aggregate with steel slag in concrete and concluded that coarse aggregate replacement level with 60% steel slag in concrete was found to be the optimum level to obtain higher value of strength and durability at 28days of curing (Figure 5).

This shows that the maximum slag replacement to enjoy optimum compressive strength of the concrete is 60%, this is also similar to the findings of the previous studies (Gokul *et al.*, 2012 and Thangaselvi, 2015).

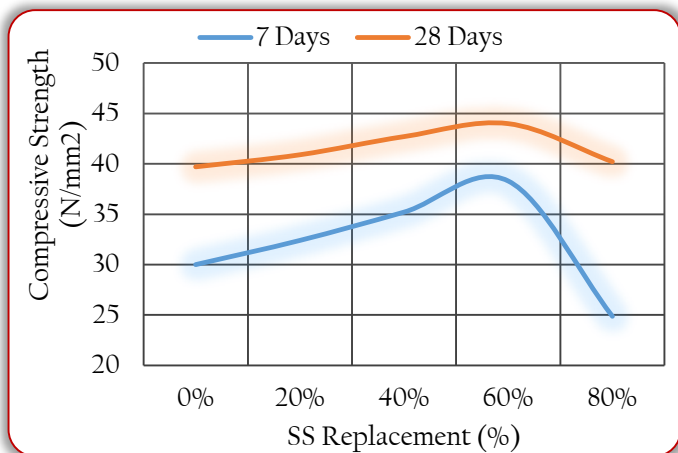


Figure 4: Compressive Strength of Steel Slag Concrete (Thangaselvi, 2015)

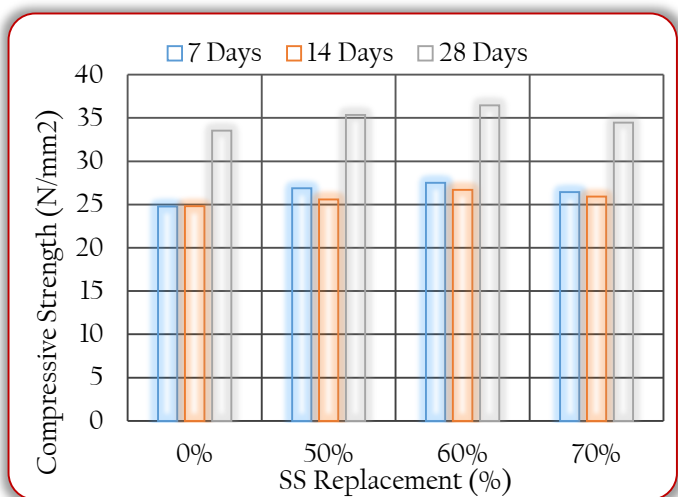


Figure 5: Compressive Strength Vs Steel Slag Concrete (Subramani and Ravi, 2015)

Awoyera *et al.* (2015) examined influence of electric arc furnace (EAF) slag aggregate sizes (as alternative) on the workability and durability of concrete. The study utilised steel slag aggregate (SSA) and natural aggregate (NA) of size 9.54, 12.7 and 19.05 mm. For all the aggregate sizes considered in the research, SSA produced an appreciable compressive strength at 28 days than the NA concrete. However, the NA concrete possesses good workability than the SSA concrete. Warudkar and Nigade (2015) assessed the performance of partial replacement of coarse aggregate with steel slag in concrete. The study concluded that compressive strength of concrete of all mix increases up to 75% steel slag but decrease with further addition of the replacement. However, the compressive strength (Figure 6) witness 14% increment with 75% of steel slag as partial replacement of coarse aggregate. The improvement in strength might be due to shape, size and surface texture of steel slag aggregates, which provide better bonding between the particles and cement paste.

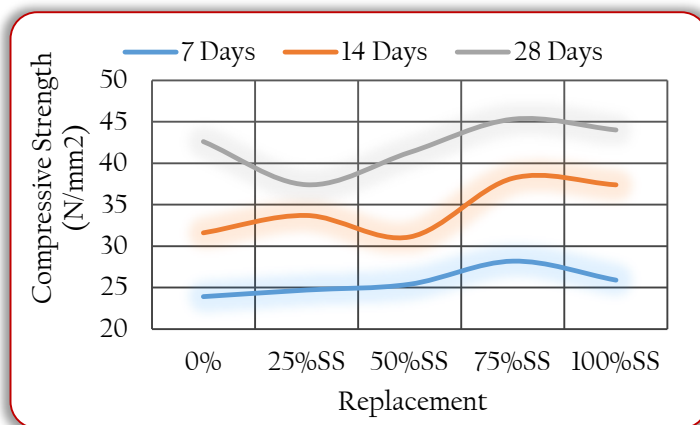


Figure 6: Compressive Strength of Concrete (Warudkar and Nigade, 2015)

Tran *et al.* (2014) investigated the properties of high strength concrete using steel slag coarse aggregate. The steel slag was used to replace 100% coarse aggregates in high strength concrete with varying compressive strengths (60, 70 and 80MPa). The results showed that the strength of the concrete using steel slag aggregate as alternative to coarse aggregate was equivalent to that of conventional concrete. Mohammed *et al.* (2016) also utilized steel slag in concrete as coarse aggregate. The steel slag aggregate was separated into lightweight (SL), heavyweight (SH), and mixed (SM) slag aggregates after collection of the slag from a local steel manufacturing company. It was noted that the compressive strength of concrete made with mixed slag aggregate is similar/better than that of concrete made with brick aggregate while concrete made with heavyweight slag aggregate gives more compressive strength than other aggregates.

Sharma *et al.* (2015) examined the effects of steel slag on concrete. From the results, it was observed that as the percentage of steel slag increases (from 0% to 50%), the strength of concrete increases but decreases at 75% and 100% replacement. The optimum compressive strength was gained at 50% replacement. Ravikumar *et al.* (2015) equally investigated the replacement of steel slag as coarse aggregate in concrete. In this study, concrete of grade M20, M30, M40 and M50 were considered for a W/C ratio of 0.55, 0.45, 0.37, 0.32 and coarse aggregate replacement with steel slag was 30, 60 and 100%. The result of this study revealed an increment in compressive strength by 4 to 6% for all the grades of concrete, and concluded that steel slag could be use up to 60% replacement in concrete with grade M20, M30, M40 and M50.

Recently, Anifowose *et al.* (2017) examined the density, workability and compressive strength assessment of steel slag in concrete. The compressive strength result shows that the strength of concrete increases with respect to curing age as the percentage of SS increases (i.e the higher the percentage of SS, the higher the compressive strengths of the concrete cubes with respect to curing age). They however concluded that steel slag (SS) can successfully be use as a

partial replacement of coarse aggregate (crushed stone) in concrete for concrete grade M20 since the strength of concrete with 10, 20, 30, 40 and 50% is higher than the control mix (Figure 7).

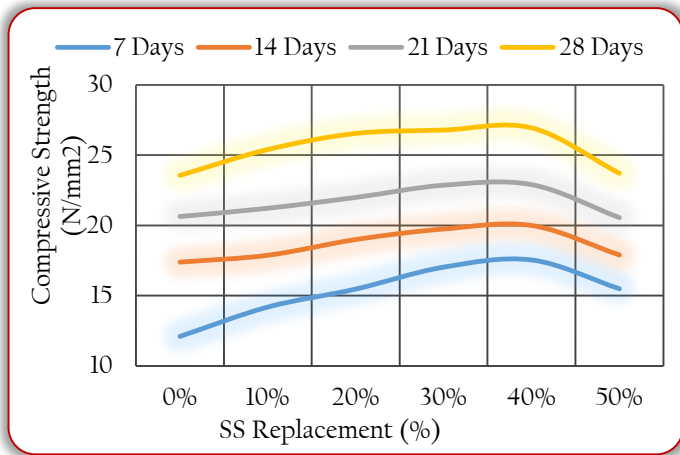


Figure 7: Graphical representation of Compressive Strength against SS Replacement (Anifowose *et al.*, 2017)

### — Split tensile strength

Khafaga *et al.* (2014) reported that the optimum split tensile strength was obtained for the mixtures with a percentage of 66.67% steel slag aggregates as a replacement of the coarse aggregate. Qurishee *et al.* (2016) also concluded that concrete with 40% replacement of coarse aggregate with steel slag may offer more tensile strength. However, the results of the study conducted by Kothai and Malathy (2013) showed that split tensile strength for steel slag aggregate concrete was similar to that conventional concrete.

Similar to the findings from Qurishee *et al.* (2016), Study by Kumar and Kumar (2016) also showed that between 30 and 35% of slag by weight of coarse aggregate gave 6% increment in split tensile strength compared to that of the conventional concrete (Figure 8). It is clearly seen from these results that steel slag can be used as an alternative material to coarse aggregates in concrete production.

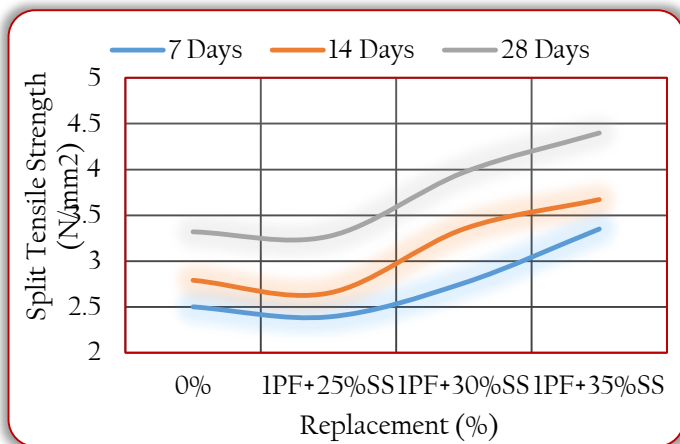


Figure 8: Split Tensile Strength for Concrete Grade 30 (Kumar and Kumar 2016)

Thangaselvi (2015) examined the strength and durability of concrete using steel slag as a partial replacement of coarse aggregate in concrete. The results showed that the optimum

split tensile strength of steel slag concrete was found at 60% replacement of coarse aggregate with steel slag (Figure 9).

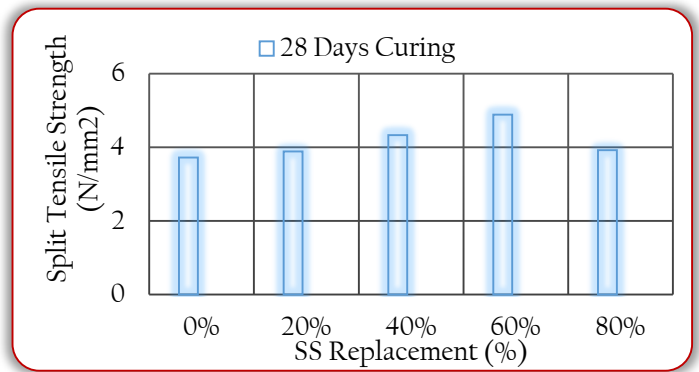


Figure 9: Split Tensile Strength of Steel Slag Concrete (Thangaselvi, 2015)

Subramani and Ravi (2015) conducted study on the partial replacement of coarse aggregate with varying proportions of steel slag (0, 50, 60 and 70%). The results presented in Figure 10 indicated an increase in compressive strength with increasing amount of the steel slag from 0 to 60%, but the strength decreased with further increment of steel slag. It was concluded that the optimum replacement level of coarse aggregate with steel slag that produced the highest tensile strength is 60%. This is an indication that steel slag can be sustainably used to improve the strength of concrete while minimizing the environmental pollution caused by the heaps of steel slag generated by steel manufacturing companies.

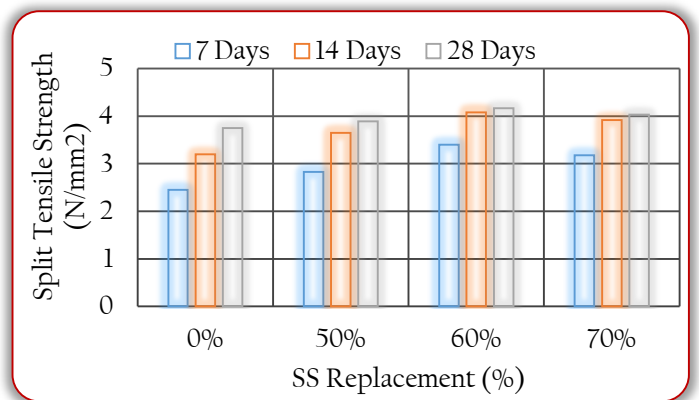


Figure 10: Split Tensile Strength against Steel Slag Concrete (Subramani and Ravi 2015)



Figure 11: Split Tensile Strength of Concrete at 28 Days Curing (Warudkar and Nigade, 2015)

Warudkar and Nigade (2015) also examined the split tensile strength of steel slag-granite concrete at 28th day. The result showed that there is increment in strength from 0 to 75% (Figure 11) replacement of steel slag but decreased at 100%. Sharma *et al.* (2015) concluded that the maximum split tensile strength was obtained at 50% replacement of coarse aggregate with steel slag. After 50% replacement of coarse aggregate with steel slag, slight decrease in concrete strength was observed. Ravikumar *et al.*, (2015) reported that split tensile strength increases as the percentage of coarse aggregate replacement with steel slag increased in M20 and M40 grade and decrease at 100% replacement, whereas in M30 and M50 grade the strength decreases at 30% and increases at 60% then decreases at 100%. This trend is also similar to the findings of the previous study (Subramani and Ravi, 2015)

— Flexural strength

Khafaga *et al.* (2014) carried out study to investigate the effect of partial replacement of coarse aggregate with steel slag and showed that the optimum concrete flexural strength was obtained at 66.67% replacement of the coarse aggregate with steel slag. Kumar and Kumar (2016) also reported that 30 and 35% of slag by weight of coarse aggregate in concrete witnessed 6% increment in flexural strength compared to conventional concrete (Figure 12).

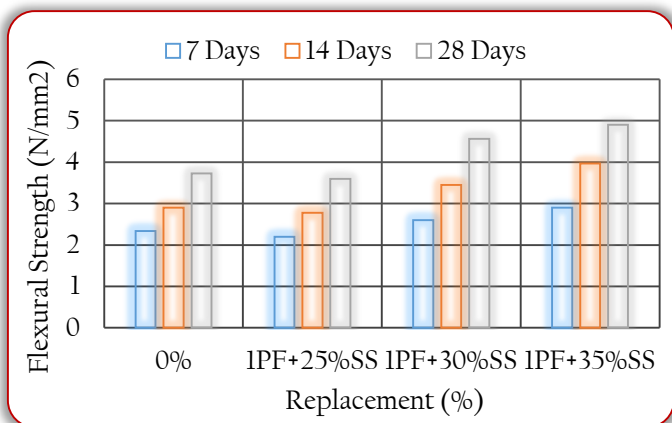


Figure 12: Flexural Strength of Concrete (Kumar and Kumar, 2016)

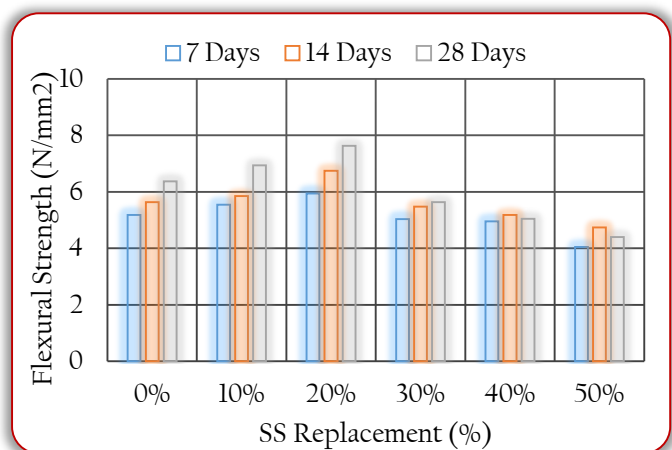


Figure 13: Flexural Strength of Steel Slag Concrete (Raza *et al.*, 2014)

Raza *et al.* (2014) conducted a study to examine the influence of steel slag on the properties of steel slag-concrete and concluded that the flexural strength of concrete with 20% steel slag is more than that of the conventional concrete (Figure 13).

Figure 14 shows the effect of steel slag addition on the flexural strength of concrete. From this study, Thangaselvi (2015) concluded that the maximum flexural strength was obtained at 60% replacement of natural aggregate by steel slag with an increment of 18.20% compared with conventional concrete. This finding is also similar to that of the previous study conducted by Khafaga *et al.* (2014).

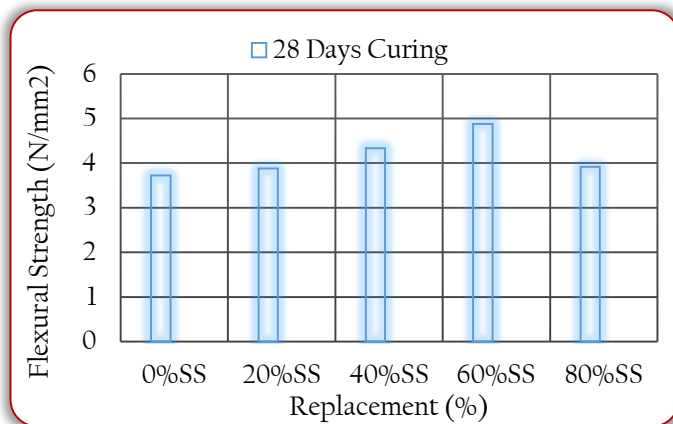


Figure 14: Effect on Flexural Strength of Steel Slag (Thangaselvi 2015)

Subramani and Ravi (2015) investigated the replacement of coarse aggregate with steel slag in concrete (Figure 15). Their results showed that concrete with 60% steel slag has the highest flexural strength at 28days of curing, which is in line with the earlier studies reported by Khafaga *et al.* (2014) and Thangaselvi (2015).

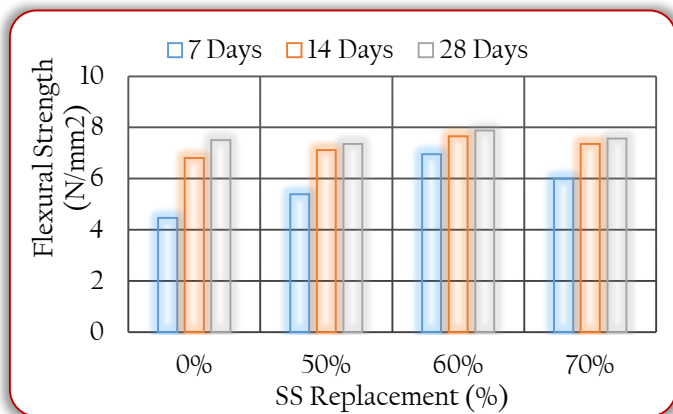


Figure 15: Flexural Strength Vs Steel Slag Concrete (Subramani and Ravi 2015)

Results of the research shown in Figure 16, which was conducted by Warudkar and Nigade (2015) showed that the flexural strength of concrete using steel slag at 28th day increased with steel slag up to 75% replacement level but decreased with further increment of steel slag.

Sharma *et al.* (2015) also studied the beneficial effects of steel slag on concrete and observed that the optimum replacement of coarse aggregate with steel slag that

produced the highest flexural strength was found at 50% replacement. Ravikumar *et al.* (2015) concluded that 60% replacement of coarse aggregate with steel slag could be used in concrete grade M20, M30, M40 and M50 while full replacement by steel slag decreased the strength considerably.

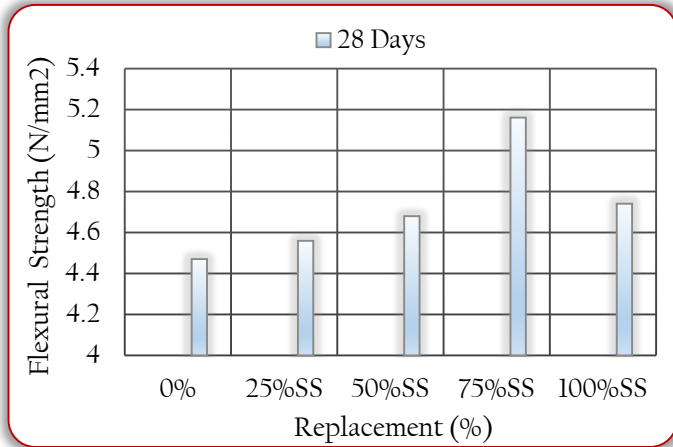


Figure 16: Flexural Strength of Concrete Using Steel Slag (Warudkar and Nigade, 2015)

## CONCLUSIONS

Based on the extensive reviews of the previous studies carried out to investigate the effects of partial replacement of coarse aggregate with steel slag, the following conclusions have been drawn:

- From chemical properties, it was observed that SiO<sub>2</sub>, Fe<sub>2</sub>O<sub>3</sub>, CaO and MgO are the major constituents of steel slag.
- Steel slag possesses higher value of specific gravity and Aggregate Impact Value (AIV) than coarse aggregate but have similar values of the Aggregate Crushing Value (ACV) and Los Angeles Abrasion Value (LAAB) with coarse aggregate. This therefore makes steel slag a suitable substitute for coarse aggregate in concrete production.
- The optimum replacement of coarse aggregate with steel slag that gives higher compressive strength than conventional concrete is found to be between the range of 30 and 60%.
- 40 to 60% steel slag (by weight of coarse aggregate) in concrete will produce an improved split tensile strength compared to conventional concrete.
- The optimum replacement of coarse aggregate with steel slag in concrete that gives enhanced flexural strength is between 20 to 60%.
- Tiwari *et al.*, (2016) reported that it is economical to use steel slag to improve the strength characteristics of concrete, as the costs of steel slag are just about 50% of that of conventional aggregates.
- Only few researchers have used different water to cement ratio and different concrete grades in steel slag-concrete production.
- In South Western part of Nigeria, there are numbers of steel/iron producing company with large deposit of steel slag. Therefore, there is need for the utilization of this by-

product (steel slag) in concrete production in Nigeria as the cost of natural aggregates (fine and coarse aggregate) is becoming higher.

## References

- [1] Abdul Kadar, J. and Dhanalakshmi, G.: Experimental Investigation on Concrete by Partial Replacement on Cement by Bentonite and Coarse Aggregate by Steel Slag, International Journal of Innovative Research in Science, Engineering and Technology, 5(6): 10302-10309, (2016).
- [2] Abrol, S.; Sharma, P.; Verma, N. and Singh, I.: Effect of Steel Slag in Concrete, International Journal of Civil Engineering (IJCE), 3(2), 1-4, (2016).
- [3] Anifowose, M.A.; Adebara, S.A.; Odeyemi, S.O.; Olan, A.B. and Aliyu, T.: Density, Workability and Compressive Strength Assessment of Steel Slag In Concrete: ACTA TECHNICA CORVINIENSIS – Bulletin of Engineering, Tome X [2017], Fascicule 4 [October -December], 63-67, (2017).
- [4] Awoyera, P. O.; Adekeye, A.W. and Babalola, O.E.: Influence of Electric Arc Furnace (EAF) Slag Aggregate Sizes on the Workability and Durability of Concrete, International Journal of Engineering and Technology (IJET), 7(3), 1049-1056, (2015).
- [5] Gokul, J.; Suganthan, S.; Venkatram, R. and Karthikeyan K.: Mild Steel Slag as a Potential Replacement for Concrete Aggregate, International Journal of Current Research, 4(11), 106-109, (2012).
- [6] Khafaga, M.A.; Fahmy, W.S.; Sherif, M.A. and AbdelHamid A.N.: Properties of High Strength Concrete Containing Electric Arc Furnace Steel Slag Aggregate, Journal of Engineering Sciences, Assiut University, Faculty of Engineering, 42(3), 582-608, (2014).
- [7] Kothai, P.S. and Malathy, R.: Enhancement of Concrete properties by Steel Slag as a Partial Replacement Material for Coarse Aggregates, Australian Journal of Basic and Applied Sciences, 7(12), 278-285, (2013).
- [8] Kothai, P.S. and Malathy, R.: Utilization of Steel Slag in Concrete as a Partial Replacement Material for Fine Aggregates, International Journal of Innovative Research in Science, Engineering and Technology, 3(4), 11585-11592, (2014).
- [9] Kumar, P.V. and Kumar, R.: An Experimental Study on Partial Replacement of Coarse Aggregate by Iron Slag with Polypropylene Fiber, International Journal of Science and Research (IJSR), 5(3), 212-216, (2016).
- [10] Mohammed, T.U.; Rahman, N.; Mahmood, A.H.; Hasan, T. and Apurbo, S.M. : Utilization of Steel Slag in Concrete as Coarse Aggregate, Fourth International Conference on Sustainable Construction Materials and Technologies, Las Vegas, USA, August 7-11, (2016).
- [11] Olonade, K.A., Kadiri, M.B. and Aderemi P.O.: Performance of Steel Slag as Fine Aggregate in Structural Concrete, Nigerian Journal of Technology (NIJOTECH), 34(3), 452-458, (2015).
- [12] Padmapriya, R.; Bupesh Raja, V.K.; Kumar, V.G. and Baalamurugan J.: Study on Replacement of Coarse Aggregate by Steel Slag and Fine Aggregate by Manufacturing Sand in Concrete, International Journal of ChemTech Research, 8(4), 1721-1729, (2015).

- [13] Palod, R.; Deo, S.V. and Ramtekkar, G.D.: Review and Suggestions on Use of Steel Slag in Concrete and Its Potential Use as Cementitious Component Combined With GGBS, *International Journal of Civil Engineering and Technology (IJCIET)*, 8(4), 1026-1035, (2017).
- [14] Priya, S.; Dhanasekar, R.; Vijayalakshmi, P.; Siva, A. and Vignesh, P.: Experimental Investigation on Partially Replacement of Cement, Coarse Aggregate by Corn Cob Ash and Steel Slag, *International Journal for Innovative Research in Science & Technology*, 3(10): 209-214, (2017).
- [15] Qurishee, M.A.; Iqbal, I.T.; Islam, M.S. and Islam, M.M.: Use of Slag as Coarse Aggregate and Its Effect on Mechanical Properties of Concrete. *Proceedings of 3rd International Conference on Advances in Civil Engineering, CUET, Chittagong, Bangladesh*, 475-479, (2016).
- [16] Ravikumar, H.; Dattatreya, J.K. and Shivananda, K.P.: Experimental Investigation on Replacement of Steel Slag as Coarse Aggregate in Concrete, *Journal of Civil Engineering and Environmental Technology*, 2(11), 58-63, (2015).
- [17] Raza, K.; Singh, A. and Patel, R.D.: Strength Analysis of Concrete by Using Iron Slag as a Partial Replacement of Normal Aggregate (Coarse) in Concrete, *International Journal of Science and Research (IJSR)*, 3(10), 190-193, (2014).
- [18] Sharma, G.; Goyal, R.; Gupta, A. and Sharma, D.: Beneficial Effects of Steel Slag on Concrete, *International journal of Recent Research Aspects*, 2(2), 51-57, (2015).
- [19] Sekaran, A.; Palaniswamy, M. and Balaraju, S.: A Study on Suitability of EAF Oxidizing Slag in Concrete: An Eco-Friendly and Sustainable Replacement for Natural Coarse Aggregate, *The Scientific World Journal*, Hindawi Publishing Corporation, 2015 (972567), 1-8. (2015).
- [20] Sezer, G.I. and Gulderen M.: Usage of Steel Slag in Concrete as Fine And/Or Coarse Aggregate, *Indian Journal of Engineering & Materials Sciences*, 22, 339-344, (2015).
- [21] Subramani, T. and Ravi G.: Experimental Investigation of Coarse Aggregate with Steel Slag in Concrete, *IOSR Journal of Engineering (IOSRJEN)*, 5(5), 64-73, (2015).
- [22] Tarawneh, S.A.; Gharaibeh, E.S. and Saraireh, F.M.: Effect of Using Steel Slag Aggregate on Mechanical Properties of Concrete, *American Journal of Applied Sciences*, 11(5), 700-706, (2014).
- [23] Thangaselvi, K.: Strength and Durability of Concrete Using Steel Slag as a Partial Replacement of Coarse Aggregate in Concrete, *International Journal of Advanced Research Trends in Engineering and Technology (IJARTET)*, 2(7), 1-6, (2015).
- [24] Tiwari, M.K.; Bajpai, S. and Dewangan, U.K.: Steel Slag Utilization: Overview in Indian Perspective, *International Journal of Advanced Research (IJAR)*, 4(8), 2232-2246, (2016).
- [25] Tran, M.V.; Nguyen, C.V.; Nawa, T. and Stitmannaitum, B.: Properties of High Strength Concrete Using Steel Slag Coarse Aggregate, *ASEAN Engineering Journal Part C*, 4(2), 22-32, (2014).
- [26] Warudkar, A.A. and Nigade, Y.M.: Technical Assessment on Performance of Partial Replacement of Coarse Aggregate by Steel Slag in Concrete, *International Journal of Engineering Trends and Technology (IJETT)*, 30(1), 37-41, (2015).
- [27] Yi, H.; Xu, G.; Cheng, H.; Wang, J.; Wan, Y. and Chen, H.: An Overview of Utilization of Steel Slag, *The 7th International Conference on Waste Management and Technology, Procedia Environmental Sciences* 16 (2012), 791-801, (2012).
- [28] Yi, T.C.: Performance Evaluation of Steel Slag as Natural Aggregates Replacement in Asphaltic Concrete. *MSC Thesis, Universiti Sains Malaysia*, 24, (2008). Accessed August 23, 2017, from [http://eprints.usm.my/10416/1/performance\\_evaluation\\_of\\_steel\\_slag\\_as\\_natural\\_aggregates\\_replacement\\_in\\_asphaltic\\_concrete.pdf](http://eprints.usm.my/10416/1/performance_evaluation_of_steel_slag_as_natural_aggregates_replacement_in_asphaltic_concrete.pdf)
- [29] Yildirim, I.Z. and Prezzi, M.: Chemical, Mineralogical, and Morphological Properties of Steel Slag, *Advances in Civil Engineering*, Hindawi Publishing Corporation, 2011(463638),1-13, (2011). doi:10.1155/2011/463638.



ISSN: 2067-3809

copyright © University POLITEHNICA Timisoara,  
Faculty of Engineering Hunedoara,  
5, Revolutiei, 331128, Hunedoara, ROMANIA  
<http://acta.fih.upt.ro>

<sup>1</sup>Ciprian BULEI, <sup>2</sup>Mihai–Paul TODOR, <sup>3</sup>Imre KISS

# RESEARCHES ON IDENTIFYING SOLUTIONS, DESIGNING AND IMPLEMENTING INNOVATIVE TECHNOLOGIES FOR RECYCLING AND REUSE OF NON–FERROUS METAL BASED RAW MATERIALS

<sup>1-2</sup>University Politehnica Timisoara, Faculty of Engineering Hunedoara, Doctoral School, Timisoara / Hunedoara, ROMANIA

<sup>3</sup>University Politehnica Timisoara, Faculty of Engineering Hunedoara, Dept. Engineering & Management, Hunedoara, ROMANIA

**Abstract:** Secondary materials are essential to the industry's survival because even new metals often require the combined use of recycled materials. The recovered materials are melted down in a furnace, poured into casters and shaped into ingots. These ingots are either used in the foundry industry or they can be transformed into flat sheets and other wrought products, which are then used to manufacture new products. Aluminium offers intelligent and practical solutions to recovering for recycling. The main activities described in this article are carried out during the experimental phase of the research and they are oriented towards the recovering aluminium for recycling. The objective of the research is to develop some recycling facilities for re–smelt and re–cast of aluminium by using charcoal briquettes into a mini metal foundry, designed and manufactured in laboratory. In this research we experimented a reusable backyard foundry that melts aluminium cans (soda and beer) easily and safely.

**Keywords:** secondary materials, recycling & reuse, non–ferrous metal based raw materials, aluminium cans (soda and beer)

## INTRODUCTION

Recycling is a modern concept in the waste management, emerged as one of the possibilities to limit waste and to use resources more efficiently.[1–3] It has become increasingly clear that the industrialization and the sustained growth of the population have led to the consumption of increasingly large amounts of resources. An economic development without metal resources is inconceivable in the 21st Century and it is not possible to be in the global competition, with about 75–85% of the world economy depending on these resources. Recovery and reusing of recyclable resources are means of solving the contradiction between the requirements of the economic growing process and the restrictive nature of natural resources.[1–5] In this broad context, non–ferrous metals and their alloys are in the centre of modern life and in many developments of high technology, especially in high–top industries.

At least 42 non–ferrous and rare metals are produced in the European Union being used in a variety of industrial applications. Non–ferrous metals are produced from a wide range of raw, primary and secondary materials. Primary raw materials are derived from ores (from deposits) and then treated before they are introduced into metallurgical processes for the production of raw metal. The secondary materials are indigenous waste and residues or residues, which may also undergo the same treatment. The production of secondary non–ferrous metals includes the production of metal from secondary raw materials (including wastes) and the rewinding and alloying processes. There are many similarities in the production of primary and secondary non–ferrous metals in some cases being impossible to distinguish between the techniques used. There have been identified 10

groups of metals with similar production methods, one being aluminium and its alloys.

In Europe, ores deposits containing metals in high concentrations have been progressively emptied only some specific sources being remained. Recycling is an important component when replacing raw materials for a number of metals, which are recyclable and which can always be recycled without losing any of their properties. In general, recycling prevents the loss of potentially useful materials and reduces the consumption of raw materials. Thus, recycling can make a significant contribution to sustain development; at the same time the introduction of secondary raw materials in a large proportion in the production process leads to a reduction in raw material consumption. Non–ferrous metals (including aluminium) can be recovered from their waste and can be reintroduced into the production cycle by recycling without losing their qualities.

Researches on identifying solutions, designing and implementing innovative technologies for recycling and reuse of non–ferrous metal based raw materials are numerous.[1–3] The specific strategic objective of capitalizing recyclable metal resources – including the non–ferrous metal raw materials area – is the implementation of new concepts and new technologies for sustainable processes in the non–ferrous metals industry and environmental protection (standards and best practices in the non–ferrous metals industry) through new technologies and innovative solutions on: [1,2]

- the efficient use of natural resources;
- improving metal recovery by recycling and reuse of raw materials;
- substitution of critical metals;

- replacing raw materials with attractive commercial alternatives with low impact on the environment;
- the development of new materials through material capitalization;
- techniques for the manufacture of metallic materials;
- prevention and minimization of metal waste;
- rehabilitation of polluted areas through metallurgical and / or mining activities;

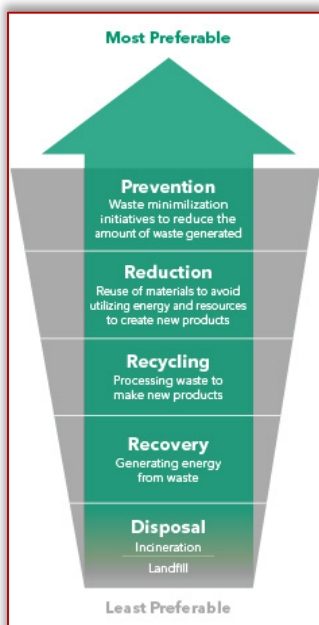


Figure 1. Different materials waste management approaches  
With the worldwide volume of wastes processed increasingly sourced from consumer and light industrial waste streams, the percentage of valuable nonferrous metals has dramatically increased. This trend, coupled with environment protection legislation and ever increasing waste minimization, has driven the need for complicated, integrated nonferrous recovery plants. Millions of tonnes of nonferrous scrap are recovered annually and used by smelters, refiners, ingot makers, foundries, and other manufacturers. Secondary materials are essential to the industry's survival because even new metals often require the combined use of recycled materials.

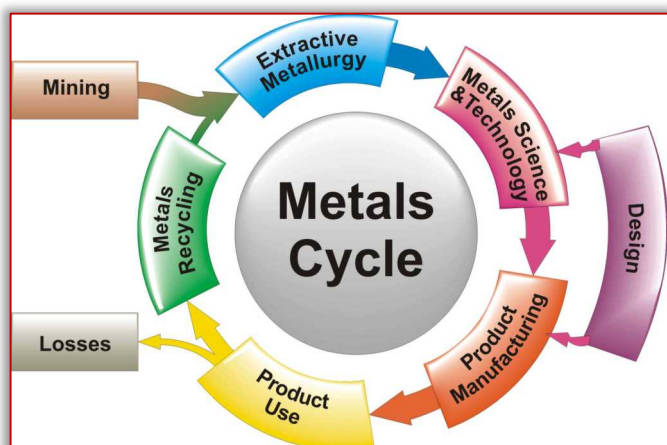


Figure 2. The metal's life cycle

All metals can be recycled with minimal or no loss of their original physical properties. They are such versatile materials that the possible applications for each metal and their combinations are endless. The most commonly used non-ferrous metals are Aluminium, Copper, Lead, Zinc, Nickel, Titanium, Cobalt, Chromium and precious metals. Non-ferrous metals, including aluminium, do not degrade during the recycling process and thus can be recycled an infinite number of times. Aluminium has (great recycling potential) and is often re-used for the same application for which it was originally manufactured. Its strength, flexibility and light weight, make it ideal for large applications.



Figure 3. Non-ferrous metals with great recycling potential  
Thus, the non-ferrous metals recovery and any recycling process has become increasingly important – both domestically and globally. The trends are continually increasing resource recovery rates with a particular focus on the reduction of metal losses to and diversion from landfills relatively low cost and isotropic properties especially in those applications not requiring extreme loading or thermal. The general trend is for improvements to be sought in every area possible – new ways of applying existing technologies are sought to gain improvements along with the development of new technologies for solutions to existing and emerging applications. The beverage cans metal recyclers are also focusing on increasing both their material recovery rates and the quality of the recovered material. In this sense, aluminium is readily recycled without any loss of quality and hence scrap aluminium has significant value. Therefore, the recycling of Aluminium is extremely important due to several economic and environmental reasons. Among all the aluminium scraps, the beverage cans is the most recycled packaging material because of the high value of the scrap and ease of collection. The recycling of aluminium beverage cans eliminate waste. It saves energy reduce emissions, reduce use of city landfills and provides added revenue for recyclers. Moreover, Aluminium is a vital material in the construction, packaging, and transportation industries. Structural components made from Aluminium and its alloys are vital to the all industries.

## KEY TRENDS IN THE METAL INDUSTRY

Materials substitution and efficient use of materials are strongly interrelated factors.[1–5] The threat of materials substitution has encouraged all producers to apply new technologies aimed at reducing the amount of material (and hence lowering the cost) required to meet consumer needs.[1–3,6–9] Materials substitution significantly affects the trend toward more efficient use of monolithic materials.[1–3,7–8] The increasing use of alternative materials in aircraft, automotive and construction applications has motivated the metal industry to provide lighter weight aluminium alloys and metal matrix composites.

The motivation for this substitution has mainly been the opportunity to achieve weight savings.[1–3,6–9] As the properties of these materials improve, their level of performance, and hence substitution, should also increase.[1–3,6–9] More important, as more experience is gained with these materials, their associated costs could decrease, providing the major motivation for their use, especially in above-mentioned advanced industries.[1–3,6–9] To develop these advanced materials, the metal industry has undergone some actions:

- efficient use of materials in technological processes, devoting significant research resources to develop lighter weight alloys and metal matrix composites products and increased process technologies that require less metal to satisfy a particular market need.
- materials substitution, knowing that when a new material can offer a cost or performance advantage over the current material in an established industrial or commercial application, the new material will begin to displace the old in that application.

Development of lightweight aluminium-based composites can be considered as one of the promising solutions to address this issue. At present, the development of metal matrix composites with light metal matrices are gaining increasing attention due to their enhanced properties coupled with weight savings. These unique properties make them attractive for automotive and aircraft industries in which the weight reduction is the critical factor. So far, extensive studies have been done for the production of aluminium matrix composites and now these are being manufactured commercially for numerous industrial applications. In light metal matrix composites, aluminium is mostly used as a base metal matrix phase.

Aluminium alloy matrix (aluminium matrix composites) constitute an important category of design and weight-efficient materials and their processing has the vast development in the various research on advanced materials to overtake the need of low cost, light-weight and high-technological properties. Their relatively low cost and properties especially in those applications not requiring extreme loading or thermal conditions. Also, the processing problems and commercial difficulties associated with continuously reinforced aluminium matrix composites are

contributory to the recent interest in their particulate composites (commonly ceramic particles such as SiC).

## RECYCLING METAL RECIPIENTS

Owing to increased urbanization and modern lifestyle, demand for use of metal packaging has tremendously increased. Metal packaging is safest form of packaging so it is the basic preference of consumers. Metal is the most recycled material than any other waste packaging materials. About 80% or more metal packaging are recycled and used again without any loss in quantity and causing any loss in nutrients of Food and beverages.



Figure 4. Recycling metal recipients

Aluminium is the most precious metal that is used in packaging, because this package has many advantages for both beverage and a consumer manufacturer, which neither PET nor glass has. [1–3] For example, the aluminium can for beverages is a lightweight, unbreakable package, cools quickly in the refrigerator, protects the content of factors such as light and air, has long life, maintains the effervescence and freshness of beverages, requires no labelling, and not last it is easy to recycle. [4,5,8,9] Aluminium cans are recycled in a closed circuit after the recycling process, and aluminium can be re-injected again or can be used for other products. Recyclable aluminium can come from a wide range of sources, including industries and private households. They also include metal containers used as packaging by large beverage manufacturers (juice and beer). [1–5,8,9]



Figure 5. Metal containers used as packaging by large beverage manufacturers (juice and beer)

Aluminium beverage cans are, like PETs, omnipresent, but similarities stop here. Unlike plastic, aluminium can be recycled to infinity without degrading at all. The recycling process is relative simple: the beverage cans are sorted, then washed to remove the contaminants and then melted. The molten metal is converted into ingots which are then transferred to another processing unit and pulled into thin sheets, which can then take the form of beverage cans. On the whole, the process is very fast, a beer can deposited at a waste collector is recycled and reaches the market again. [4,5,8,9]

There are many initiatives involved in improving the return of aluminium waste and the industry is an active player in this area. Recycling empty beverage cans is only an example. Aluminium dosages are an important and extremely valuable resource, representing an important source of secondary aluminium. Once the beer or juice is consumed, if the empty can is properly collected and subsequently recycled, it can be revalued indefinitely without losing anything. Thus, aluminium cans can become raw material.

Aluminium packaging has an intrinsic quality and cannot be said about it as a waste, but as a resource, being 100% recyclable.[1–9] Thus, out of all recyclable packaging, aluminium cans have become the most innovative and durable packaging. Aluminium can be recycled indefinitely without losing its properties unlike other recyclable materials such as plastic, paper or glass, which can be recycled for a limited number of times. The aluminium industry has all the interest to promote recycling as part of the industrial strategy. In Europe, about 50% of the total aluminium used to produce new beverage cans and other aluminium packaging products comes from recycled aluminium. [1–3]

However, a large proportion of packaging waste is generated in households, which requires a separate waste collection infrastructure from metallic cans which are mixed with other household waste or separately through locally developed networks. [1–3,7–9] The volume / weight ratio for aluminium metal dosages is quite high: one aluminium box has 13–15 grams, the boxes are made of 0.17 mm aluminium sheet. Thus, a pound of aluminium cans consists of approx. 60–70 pieces, which can be collected, flattened or even perforated. That is why the sustainable solution for fulfilling the recycling obligations and, implicitly, increasing the recycled quantities is the further extension of the population's access to the selective waste collection services. Creating and promoting the market for recycling and developing recycled materials from these packaging are fundamental. Thus, aluminium cans are an important resource that is also extremely valuable.

The aluminium can is the most recycled beverage packaging. [1–5,8,9] Obviously, this is only possible if they are collected and (re)introduced into the recycling circuit. If a can is left in nature, obviously it cannot fulfil its recycling potential. All the cans are 100% recyclable once they have been collected and reached a recycling point, even the smallest piece of aluminium is not lost. There are several forms to recycle beer

or soft drinks cans. [1–3,6] As a rule, they can be melted and reused by an infinite number of times without losing quality.



Figure 6. Recycling aluminium cans by melting

In the European Union the recovery rate of these wastes varies between 40–70%, the latest statistical data indicating that the rate of recycling of aluminium cans reaches approx. 65%. [1,2] Worldwide, two out of three cans are recycled, but only one in three is recycled in Romania, or about 30–35%. [1,2] In 2007, the Recycling Standard for Romania required recycling at least half of aluminium waste by 2020. The recycling rate was then 3%, then rose to 5% and only in 2010 the growth was more significant, reaching 10%. [1–3]

Nowadays a recycling rate of approx. 35% of the quantity placed on the market due to the sustained increase of the industry's contribution to a coherent and efficient system of selective collection of packaging waste, capable of meeting these obligations through the development of waste management services for recycling purposes. This is due to the efficiency of the partnership with over 200 management companies that carry out waste collection, sorting and transport services for recycling purposes. [1–3]

In Romania there are only small collection centers for aluminium cans, but there are also small units processing them. [1–3] Our country is lacking in recycling facilities, so the 33 or 50 centiliters cans are taking the road to Europe, to European recyclers that actually do the recycling of can bales, the aluminium being melted in factories with special technologies. This raw material is brought back in the form of an aluminium sheet and is transformed into another can. [1–4,8,9]

### RECYCLING THE ALUMINIUM CANS

Aluminium is the most expensive recycled product and recycling of aluminium is economic: it uses less energy and recycling is self-sustained due to the high value of the aluminium used. In other words, it is worth recycling it from all points of view: it is easy to carry, recyclable, infinitely reusable, it does not rust. For this reason, aluminium is rarely lost.

Recycling is the reprocessing of materials in new products [1]. Thus, in order to carry out the recycling process of collected non-ferrous metal waste, aluminium waste melting facilities are required. This enables cost efficiency and faster recycling of waste from aluminium [1]. Many of the drink products we buy are packaged in cans made from aluminium and this material can be recycled after we have finished with them to make either new cans or other products.



Figure 7. Recycling metal recipients

In this direction we propose a micro station for melting of aluminium wastes from the beverage cans (Figure 8). Research refers to a process for obtaining secondary aluminium from waste, by directly melting it into an experimental aggregate. All the soda cans came from a local recycling depot.

A lot of charcoal briquettes are placed around the crucible until they are filled. The charcoal is ignited and when the crucible is hot, the aluminium cans are introduced. Melting takes place at a temperature of 680–750°C. Thus, small ingots or secondary aluminium chips are obtained.

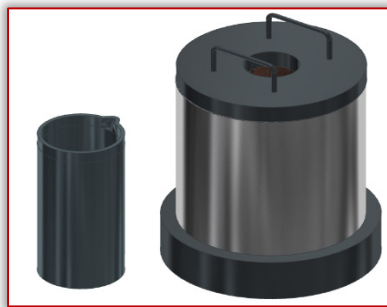


Figure 8. Designing technologies for recycling wastes from the beverage cans

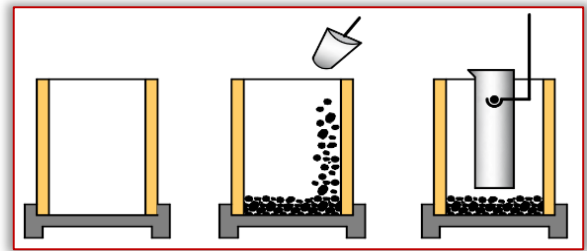


(a)

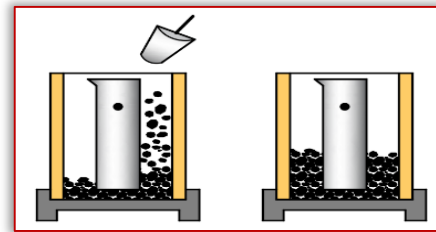


(b)

Figure 9. Micro station for melting of aluminium wastes from the beverage cans: (a) the melting aggregate; (b) the crucible

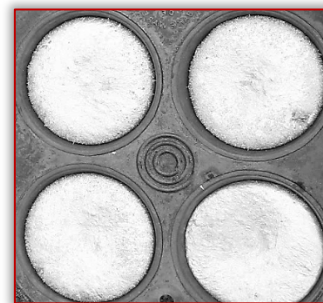


(a)



(b)

Figure 10. Micro station for melting of aluminium wastes from the beverage cans: (a) preparing the micro-station; (b) preparing for melting;



(a)



(b)

Figure 11. Casting of recovered aluminium wastes from the beverage cans: (a) ingots casting; (b) aluminium ingots

## CONCLUSIONS

Many products are designed so that they can be recycled, at the end of their useful lifetime. This was not always the case. In the past, products were manufactured largely from new raw materials, mined from the earth's crust. When they ceased to work, they were 'dumped' in a landfill sites, often causing pollution and environmental damage. Aluminium drinks cans are usually recycled into ingots at a special "closed-loop" plant. This is the ultimate recycling process for environmental efficiency and used cans are often recycled. Aluminium cans (soda or beer) are easy to recycle and there are huge environmental benefits for doing this – yet many cans still go to landfill. If we recycle more cans we can reduce the amount of raw materials needed to produce new products.

All the Aluminium drinks cans can be melted down and used again and again. For this reason, recycling is part of the normal lifecycle for large industrial products – around 75% of all the aluminium ever made is still in circulation. The metal can be recycled time and time again without loss of properties, so getting the aluminium recycling habit is one of the best things we can do for the environment. Moreover, many of the drink products we buy are packaged in cans made from aluminium and this material can be recycled after we have finished with them to make either new cans or other products.

#### References

- [1] Centrul Național pentru Dezvoltare Durabilă / National Centre for Sustainable Development 2007 Strategia Națională pentru Dezvoltare Durabilă a României: Orizonturi 2013–2020–2030 / National Sustainable Development Strategy for Romania: Horizons 2013–2020–2030 Bucuresti <http://www.mmediu.ro>
- [2] Capră G S and Stan A-C 2013 Strategia Națională de Gestionare a Deșeurilor 2014–2020 / National Waste Strategy 2014–2020, Bucuresti <http://www.mmediu.ro>
- [3] Ganea O, Simionescu A, Boța I and Popa M 2011 Reciclarea deșeurilor, o piață emergentă – Raport privind piața muncii în domeniul gestiunii deșeurilor în România București [www.eco-social.ro](http://www.eco-social.ro)
- [4] Niero M and Olsen S I 2016 Circular economy: To be or not to be in a closed product loop? A Life Cycle Assessment of aluminium cans with inclusion of alloying elements Resources, Conservation & Recycling 114, 18–31
- [5] Wernick I K and Themelis N J 1998 Recycling metals for the environment Annual Review of Energy and the Environment 23(1), 465–497
- [6] Verran G O and Kurzawa U 2008 An experimental study of aluminium can recycling using fusion in induction furnace, Resources, Conservation and Recycling 52(5), 731–736
- [7] Thomas M P and Wirtz A H 1994 The ecological demand and practice for recycling of aluminium, Resources, Conservation and Recycling 10(1–2) pp 193–204
- [8] Das S K and Yin W 2007 The worldwide aluminium economy: The current state of the industry, JOM, 59(11), 57–63
- [9] Millbank P 2004 Aluminium recycling vital to global supply chain, Aluminium International Today 16(5), 44–49
- [10] Bulei C, Todor MP and Kiss I (2018) Metal matrix composites processing techniques using recycled aluminium alloy IOP Conference Series: Materials Science and Engineering 393 1–6
- [11] Bulei C, Todor MP, Heput T and Kiss I (2018) Recovering aluminium for recycling in reusable backyard foundry that melts aluminium cans, The 7th International Conference on Advanced Materials and Structures (AMS 2018), 28–31 March 2018, Timisoara, Romania
- [12] Bulei C, Todor MP, Kiss I and Alexa V (2018) Aluminium matrix composites: Processing of matrix from re-melted aluminium wastes in micro-melting station, International Conference on Applied Sciences (ICAS 2018), 9–10 May 2018, Hunedoara, Romania
- [13] Gabrielle Gaustad, Elsa Olivetti, Randolph Kirchain, Improving aluminum recycling: A survey of sorting and impurity removal technologies, Resources, Conservation and Recycling, 58, 2012, 79–87
- [14] G.O. Verran, U. Kurzawa, An experimental study of aluminum can recycling using fusion in induction furnace, Resources, Conservation and Recycling, 52(5), 2008, 731–736
- [15] Strategia Națională pentru Dezvoltare Durabilă a României: Orizonturi 2013–2020–2030 (National Sustainable Development Strategy for Romania: Horizons 2013–2020–2030), Centrul Național pentru Dezvoltare Durabilă (National Centre for Sustainable Development), Bucuresti, 2007
- [16] Oana Ganea, Adriana Simionescu, Irina Boța, Maria Popa, Reciclarea deșeurilor, o piață emergentă – Raport privind piața muncii în domeniul gestiunii deșeurilor în România, București 2011, [www.eco-social.ro](http://www.eco-social.ro)



ISSN: 2067–3809

copyright © University POLITEHNICA Timisoara,  
Faculty of Engineering Hunedoara,  
5, Revolutiei, 331128, Hunedoara, ROMANIA  
<http://acta.fih.upt.ro>

<sup>1</sup>Y.L. SHUAIB-BABATA, <sup>1</sup>Y.O. BUSARI, <sup>1</sup>R.A. YAHYA, <sup>2</sup>J. M. ABDUL

## CORROSION INHIBITION OF AISI 1007 STEEL IN HYDROCHLORIC ACID USING *CUCUMIS SATIVUS* (CUCUMBER) EXTRACTS AS GREEN INHIBITOR

<sup>1</sup>Department of Materials & Metallurgical Engineering, University of Ilorin, Ilorin, NIGERIA

<sup>2</sup>Department of Mechanical Engineering, Federal Polytechnic, Offa, NIGERIA

**Abstract:** The inhibiting effect of cucumber peel and seed extracts on corrosion of AISI 1007 steel in 2M solution of Hydrogen Chloride (HCl) at ambient temperature was studied using gravimetric and electrochemical measurements (TAFEL polarization). It was observed that corrosion rates reduced with increase in the extracts' concentration, and inhibition efficiency (IE%) increased with the concentration. The study revealed that the cucumber extracts possessed good inhibiting efficiency. Though, the cucumber peel extract's efficiency was greater than that of the seed (oil) extract during gravimetric measurement. The highest inhibition efficiency (IE) of 86.63% was achieved using the cucumber peel extract as inhibitor with 1.0 g/l concentration, while cucumber seed (oil) extract recorded 39.23%. The electrochemical measurements (TAFEL polarization) results revealed that the corrosion current density decreased with the increased in the concentration of the cucumber peel extract. The decreased in corrosion was due to increased blocking of the metal surface by adsorption of the leaf extract. Therefore, the extracts could be used as a green inhibitor to the corrosion of AISI 1007 steel in the hydrochloric acid medium as a replacement for toxic inhibitors.

**Keywords:** Tafel Polarization, Gravimetric, Current Density, Metal Surface Adsorption, Inhibiting Efficiency

### INTRODUCTION

For safety, environmental and economic purposes, corrosion has been identified as a major problem to be confronted (Umoren, *et al.*, 2016; Prithiba & Rajalakshmi, 2016; Sharma, *et al.*, 2009; Gupta & Jain, 2014; Thompson *et al.*, 2007; Gunavathy, 2013; Satris, 2011). Most organic compounds used as corrosion inhibitors are found to be biodegradable, expensive and toxic (Gunavathy, 2013; El Ibrahim *et al.*, 2017; Adeyemi & Olubomehin, 2017; Sharkma, *et al.*, 2011). These organic compounds are not only expensive but also harmful to the environment. As a result of these, the development of cost effective and non-toxic corrosion inhibitors came into existence. According to Omotosho *et al.*, (2011), "green inhibitors are known to be cheaply available, easily applicable and disposable without contaminating the environment". The concern of the toxicity and biodegradability of corrosion inhibitors discharged into the environment is increasing. Environmental problems should be of primary concern due to the importance of protecting marine life and the preservation of the ecosystem (El Ibrahim *et al.*, 2017; Neha *et al.*, 2013).

Plant products and some other sources of organic compounds are rich sources of environmentally acceptable corrosion inhibitors. Plant products are the main sources of environmentally friendly green inhibitors such as phthalocyanines (Satris, 2011). The yield of these natural products as well as the corrosion inhibition abilities of the plant extracts vary widely depending on the part of the plant and its location (Okafor, *et al.*, 2008). Extract of different parts of plant like root, seeds, leaves, stem, flower and fruits can be used as inhibitor to reduce the corrosion rate of various ferrous and non-ferrous Salhi, *et al.*, 2017; Neha *et al.*, 2013; Gunasekaran & Chauhan, 2004; Uwah *et al.*, 2013; Dharmaraj *et al.*, 2017; Allam *et al.*, 2017).

The basic components of the extracts are sugars, steroids, aloin, gallic acid, ellagic acid, tannic acid, flavanoids, etc. The presence of tannins, cellulose, and polycyclic compounds has been reported to enhance a film formation over the metal surface, thus decreasing corrosion (Mohamed *et al.*, 2015; Chris *et al.*, 2016; Arockia *et al.*, 2018; Abd El-Aziz, *et al.*, 2016). However, the constituent that provides inhibitive action, the mechanism of inhibition and the best condition for inhibition are still unclear.

Cucumber peels are rough and difficult to chew and digest as a result of the ignorance of the benefits the peel has to offer (Anne, 2018). Then this peels are been disposed indiscriminately which leads to environmental pollution. In addition, plant products are organic in nature, and contain certain photochemical including tannins, flavonoids, saponins, organic and amino acids, alkaloids, and pigments which could be extracted by simple less expensive procedures. Extracts from different parts of plant have been widely reported as effective and good metal corrosion inhibitors in various corrosive environments (Ji *et al.*, 2012; Umoren *et al.*, 2013).

Low carbon steels, such as AISI 1007, are most widely used both in construction and structural applications, pressure vessels, marine and offshore equipment, and military applications, because they are cheap, strong, stiff, and possess good mechanical properties (Charmers, 1988; Chakravarthy & Mohana, 2014). The steel grade, elements and parameters are also important in how it is being used (Kennedy, 2017). Steels are also used as structural materials where they are exposed to outdoor conditions especially in acidic media (Fekry & Mohamed, 2010). One of the common problems being experienced by the materials in this environment is corrosion (Abdul Amir, *et al.*, 2010; Chinwko *et al.*, 2014).

Corrosion inhibition of *Cucumis sativus* peel extract (CSP) on carbon steel in 1M HCl solution was investigated by potentiodynamic polarization, and electrochemical impedance spectroscopy (EIS) techniques. The inhibition efficiency from potentiodynamic polarization and impedance measurements was agreement where the maximum inhibition was around 82%. The inhibition efficiency decreased as the temperature increased. The results obtained showed that CSP extract inhibited the corrosion process by a physical adsorption mechanism that followed the Langmuir adsorption isotherm models. The adsorption thermodynamic parameters that were calculated include, free energy of adsorption ( $\Delta G^{\circ}_{ads}$ ), activation energy ( $E_a$ ), enthalpy of adsorption ( $\Delta H^{\circ}_{ads}$ ), and entropy of adsorption ( $\Delta S^{\circ}_{ads}$ ) revealed that the adsorption process are spontaneous and endothermic. All the results show that the CSP extract can act as an inhibitor against the corrosion of carbon steel in the HCl medium (Al-Senani, 2016).

In an attempt to extend the investigation to other Cucumber extracts, which most of them (peel in particular) are regarded as waste product, especially in Nigeria, the present research reports on the suitability assessment of cucumber peel and seed oil as green inhibitor for AISI 1007 steel corrosion in HCl using gravimetric and Electrochemical Measurement (TAFEL Polarization).

## MATERIALS AND METHODS

### — Materials

Sample of the metal sheet used for this study was obtained in a local steel market in Surulere Area of Ilorin, Nigeria. The elemental composition (wt.%) of AISI 1007 steel sample include: C = 0.033; Si = 0.034; Mn = 0.220; Cr = 0.038; Al = 0.011; Cu = 0.021, Ni = 0.007; P = 0.015; S = 0.008; and Fe = 99.50. This was obtained using Spectromaxx LMF06 Spectrometer (Serial Number: 15007384). The results show that the carbon steel falls under AISI 1007 steel from AISI-SAE standard of carbon steel.

### — Steel Samples (Coupon) Preparation

To produce the specimens (coupons) for gravimetric measurements, the steel sheet was cut into 2.2 cm x 1.7 cm x 0.15 cm using guillotine machine. The coupons were drilled at the top center with drill bit (1.0mm diameter) for ease hanging, identification and easy withdrawal of the specimens from medium of exposure. The specimens were abraded with 220, 320, 400, 600, 800, 1000 grade of emery papers for removal of debris on the metal surfaces and to obtain uniformity on the surfaces of the coupons, then degreased with acetone, washed with double distilled water and dried in air in accordance with the ASTM guidelines for specimen preparation (ASTM, 2017) and immediately stored in desiccators.

### — Electrolytic Solution

The corrosive solution of Hydrochloric Acid (HCl, sp. gr. 1.18) was prepared in the Corrosion Laboratory, Department of Materials and Metallurgical Engineering, University of Ilorin, Ilorin, Nigeria to obtain 2 Molarity of HCl.

## — Preparation of Inhibitors

### » Cucumber peel

The cucumber peel (Plate 1a) was recovered from fruit vendor waste bin and was thoroughly washed and cut into smaller size. The peel was air dried at room temperature and pulverized into desired microns as shown in Plate 1b.



(a) Cucumber peel



(b) Pulverized cucumber peel

Plate 1: Cucumber Peel Extract (a) Cucumber peel (b) Pulverized cucumber peel

### » Cucumber seed extract

Cucumber plants (*cucumis sativus*) were obtained from a commercial fruit vendor in Ilorin (Nigeria), thoroughly washed and cut for proper view of the plants' seeds. The seeds were carefully removed and air dried at room temperature and subsequently pulverized. The pulverized seed was degreased in ethanol, and left open for about 48 hours at room temperature for evaporation of the ethanol for the production of oil. The production of the oil was carried out in a laboratory at the Department of Chemistry, University of Ilorin, Ilorin, Nigeria. Sample of the oil extracted from cucumber seed is shown in Plate 2.



Plate 2: Oil extracted from cucumber seed

## — Gravimetric measurements

The gravimetric measurements method of corrosion tests were carried out using ASTM standard guidelines (ASTM, 2017; ASTM NACE 2012). The pre-treated specimens from the desiccators were weighed with an electronic weighing balance (HX 302T with 0.01 g accuracy) to determine the initial weight of the specimens ( $M_1$ ) and completely immersed in different containers, each containing 750 ml of

2M Hydrochloric Acid with or without cucumber extract (peel or seed oil) as shown in Plate 3. The concentrations of the cucumber extracts (peel and seed oil) used varied from 0.0, 0.2, 0.4, 0.6, 0.8 and 1.0 g/l. The test specimens were exposed to the medium between 24 hours and 672 hours.



Plate 3: Gravimetric measurements Set-up

Sequel to removal of the specimens from the medium of exposure, the corrosion products formed on the surfaces and edges of the specimens were removed using chemical method of cleaning. This procedure involved the cleaning of the specimens in the prepared solution and air dried in accordance with the ASTM standard guidelines (ASTM, 2017; ASTM NACE 2012 ASTM 2014). The solution containing 200 g of Sodium hydroxide (NaOH), 20 g of granulated zinc and reagent water which makes it 1000 ml solution as recommended by ASTM (2017). The dried specimen was then reweighed using electronic weighing balance (HX 302T with 0.01g accuracy) to determine the difference in weight (weight loss). The cleaned specimens are shown in Plate 4. This procedure was repeated for all specimens exposed to the medium of exposure between 24 hours and 672 hours.



Plate 4: Cleaned specimen after corrosion test

From the weight loss, the Corrosion rate and inhibiting efficiency (IE %) of the plant extracts were calculated using Equation 1 and 2 respectively.

$$\text{Corrosion rate (gcm}^{-2}\text{h}^{-1}) = \frac{\Delta W}{AT} \quad (\text{Adewuyi \& Talabi, 2017}) \quad (1)$$

where: W = Weight loss (g); A = Surface area of the AISI 1007 steel coupon (cm<sup>2</sup>);

T = Time of exposure (hours)

The percentage inhibiting efficiency:

$$(\text{IE } \%) = \frac{\text{CR}_{\text{Blank}} - \text{CR}_{\text{inh}}}{\text{CR}_{\text{Blank}}} \times 100 \quad (\text{Adewuyi \& Talabi, 2017}) \quad (2)$$

where: CR<sub>Blank</sub> = Corrosion rate in the absence of inhibitor;

CR<sub>inh</sub> = Corrosion in the presence of inhibitor

### — Electrochemical Measurement (TAFEL Polarization Technique)

A flexible cable was connected to the specimen with the use aluminum foil which held it together, and it was placed on a

cup mould. Hardener was added to a polyester resin and mixed thoroughly in another cup mould, and then an accelerator was added to it in which they were all mixed together. The prepared solution was poured in the mould where the specimens were placed. It was then left for about 15-20 minutes to solidify. The coupon was further polished for surface exposure into the aggressive environments.

A single compartment electrochemical cell designed for varieties of flat samples for electrochemical test at room temperature was used to perform the electrochemical measurements. It consists of a three electrode systems; working electrode (AISI 1007 Steel), saturated calomel electrode as the reference electrode and graphite rod as the auxiliary/counter electrode. Potentiostat (VersaSTAT) was used as electrochemical work station. For connection of the specimen to the working cable, it has to be connected through a cable. Electrochem softwares were used for data analysis. This test was carried out at the Corrosion Laboratory of the Federal University of Technology, Akure. Plate 5 and 6 respectively shows the electrochemical measurement (TAFEL polarization) set up and some samples of the coupons after the test.



Plate 5: Electrochemical Measurement (TAFEL Polarization set-up)



Plate 6: Coupons after TAFEL Polarization test

## RESULTS AND DISCUSSION

### — Phytochemical Properties of Cucumber Extracts

The results of phytochemical constituents of cucumber peel and cucumber seed are presented in Table 1 and 2 respectively. The phytochemical properties of cucumber extracts (peel and seed) were determined to check for the presence of inhibitive functional groups.

Table 1: Phytochemical analysis of cucumber peel extract

Parameters (mg/100g)	Cucumber Peel	Parameter (mg/100g)	Cucumber Peel
Alkaloids	0.89 (+)	Saponins	0.06 (+)
Flavonoids	2.72 (+)	Terpinodols	0.07 (+)
Tannins	0.15 (+)	Phenols	0.20 (+)
Cardiac glycoside	0.08 (+)	Phoxatanninu	0.14 (+)
Steroids	1.32 (+)		

Table 2: Phytochemical analysis of cucumber seed

Parameters (mg/100g)	Cucumber Seed oil	Parameter (mg/100g)	Cucumber Seed oil
Alkaloids	1.32 (+)	Saponins	0.09 (+)
Flavonoids	2.86 (+)	Terpinodols	0.13 (+)
Tannins	1.16 (+)	Phenols	0.28 (+)
Cardiac glycoside	0.09 (+)	Phoxatanninu	0.18 (+)
Steroids	1.38 (+)		

In the results (Tables 1 and 2), it is shown that out of all constituents present in the extracts, the flavonoid has the higher proportion, followed by the Steroids. It can be suggested that flavonoid which has the highest constituents might be the most active ingredient in inhibiting the efficiency corrosion (Umoren, *et al.*, 2016; Odewumi *et al.*, 2015; Al-Otaibi *et al.*, 2014).

### — Gravimetric Measurement

#### » Cucumber Peel Extract

The weight loss results, the variation of corrosion rate and inhibition efficiency in AISI 1007 steel at different concentrations of cucumber peel extract in 2M HCl at different time of immersion are represented in the Figures 1 to 3.

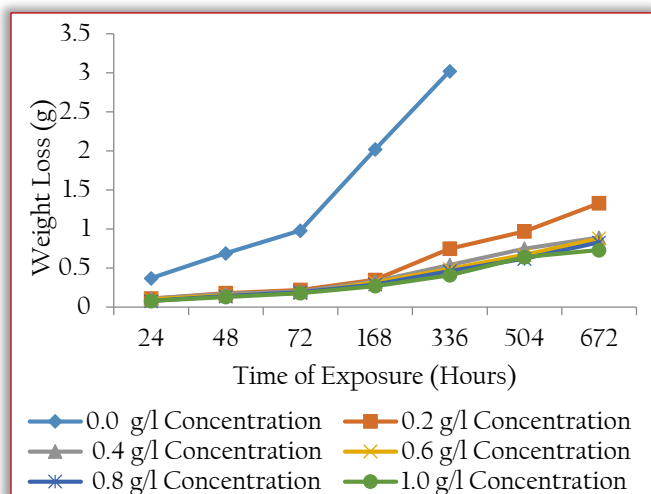


Figure 1: Variation of weight loss with time for the corrosion of AISI 1007 Steel in 2M HCl with and without inhibitor (peel extract)

Figure 1 clearly shows increased in the specimens' weight loss with increased in time of exposure. The figure also revealed reduction in the weight loss of the specimens in the presence of inhibitors; but decreased with increased in the concentration of the inhibitors (peel). The reduction in weight loss may be as a result of adsorption of the inhibitor on the metal surface (Karthikaiselvi & Subhashini, 2014; Lai *et al.*, 2017; Andreani *et al.*, 2016). This indicates good inhibiting potential of cucumber extracts at all concentrations. After 672 hours of exposure, 0.2, 0.4, 0.6, 0.8 and 1.0 g/l concentration of peel recorded weight loss of 1.33, 0.88, 0.88, 0.83, and 0.73 g respectively. This is an indication of significant inhibitory properties of passive film formed on the surface and edges of the steel specimens. The passivity could be traced to synergistic concentrations of phytochemical constituents of

the extract, which is in line with the observation of Loto *et al.* (2017) that the weight loss of mild steel in H<sub>2</sub>SO<sub>4</sub> decreased with increase in concentration of inhibitor (*Benzamide*).

Figure 2 shows the variation of corrosion rates within the time of exposure. The results indicate that the corrosion rate of the specimens with plant extract (peel) decreased with concentration of the extract within the period of exposure. This is in line with the findings of Guinavathy *et al.* (2013), Chinweuba (2014) and Ahmed *et al.* (2014) that corrosion rate of mild steel decreased with increase in inhibitors' concentration.

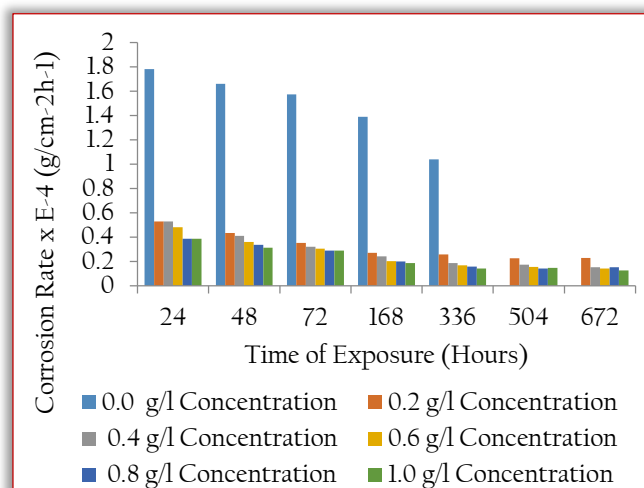


Figure 2: The variation of Corrosion rate in cucumber peel extracts

After 672 hours of exposure in 2M HCl, the calculated corrosion rates were  $2.288 \times 10^{-4}$ ,  $1.531 \times 10^{-4}$ ,  $1.514 \times 10^{-4}$ ,  $1.428 \times 10^{-4}$  and  $1.256 \times 10^{-4}$  g/cm<sup>2</sup>h<sup>-1</sup> with concentration of the cucumber peel extract of 0.2, 0.4, 0.6, 0.8 and 1.0 g/l respectively. As a result of this, it could be deduced that there was an increase in adsorption of the constituents of the extract on the surface of the AISI 1007 steel (specimen) that led to the loss of corrosion rate (Okoronkwo, 2015; Nnanna & Owate, 2014).

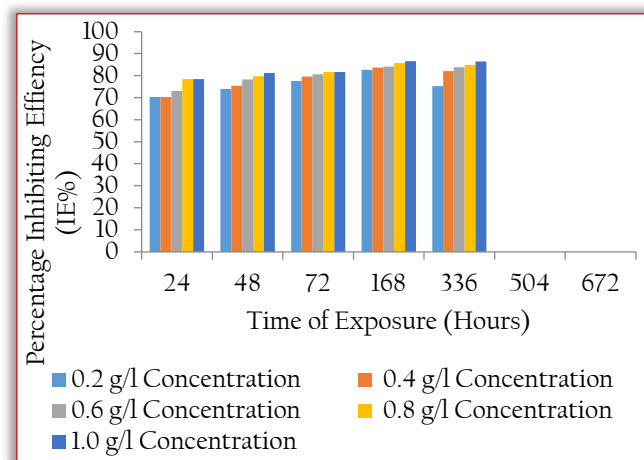


Figure 3: The value of Percentage Inhibition Efficiency for concentration of cucumber peel extracts

The steadiness of the inhibitive behaviour of the extract was evaluated by trend of the inhibition efficiency as a function of time. Figure 3 shows the values of percentage inhibition

efficiency (I.E%) for each concentration of cucumber peel extract. The results show that the calculated IE% range between 70.28 and 86.63% with the presence of cucumber peel as an inhibitor in HCl medium during the time of exposure. The highest IE (86.63%) was achieved using 1.0 g/l cucumber peel after 168 hours of immersion. Although a close value of 86.42% was also achieved after 336 hours of immersion with 1.0 g/l peel. The least IE value (70.28%) was attained with 0.2 and 0.4 g/l after 24 hours of immersion in the media. It indicates that the Inhibition Efficiency (I.E%) increased with increase in inhibitor's concentration. For instance, after 336 hours of exposure in in 2M HCl, the calculated IE% using 0.2, 0.4, 0.6, 0.8 and 1.0 g/l inhibitor (peel) were 75.16, 82.11, 83.77, 84.76 and 86.42% respectively. Also, after 24 hours, the IE% were 70.28, 70.28, 72.98, 78.38 and 78.38% with 0.2, 0.4, 0.6, 0.8 and 1.0 g/l inhibitor (peel). This is might be a result of formation of a protective film which results to transition of metal interface from an active dissolution state to a passive state.

The IE% of the specimens immersed for periods beyond 336 hours could not be determined since the specimens in the medium of exposure without inhibitor could not survive beyond the period due to the aggressiveness of the environment as shown in Plate 7.



Plate 7: AISI 1007 steel that could not withstand beyond 336 hours  
» **Cucumber Seed oil Extract**

The results for the weight loss, the variation of corrosion rate and Inhibition efficiency in AISI 1007 steel at different concentrations of Cucumber Seed oil extract in 2M HCl at different time of immersion are graphically presented in Figure 4, 5 and 6 respectively.

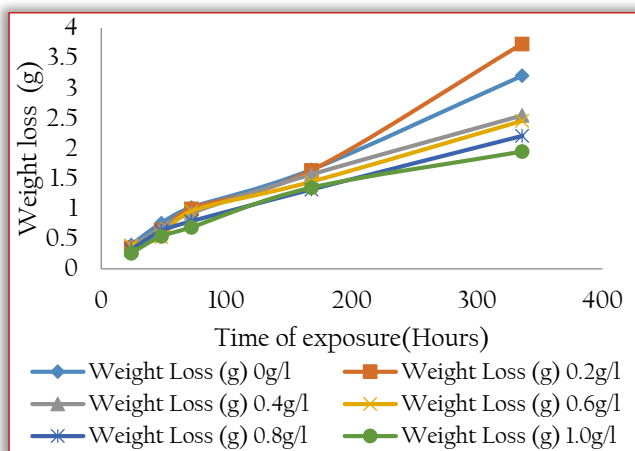


Figure 4: Variation of weight loss with time for the corrosion of AISI 1007 Steel in 2M HCl

The variation of weight loss against time of exposure for corrosion of AISI 1007 Steel in 2M HCl containing various

concentration of cucumber seed oil is shown in Figure 4. It is found from Figure 4 that the weight loss of the AISI 1007 steel specimens also increased with time of exposure; but decreased as the concentration of inhibitor increased. It could be deduced that the rate of corrosion of AISI 1007 steel increased within the period of exposure, and decreased as the concentration of the extract increased. The reduction in weight loss might be as a result of adsorption of the inhibitor on the metal surface. The weight loss of steel decreases as the concentration of the inhibitor increases (Salami, *et al.*, 2012). With the 0.2 g/l of cucumber oil (inhibitor), weight loss of 3.74 g after 336 hours of exposure was recorded, while at the same time 0.4 g/l cucumber oil recorded 2.55 g, 0.6 g/l cucumber oil recorded 2.46g, 0.8g/l cucumber oil recorded 2.21 g and 1.0 g/l cucumber oil recorded 1.95 g weight loss as shown in Figure 4. The reduction in the specimens' weight loss revealed stable coverage of the passive layers formed by the inhibitor on the steel surfaces, which prevent further attack of the medium on the steel surface. This is in line with the findings of Aji *et al.*(2016) that at higher concentration of inhibitors, weight loss becomes almost constant. The specimens could also not withstand the corrosion beyond 336 hours due to the aggressiveness of the environment as revealed in Figure 5 and shown in Plate 7.

Figure 5 shows the variation of corrosion rate within the time of exposure. It is shown that the samples' corrosion rates in the medium of exposure with cucumber extract are lower than that of specimens (samples) in the same medium without inhibitor throughout the periods of this study. Continuous formation of protective passive film on the surfaces of the steel samples serves as a strong barrier for the acid to penetrate onto the steel surfaces. This inhibited the corrosion of the steel ion the study medium of exposure (HCl). More so, the calculated corrosion rates of AISI 1007 Steel in HCl with or without the plant extract generally decreased with time of exposure.

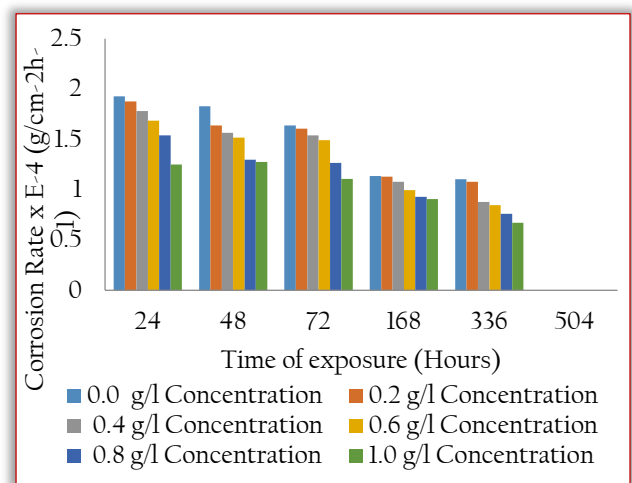


Figure 5: The variation of corrosion rate against the time of exposure

The corrosion rate values also decreased with the concentration of cucumber seed oil extract. For instance after 336 hours of immersion, the calculated corrosion rate values

of AISI 1007 steel samples in 2M HCl were respectively 1.104, 1.0804, 0.8774, 0.8464, 0.7604, 0.6709  $\times 10^{-4}$  g/cm<sup>2</sup>h<sup>-1</sup> in the medium with 0.0, 0.2, 0.4, 0.6, 0.8 and 1.0 g/l concentration of cucumber seed oil extract. This implies that decreased in corrosion rate of the samples with the concentration of cucumber seed oil extract in the medium of exposure is an indication that there was increased in adsorption of the constituents of the extract on the surface of the AISI 1007 steel that led to the loss of corrosion rate (Okoronkwo, *et al.*, 2015; Nnanna & Owate, 2014; Ghames *et al.*, 2017; Verma *et al.*, 2017; Arthur *et al.*, 2013). Inhibiting potential of the extracts might be as result of the presence of organic compounds, like steroids, amino acids, alkaloids, flavonoids, tannins, cardiac glycoside, phenols, saponins, terpinodols, and phoxatanninu, etc. This has been asserted in previous studies (Sattris, 2011; Mohamed *et al.*, 2015; Chris & Emeka, 2016; Salami *et al.*, 2015; Okewale & Olaitan, 2017).

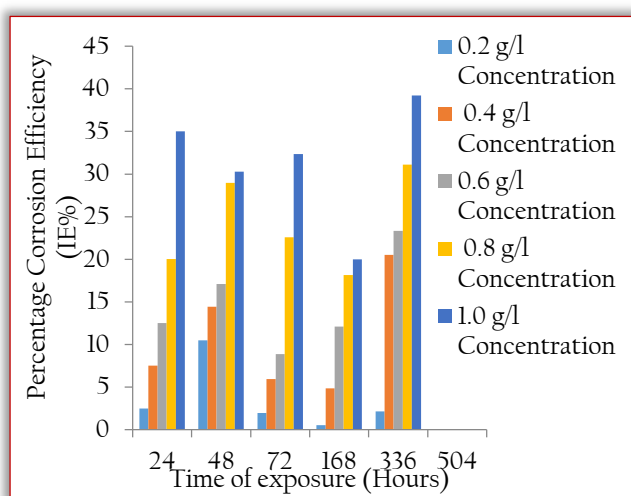


Figure 6: The value of Inhibition Efficiency for concentration of cucumber seed oil extracts

The steadiness of the inhibitive behaviour of the extract was evaluated by trend of the Inhibition Efficiency as a function of time. Figure 6 shows the values of Inhibition Efficiency (IE%) for each concentration of cucumber seed oil extract. The Inhibition Efficiency (IE%) achieved using cucumber seed oil range between 2.49 and 39.23%. The lowest IE% value (2.49%) was achieved after 24 hours of immersion in HCl with 0.2 g/l cucumber oil concentration, while the highest value (39.23%) was achieved after 336 hours of immersion with 1.0 g/l cucumber oil. The IE% increased with inhibitor concentration and time of exposure. The result is in agreement with the findings of Ramya *et al.* (2016), Hui *et al.* (2012) and Popoola *et al.* (2012). This is an indication that the inhibitor acts through adsorption on iron surface and formation of a barrier layer between the metal and the corrosive media (Laamaria, *et al.*, 2012). According to Abbasov *et al.* (2013), the surface of the steel is effectively separated from the medium as adsorption and surface coverage increase with the increase in concentration which results to decrease in in corrosion rate as inhibitor concentration increases to attain higher inhibition efficiency. Omotosho *et al.* (2013) was also of the view that occurrence of physical absorption on the surface of the metal

leads to increase in the IE%. The results therefore revealed that the extract (seed oil) could be used as potential corrosion inhibitor of AISI 1007 steel samples in 2M HCl in industries.

### — Electrochemical Measurements (Tafel Polarization Technique) Cucumber Peel

Tafel extrapolation measures corrosion rate. For an electrochemical reaction under activation control, polarization curves exhibit linear behaviour in the Corrosion potential ( $E_{corr}$ ) Vs log Corrosion current density ( $i_{corr}$ ) plots called TAFEL behaviour. Polarization measurements were carried out starting from a cathodic potential of -200mV/s to an anodic potential of +250mV/s at a cam rate of 0.166. The linear Tafel segments of the cathodic curves and the calculated anodic Tafel lines were extrapolated to corrosion potential to obtain the corrosion current densities  $i_{corr}$  (Amin *et al.*, 2009).

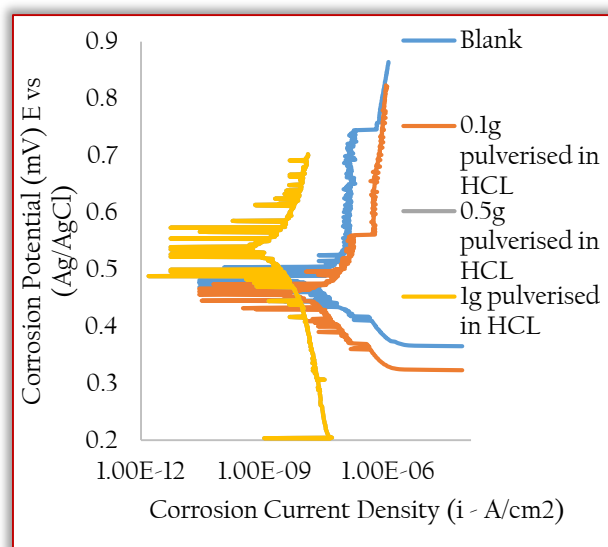


Figure 7: Corrosion Potential against Corrosion Current Density (Pulverised Peel)

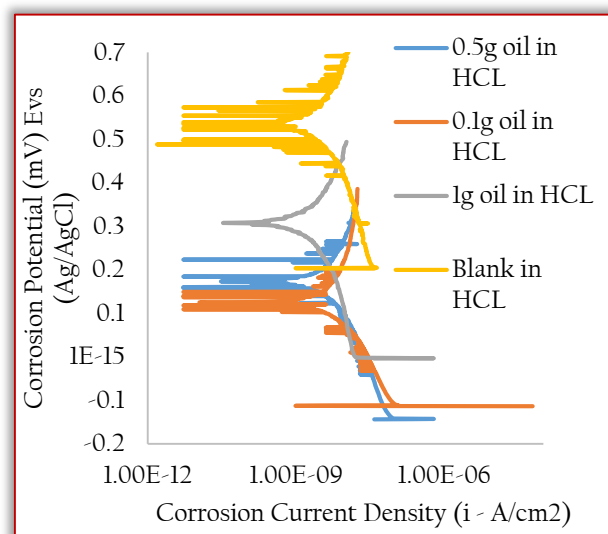


Figure 8: Corrosion Potential against Corrosion Current Density (Cucumber Seed Oil)

It is shown that as the concentration of cucumber peel increased the corrosion potential shifts toward a more noble direction (Figures 7 and 8). Furthermore, the corrosion current

decreases markedly in the presence of cucumber peel extract, and the magnitude of such an effect increases with increasing cucumber peel extract concentration. These results showed the inhibitive action of the extract to corrosion of AISI 1007 steel in the 2M HCl. It could be seen that the inhibition efficiency increases with increasing extract concentration. This result reflects the effect of the extract on both anodic and cathodic reactions. Therefore, it could be concluded that cucumber peel extract and cucumber seed oil acts as a mixed inhibitor.

### CONCLUSIONS

Based on the on the study of inhibition of the corrosion of AISI 1007 steel in Hydrochloric Acid solution by the cucumber peel and seed oil extracts using gravimetric and electrochemical measurement (TAFEL Polarization Technique). The following conclusions were drawn:

- Gravimetric technique shows that the corrosion rate of AISI 1007 steel in HCl solution was found to decrease with increasing concentration of the cucumber peel and seed oil extract.
- Cucumber seed and oil exhibited good inhibiting tendency on corrosion of AISI 1007 in HCl up to period of 336 hours. The IE% achieved ranged between 70.28 and 86.63%; 2.49 and 39.23% for cucumber peel extract and seed (oil) extract respectively
- The inhibition of the corrosion of AISI steel by acid extracts of cucumber was due to the phytochemical constituents in the plant extract.
- The inhibition efficiency of the cucumber peel and seed extracts in gravimetric technique was dependent on the concentration of the extract, and it increased with increasing concentration of the extract in the acidic medium.
- Maximum IE% of 86.63 % and 86.42 % was attained after 168 and 336 hours of exposure in the presence of 1.0 g/l cucumber peel extract concentration respectively. While 39.23% of IE% was obtained after 336 hours exposure with 1.0 g/l cucumber seed (oil) extract. Hence, the cucumber peel extract inhibition efficiency was greater than that of the cucumber seed oil extract (CSP > CSS).
- Tafel polarization technique results showed that the extract acted as a mixed type inhibitor via a simple adsorption of the phytochemicals present in the extract on the AISI steel surface in HCl solution.
- The cucumber extracts (peel and oil) could serve as effective inhibitor of corrosion of AISI steel in Hydrochloric Acid solution.

### References

[1] Abbasov, V.M. Abd El-Lateef, H. M., Aliyeva, L.I., Qasimov, E.E., Ismayilov, I.T. and Khalaf, M. M.: A Study of the Corrosion Inhibition of Mild Steel C1018 in CO<sub>2</sub>-Saturated Brine Using Some Novel Surfactants Based on Corn Oil, Egyptian Journal of Petroleum, 22, 451–470, 2013.

[2] Abd El-Aziz S. F., Ayman Y. E., Hesham H. E., and Mohamed F.: The Role of Aqueous Ocimum Basilicum Extract for

Monitoring the Corrosion Inhibition of Carbon Steel used in Sanitation Plants and its Effect on Escherichia Coli, ZASTITA MATERIJALA, 57 (broj 4), 583-596, 2016.

[3] Abdul Amir H. K., Abu Bakar M. , Leiqaa A. H., Ahmed A. A., Ng Hooi San 1 and Ahmed Y. Musa: Inhibition of Mild Steel Corrosion in Hydrochloric Acid Solution by New Coumarin, Materials, 7 (2010), 4335-4348, 2014.

[4] Adeyemi, O. O. and Olubomehin, O.O.: Investigation of Anthocleista djalonensis Stem Bark Extract as Corrosion Inhibitor for Aluminum. The Pacific Journal of Science and Technology, 11(2), 455 -462, 2017.

[5] Adewuyi, B.O. and Talabi, H. K.: Inhibiting Efficiency of Locally Developed Inhibitors (Amaranthusspinosus, Euphorbia heterophylla, Imperatacylindrica and Panicum Maximum) on Low Carbon Steel in Acidic and Saline Media, International Journal of Engineering, Tome XV (Fascicule 2), 69-76, 2017.

[6] Ahmed, A. A., Abdul Amir, H. K., Abdullahi, K. Abu Bakar, M., Chong, K. H. and Sutiana, J.: Inhibition of Mild Steel Corrosion in Sulfuric Acid Solution by New Schiff Base, Materials, 7(2), 787-804, 2014.

[7] Aji, I. S., Zadvá, Y. P., Madu, M. J., Hybridization of plant extract for Corrosion Prevention of Mild Steel, International Journal of Engineering Research Technology, 4(1), 119-127, 2016.

[8] Al-Otaibi, M. S., Al-Mayouf, A. M., Khan, M., Mousa, A. A., Al-Mazroa, S. A., Alkhatlan, H. Z.: Corrosion Inhibitory Action of some Plant Extracts on the Corrosion of Mild Steel in Acidic Media, Arabian Journal of Chemistry, 7, 340–346, 2014.

[9] Al-Senani, G. M.: Corrosion Inhibition of Carbon Steel in Acidic Chloride Medium by Cucumis Sativus (Cucumber) Peel Extract, International Journal of Electrochemistry Science, 11, 291-302, 2016.

[10] Allam, L., Oulmas, C., Boughrara, D. Kadri, A. Benbrahim, N.: Eugenia Caryophyllata Extract as Green Inhibitor for Steel Corrosion in 1M HCl Solution, Journal of Materials, Processes and Environment. 5 (1), 18, 2017.

[11] Amin, M. A., Abd El Rehim, S.S., Abdel-Fatah, H. T. M.: Electrochemical Frequency Modulation and Inductively Coupled Plasma Atomic Emission Spectroscopy Methods for Monitoring Corrosion Rates and Inhibition of Low Alloy Steel Corrosion in HCl Solutions and a Test for Validity of The Tafel Extrapolation Method, Corrosion Science, 51, 882-894, 2009.

[12] Andreani, S. Znini, M. Paolini, J. Majidi, L. Hammouti, B., Costa, J., Muselli, A.: Study of Corrosion Inhibition for Mild Steel in Hydrochloric Acid Solution by Limbarda crithmoides (L.) Essential Oil of Corsica, J. Mater. Environ. Sci., 7(1), 187-195, 2016.

[13] Anne, M.: Cucumber Peel Benefits, Cucumber, <http://www.livestrong.com/article/529707-nutrition-in-cucumbers-without-the-peel/>, February, 2018.

[14] Arockia, S. J., Pushpa, M. T, Arthanareeswari, M., Kamaraj P., Mohan Kumar R, Sneh R P. and Subasree, N.: Evaluation of Inhibitory Effect of Nerium Oleander Leaf Extract on Mild Steel Corrosion in Aqueous Medium, Der Pharma Chemical, 10(S1), 1-6, 2018.

- [15] Arthur, D. E., J, Achika, Ameh, P. O. and Anya, C.: A Review on the Assessment of Polymeric Materials used as Corrosion Inhibitor of Metals and Alloys, *International Journal of Industrial Chemistry*, 4(2), 1-9, 2013.
- [16] ASTM G1-03 e1: Practice for Preparing, Cleaning, and Evaluating Corrosion Test Specimens, ASTM International, 100 Barr Harbor Drive, West Conshohocken, PA 19428-2959, United States, 2017.
- [17] ASTM NACE/ASTM G31- 12a: Standard Guide for Laboratory Immersion Corrosion Testing of Metals, ASTM International, 100 Barr Harbor Drive, West Conshohocken, PA 19428-2959, United States, 2012.
- [18] ASTM G4: Standard Guide for Conducting Corrosion Coupon Tests in Field Applications,, ASTM International, 100 Barr Harbor Drive, West Conshohocken, PA 19428-2959, United States, 2014.
- [19] Chakravarthy, M. P. and Mohana, K. N.: Adsorption and Corrosion Inhibition Characteristics of Some Nicotinamide Derivatives on Mild Steel in Hydrochloric Acid Solution, *Hindawi Corrosion*, 1-13, 2014.
- [20] Charmers, D.W.: The Properties and uses of Marine Structural Materials, *Marine Structures*, 191, 47-70, 1988.
- [21] Chinweuba, A. J.: Comparative Analysis of Corrosion Inhibition Properties of Allium Cepa Extract on Mild Steel and Zinc, *Journal of Natural Sciences Research*, 4(6), 1-6, 2014.
- [22] Chinwko E. C., Odio B. O., Chukwunke J. L., Sinebe J. E.: Investigation of the Effect of Corrosion on Mild Steel in Five Different Environments, *International Journal of Scientific & Technology Research*, 3(7), 306-310, 2014.
- [23] Chris O. A. and Emeka E. E. Oguzie: Evaluation of Anticorrosion Properties of Chrysophyllum Albidum Leaves Extract for Mild Steel Protection in acidic media, *International Journal of Industrial Chemistry*, 7, 81–92, 2016.
- [24] Dharmaraj, E., Pragathiswaran, C. Govindhan, P., Arockia Sahayaraj, P., John Amalraj, A. and Dharmalingam, V.: Corrosion Inhibition of Mild Steel By Natural Product Compound, *International Journal of Research in Pharmacy and Chemistry*, 7(1), 132-137, 2017.
- [25] El Ibrahim, B., Jmiai, A., Bazzi, L., El Issami, S.: Amino acids and their Derivatives as Corrosion Inhibitors for Metals and Alloys, *Arabian Journal of Chemistry*, In Press, 2017.
- [26] Fekry, A. M. and Mohamed, R. R.: Acetyl Thiourea Chitosan as an Eco-Friendly Inhibitor for Mild Steel in Sulphuric Acid Medium, *Electrochimica Acta*, 55 (6), 1933–1939, 2010.
- [27] Ghames, A., Douadi, T., Issaadi, S., Sibous, L., Alaoui, K. I., Taleb, M. and Chafaa S.: Theoretical and Experimental Studies of Adsorption Characteristics of Newly Synthesized Schiff Bases and their Evaluation as Corrosion Inhibitors for Mild Steel in 1M HCl, *International Journal of Electrochemical Science*, 12, 4867–4897, 2017.
- [28] Gupta P. and Jain, G.: Corrosion Inhibition by ALOE BARBADENSIS (ALOE VERA) Extract as Green Inhibitor for Mild Steel in HNO<sub>3</sub>, *International Journal of Scientific Research and Reviews*, 3 (4 Suppl.), 72 – 83, 2014.
- [29] Gunasekaran, G. and Chauhan, L.R.: Eco-Friendly Inhibitor for Corrosion Inhibition of Mild Steel in Phosphoric Acid Medium, *Electrochimica Acta*, 49(25), 4387-4395, 2004.
- [30] Gunavathy, N.: Phytochemical Constituents and Antioxidative Property of Musa Acuminata Flower as Green Corrosion Inhibitor of Mild Steel in Acid Media, *Ancient Science of Life*, V32 (Suppl.2), S8, 2013.
- [31] Hui, C., Zhenghao, F., Hairong, X., Jiali, H. and Qixu: Inhibition Effect of Reed Leaves Extract on Steel in HCl and H<sub>2</sub>SO<sub>4</sub>. *International Journal of Electrochemical Science*, 7, 8869-8882, 2012.
- [32] Ji, G., Shukla, S. K., Dwivedi, P., Sundaram, S., Ebenso, E. E. and Prakash, R.: Parthenium Hysterophorus Plant Extract as an Efficient Green Corrosion Inhibitor for Mild Steel in Acidic Environment, *International Journal Electrochemical Science*, 7, 9933-9945, 2012.
- [33] Karthikaiselvi, R. and Subhashini, S.: Study of Adsorption Properties and Inhibition of Mild Steel Corrosion in Hydrochloric Acid Media by Water Soluble Composite Poly (Vinyl Alcohol-Omethoxyaniline), *Journal of the Association of Arab Universities for Basic and Applied Sciences*, 16, 74-82, 2014.
- [34] Kennedy, D., Uses of Steel Plate, [http://www.ehow.com/about\\_5818097\\_uses-steel-plates.html](http://www.ehow.com/about_5818097_uses-steel-plates.html), December, 2017.
- [35] Laamaria, M. R., Benzakoura, J., Berrekhisb, F., Bakassec, M., Villemin, D.: Adsorption and Kinetic Studies of Piperidin-1-yl-Phosphonic Acid as a Corrosion Inhibitor of Iron in Sulphuric Acid Medium, *J. Mater. Environ. Sci.*, 3 (3), 485-496, 2012.
- [36] Lai, C., Xie, B., Zou, L, Zheng, X., Mab, X., Zhu, S.: Adsorption and Corrosion Inhibition of Mild Steel in Hydrochloric Acid Solution by S-allyl-O,OO-dialkyldithiophosphates, *Results in Physics*, 7, 3434–3443, 2017.
- [37] Loto, C. A., Loto, R. T. and Joseph, O. O.: Effect of Benzamide on the Corrosion Inhibition of Mild Steel in H<sub>2</sub>SO<sub>4</sub>, *South African Journal of Chemistry*, 70, 38-43, 2017.
- [38] Mohamed T., Leila, D. and Naceur, E.: Corrosion Inhibition of Carbon Steel in 1M Sulphuric Acid Solution by Extract of Eucalyptus Globulus Leaves Cultivated in Tunisia Arid Zones, *J. Bio Tribo Corros*, 1-16, 2015.
- [39] Neha P., Shruti A., and Pallav, S.: Greener Approach towards Corrosion Inhibition, *Chinese Journal of Engineering*, 1-10, 2013.
- [40] Nnanna, L. A. and Owate, I. O.: An interesting and Efficient Green Corrosion Inhibitor for Aluminum from Extracts of Moringa Oleifera in Acidic Solution. *Scientia Africana*, 13, 52-63, 2014.
- [41] Odewunmi, N. A., Umoren, S. A., and Gasem, Z. M.: Watermelon Waste Products as Green Corrosion Inhibitors for Mild Steel in HCl Solution. *Journal of Environmental Chemical Engineering*, 3, 286-296, 2015.
- [42] Okafor, P.C., Ikpi, M.E., Uwah, I.E., Ebenso, E.E., Ekpe, U.J., Umoren, S.A.: Inhibitory Action of Phyllanthus Amarus Extracts on the Corrosion of Mild Steel in Acidic Media, *Corrosion Science*, 50, 2310–2317, 2008.
- [43] Okewale A. O. and Olaitan A.: The use of Rubber Leaf Extract as a Corrosion Inhibitor for Mild Steel in Acidic Solution, *International Journal of Materials and Chemistry*, 7 (1), 5-13, 2017.

- [44] Okoronkwo, A. E., Olusegun, S. J. and Oluwasina, O. O.: The Inhibitive Action of Chitosan Extracted from Archachatina Marginata Shells on the Corrosion of Plain Carbon Steel in Acid Media, *Anti-Corrosion Methods and Materials*, 62,13-18, 2015.
- [45] Omotosho, O. A. Ajayi, O.O. Fayomi, O. S. Ifepe, V. O.: Assessing the Deterioration Behaviour of Mild Steel in 2M H<sub>2</sub>SO<sub>4</sub> using Bambusa Glauscescens. *International Journal of Applied Engineering Research, DINDIGUC*, 2(2), 406-418, 2011.
- [46] Popoola, A. P. I., Abdulwahab, M. and Fayomi, O. S. I.: Corrosion Inhibition of Mild Steel in Sesamum Medium – 2M HCl/ H<sub>2</sub>SO<sub>4</sub> Interface. *International Journal of Elechemical Science*, 7, 5805-5816, 2012.
- [47] Prithiba, A. and Rajalakshmi, R.: An Ecofriendly Initiative for the Corrosion Inhibition of Mild Steel in 1M HCl Using Tecoma capensis Flower Extract, *International Journal of Metals*, 1-9, 2016.
- [48] Ramya, K. and Muralimohan, N.: Study on Corrosion Inhibitor in Mild Steel by Various Habitual Plant Extract–Review, *International Journal of Chemical Concepts*, 2 (2), 70-75, 2016.
- [49] Salami L., Wewe T., Akinyemi O.P., Patinvoh R. J.: A Study of the Corrosion Inhibitor of Mild Steel in Sulphuric Acid using Musa Sapientum Peels Extract. *Global Engineers & Technologists Review*. 2(12), 1-6, 2012.
- [50] Salami L., Fadayini O.M. and Olafadehan O. A.: Comparative Adsorption Mechanism of Musa Sapientum Peels Extracts for Green Corrosion Inhibition of Mild Steel in Sulphuric Acid. *Greener Journal of Physical Sciences*, 5(1), 1-10, 2015.
- [51] Salhi, A., Bouyanzer<sup>1</sup>, A., Chetouani, A., El Ouariachi, E., Zarrouk, A., Hammouti, B., Desjobert, J.M. and Costa, J.: Chemical Composition, Antioxidant and Anticorrosion Activities of Mentha Suaveolens, *Journal of Materials and Environmental Sciences, JMES*, 8 (5), 1718-1728, 2017.
- [52] Satris, V. S.: *Green Corrosion Inhibition: Theory and Practice*, 1<sup>st</sup> Edition, A John Wiley & Sons Inc., Publication, Hoboken, New Jersey, 2011. ISBN: 111801541X
- [53] Sharkma, K. S, Mudhoo, A. and khamis, E.: Adsorption Studies, Modeling and use of Green Inhibition: An Overview of Present Research. In: Sharma, K. S. Editor., *Green Corrosion Chemistry and Engineering: Opportunity and Challenges*. Wiley-VCH Verlag GmbH & Co., KGaA Germany, 2011, ISBN: 978-3-527-32930-4.
- [54] Sharma , S. K., Mudhoo , A., Jain, G. and Khamis, E.: Corrosion Inhibition of Neem (Azadirachta indica) Leaves Extract as a Green Corrosion Inhibitor for Zinc in H<sub>2</sub>SO<sub>4</sub>, *Green Chemistry Letters and Reviews*, 2 (1), 47-51, 2009.
- [55] Thompson, N.G., Yunovich, M., and Dunmire, D.: Corrosion Cost and Control, *Corr. Rev.* 25, 247-267, 2007.
- [56] Umoren, S.A., Eduok, U.M., Solomon, M. M. and Udoh, A.P.: Corrosion Inhibition by Leaves and Stem Extracts of Sida Acuta for Mild Steel in 1M H<sub>2</sub>SO<sub>4</sub> Solutions Investigated by Chemical and Spectroscopic Techniques, *Arabian Journal of Chemistry*, 9, S209–S224, 2016
- [57] Uwah, I.E. Okafor, P.C. and Ebiekpe, V.E.: Inhibitive Action of Ethanol Extracts from Nauclea Latifolia on the Corrosion of Mild Steel in H<sub>2</sub>SO<sub>4</sub> Solutions and their Adsorption Characteristics, *Arabian Journal of Chemistry*, 6, 285–293, 2013.
- [58] Umoren, S.A., Zuhair, B. O. and Ime, B. O.: Natural Products for Materials Protection: Inhibition of Mild Steel Corrosion by Date Palm Seed Extracts in Acid Media, *Industrial & Engineering Chemistry Research*, 52(42), 16349–16355, 2013.
- [59] Verma, N., Chauhan, D. S., Quraishi, M. A.: Drugs as Environmentally Benign Corrosion Inhibitors for Ferrous and Nonferrous Materials in Acid Environment: An Overview Chandrabha, *Journal of Materials and Environmental Sciences, JMES*, 8 (11), 4040-4051, 2017.



ISSN: 2067-3809

copyright © University POLITEHNICA Timisoara,  
Faculty of Engineering Hunedoara,  
5, Revolutiei, 331128, Hunedoara, ROMANIA  
<http://acta.fih.upt.ro>

# Fascicule 4

## [October - December]

t o m e

# [2018] XI

**ACTA**Technica**CORVINIENSIS**  
BULLETIN OF ENGINEERING



**ISSN: 2067-3809**

copyright © University POLITEHNICA Timisoara,  
Faculty of Engineering Hunedoara,  
5, Revolutiei, 331128, Hunedoara, ROMANIA  
<http://acta.fih.upt.ro>

## MANUSCRIPT PREPARATION – GENERAL GUIDELINES

Manuscripts submitted for consideration to **ACTA TECHNICA CORVINIENSIS – Bulletin of Engineering** must conform to the following requirements that will facilitate preparation of the article for publication. These instructions are written in a form that satisfies all of the formatting requirements for the author manuscript. Please use them as a template in preparing your manuscript. Authors must take special care to follow these instructions concerning margins.

### INVITATION

We are looking forward to a fruitful collaboration and we welcome you to publish in our **ACTA TECHNICA CORVINIENSIS – Bulletin of Engineering**. You are invited to contribute review or research papers as well as opinion in the fields of science and technology including engineering. We accept contributions (full papers) in the fields of applied sciences and technology including all branches of engineering and management.

**ACTA TECHNICA CORVINIENSIS – Bulletin of Engineering** publishes invited review papers covering the full spectrum of engineering and management. The reviews, both experimental and theoretical, provide general background information as well as a critical assessment on topics in a state of flux. We are primarily interested in those contributions which bring new insights, and papers will be selected on the basis of the importance of the new knowledge they provide.

Submission of a paper implies that the work described has not been published previously (except in the form of an abstract or as part of a published lecture or academic thesis) that it is not under consideration for publication elsewhere. It is not accepted to submit materials which in any way violate copyrights of third persons or law rights. An author is fully responsible ethically and legally for breaking given conditions or misleading the Editor or the Publisher.

**ACTA TECHNICA CORVINIENSIS – Bulletin of Engineering** is an international and interdisciplinary journal which reports on scientific and technical contributions. Every year, in four online issues (fascicules 1–4), **ACTA TECHNICA CORVINIENSIS – Bulletin of Engineering [e-ISSN: 2067-3809]** publishes a series of reviews covering the most exciting and developing areas of engineering. Each issue contains papers reviewed by international researchers who are experts in their fields. The result is a journal that gives the scientists and engineers the opportunity to keep informed of all the current developments in their own, and related, areas of research, ensuring the new ideas across an increasingly the interdisciplinary field. Topical reviews in materials science and engineering, each including:

- surveys of work accomplished to date
- current trends in research and applications
- future prospects.

As an open-access journal **ACTA TECHNICA CORVINIENSIS – Bulletin of Engineering** will serve the whole engineering research community, offering a stimulating combination of the following:

- Research Papers – concise, high impact original research articles,
- Scientific Papers – concise, high impact original theoretical articles,
- Perspectives – commissioned commentaries highlighting the impact and wider implications of research appearing in the journal.

**ACTA TECHNICA CORVINIENSIS – Bulletin of Engineering** encourages the submission of comments on papers published particularly in our journal. The journal publishes articles focused on topics of current interest within the scope of the journal and coordinated by invited guest editors. Interested authors are invited to contact one of the Editors for further details.

### BASIC INSTRUCTIONS AND MANUSCRIPT REQUIREMENTS

The basic instructions and manuscript requirements are simple:

- Manuscript shall be formatted for an A4 size page.
- The all margins (top, bottom, left, and right) shall be 25 mm.
- The text shall have both the left and right margins justified.
- Single-spaced text, tables, and references, written with 11 or 12-point Georgia or Times Roman typeface.
- No Line numbering on any pages and no page numbers.
- Manuscript length must not exceed 15 pages (including text and references).
- Number of figures and tables combined must not exceed 20.
- Manuscripts that exceed these guidelines will be subject to reductions in length.

The original of the technical paper will be sent through e-mail as attached document (\*.doc, Windows 95 or higher). Manuscripts should be submitted to e-mail: [redactie@fih.upt.ro](mailto:redactie@fih.upt.ro), with mention "for ACTA TECHNICA CORVINIENSIS".

## STRUCTURE

The manuscript should be organized in the following order: Title of the paper, Authors' names and affiliation, Abstract, Key Words, Introduction, Body of the paper (in sequential headings), Discussion & Results, Conclusion or Concluding Remarks, Acknowledgements (where applicable), References, and Appendices (where applicable).

### THE TITLE

The title is centered on the page and is CAPITALIZED AND SET IN BOLDFACE (font size 14 pt). It should adequately describe the content of the paper. An abbreviated title of less than 60 characters (including spaces) should also be suggested. Maximum length of title: 20 words.

### AUTHOR'S NAME AND AFFILIATION

The author's name(s) follows the title and is also centered on the page (font size 11 pt). A blank line is required between the title and the author's name(s). Last names should be spelled out in full and succeeded by author's initials. The author's affiliation (in font size 11 pt) is provided below. Phone and fax numbers do not appear.

### ABSTRACT

State the paper's purpose, methods or procedures presentation, new results, and conclusions are presented. A nonmathematical abstract, not exceeding 200 words, is required for all papers. It should be an abbreviated, accurate presentation of the contents of the paper. It should contain sufficient information to enable readers to decide whether they should obtain and read the entire paper. Do not cite references in the abstract.

### KEY WORDS

The author should provide a list of three to five key words that clearly describe the subject matter of the paper.

### TEXT LAYOUT

The manuscript must be typed single spacing. Use extra line spacing between equations, illustrations, figures and tables. The body of the text should be prepared using Georgia or Times New Roman. The font size used for preparation of the manuscript must be 11 or 12 points. The first paragraph following a heading should not be indented. The following paragraphs must be indented 10 mm. Note that there is no line spacing between paragraphs unless a subheading is used. Symbols for physical quantities in the text should be written in italics. Conclude the text with a summary or conclusion section. Spell out all initials, acronyms, or abbreviations (not units of measure) at first use. Put the initials or abbreviation in parentheses after the spelled-out version. The manuscript must be writing in the third person ("the author concludes...").

### FIGURES AND TABLES

Figures (diagrams and photographs) should be numbered consecutively using Arabic numbers. They should be placed in the text soon after the point where they are referenced. Figures should be centered in a column and should have a figure caption placed underneath. Captions should be centered in the column, in the format "Figure 1"

and are in upper and lower case letters. When referring to a figure in the body of the text, the abbreviation "Figure" is used. Illustrations must be submitted in digital format, with a good resolution. Table captions appear centered above the table in upper and lower case letters.

When referring to a table in the text, "Table" with the proper number is used. Captions should be centered in the column, in the format "Table 1" and are in upper and lower case letters. Tables are numbered consecutively and independently of any figures. All figures and tables must be incorporated into the text.

### EQUATIONS & MATHEMATICAL EXPRESSIONS

Place equations on separate lines, centered, and numbered in parentheses at the right margin. Equation numbers should appear in parentheses and be numbered consecutively. All equation numbers must appear on the right-hand side of the equation and should be referred to within the text.

### CONCLUSIONS

A conclusion section must be included and should indicate clearly the advantages, limitations and possible applications of the paper. Discuss about future work.

### Acknowledgements

An acknowledgement section may be presented after the conclusion, if desired. Individuals or units other than authors who were of direct help in the work could be acknowledged by a brief statement following the text.

The acknowledgment should give essential credits, but its length should be kept to a minimum; word count should be <100 words.

### References

References should be listed together at the end of the paper in alphabetical order by author's surname. List of references indent 10 mm from the second line of each references. Personal communications and unpublished data are not acceptable references.

**Journal Papers:** Surname 1, Initials; Surname 2, Initials and Surname 3, Initials: Title, Journal Name, volume (number), pages, year.

**Books:** Surname 1, Initials and Surname 2, Initials: Title, Edition (if existent), Place of publication, Publisher, year.

**Proceedings Papers:** Surname 1, Initials; Surname 2, Initials and Surname 3, Initials: Paper title, Proceedings title, pages, year.



ISSN: 2067-3809

copyright © University POLITEHNICA Timisoara,  
Faculty of Engineering Hunedoara,  
5, Revolutiei, 331128, Hunedoara, ROMANIA  
<http://acta.fih.upt.ro>

**ACTA TECHNICA CORVINIENSIS – Bulletin of Engineering** is an international and interdisciplinary journal which reports on scientific and technical contributions.

The **ACTA TECHNICA CORVINIENSIS – Bulletin of Engineering** advances the understanding of both the fundamentals of engineering science and its application to the solution of challenges and problems in engineering and management, dedicated to the publication of high quality papers on all aspects of the engineering sciences and the management.

You are invited to contribute review or research papers as well as opinion in the fields of science and technology including engineering. We accept contributions (full papers) in the fields of applied sciences and technology including all branches of engineering and management. Submission of a paper implies that the work described has not been published previously (except in the form of an abstract or as part of a published lecture or academic thesis) that it is not under consideration for publication elsewhere. It is not accepted to submit materials which in any way violate copyrights of third persons or law rights. An author is fully responsible ethically and legally for breaking given conditions or misleading the Editor or the Publisher.

The Editor reserves the right to return papers that do not conform to the instructions for paper preparation and template as well as papers that do not fit the scope of the journal, prior to refereeing. The Editor reserves the right not to accept the paper for print in the case of a negative review made by reviewers and also in the case of not paying the required fees if such will be fixed and in the case time of waiting for the publication of the paper would extend the period fixed by the Editor as a result of too big number of papers waiting for print. The decision of the Editor in that matter is irrevocable and their aim is care about the high content-related level of that journal.

The mission of the **ACTA TECHNICA CORVINIENSIS – Bulletin of Engineering** is to disseminate academic knowledge across the scientific realms and to provide applied research knowledge to the appropriate stakeholders. We are keen to receive original contributions from researchers representing any Science related field. We strongly believe that the open access model will spur research across the world especially as researchers gain unrestricted access to high quality research articles. Being an Open Access Publisher, Academic Journals does not receive payment for subscription as the journals are freely accessible over the internet.

## GENERAL TOPICS

### ENGINEERING

- ✓ Mechanical Engineering
- ✓ Metallurgical Engineering
- ✓ Agricultural Engineering
- ✓ Control Engineering
- ✓ Electrical Engineering
- ✓ Civil Engineering
- ✓ Biomedical Engineering
- ✓ Transport Engineering
- ✓ Nanoengineering

### CHEMISTRY

- ✓ General Chemistry
- ✓ Analytical Chemistry
- ✓ Inorganic Chemistry
- ✓ Materials Science & Metallography
- ✓ Polymer Chemistry
- ✓ Spectroscopy
- ✓ Thermo-chemistry

### ECONOMICS

- ✓ Agricultural Economics
- ✓ Development Economics
- ✓ Environmental Economics
- ✓ Industrial Organization
- ✓ Mathematical Economics
- ✓ Monetary Economics
- ✓ Resource Economics
- ✓ Transport Economics
- ✓ General Management
- ✓ Managerial Economics
- ✓ Logistics

### INFORMATION SCIENCES

- ✓ Computer Science
- ✓ Information Science

### EARTH SCIENCES

- ✓ Geodesy
- ✓ Geology
- ✓ Hydrology
- ✓ Seismology
- ✓ Soil science

### ENVIRONMENTAL

- ✓ Environmental Chemistry
- ✓ Environmental Science & Ecology
- ✓ Environmental Soil Science
- ✓ Environmental Health

## AGRICULTURE

- ✓ Agricultural & Biological Engineering
- ✓ Food Science & Engineering
- ✓ Horticulture

## BIOTECHNOLOGY

- ✓ Biomechanics
- ✓ Biotechnology
- ✓ Biomaterials

## MATHEMATICS

- ✓ Applied mathematics
- ✓ Modeling & Optimization
- ✓ Foundations & Methods

**ACTA TECHNICA CORVINIENSIS – Bulletin of Engineering** has been published since 2008, as an online, free-access, international and multidisciplinary publication of the Faculty of Engineering Hunedoara.

We are very pleased to inform that our international and interdisciplinary journal **ACTA TECHNICA CORVINIENSIS – Bulletin of Engineering** completed its ten years of publication successfully [issues of years 2008 –2017, Tome I–X]. In a very short period it has acquired global presence and scholars from all over the world have taken it with great enthusiasm.

Every year, in four online issues (fascicules 1 – 4), **ACTA TECHNICA CORVINIENSIS – Bulletin of Engineering** [e-ISSN: 2067-3809] publishes a series of reviews covering the most exciting and developing fields of science and technology. Each issue contains papers reviewed by international researchers who are experts in their fields. The result is a journal that gives the scientists and engineers the opportunity to keep informed of all the current developments in their own, and related, areas of research, ensuring the new ideas across an increasingly the interdisciplinary field.



Now, when we celebrate the tenth years anniversary of **ACTA TECHNICA CORVINIENSIS – Bulletin of Engineering**, we are extremely grateful and heartily acknowledge the kind of support and encouragement from all contributors and all collaborators!

On behalf of the Editorial Board and Scientific Committees of **ACTA TECHNICA CORVINIENSIS – Bulletin of Engineering**, we would like to thank the many people who helped make this journal successful. We thank all authors who submitted their work to **ACTA TECHNICA CORVINIENSIS – Bulletin of Engineering**.

**ACTA TECHNICA CORVINIENSIS – Bulletin of Engineering** exchange similar publications with similar institutions of our country and from abroad.



ISSN: 2067-3809

copyright © University POLITEHNICA Timisoara,  
Faculty of Engineering Hunedoara,  
5, Revolutiei, 331128, Hunedoara, ROMANIA  
<http://acta.fih.upt.ro>

## INDEXES & DATABASES

We are very pleased to inform that our international scientific journal **ACTA TECHNICA CORVINIENSIS – Bulletin of Engineering** completed its ten years of publication successfully [2008–2017, Tome I–X].

In a very short period the **ACTA TECHNICA CORVINIENSIS – Bulletin of Engineering** has acquired global presence and scholars from all over the world have taken it with great enthusiasm.

We are extremely grateful and heartily acknowledge the kind of support and encouragement from all contributors and all collaborators!

**ACTA TECHNICA CORVINIENSIS – Bulletin of Engineering** is accredited and ranked in the “B+” CATEGORY Journal by CNCIS – The National University Research Council’s Classification of Romanian Journals, position no. 940 (<http://cncsis.gov.ro/>).

**ACTA TECHNICA CORVINIENSIS – Bulletin of Engineering** is a part of the ROAD, the Directory of Open Access scholarly Resources (<http://road.issn.org/>).

**ACTA TECHNICA CORVINIENSIS – Bulletin of Engineering** is also indexed in the digital libraries of the following world’s universities and research centers:

WorldCat – the world’s largest library catalog

<https://www.worldcat.org/>

National Library of Australia

<http://trove.nla.gov.au/>

University Library of Regensburg – GIGA German Institute of Global and Area Studies

<http://opac.giga-hamburg.de/ezb/>

Simon Fraser University – Electronic Journals Library

<http://cufts2.lib.sfu.ca/>

University of Wisconsin-Madison Libraries

<http://library.wisc.edu/>

University of Toronto Libraries

<http://search.library.utoronto.ca/>

The University of Queensland

<https://www.library.uq.edu.au/>

The New York Public Library

<http://nypl.bibliocommons.com/>

State Library of New South Wales

<http://library.sl.nsw.gov.au/>

University of Alberta Libraries - University of Alberta

<http://www.library.ualberta.ca/>

The University of Hong Kong Libraries

<http://sunzi.lib.hku.hk/>

The University Library - The University of California

<http://harvest.lib.ucdavis.edu/>

**ACTA TECHNICA CORVINIENSIS – Bulletin of Engineering** is indexed, abstracted and covered in the world-known bibliographical databases and directories including:

INDEX COPERNICUS – JOURNAL MASTER LIST

<http://journals.indexcopernicus.com/>

GENAMICSJOURNALSEEK Database

<http://journalseek.net/>

DOAJ – Directory of Open Access Journals

<http://www.doaj.org/>

EVISA Database

<http://www.speciation.net/>

CHEMICAL ABSTRACTS SERVICE (CAS)

<http://www.cas.org/>

EBSCO Publishing

<http://www.ebscohost.com/>

GOOGLE SCHOLAR

<http://scholar.google.com>

SCIRUS- Elsevier

<http://www.scirus.com/>

ULRICHWeb – Global serials directory

<http://ulrichweb.serialssolutions.com>

getCITED

<http://www.getcited.org>

BASE - Bielefeld Academic Search Engine

<http://www.base-search.net>

Electronic Journals Library

<http://rzblx1.uni-regensburg.de>

Open J-Gate

<http://www.openj-gate.com>

ProQUEST Research Library

<http://www.proquest.com>

Directory of Research Journals Indexing

<http://www.drji.org/>

Directory Indexing of International Research Journals

<http://www.citefactor.org/>



ISSN: 2067-3809

copyright © University POLITEHNICA Timisoara,

Faculty of Engineering Hunedoara,

5, Revolutiei, 331128, Hunedoara, ROMANIA

<http://acta.fih.upt.ro>



copyright © University POLITEHNICA Timisoara,  
Faculty of Engineering Hunedoara,  
5, Revolutiei, 331128, Hunedoara, ROMANIA  
<http://acta.fih.upt.ro>